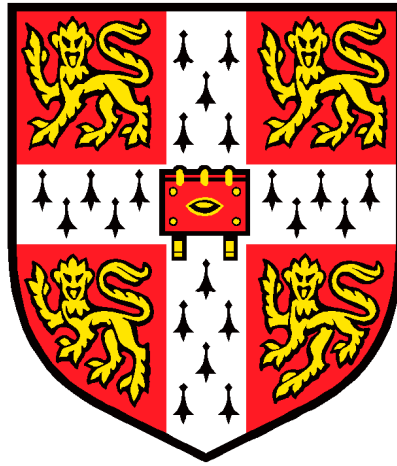


THE IMPACT OF SUBSTRATE TEXTURE ON CELL BEHAVIOR



A THESIS SUBMITTED IN PARTIAL FULFILLMENT OF
THE REQUIREMENTS FOR THE DEGREE OF

Doctor of Philosophy

in

DEPARTMENT OF PHYSICS
THE UNIVERSITY OF CAMBRIDGE

Pooya Karimbabanezhadmamaghani

Peterhouse College, March 2019

Declaration

This thesis is the result of my own work and includes nothing which is the outcome of work done in collaboration except as declared in the Preface and specified in the text. It is not substantially the same as any that I have submitted, or, is being concurrently submitted for a degree or diploma or other qualification at the University of Cambridge or any other University or similar institution except as declared in the Preface and specified in the text. I further state that no substantial part of my thesis has already been submitted, or, is being concurrently submitted for any such degree, diploma or other qualification at the University of Cambridge or any other University or similar institution except as declared in the Preface and specified in the text. It does not exceed the prescribed word limit for the relevant Degree Committee.

Abstract

Traditionally, cell studies have focused mainly on the effects of biochemical signals on cellular behaviour; however, there is a growing interest in investigating the effects of physical cues on the behaviour of the cells. Development of fabrication techniques has allowed researchers to design topographical cues at the micro and nanometer scale. In this study, we fabricated fibronectin stripes, which mimic some of the frequent patterns that cells are exposed to in their natural microenvironment, and studied the effects of these patterns on 3T3 fibroblasts and human mesenchymal stem cells which are of significant importance in the field of regenerative medicine and tissue engineering. Our results show that cells align and elongate in the direction of the patterns and the morphological features of cell, nucleus and architecture of force-bearing stress fibers of the actin cytoskeleton are all highly dependent on the stripe width. 3D confocal measurements showed that the cell thickness and nuclear shape is regulated through the different arrangement of perinuclear actin stress fibers depending on the stripe sizes. We also observed that when the size of stripes (5 μm) is significantly smaller than the size of cell nuclei (subnuclear stripes), cells exhibit 3 different morphological responses to the patterns. Minimal confinement, branching on the stripes and elongation on a single stripe. The majority of cells and nuclei align themselves with the subnuclear stripes; however, a substantial number of hMSCs nuclei are elongated perpendicular to the direction of the pattern, a finding which we explained using a geometrical model based on cell size. The behaviour of 3T3 cell lines and the hMSCs were compared for the different types of pattern.

We designed setups that allow us to perform Raman microspectroscopy both in 2D and 3D topographical patterns in order to be able to study their morpho-chemical effects on cells. We also genetically modified 3T3 fibroblasts to express fluorescent-tagged proteins that visualize the actin cytoskeleton and the nucleus which allow us to perform live cell imaging to study the dynamics of cell behaviour on topographical patterns.

Thesis Title: The Impact of substrate texture on cell behavior

Author: Pooya Karimbabanezhadmamaghani

*To my beloved father and grandma
Who celebrated with me my admission to this course
But could not join me in the joy of graduation.*

Table of Contents

Abstract.....	i
Table of Contents	iii
List of Abbreviations	vii
List of Tables	ix
List of Figures.....	x
Acknowledgement	xv
Chapter 1: Introduction to the cell and its mechanical structure	1
1.1 Structure of a eukaryotic cell.....	1
1.2 Cytoskeleton structure.....	3
1.2.1 Microtubules.....	4
1.2.2 Intermediate filaments.....	6
1.2.3 Microfilaments (Actin filaments).....	7
1.3 Cytoskeleton mechanics and mechanotransduction	9
1.4 Nuclear mechanics and mechanotransduction.....	11
1.5 Cell Adhesion.....	13
1.6 Structure of extracellular matrix	17
Chapter 2: Materials and Methods	20
2.1 Cell line	20
2.1.1 NIH/3T3 fibroblasts	20
2.1.2 Human mesenchymal stem cells	20
2.2 Cell culture	21
2.2.1 Recovery and maintenance of NIH/3T3 cells	21
2.2.2 Recovery and maintenance of hMSCs	22
2.2.3 Cell Banking	24
2.3 The Polydimethylsiloxane (PDMS) substrate.....	25
2.3.1 PDMS preparation	25

2.4 Soft Lithography	26
2.5 Substrate preparation.....	27
2.6 Micro-contact printing	28
2.7 Fluorescent staining	29
2.7.1 Filamentous actin staining	29
2.7.2 Nuclear staining	30
2.7.3 Image analysis.....	30
2.8 Transfection.....	32
2.8.1 Principles of cell transfection.....	32
2.8.2 Transfection for the visualization of the actin cytoskeleton	33
2.8.3 Transfection for the visualization of nuclear Lamin A.....	34
2.9 Microscopy.....	37
2.9.1 Live cell microscopy setup	38
2.9.2 Confocal microscopy	39
2.9.4 Reflection Interference Contrast (RIC) microscopy.....	41
2.9.5 Phase contrast microscopy.....	44
2.10 Raman spectroscopy	45
2.10. 1 Sample preparation on the gold-coated mirrors.....	47
2.10.2 Metal coating of the patterned substrate	48
Chapter 3: Review of the effects of topographical patterns on cell behaviour	50
3.1 Origin of the subject	50
3.2 Different types of topographical cues.....	55
3.3 Application of topographical patterns in study and control of cellular and nuclear mechanics	57
3.4 The effect of ridge-groove and microprinted stripes on the cell.....	60
Chapter 4: A review on stem cells and how they are affected by physical cues.....	65

4.1 Differentiation hierarchy of stem cells	67
4.1.1 Totipotent	68
4.1.2 Pluripotent	68
4.1.3 Multipotent	69
4.1.4 Oligopotent	70
4.1.5 Unipotent	70
4.2 Human stem cell classification	71
4.2.1 Embryonic stem cells (ESCs)	71
4.2.2 Foetal Stem cells	72
4.2.3 Cord blood stem cells	72
4.2.4 Adult stem cells	73
4.2.5 Induced pluripotent stem cells	74
4.3 Mesenchymal stem cells (MSCs)	75
4.3.1 Mechanical and cytoskeletal properties of MSCs	77
4.3.2 The effect of physical cues on MSCs	79
Chapter 5: The impact of fibronectin stripe patterns on the cellular and nuclear morphology of fibroblasts	93
5.1 Fibroblasts	93
5.2 Adhesion process of fibroblasts	98
5.3 Fibroblasts on the fibronectin stripes	99
5.4 3D shape of fibroblasts on fibronectin stripes	104
5.5 Fibroblasts on sub-nuclear fibronectin stripes	113
Chapter 6: The impact of fibronectin stripe patterns on the cellular and nuclear morphology of mesenchymal stem cells	120
6.1 Mesenchymal stem cells in culture	120
6.2 Mesenchymal stem cells on fibronectin stripe patterns	126
6.2.1 How patterns influence the orientation of the nucleus inside the cell	130

6.2.2 Interaction between the cytoskeleton and the nucleus of hMSCs on fibronectin stripe patterns in the single cell level	131
6.3 3D shape of hMSCs on fibronectin stripes	133
6.4 hMSCs on sub-nuclear fibronectin stripes	136
6.4.1 Morphological features of the hMSCs on sub-nuclear stripes	136
6.4.2 Orientation of the hMSCs on sub-nuclear stripes	140
Chapter 7: Potential further avenues for studying substrate topography effects on cells	145
7.1 Raman micro-spectroscopy as a tool for studying the effect substrate topography on cells	145
7.1.1 Principles of Raman spectroscopy	145
7.1.2 Raman micro-spectroscopy for cells	148
7.2 Genetic modification of cells for live cell imaging	160
7.2.1 Cell transfection for visualization of the actin cytoskeleton	160
7.2.2 Cell transfection for visualization of the nucleus	163
Chapter 8: Conclusion and future works	166
8.1 Conclusion	166
8.2 Suggested further work	174
Bibliography	177

List of Abbreviations

3T3	3-day Transfer, inoculum 3×10^5 cells
A	Adenine
ACAFs	Actin cap associated fibres
AFM	Atomic force microscopy
AR	Aspect ratio
Arp	Actin-related proteins
BSA	Bovine Serum Albumin
CAMs	Cell adhesion molecules
CCD	Charge-Coupled Device
DMEM	Dulbecco's Modified Eagle's medium
DMSO	Dimethyl Sulfoxide
DNA	Deoxyribonucleic acid
DPBS	Dulbecco's Phosphate Buffered Saline
ECM	Extracellular Matrix
EDTA	Ethylenediaminetetraacetic Acid
EGFP	Enhanced Green Fluorescent Protein
ES cells	Embryonic Stem cells
FA	Focal adhesion
F-actin	Filamentous actin
FAK	Focal Adhesion Kinase
FBS	Fetal Bovine Serum
FN	Fibronectin
G-actin	Globular actin
GAGs	Glycosaminoglycans
GTP	Guanosine Triphosphate
GFP	Green Fluorescence Protein
hMSCs	human Mesenchymal Stem Cells
HSCs	Hematopoietic Stem Cells
IFs	Intermediate Filaments
IgSF CAMs	Immunoglobulin superfamily Cell Adhesion Molecules
INM	Inner Nuclear Membrane
KASH	Klarsicht, Anc-1, Syne homology
LB	Lysogeny broth
LINC	Linker of Nucleoskeleton and Cytoskeleton

MAP2	Microtubule-Associated Protein 2
MFs	Actin filaments
MTs	Microtubules
mRNA	Messenger ribonucleic acid
MSCs	Mesenchymal stem cells
NeuN	Neuronal nuclear antigen
ONM	Outer Nuclear Membrane
PBS	Phosphate Buffered Saline
PDMS	Polydimethylsiloxane
PNS	Perinuclear Space
PUV	Polyurethane acrylate
RGD	Arginyl-glycyl-aspartic acid
RICM	Reflection Interference Contrast Microscopy
RNA	Ribonucleic acid
RPM	Revolutions per Minute
rRNA	Ribosomal ribonucleic acid
SCCM	Standard Cubic Centimeters per Minute
SEM	Scanning Electron Microscopy
SMCs	Smooth Muscle Cells
SSP	Single Side Polished
SUN	Sad1 and UNC-84 homology domain
TB	Trypan-Blue
TCP	Tissue Culture Polystyrene
TE	Tris-EDTA
TEM	Transmission Electron Microscopy
TGF- β	Transforming Growth Factor-beta
UCB-MSCs	Umbilical cord blood-derived mesenchymal stem
tRNA	Transfer ribonucleic acid
UV	Ultra Violet

List of Tables

Table 7-1: Raman peak assignments of dominant peaks.	153
---	-----

List of Figures

Figure 1-1: Internal structure and internal organelle of an animal eukaryotic cell.....	2
Figure 1-2: Cytoskeletal elements.	4
Figure 1-3: Microtubules	6
Figure 1-4: Molecular structure of Intermediate filaments.....	7
Figure 1-5: Formation of actin filaments.....	8
Figure 1-6: Network of cytoskeletal filaments.	9
Figure 1-7: The molecular structure of linkage between nuclear lamina, cytoskeletal filaments and chromatins.	12
Figure 1-8: Diagram of the adhesion mechanism of major types of CAMs.....	14
Figure 1-9: Diagram of an adherent cell, illustrating the close connection between adhesion process and cell protrusions.	15
Figure 1-10: The molecular machinery of changing actin cytoskeleton in the focal complex sites.	16
Figure 1-11: Composition and schematic view of ECM	17
Figure 1-12: Structure of fibronectin molecule and fibronectin matrices.....	19
Figure 2-1: Phase contrast image of adherent NIH/3T3 cells on a 25 cm ² cell culture flask	20
Figure 2-2: Phase contrast image of adherent hMSCs cells on a 25 cm ² cell culture flask	21
Figure 2-3: Schematic view of the fabrication process of pattern printing on the SU-8 film using soft lithography technique.....	27
Figure 2-4: Fabrication of PDMS stamps from SU-8 patterns.	27
Figure 2-5: Materials used in the pattern preparation.....	28
Figure 2-6: Micro-contact printing of the fibronectin stripe patterns from PDMS stamps.	29
Figure 2-7: Error estimation for area measurement.....	32
Figure 2-8: Liposome-based transfection schematic diagram.	33
Figure 2-9: Structure and experimental items for storing, amplification, stocking and transfection of pBABE-puro-GFP-wt-lamin A plasmid DNA.	36
Figure 2-10: Measurement of purified DNA plasmid concentration.....	37
Figure 2-11: Microscope setting for live cell imaging.....	38

Figure 2-12: Schematic view of confocal microscopy.	39
Figure 2-13: Schematic view of DIC microscopy.	40
Figure 2-14: Schematic view of a RIC microscope.	42
Figure 2-15: Conceptual illustration of image formation in RIC as a result of interference between reflected rays from the sample and the substrate.	42
Figure 2-16: Dependency of the intensity of reflected ray to the distance between sample and substrate.	43
Figure 2-17: The phase contrast microscopy.	44
Figure 2-18: Calibration spectrum of Raman microscope using silicon wafer.	46
Figure 2-19: A gold mirror for Raman microscopy.	47
Figure 2-20: Schematic illustration of E-beam evaporator function's principle.	49
Figure 3-1. The effect of substrate texture on the chick embryonic cells (duodenum of 9-day chick embryo).	51
Figure 3-2: The polarization of medullary cord cells on the patterns made of a spider web.	52
Figure 3-3: Diagram illustration of different groove patterns on mica substrate used by Weiss in 1945 to study nerve growth.	53
Figure 3-4: Contact guidance of cells on grooved mica and glass fibres.	54
Figure 3-5: Typical geometries of micropatterns in biomaterials.	56
Figure 3-6: Fibronectin-doted micropatterns for the quantitative study of actin edge bundles.	57
Figure 3-7: Using nanopillar arrays to probe the mechanics of the nucleus.	59
Figure 3-8: Three different attachment regime observed on 3T3 fibroblast spreading on ridge-groove substrates with different ridge/groove sizes.	62
Figure 4-1: Division and differentiation of stem cells.	66
Figure 4-2: Zygote is the first totipotent stem cell created by the fusion of sperm and Oocyte cells.	67
Figure 4-3: Blastula undergoes a gastrulation process and becomes a gastrula which consists of three groups of cells or three germ layers. Endoderm (green), Mesoderm (red) and Ectoderm (yellow).	69
Figure 4-4: Differentiation hierarchy for HSCs as an illustration for multipotent, oligopotent and terminal mature blood cells.	70
Figure 4-5: Classification of human stem cells and the origin of their isolation (yellow). 71	

Figure 4-6: The proposed cycle of application of cell reprogramming in regenerative medicine.....	75
Figure 4-7: Differentiation of MSCs into cells with different lineages.	76
Figure 4-8: Stiffness range of MSCs and cell lineages that are differentiated from them measured by AFM.....	77
Figure 4-9: The approximate elastic modulus of tissues and matrix microenvironments that host different cell lines differentiated from MSCs.	80
Figure 4-10: Bright field microscopy of morphological evolution of MSCs cultured on collagen type I coated polyacrylamide substrate with different stiffness.	81
Figure 4-11: Mechanotransduction mechanism of matrix stiffness mediated stem cells differentiation.....	83
Figure 4-12: Cytoskeletal structure and adhesion state of MSCs cultured on substrates with different stiffness.	84
Figure 4-13: Classification of different topographic features of synthetic substrates (biomaterials) that affect MSCs behaviour and fate.	86
Figure 4-14: The effect of aligned TiO ₂ nanotubes with different diameters on MSCs and osteoblasts.....	87
Figure 4-15: The effect of micro and nano-scale ridge-groove pattern on PI on MSCs. ..	89
Figure 4-16: The influence of fibronectin patterns shape on the cytoskeletal structure of MSCs.....	92
Figure 5-1: Morphological diversity of NIH/3T3 fibroblasts.....	94
Figure 5-2: Phase contrast microscopy of 3T3 fibroblasts detachment from the substrate	95
Figure 5-3: NIH/3T3 fibroblasts in the suspension.....	97
Figure 5-4: The adhesion evolution of NIH/3T3 fibroblasts on 25 cm ² flask substrate....	98
Figure 5-5: The fibronectin stripe patterns and their <i>in vivo</i>	100
Figure 5-6: The fibronectin stripe patterns and morphological effects of them on the NIH/3T3 fibroblasts.	102
Figure 5-7: Confocal microscopy of cells on fibronectin stripes.....	104
Figure 5-8: The 3D shape of fibroblasts on the fibronectin fibres with different geometry.	105
Figure 5-9: Perinuclear actin stress fibers of 3T3 fibroblasts on fibronectin patterns.....	108
Figure 5-10: The 3D shape of the nucleus and organization of actin stress fibres of fibroblasts on the fibronectin stripes.....	109

Figure 5-11: Schematic of the configuration of actin fibres and associated focal adhesions in adherent cells.	110
Figure 5-12: Cellular and nuclear volume change on fibronectin stripes.	111
Figure 5-13: Fluorescent micrographs of different morphology of 3T3 fibroblasts on a sub-nuclear fibronectin pattern of stripes.	114
Figure 5-14: The aspect ratio of 3T3 fibroblasts on the sub-nuclear pattern.	115
Figure 5-15: Projected area of 3T3 Fibroblasts on sub-nuclear pattern and control substrate.	116
Figure 6-1: Phase contrast images of hMSCs on a 25 cm ² cell culture flask.	122
Figure 6-2: hMSCs in suspension.	124
Figure 6-3: Anoikis and long-term culture of hMSCs.	126
Figure 6-4: The morphological effects of fibronectin stripe patterns on the hMSCs.	128
Figure 6-5: The orientation of nuclei of hMSCs relative to cytoskeleton on fibronectin stripes.	130
Figure 6-6: Single cell-based relationship between nucleus size and cell size of hMSCs on fibronectin stripes.	132
Figure 6-7: The 3D shape of hMSCs on the fibronectin fibres with different geometry.	134
Figure 6-8: Maximum cell thickness and number of perinuclear actin stress fibers of hMSCs on fibronectin patterns.	135
Figure 6-9 Single cell-based relationship between maximum cell thickness and number of perinuclear actin fibers of hMSCs on fibronectin stripes.	135
Figure 6-10: The 3D shape of the nucleus of hMSCs on the fibronectin stripes.	136
Figure 6-11: Fluorescent micrographs of the different morphologies of hMSCs on a sub-nuclear fibronectin pattern of stripes.	137
Figure 6-12: The aspect ratio of hMSCs on the sub-nuclear pattern.	139
Figure 6-13: Projected area of hMSCs on sub-nuclear pattern and control substrate.	140
Figure 6-14: The orientation of hMSCs' cytoskeleton on sub-nuclear stripes pattern.	141
Figure 6-15: The orientation of hMSCs nuclei on the sub-nuclear stripes pattern.	142
Figure 6-16: Perpendicular hMSCs nuclei that defy basal and perinuclear actin fibers on sub-nuclear strip patterns.	143
Figure 6-17: Schematic illustration for orientation of nucleus perpendicular to sub-nuclear stripes pattern.	144
Figure 7-1: Different scattering modes.	146
Figure 7-2: Energy level diagram of Raman and Rayleigh scattering.	147

Figure 7-3: Schematic diagram of spontaneous confocal Raman micro-spectroscopy. ...	148
Figure 7-4: Bright field image of a 4% formaldehyde fixed adherent 3T3 cell on fibronectin-coated PDMS surface prepared for the Raman micro-spectroscopy.	149
Figure 7-5: Spatial Raman micro-spectroscopic map of a formaldehyde 3T3 cells spreading on fibronectin-coated PDMS substrate.	150
Figure 7-6: Spatial Raman micro-spectroscopic map of a protein and DNA/RNA associated with a formaldehyde-fixed 3T3 cell spreading on the fibronectin PDMS substrate.....	151
Figure 7-7: Raman spectra from a methanol fixed 3T3 cell.	152
Figure 7-8: Spatial Raman micro-spectroscopic map of a DNA/RNA associated peak (780 cm-1) of a methanol-fixed 3T3 cell on the silica-coated gold mirror.....	154
Figure 7-9: Formaldehyde fixed NIH/3T3 cells after 12 hours spreading on the silica protected the gold mirror.	155
Figure 7-10: Morphological parameters of 3T3 cells spreading on a silica-coated gold mirror and on the fibronectin-coated PDMS substrate.	156
Figure 7-11: Proposed novel setup to shield the Raman signal of the 3D PDMS patterns.	157
Figure 7-12: Actin visualization using pCMVLifeAct-TagGFP2 transfection.	161
Figure 7-14: Morphological effects of transfection on 3T3 fibroblasts.....	163
Figure 7-15: Nucleus visualization using pBABE-puro-GFP-wt-lamin A transfection. .	164
Figure 8-1: Connected 3T3 fibroblasts.	175

Acknowledgement

There are many people without whose help, I would have never developed this project so far and I would like to express my sincere thanks to all of them.

Professor Dame Athene Donald (supervisor), Dr. Ottavio Croze (co-supervisor), Dr. Chenh-kuang Huang (former PhD student in the group and major contributor to foundations of the project), Fiona Morgan (cell culture lab manager at the physics of medicine lab), and all staff of the Cavendish Laboratories, Biological and Soft Systems group, Peterhouse college and the Cambridge Nanoscience Centre.

I would like also to sincerely thank Liung Wang and Dr Estelle Brendon for bacterial lab training and Lindsey Ibbotson and Juan A. Rubio-Lara for e-Beam Evaporator training.

I would also like to especially thank Dr Sarah Bohndiek and her students, Ben Woodhams and Dr Jakub Surmacki for cooperating with me to use Raman spectroscopy lab, Professor Pietro Cicuta, Dr Lorenzo Di Michele, Dr Kevin Chalute and Professor Eugene Terentjev for their valuable scientific and technical advice.

Chapter 1:

Introduction to the cell and its mechanical structure

Cells are the building blocks of the life and similar to every other machine, they are made of smaller building blocks that perform a cascade of coordinated functions and they influence each other via numerous chemical and mechanical feedback circuits. These interactions result in complex cellular behaviour. In order to understand the physics of cell function and the effect of substrate topography on them, we first need to understand the physical structure of elements that bear, generate and transmit mechanical signals inside a cell. In this chapter, we will try to give a brief overview of vital organelles of a eukaryotic cell and elements of the cytoskeleton and nucleus that play key roles in sensing and transducing mechanical cues of the microenvironment and generating mechanical reactions of the cells to these cues. In addition, we will introduce briefly the composition and mechanical properties of the extracellular matrix (ECM) that form the natural microenvironment of the cell and the mechanism of interaction of the cell and ECM which regulates cell adhesion to this matrix.

Chapter one will give necessary knowledge about the biology and structure of cells and their microenvironment which is required for understanding the next chapters and particularly the findings of this thesis.

1.1 Structure of a eukaryotic cell

Eukaryotic cells are the building blocks of various unicellular and multicellular living organisms such as algae, yeasts, fungi, protozoa, plants and animals ('Eukaryotic Cell', 2011). As the etymology of their name suggests (Greek: EU 'well'+ karyon 'nut'), eukaryotic cells are enclosed by a cellular membrane and are made of internal membrane-bound organelles which together make up the endomembrane system (Burnap & Vermaas 2012) (Figure 1-1). The size of eukaryotic cells can vary within the range of 10-100 μm and this makes them huge cells in comparison with prokaryotic cells (bacteria and archaea) with a typical size of 1-10 μm .

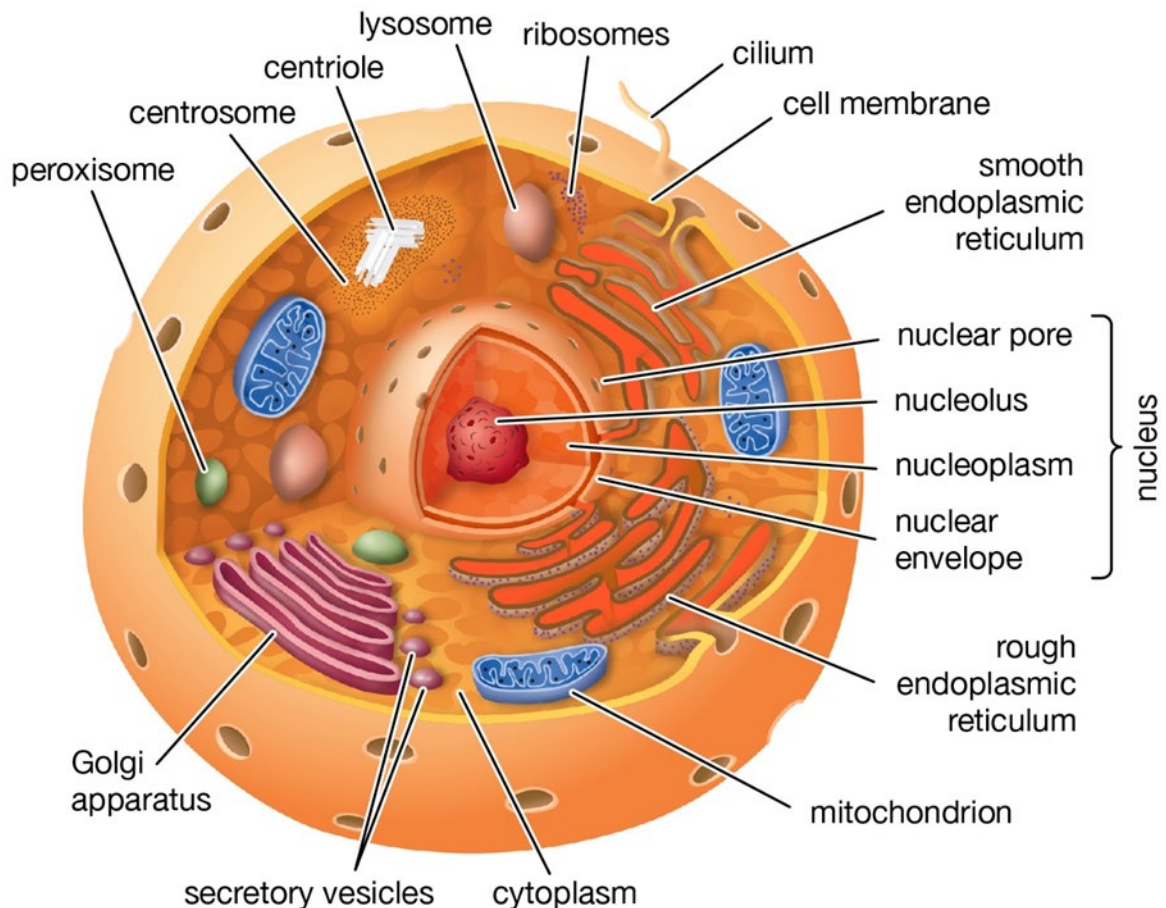


Figure 1-1: Internal structure and internal organelle of an animal eukaryotic cell. (Encyclopædia Britannica, Inc, 2018).

Unlike prokaryotic cells, eukaryotic cells have a well-structured and enclosed nucleus inside a membrane boundary that contains genetic material of the cells. The nucleus is the biggest organelle of the cells and it can occupy approximately 10% of the cell volume with an approximate diameter of 6 μm in mammalian cells (Lodish 2000). The nuclear membrane consists of a double-layer structure with an approximate distance of 10-50 nm between the inner nuclear membrane (INM) and the outer nuclear membrane (ONM) which is called the perinuclear space (PNS). On the nucleus membrane, there are pores with an approximate diameter of 100 Å that acts as a size exclusion filter that restricts diffusion of macromolecules between the cytoplasm and the nucleus while permitting passage of smaller molecules with vital functions, such as mRNA (Paine et al. 1975). The nucleolus is a dense domain inside the nucleus, with an approximate diameter of 0.5 μm , that is not enclosed by a membrane (sometimes it is called a suborganelle) and which acts as the ribosome factory of the cell by synthesizing ribosomal RNA (rRNA) and assembling ribosomes (Hernandez-Verdun 2006).

Similar to the cytoplasm in the cell itself, the nucleus also has a nucleoplasm that accommodates chromosomes and other nuclear structures and organelles (Lodish 2000).

Ribosomes are small (25-30 nm) but complex molecular machines that act as sites for protein synthesizing inside the cell by linking messenger RNA (mRNA), which encodes a recipe for a synthesizing protein, and transfer RNAs (tRNA) which carry amino acids sequence of the protein (Wilson & Doudna Cate 2012).

The protein-synthesizing ribosomes are attached to a network of membranous tubules (known as cisternae) that are continuous with the outer membrane of the nucleus and which is known as the rough endoplasmic reticulum. The soft endoplasmic reticulum doesn't play a role in protein synthesis as it doesn't host ribosomes; however, it is involved in lipid synthesis and metabolism and is abundant in some mammalian cells such as liver cells (*Endoplasmic Reticulum (Rough and Smooth) | British Society for Cell Biology*).

The synthesized proteins are packaged by the Golgi apparatus inside lipid bilayer membrane-enclosed vesicles such as secretory vesicles before they are sent to their destination inside the cell (Short & Barr 2000).

The cell uses adenosine triphosphate (ATP) as the main source of chemical energy which is mostly supplied by the mitochondria which vary in size (0.75 to 3 μm) and number in different cells (Wiemerslage & Lee 2016).

Lysosomes (0.1 to 1.2 μm) and peroxisomes (0.5 to 1.5 μm) are vesicles that are filled with enzymes and help the cell to break down various types of biomolecules (Kühnel & Kühnel 2003),(Wanders & Waterham 2006).

Centrosomes and the centriole produce structures that stretch chromosomes during cell mitosis cell division (see 1.2.1)(Rieder et al. 2001).

1.2 Cytoskeleton structure

The main function of the cytoskeleton is to maintain cell shape and internal organization and provide the cell with essential mechanical support and machinery to carry out key cellular functions such as cell division, adherence and motility. In eukaryotic cells, the cytoskeleton is composed of interconnected filamentous polymers and regulatory proteins. The cytoskeletal polymers can be classified into three major groups based on their size and protein compositions: actin filaments or microfilaments, intermediate filaments (IFs) and microtubules (Figure 1-2).

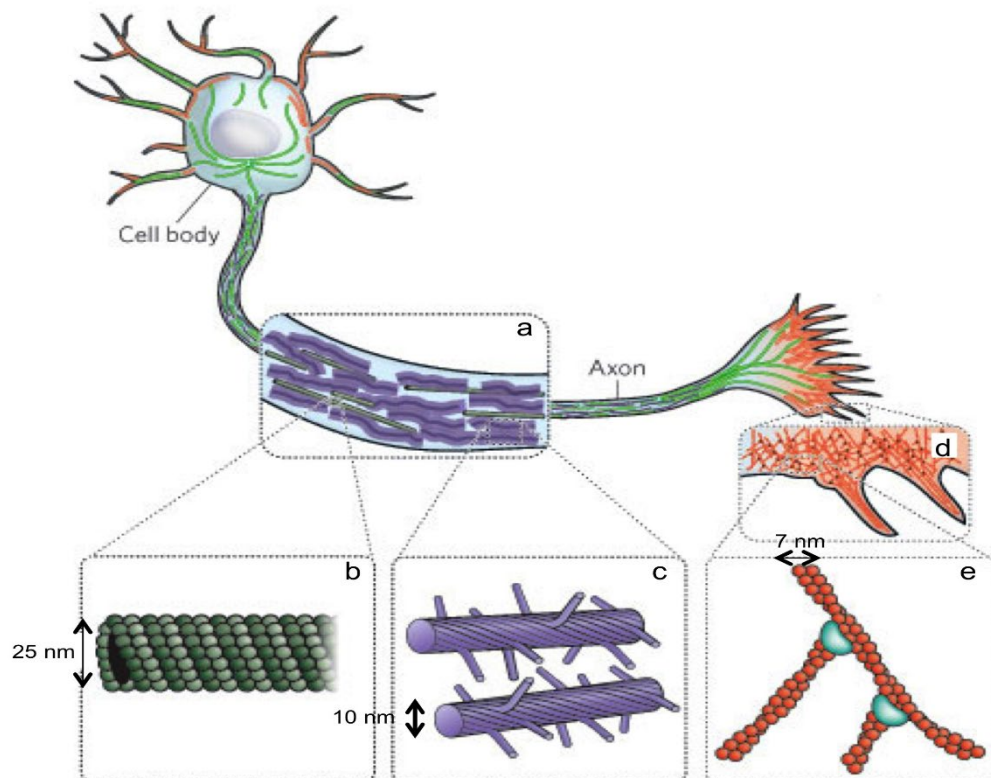


Figure 1-2: Cytoskeletal elements. The cytoskeleton of eukaryotic cells helps to maintain the cell shape and carry out essential cell functions. It consists of three major building block polymers: actin filaments (orange), intermediate filaments (purple) and microtubules (green). A neuron cell is selected to demonstrate these filaments. **(a)** The axon is an extended part of the cytoskeleton that enables the cell to transport materials from the cell body to axon terminal using a network of microtubules embed in neurofilaments which is a class of intermediate filaments. **(b)** Microtubules with an outer diameter of 25 nm and the inner diameter of 12 nm, the length of these polymers can grow to 5,000 μm . **(c)** Intermediate filaments have a diameter of 10 nm and their length can grow to 0.5 μm . They can create many branches formed by Arp2/3 complex (blue). **(d)** A network of dendritic filaments and parallel actin-filament filopodia enables the cell to migrate in response to chemical cues. **(e)** Actin filaments are the smallest cytoskeletal elements with 7 nm diameter and they can grow to 13.5 μm in length. After (Fletcher & Mullins 2010a).

1.2.1 Microtubules

Microtubules are the largest building blocks of the cytoplasm. Their shape is that of a rigid hollow cylinder with an outer diameter of approximately 25 nm and an inner diameter of 14 nm. Microtubules consist of a dimer composed of two globular proteins, α and β tubulins, assembled into linear protofilaments (Cooper 2000). In mammalian cells, a single microtubule is made up from 13

protofilaments; however, this number varies from 10 to 15 for other cells (Burton et al. 1975),(Voglis & Tavernarakis 2005),(Lodish et al. 2000b). Microtubules can grow up to 5 mm in length to form a linear track long enough to span the length of a cell (Jordan & Wilson 2004). The growing and shrinking of microtubules is a result of a rapid polymerization and depolymerization process driven by energy released from dephosphorylation of Guanosine Triphosphate (GTP), an ATP analogous molecule (Figure 1-3). The possibility of a rapid switch between polymerization and depolymerization, 'dynamic instability', allows the cytoskeletal microtubules to search the cell 1,000 times faster than a polymer that is only sensitive to the concentration gradient of its building units or to the actions of regulatory proteins (Holy & Leibler 1994). Microtubules are the stiffest among the cytoskeletal filaments and are polarized polymers with the fast-growing (plus) end and the slow-growing (minus) end. Microtubules are the highways of cytoplasm with motor proteins like kinesin and dynein transporting cellular cargo along with them. The polarity of microtubules is very important in defining the direction of movement for motor proteins (Hirokawa et al. 2009). The third type of tubulin (γ -tubulin), plays an essential role in initiating microtubule assembly (Conde & Cáceres 2009). In non-dividing cells, microtubules radiate from the centrosome toward the plasma membrane. This way, the arrangement defines the basic organization of the cytoplasm and positions of the cellular organelles (Conde & Cáceres 2009) (Figure 1-3).

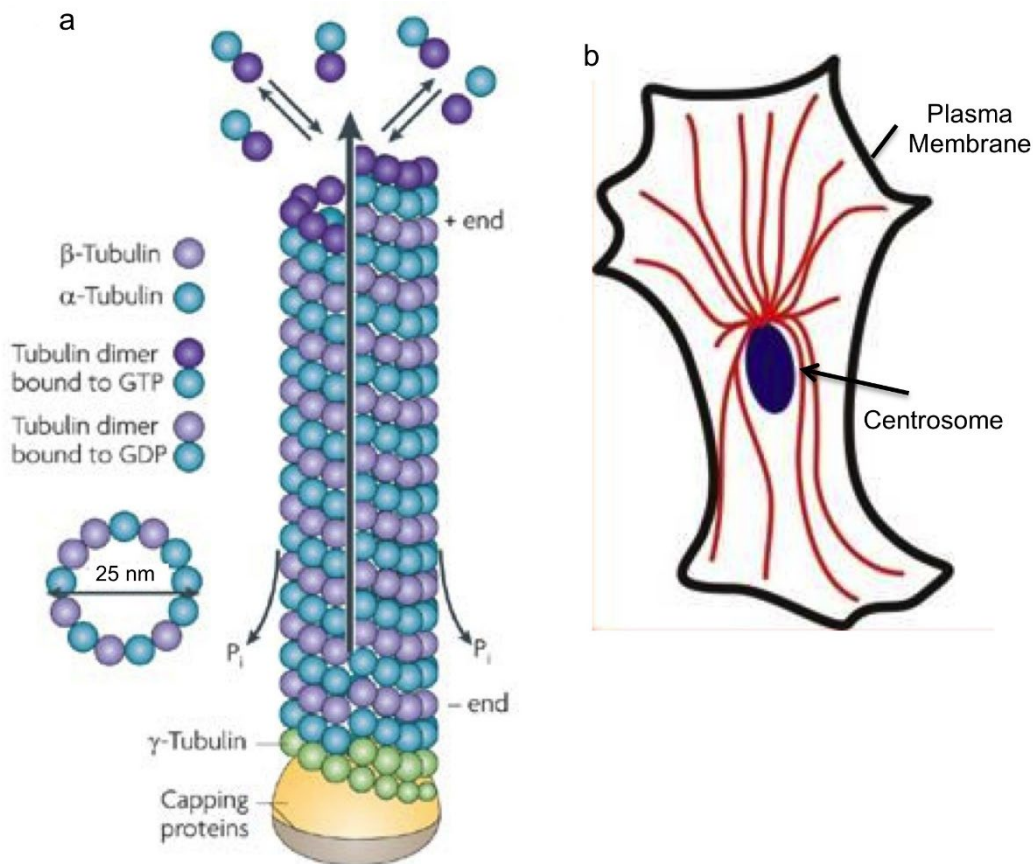


Figure 1-3: Microtubules. (a) The molecular structure of the microtubules and mechanism of polymerization (growing) and depolymerization (shrinking). (b) The schematic configuration of cytoskeletal microtubule filaments (red) in a non- dividing eukaryotic cell. After (Conde & Cáceres 2009) and (Miroslav Holeček 2011).

1.2.2 Intermediate filaments

Unlike microtubules and actin filaments, IF proteins come in many types and classes. In the human cell, there are at least 65 genes that encode for intermediate filaments (Fuchs & Weber 1994). The average diameter of these filaments is about 10 nm (9-11 nm). They are composed of eight smaller rod-shaped protofilaments twist-bundled together to form rope-like filaments (Figure 1-4). The persistence length of IFs can reach $\sim 1 \mu\text{m}$ and they are the least stiff of the three cytoskeletal filaments.

They are unusually extensible with a strong resistance to breakage compared to other filaments. They can resist tensile forces more effectively than compressive forces (Kreplak & Fudge 2007). IFs can

be interconnected to each other or be crosslinked to the microtubules and actin filaments using a group of large size (>500 KD) proteins called plectins, a subunit of plakins (Wiche 1998) (Figure 1-6).

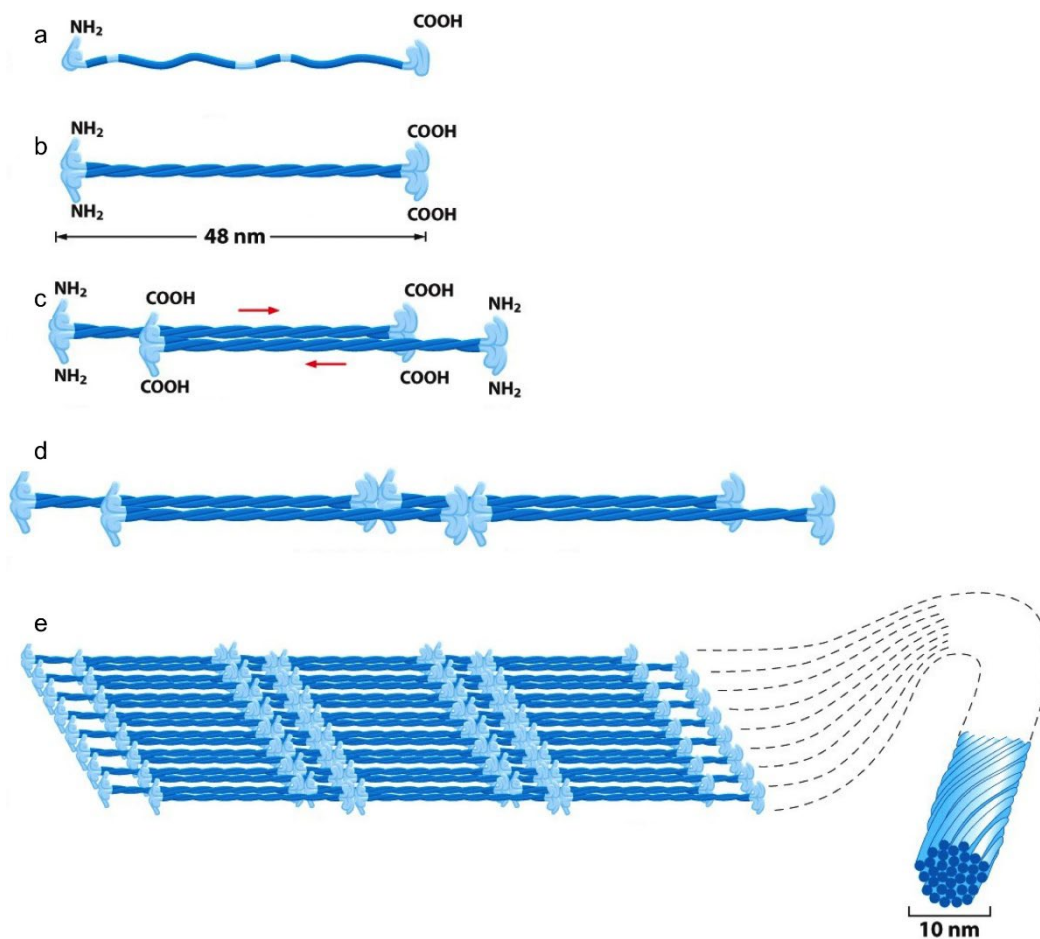


Figure 1-4: Molecular structure of Intermediate filaments. (a) The α -helical region in the monomer. (b) Two monomer bundle together to make the coil-coiled parallel dimer. (c) Two coil-coiled dimers twist together to make the antiparallel tetramer. (d) Two tetramer pack together to make a protofilament. (e) A bundle of eight protofilaments builds the rope-like conformation of an Intermediate filament. After, Essential cell biology, 3rd edition, @ Garland Science 2010.

Most IFs are cytoskeletal filaments, however, one class of IFs are nuclear lamins. This class of polymers is the main contributor to nuclear integrity and mechanical behaviour in the eukaryotic cells (Gruenbaum & Foisner 2015). Unlike microtubules and actin filaments, IFs are not polarized; therefore, they don't support the directional movement of motor proteins.

1.2.3 Microfilaments (Actin filaments)

With a radius of 7 nm and a helical structure repeating every 37 nm, these filaments are the smallest cytoskeletal filaments of eukaryotic cells. Filamentous actin (F-actin) is polymerized from the free

monomer G-actin (globular actin). G-actin monomers bind to ATP in a process called activation. In the presence of nucleation factors (i.e. Arp 2/3), an ATP-actin complex forms the nucleus of a growing filament (nucleation). The formed filament elongates with the addition of more ATP-actin complexes (elongation). The force that has been created during the elongation stage supplies the required force for the advancing leading edge of a migrating cell (Gruenbaum & Foisner 2015). The filament is a polarized molecule with ATP-powered growth at the plus end and shrinkage at the minus end due to the low affinity of ADP-actin complexes. In the steady state, the rate of ATP powered polymerization is equal to depolymerization at the minus end (Figure 1-5).

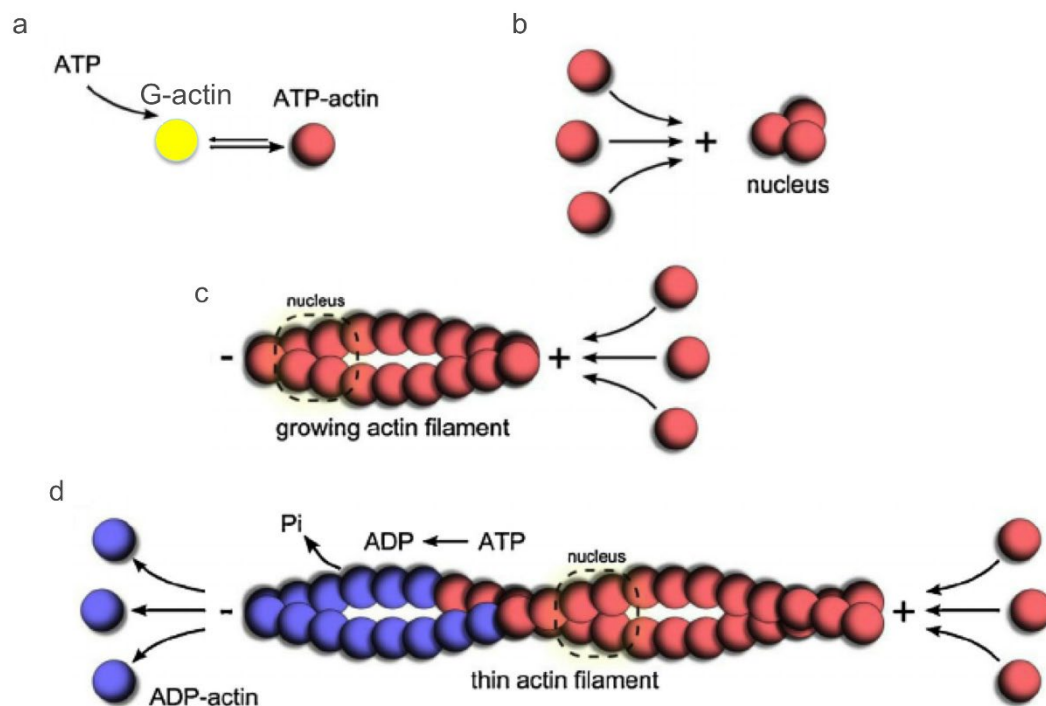


Figure 1-5: Formation of actin filaments. (a) Activation of G-actin by ATP. (b) ATP-actin condensate to form the nucleus of the emerging filament (nucleation). (c) More ATP-actin monomers add to elongate the filament (elongation). (d) The equal rate of depolymerization and polymerization gives the steady-state length to the filament. After (Grzanka et al. 2013).

Actin filaments can make branched and crosslinked structures using Arp 2/3 junction proteins (Figure 1-2) and crosslinking proteins. Therefore, they can form highly organized and stiff structures, such as bundled networks, branched networks and isotropic networks (Fletcher & Mullins 2010a). Unlike microtubules that organize around one or two organization centres, the actin cytoskeleton constantly gets polymerized and depolymerized in response to the local activity of signalling systems (Parent 2004). The polarized structure of the actin filaments builds intercellular highways for the ATP driven

myosin motor proteins. In non-dividing cells, actin filaments are locally aligned and the direction of these aligned filaments are dynamically changing (see chapter 5) in the cell (cytoplasmic contractile bundles) (Figure 1-6), as lamellipodia and filopodia in adherent cells (Figure 1-9) and in the microvilli.

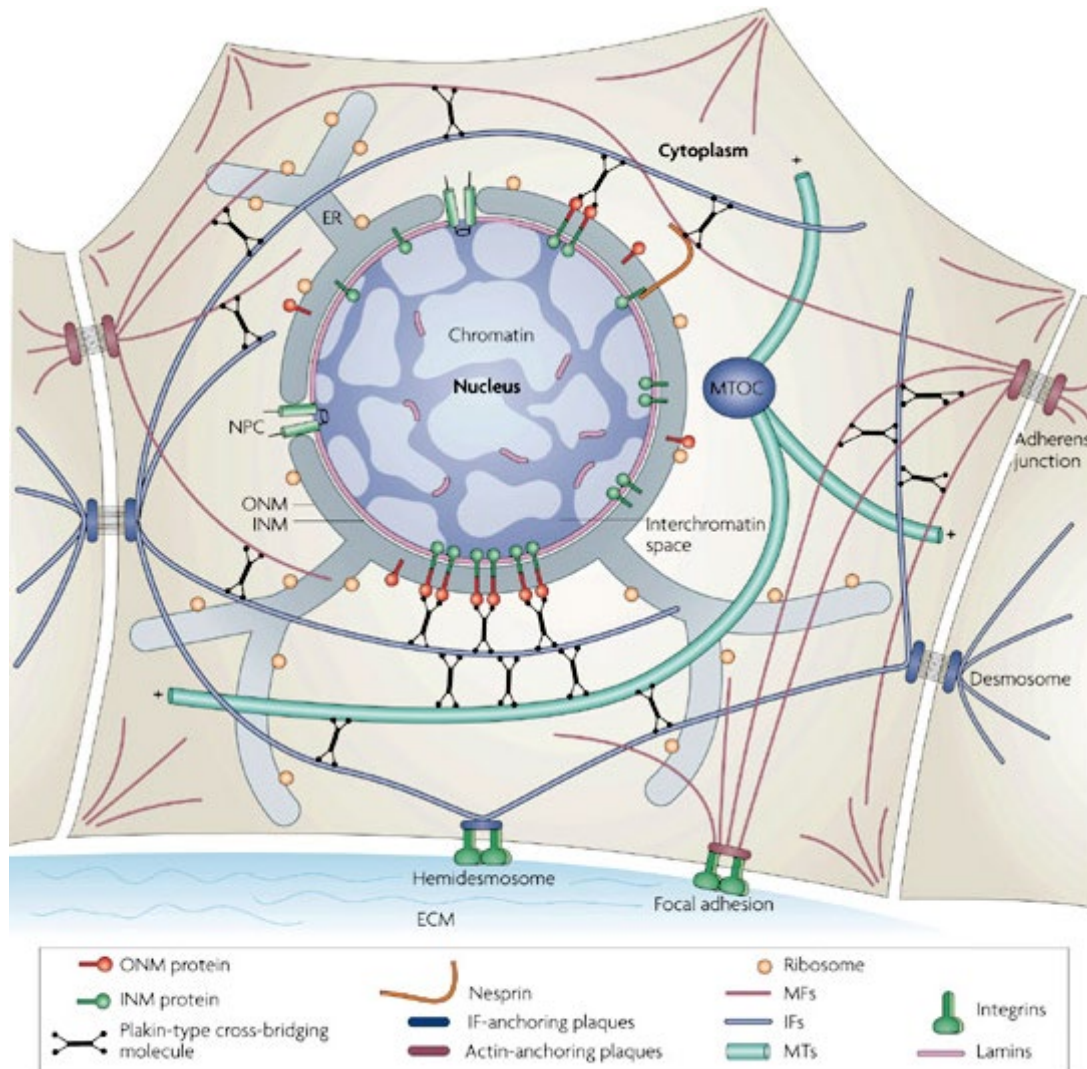


Figure 1-6: Network of cytoskeletal filaments. The configuration and interconnection of microtubules (MTs), IFs and actin filaments (MFs) in the cytoskeleton of a non-dividing eukaryotic cell (Herrmann et al. 2007).

1.3 Cytoskeleton mechanics and mechanotransduction

In general, the mechanical ordering that transforms the cytoskeleton from a chaotic collection of proteins to a highly organized system can be classified into two categories: long-range order with an effective range of tens of micrometers (cell dimensions) and a short, local order that dominates the cytoskeletal events at a molecular level (a few nanometers). The long-range order is mainly established

by actin and tubulin networks; however, the short-range order is governed by highly sophisticated protein machinery (Fletcher & Mullins 2010b). A wide range of crosslinkers links cytoskeletal polymers together to create an architecture that plays a central role in transmitting tensile and compressive stresses as well as sensing the mechanical microenvironment (Janmey & McCulloch 2007). Most of the models which have been generated for the mechanical behaviour of the cytoskeleton are based on *in vitro* studies on gels formed from purified cytoskeletal polymers. However motivated by new microscopic and rheological techniques, there is a rising interest for more complex *in vivo* studies of force transmission mechanisms (both internally and externally generated forces), of the cell.

The elastic modulus for the tissue matrix varies from ~100 Pa for less stiff tissues such as neurons to ~100 kPa for collagenous bone (Engler et al. 2006). The elastic modulus of single cells in culture has been measured by various microrheological methods such as elongation between plates, atomic force microscopy (AFM), microaspiration, optical stretchers, magnetic twisting rheometry, tracer diffusion, uniaxial stretching rheometer global rheometry, uniaxial compression and global compression (Ahmed et al. 2015). Although the measured value for elastic modulus is generally dependent on the method of measurement and the region of the cell that the measurement is performed, the results illustrate that the modulus for living cells varies ranges from ~100 Pa to ~30 kPa (Engler et al. 2006)(Guz et al. 2014). This range can be linked to the stiffness of cytoskeletal polymers by consideration of some simple estimations. *In vitro* studies have shown that the elastic modulus of the actin (at a concentration of 15 μM (0.63 mg/mL)) when crosslinked by actin-binding proteins such alpha-actinin (is of the order of 1000 dyne/cm² (100 Pa) (Wachsstock et al. 1993). The concentration of actin is typically 2-3 mg/ml (46-70 μM) in non-muscle cells and is approximately 10-30 mg/mL (230-960 μM) for muscle cells. Therefore, an approximation of 10 mg/mL sounds reasonable. There is an experimentally supported theory that shows the elastic modulus of semiflexible polymers is proportional to the square of the polymer concentration (MacKintosh et al. 1995). Taking this into account the elasticity modulus of actin at 10 mg/ml is of the order of 10 kPa, which is within the typical range of cell elasticity. It has been shown that intermediate filaments also contribute to the cell stiffness only when they deform due to other strains (Wachsstock et al. 1993). Microtubules' contribution to the cell stiffness is less unless their depolymerization causes disassembly or rearrangement of other filaments (Trickey et al. 2004). The median Young's modulus for the live NIH/3T3 fibroblast cells in an incubator measured by AFM is about 5.2 kPa (Codan et al. 2013). However, when the cells are fixed by 3.5% paraformaldehyde, the modulus increases dramatically to 82 kPa, as the fixation process crosslinks cytoskeletal proteins and forms strong covalent imine bonds (Codan et al. 2013).

Although the exact response to mechanical force and force transmission in the highly sophisticated architecture of the cytoskeleton depends on the exact configuration of polymers and crosslinks, there have been efforts to describe cytoskeletal mechanotransduction. The main theory suggests that the structure of mechanosensitive ion channel (Ca^{+2} , K^{+} , Na^{+} channels) of the cell changes in response to

the membrane and cytoskeleton deformation (Martinac 2004). This way, the mechanosensitive ion channels can get either activated or deactivated as the result of the applied force. The alteration in the state of these channels regulates the influx of ions to the cytoskeleton and consequently triggers a chemical signalling (ATP dependent usually) pathway to alter the cytoskeletal architecture accordingly (Janmey & McCulloch 2007).

1.4 Nuclear mechanics and mechanotransduction

The nucleus is the biggest and stiffest organelle inside the cell with a 2 to 10 times greater stiffness than the cytoskeleton (Guilak et al. 2000) and within the nucleus, the nucleolus is the stiffest domain as has been shown by AFM measurements (Melling et al. 2001). The stiffness of the nucleus varies significantly among different cell lines and the precise experimental method that has been used for the measurement; however, it generally varies between 0.1 to 10 kPa (Dahl, Alexandre J.S. Ribeiro, et al. 2008). For example, for mouse fibroblasts, the nuclear Young's modulus was reported about 1.8 kPa when it was measured by AFM (Efremov et al. 2014). Micropipette aspiration method showed the nuclear stiffness of chondrocytes is about 1 kPa (Guilak et al. 2000).

As figure 1-5 shows, the chromatin network which consists of macromolecules that are made of compact DNA strings woven around histone proteins occupies most of the nucleoplasm. However, it is the nuclear lamina that provides physical support to the nucleus and regulates nuclear mechanics (Lammerding et al. 2006). The chromatin network has a viscous nature (a tendency to flow) compared to the elastic nature of filamentous nuclear lamina and can deform permanently (plastically) under mechanical stress (Pajerowski et al. 2007). The nuclear lamina is a meshwork of intermediate filaments with a thickness of about 30 to 100 nm that lies on the inner surface of the inner nuclear membrane and acts as an anchoring site for interphase (the phase in which a cell copies its DNA in preparation for the next mitosis cell division) chromatin at the nuclear periphery (Aebi et al. 1986) (Figure 1-7). The nuclear lamina consists of lamins and proteins that are associated with the lamins in order to link the lamins to the inner nuclear membrane or chromatin (Coutinho et al. 2009). Lamins are classified in two (A and B) subtypes based on the homology of their encoding genes and their molecular weight. The A-type lamins consist of Lamin A and Lamin C and B-type lamins consist of Lamin B₁ and Lamin B₂ (Young et al. 2014). It has been shown the nuclear stiffness is mainly regulated by the A-type lamins while the loss of type B lamins can result in moderate morphological changes to the nucleus such as increased nuclear blebbing while having minor effects on the nuclear stiffness (Lammerding et al. 2006).

The nuclear lamina is coupled with the cytoskeleton filaments through a set of proteins that are named the LINC (linker of nucleoskeleton and cytoskeleton) (Crisp et al. 2006).

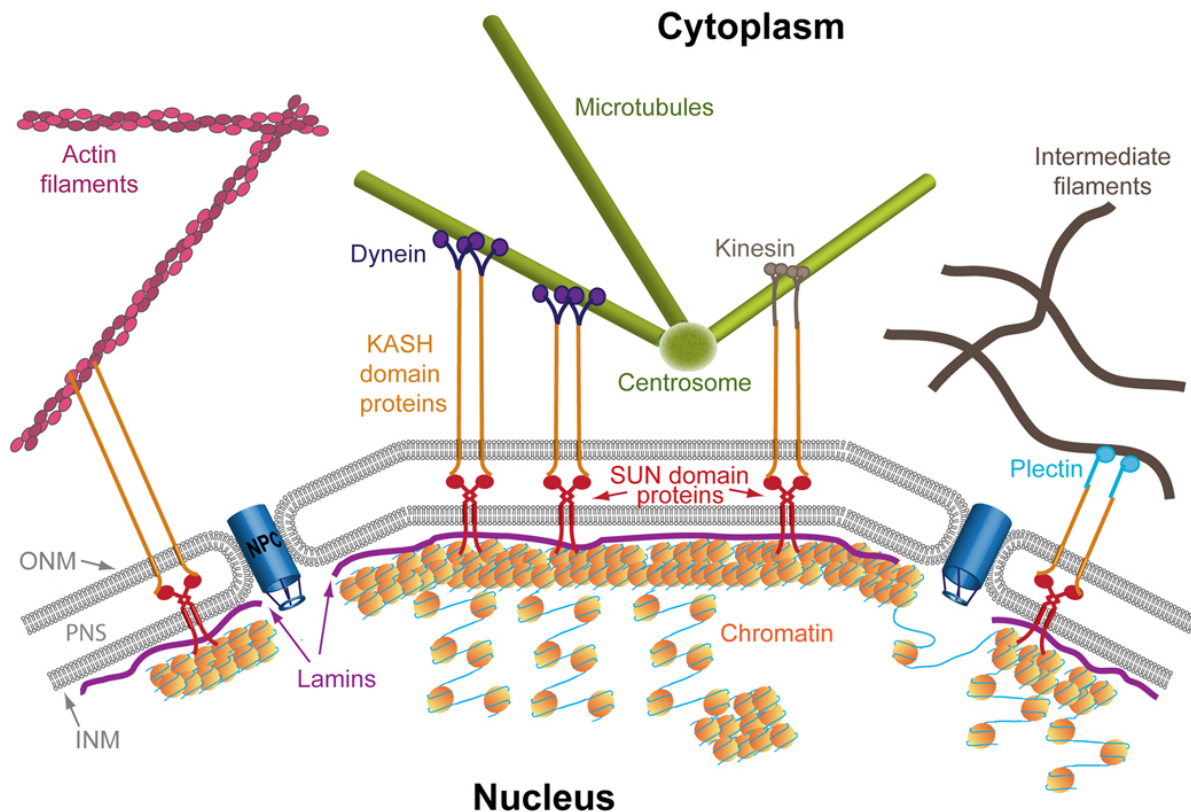


Figure 1-7: The molecular structure of linkage between nuclear lamina, cytoskeletal filaments and chromatin. (Gerlitz & Bustin 2011).

The SUN-domain (Sad1 and UNC-84 homology domain) family of protein link with their partner KASH (Klarsicht, Anc-1, Syne homology) domain protein family to build the molecular bridge across inner and outer nuclear membrane that physically connects nuclear lamin to the cytoskeletal filaments (Tzur et al. 2006). KASH proteins directly interact with actin filaments; however, plectin which is a cytoskeletal linker protein helps KASH domain protein to bind to intermediate filaments of the cytoskeleton. Dynein and kinesin which are microtubule motor proteins link the KASH domain proteins and the microtubule filaments (Gerlitz & Bustin 2011) (Figure 1-7).

Mechanical cues of the ECM are transmitted via focal adhesions to the cytoskeletal filaments of the cells and then are transduced via the physical connection that was discussed earlier to the nuclear and chromatin content of the nucleus. It is believed that this physical connection provides a direct link between the extracellular microenvironment and the genetic material of the cells and gives the cell

opportunity to respond to the mechanical stimuli (Dahl, Alexandre J.S. Ribeiro, et al. 2008) (see cell adhesion 1.5).

1.5 Cell Adhesion

Some cells can attach to the surface (substrate), ECM or to other cells. Cell adhesion plays a critical role in the structural integrity of tissues, maintaining multicellular structures, pathogenesis of infectious organisms and signal transduction. A complex set of proteins, such as selectins, the immunoglobulin superfamily (IgSF), integrins, mucins, and cadherins, underlies the molecular mechanism of cell adhesion (Gumbiner 1996). The aforementioned five groups of proteins are major classes of cell adhesion molecules. These molecules are generally referred to as cell adhesion molecules (CAMs) or adhesins. CAMs usually are classified based on their dependence on calcium for their action. IgSFs and mucins are calcium (Ca^{+2}) independent while selectins, integrins, and cadherins are calcium-dependent (Brackenbury et al. 1981). CAMs are not only responsible for cell adhesion to adjacent cells and to the ECM, but also they initiate intracellular signalling pathways that modulate crucial cell proliferation and survival events. Lack of sufficient attachment of adherent cells to ECM initiates apoptosis cell death. Anoikis is the term that refers to this particular category of apoptosis. Molecular initiators of anoikis are integrins. Anoikis is a common mechanism of homeostasis. Failure of the cell response to anoikis will cause cell survival under suspension conditions, which is an essential requirement for the initiation of metastatic cancer (Zhong & Rescorla 2012). There are several types of CAMs on a cell surface and they usually spread uniformly on those regions of the plasma membrane that contact other cells. Integrins participate mainly in adhesion of cells to ECM whereas other major families of CAMs take part in cell-cell adhesion. Integrins consist of α and β subunits. These subunits bind to the cell-binding domain of fibronectin, laminin, or other molecules on the ECM (Figure 1-8). As Figure 1-8 illustrates, cadherins and IgSFs mediate hemophilic cell-cell adhesion whereas mucins and integrins are involved in heterophilic adhesion interaction (Lodish et al. 2000a). Binding of similar adhesion molecules facilitates hemophilic adhesion whereas heterophilic adhesions are associated with binding of unlike adhesion molecules.

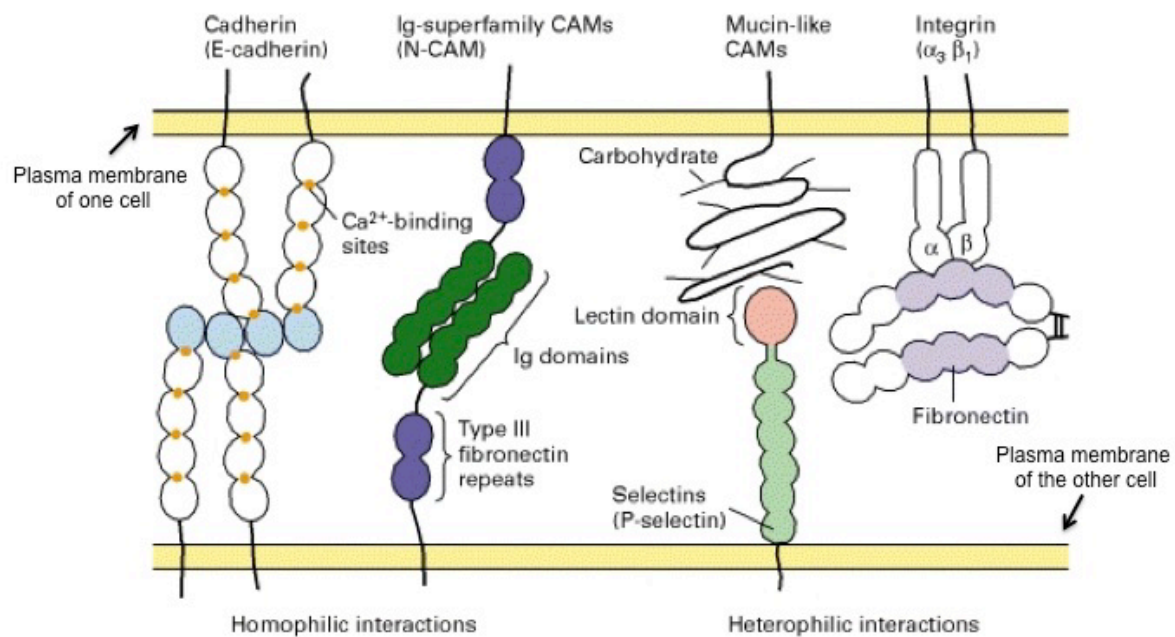


Figure 1-8: Diagram of the adhesion mechanism of major types of CAMs. (Lodish 2000).

Cytosol facing tails of CAMs are usually connected to the cytoskeleton. Adhesion is closely connected with the protrusions of the leading edge of the adherent cell. A nascent adhesion usually starts from broad lamellipodia or spike-like filopodia (Figure 1-9). The formation rate of protrusions is a determining factor in the assembly of a nascent adhesion. The transition zone (the convergence of the lamellipodium and lamellum) is the site at which the nascent adhesion may elongate or disassemble. Bundling and cross-bridging of actin filaments allow the adhesion to mature and lead to the formation of focal complexes and focal adhesions (J Thomas Parsons et al. 2010a).

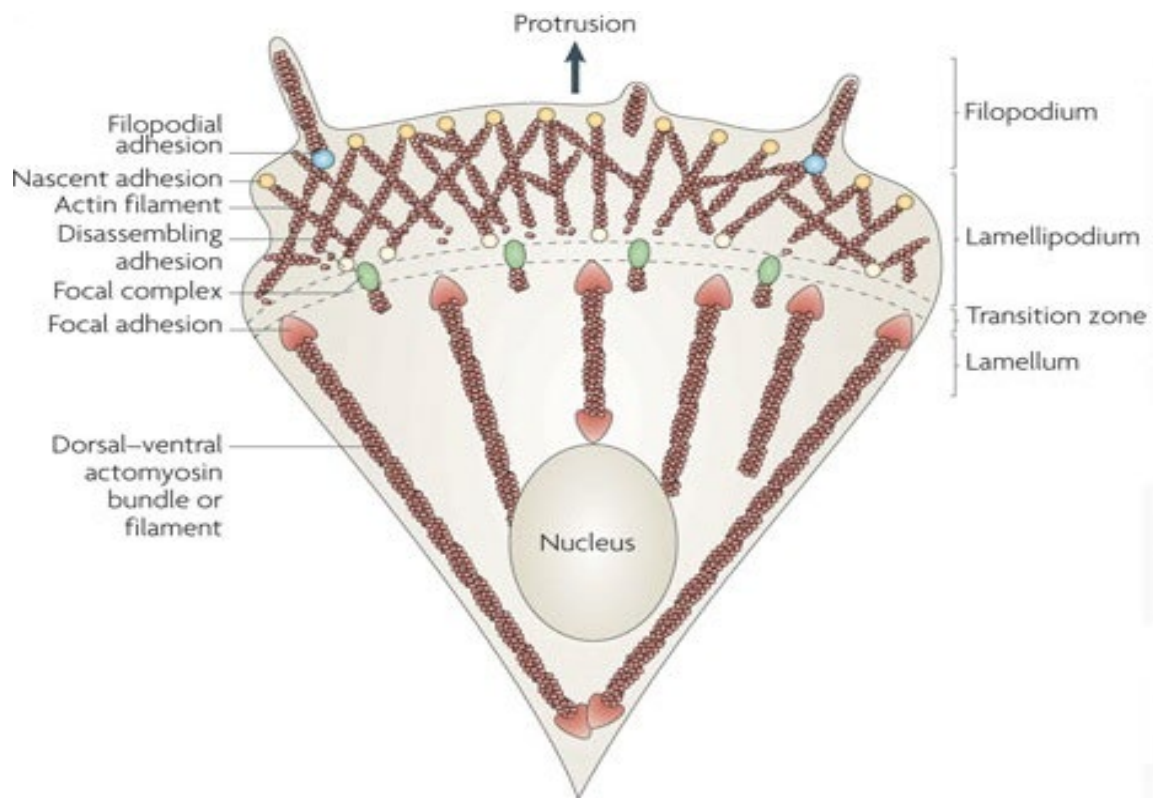


Figure 1-9: Diagram of an adherent cell, illustrating the close connection between adhesion process and cell protrusions. Cell adhesion: integrating cytoskeletal dynamics and cellular tension after (J. Thomas Parsons et al. 2010).

Focal adhesions are the sites at which cells adhere tightly to the underlying ECM. They are regions for growth control signal transduction and secure a structural link between the actin cytoskeleton and the ECM (BurrIDGE & Chrzanowska-Wodnicka 1996). At the focal contact points, ECM-bound integrin interacts with other integrin-binding molecules such as paxillin and talin inside the cytoskeleton and these proteins recruit focal adhesion kinase (FAK) and vinculin to the site of focal complexes. Activated FAK phosphorylates actin-binding alpha-actinin and makes it bind to the vinculin and cross-link actin stress fibres and tether them to the focal point (Figure 1-10) (Mitra et al. 2005).

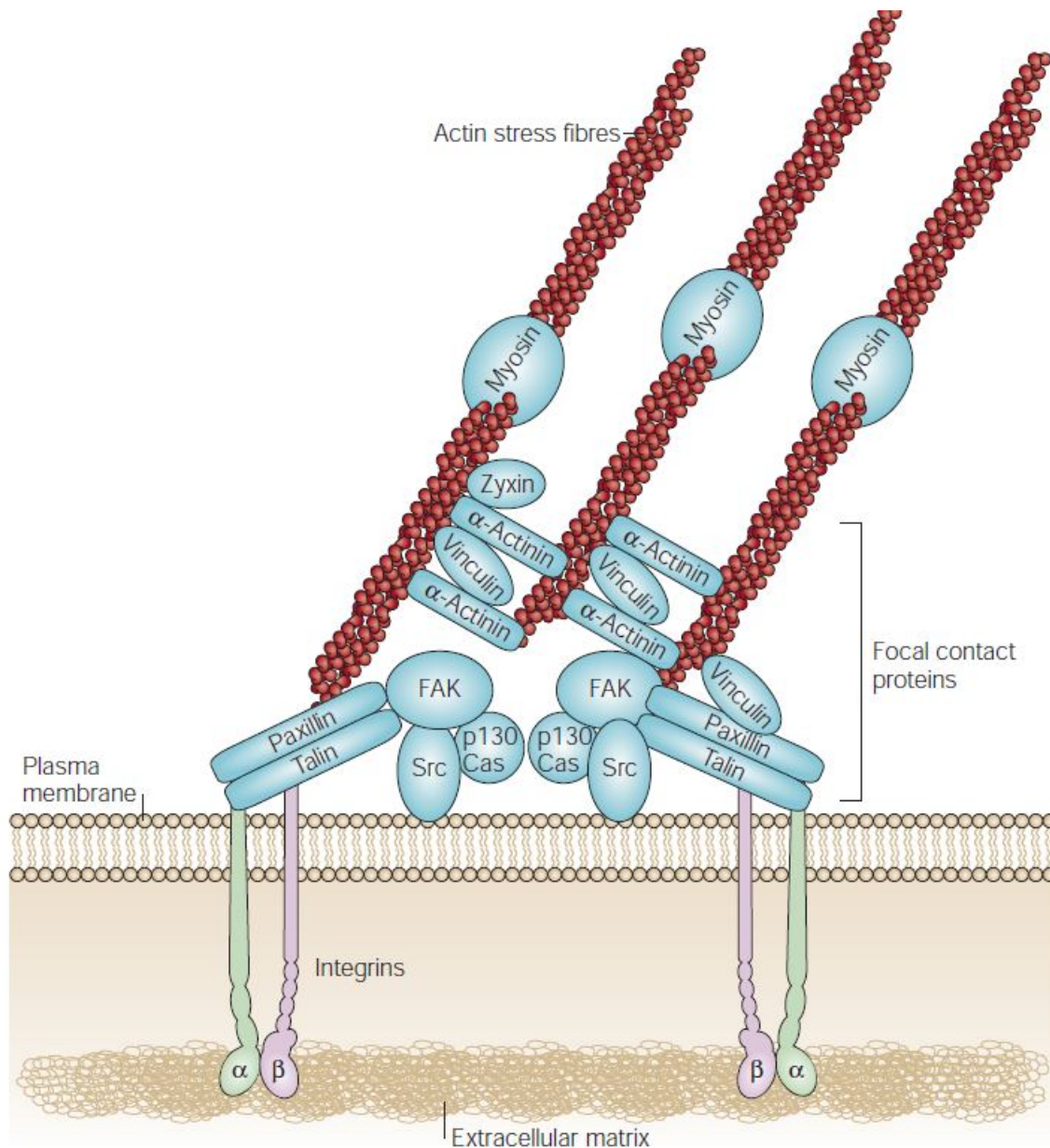


Figure 1-10: The molecular machinery of changing actin cytoskeleton in the focal complex sites. (Mitra et al. 2005).

Focal complexes are small focal adhesions at peripheral sites of a migrating or spreading cell (Nobes & Hall 1995). The distinction between focal complexes and focal adhesions is not completely clear (Pankov et al. 2000). It has been revealed that inserting a local mechanical force on cells can cause the development of focal complexes into larger focal adhesions (Riveline et al. 2001).

1.6 Structure of extracellular matrix

The ECM is an organized meshwork of extracellular molecules that are secreted locally mainly by the cells in the matrix and mainly provides essential physical scaffolding for the cell within all the tissues and organs (Alberts B, Johnson A, Lewis J 2002). Alongside physical support to the cell, the ECM provides crucial biochemical and biophysical cues that, by a dynamic and reciprocal interaction with the cells, play a pivotal role in tissue morphogenesis, homeostasis and differentiation (Frantz et al. 2010). It has been shown that by ageing the ECM becomes less deformable and stiffer and this is linked with many age-related diseases and tissue dysfunctions (Phillip et al. 2015). The main macromolecules that build the ECM are proteoglycans, which are covalent bonded proteins and chains of glycosaminoglycans (GAGs), a class of polysaccharides, and fibrous proteins such as collagens, fibronectins, elastins and laminins (Figure 1-11). Proteoglycans form a ‘‘ground substance’’ that is a hydrated gel-like base and fibrous proteins of the ECM are embedded in this hydrated gel. (Alberts B, Johnson A, Lewis J 2002).

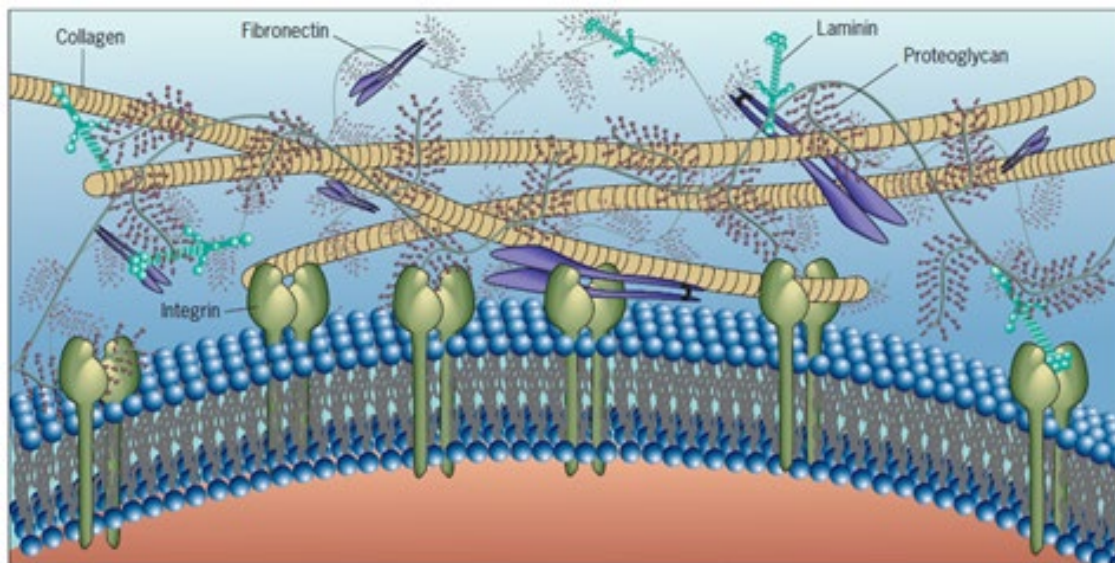


Figure 1-11: Composition and schematic view of ECM. Proteoglycans act as a base gel-like support for ECM while interconnected fibril proteins such as collagens, Laminin and fibronectin make a scaffold that gives physical support to the cells adhering to the network via integrins on the cell surface (Karp 2010).

The ECMs are usually classified into two major categories of the interstitial and pericellular matrices. Interstitial matrices completely surround the cells; however, pericellular matrices are partially in contact with cells (Theocharis et al. 2016).

Collagens are insoluble proteins, the most abundant fibrous proteins in ECM (about 90%) and comprising about 30% of the total protein content of the human body (Gilkes et al. 2014)(Ricard-Blum 2011). There are at least 28 types of collagen; however, 80-90 % of collagen in the body consists of collagen type I, II, III which pack together and form long thin fibrils structure (10-300 nm in diameter) (Heino 2007). Fibroblasts synthesize and secrete most of the collagen in the connective tissue, however, epithelial cells also can make collagens. Fibroblasts organize the collagen that they have secreted into sheets and cables by crawling on and exerting a force on the collagens (Lodish 2000).

Elastins are highly elastic proteins that give elasticity to the ECM and can be in the form of microfibrils or as a major constituent of tissues (Theocharis et al. 2016).

Laminins are mostly found in the ECM, the basement membrane under the epithelial cells. Laminins make a web-like structure in the basement membrane which can resist tensile forces (Timpl et al. 1979). Fibronectins are high molecular weight multi-domain proteins that usually exist in a dimer form consisting of two nearly identical monomers of disulfide-bound polypeptides near their C-termini with a molecular weight of approximately 250 kDa (Figure 1-12 (a)). Fibronectin exists in both soluble and insoluble form in vertebrates. The soluble fibronectin is mainly synthesized by the liver and is found in plasma at a concentration of 300 µg/mL and is also present in other bodily fluids. The insoluble fibronectin, which is known also as the cellular fibronectin, is one of the fibrous proteins of the ECM (Pankov & Yamada 2002). The fibronectin that is secreted from fibroblasts is very similar to the plasma fibronectin; however, some structural and functional differences have been observed (McKeown-Longo & Mosher 1984). The cellular fibronectin binds to numerous members of the integrin family via a tripeptide Arginylglycylaspartic acid (RGD) domain and therefore plays a key role in the adhesion of many cell types (Van Agthoven et al. 2014). Fibroblasts secrete and also help the formation of a fibrillar network when they are seeded on fibronectin-coated surfaces (Figure 1-12(b))(Corall et al. 2014). *In vivo*, lack of fibronectin is associated with impaired cell migration during embryogenesis, poor cell differentiation and highly metastatic tumours (Ruoslahti 1984). Fibronectin also binds to collagens and fibrins and this gives them a very important role in wound healing as the fibronectin is present in two critical part of the healing process; the formation of fibrin clots and collagen aligned fibrils coated with the fibronectin(Grinnell et al. 1981).

The pivotal role of fibronectin in cell adhesion and migration has made it one of the most frequently used in micropatterning for the study of cell adhesion (M.-C. Kim et al. 2013)(Fitzpatrick et al. 2017).

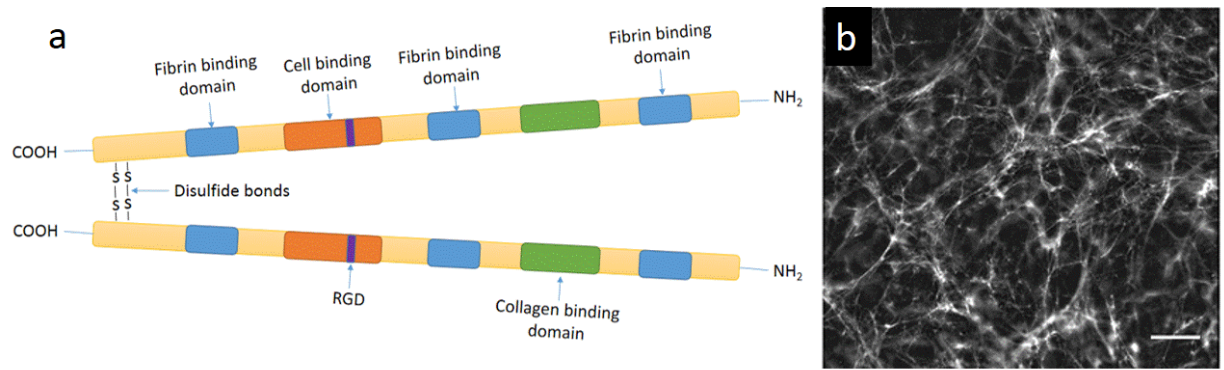


Figure 1-12: Structure of fibronectin molecule and fibronectin matrices. (a) Fibronectin is a multidomain dimer consisting of two almost identical monomers that are linked with a disulfide bond near their c-termini. (b) Epifluorescence microscopy of a fibronectin network that has been formed by seeding human fibroblasts on a cellular fibronectin-coated substrate (after cell lysis). Scale bar is 20 μm (Corall et al. 2014). The cited source is only for Figure 1-12 (b). Figure 1-12(a) is result of my own work.

Chapter 2:

Materials and Methods

2.1 Cell line

2.1.1 NIH/3T3 fibroblasts

The NIH/3T3 cell line, which is known as the standard fibroblast cell line was used in the first part of this study (Figure 2-1). 3T3 cells are mouse embryonic fibroblast cells. The name of this cell line refers to its cell transfer and incubation protocol, “3-day Transfer, inoculum 3×10^5 cells” (Wells 2005). Statistical analysis of standard-bright field images of 3T3 cells has revealed that the peak of Gaussian distributions of their size is approximately $17 \mu\text{m}$ (see chapter 5.2). The NIH/3T3 cell line used in this project was purchased from ATCC- LGC Standards (Middlesex, UK).

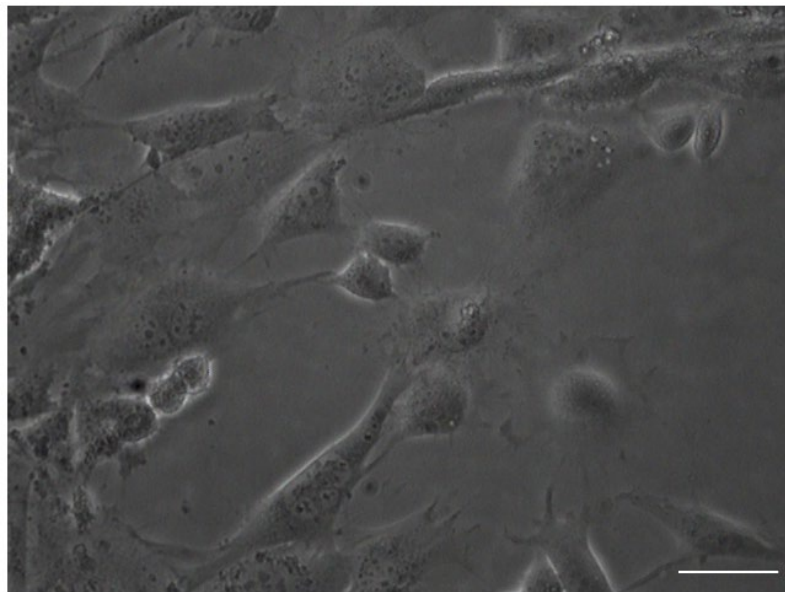


Figure 2-1: Phase contrast image of adherent NIH/3T3 cells on a 25 cm² cell culture flask. Scale bar is 50 μm .

2.1.2 Human mesenchymal stem cells

Bone marrow is the main tissue that mesenchymal stem cells (MSCs) are isolated from. MSCs comprise a tiny fraction (10^{-4} - 10^{-6}) of total bone marrow cells and therefore isolating them is not a trivial task (Alvarez-Viejo et al. 2013). PoieticsTM Human Bone Marrow-Derived Mesenchymal Stem Cells (hMSC) used in this study was purchased from Lonza (Basel, Switzerland) (Figure 2-2). The

cells were withdrawn from bilateral punctures of the posterior iliac crests of healthy nondiabetic volunteers and cryopreserved after the second passage. hMSCs mostly express polygonal fibroblast-like morphology when they are seeded in low concentration and show a polarized elongated shape at higher concentrations (see Figure 6-1). Suspended hMSCs are slightly larger than fibroblasts with a peak of Gaussian distribution around 22 μm (see chapter 6-1).

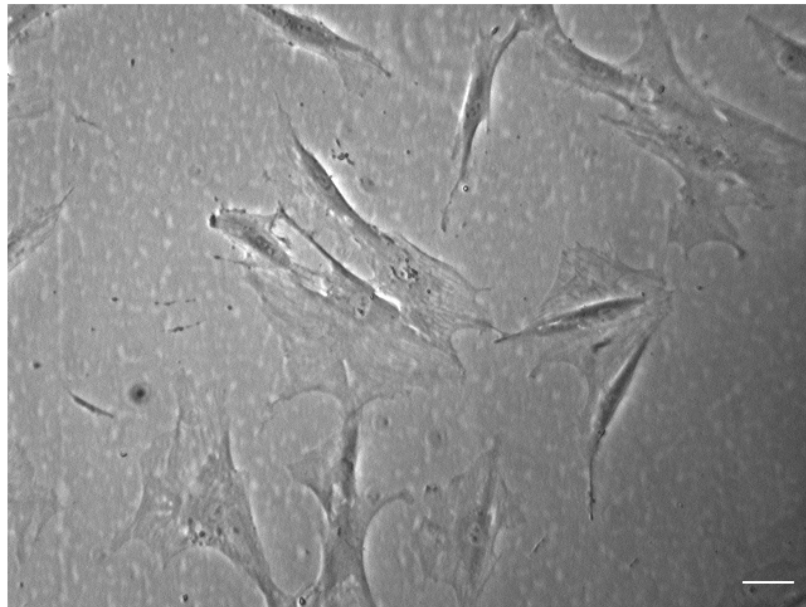


Figure 2-2: Phase contrast image of adherent hMSCs cells on a 25 cm² cell culture flask. Scale bar is 50 μm .

2.2 Cell culture

We used 25 cm² sterile TC-treated screw red cap flasks (Cell star, Stonehouse, UK) for culturing the cells. Cell cultures were performed in a 5% CO₂ humidified incubator with the maintained temperature at 37 °C (BINDER, Tuttlingen, Germany).

2.2.1 Recovery and maintenance of NIH/3T3 cells

1 mL vials were used for the cell storage. The cells were stored at $\sim 10^6$ cell/mL and in the liquid nitrogen tank ($< -150^\circ\text{C}$). The maintenance medium for cells consisted of Dulbecco's Modified Eagle's Medium enriched with 1 g/L D-glucose, L-glutamine, and pyruvate (Life Technologies, Paisley, UK), supplemented with 10% v/v foetal bovine serum (Sigma-Aldrich, Dorset, UK) and 1 % v/v (100 units/mL) 100 \times penicillin/streptomycin (Life Technologies, Paisley, UK).

First, the vials of cells and maintenance medium were thawed in a 37°C water bath. Afterwards, the 1 mL of thawed cells were transferred to a 25 cm² flask containing 10 mL of fresh maintenance medium.

The maintenance medium was warmed to avoid thermal shock. At least 3 cell passages were performed before using newly thawed cells in experiments. The passaging was carried out when the cell concentration reached $\sim 2 \times 10^4/\text{cm}^2$. Usually, at this stage, NIH/3T3 cells reach about 95% confluency and they are ready for the next passage. 3T3 cells are capable of surviving approximately 3 days after reaching 95% confluency (Huang 2015). The cell passage (for cultures with 10 mL medium) was performed according to the following protocol: 1- Old medium was disposed of. 2-The cell-adhered surface of the culture flask was carefully rinsed twice with 6 mL of Dulbecco's Phosphate-Buffered Saline (D-PBS) in order to remove old residual medium as this medium may interfere with the trypsin action in the third step (D-PBS should aspirate off afterwards). 3-The cells were incubated with 2 mL of 0.25% trypsin-EDTA solution (Sigma-Aldrich, Dorset, UK) at 37°C for 3 minutes to detach from the growing surface. 4-8 mL of pre-warmed growth medium was added to dilute trypsin in order to avoid its potential toxic effect on cells after the incubation period. 5-The cells were centrifuged at 1000 rpm for 5 minutes. 6-The supernatant was removed and the cells re-suspended in 6 mL of the fresh growth medium. 6- Cells were counted by a haemocytometer (Hawksley, Sussex, UK) and $\sim 7.5 \times 10^4$ cells (enough for 3×10^3 cells/cm²) were extracted and diluted in the pre-warmed fresh medium to start a fresh culture.

The viability, cell size and cell density were measured by the haemocytometer on a regular basis to check the performance of the cells. The cells were stained with 0.4% trypan-blue dye (Sigma-Aldrich, Dorset, UK) to monitor cell viability using the haemocytometer. The growth curve of the cells was monitored to ensure that the cells were in exponential growth phase prior to starting experiments.

2.2.2 Recovery and maintenance of hMSCs

For both recovering the cryopreserved and culturing of hMSCs we used MesenPRO RS™ (ThermoFisher Scientific, Loughborough, UK) medium which is constituted of MesenPRO RS™ Basal Medium (97% v/v), MesenPRO RS™ Growth Supplement (2% v/v) and 200 mM L-Glutamine (Life Technologies, Paisley, UK) (thawed in 37 °C water bath ,1% v/v, 2 mM final concentration). The growth supplement was stored in a -20°C freezer and was thawed in the 4°C fridge overnight and immediately on withdrawal from the fridge was mixed with the other constituent of the MesenPRO™ RS medium. The supplemented complete MesenPRO RS™ was covered with aluminium foil to protect it the light and were stored at 4°C for up to 2 weeks. For recovery and culturing of hMSCs, the complete MesenPRO RS™ medium was warmed always at room temperature as warming it at 37°C would harm the MesenPRO RS™ Growth Supplement found in the complete medium.

2.2.2.1 Recovery of cryopreserved hMSCs

hMSCs were cryopreserved in 1 mL vials ($\sim 10^6$ cells per vial) inside the liquid nitrogen tank ($< -150^\circ\text{C}$) according to the supplier protocol (ThermoFisher scientific 2014). For the recovery of cryopreserved cells, they are rapidly thawed in a 37°C water bath for less than a minute and the whole content of the vial immediately was pipetted into a sterile 50 mL conical tube. The complete MesenPROTM RS medium was prewarmed at room temperature until it was not cool to touch and 5 mL of the prewarmed medium was added dropwise with an approximate rate of 2-3 drops per 10 seconds into a 50 mL tube. The tube was gently swirled and another 5 mL of the prewarmed complete MesenPROTM RS medium was added carefully while swirling. The whole content of 50 mL conical tube was transferred to a 25 cm^2 culture flask that was incubated in 37°C and 5% CO_2 (see 2.2 for details). The medium was exchanged after 24 hours with fresh prewarmed complete MesenPROTM RS medium.

2.2.2.2 Subculturing hMSCs

After recovery of cryopreserved hMSCs, cells were allowed to grow for 3-5 days and observed under the inverted bright field microscope to confirm that they had reached about 60-80% confluency in order to be subcultured. The subculturing procedure was carried out according to the supplier protocol (ThermoFisher scientific 2014). The old medium was aspirated and subsequently, cells were washed 10 mL of CTSTM (Cell Therapy Systems) Dulbecco's Phosphate Buffered Saline (DPBS) which doesn't contain calcium chloride, magnesium chloride or phenol red (ThermoFisher Scientific, Loughborough, UK). The DPBS was aspirated off and 5 mL of CTSTM TrypLETM Select Enzyme that was prewarmed at room temperature was added to the culture flask and cells were incubated at 37°C for 5 minutes as more aggressive Trypsin may negatively influence hMSCs (see chapter 6.1 for details). Afterwards, the culture flask was removed from the incubator and the cells observed under a bright field inverted microscope to ensure that the monolayer of hMSCs was fully detached. Immediately, 10 mL of prewarmed complete MesenPRO RSTM medium was added to the culture flask in order to stop the dissociation activity of the detachment enzyme. The liquid inside the flask was gently pipetted in and out in order to dissociate conjoined cells from each other. The suspension was transferred into a 50 mL sterile conical tube afterwards. The flask was washed with an additional 5 mL prewarmed complete MesenPRO RSTM medium to ensure detachment of the remaining hMSCs in the flask and the medium was combined into the 50 mL conical tube. The cell suspension was centrifuged at $100\times g$ acceleration for 10 minutes. The supernatant was aspirated off and the cell pellet was resuspended in 5 mL of fresh prewarmed complete MesenPRO RSTM medium. In order to assess cell count and viability, a small fraction of cells were stained with 0.4% trypan-blue dye and was counted in C-Chip haemocytometers.

(Source BioScience LifeSciences, Nottingham, UK). After making sure that cells have at least 90% viability, the required number of cells were transferred to either 25 cm² or 75 cm² to culture cells at 5x10³/cm². The required volume of prewarmed complete MesenPRO RS™ medium was added accordingly to the flask to achieve the final optimum medium volume in the culture flask (25 cm²: 10 mL, 75 cm²: 30 mL). Cells were moved to 37 °C incubator with 5% CO₂ level and the culture was re-fed with the fresh prewarmed complete MesenPRO RS™ medium after 3 days in order to achieve optimal cell growth.

2.2.3 Cell Banking

2.2.3.1 Cell banking of NIH/3T3 cells

The NIH/3T3 cells used in this study had originally been bought from ATCC- LGC Standards (Middlesex, UK) and were stored in 1 mL vials at 10×10⁶ cells/mL in the cryopreservation medium consisting of 95%(v/v) of the growth medium and 5%(v/v) DMSO (Sigma-Aldrich, Dorset, UK). For banking, cells in exponential growth were recovered from a fed-batch culture and centrifuged at 1000 rpm for 5 minutes. The supernatant was removed and the cells re-suspended in the cryopreservation medium at 10×10⁶ cells/mL. The cells were then transferred to 1 mL labelled cryovials (Starlab, Blakelands, UK) and placed in Mr. Frosty™ (ThermoFisher Scientific, Loughborough, UK) freezing container filled with 100% isopropanol at -80°C. After 24 hours, the vials were transferred to cryostorage boxes at -150 °C under liquid nitrogen.

2.2.3.2 Cell banking of hMSCs

2x cryopreservation solution was prepared by mixing 80% v/v complete MesenPRO RS™ medium and 20% DMSO and was stored at 4°C until use. hMSCs were harvested and counted according to the protocol that was used in subculturing of the hMSCs (see 2.2.2.2) and the cell pellet was reconstituted in 0.5 mL of the prewarmed complete MesenPRO RS™ medium at a density of 2x10⁶ cells/mL (twice the desired final cell density). 0.5 mL of 2x cryopreservation solution was slowly added to the cell suspension and was mixed gently in order to achieve a homogenous cell distribution. 1 mL cell suspension was then transferred quickly to cryovials that were pre-chilled at 4°C. Cryovials were placed in Mr. Frosty™ containers and transferred to the liquid nitrogen tank similar to the banking procedure of NIH/3T3 cells (see. 2.2.3.1)

2.3 The Polydimethylsiloxane (PDMS) substrate

Polydimethylsiloxane is a polymeric organosilicon. The chemical formula of PDMS is $\text{CH}_3[\text{Si}(\text{CH}_3)_2\text{O}]_n\text{Si}(\text{CH}_3)_3$ in which n is the repeating polymer number of $[\text{Si}(\text{CH}_3)_2\text{O}]$. PDMS belongs to a group of polymers referred to as the silicones (Seethapathy & Górecki 2012). It is widely used for many biological applications such as micro and nano-pillars, stretchable cell substrates, micropatterned substrates and microfluidic channels and chips. Its properties including optical transparency, thermal stability, cost-effectiveness, simple fabrication techniques and biocompatibility have made PDMS a very common choice for biological setups (Bartalena et al. 2012). The toxic effect of PDMS on living cells is a subject of controversy. There are some reports claiming non-toxicity of PDMS for the living cells (Bartalena et al. 2012), (Wipff et al. 2009) while there are reports claiming low-grade toxic properties of PDMS. It has been observed that culturing of mouse mammary fibroblasts (MMF) in PDMS micro-channels has increased basal level of glucose consumption and caused hyper-activation in the ribosomal subunits, which is a possible indicator of elevated endoplasmic reticulum stress (Paguirigan & Beebe 2009). Even though it is not obviously clear whether PDMS micro-channels cause the toxic effect or microscale culturing is the source of toxicity (Paguirigan & Beebe 2008), it has been suggested that possible interference from the long chain PDMS molecules with the signalling pathways of the cells may be the underlying reason for the observation (Regehr et al. 2009).

There are also observations implying a non-toxic effect of PDMS on the biological mechanisms of the cell. It has been observed that uncured oligomers of PDMS can leach from the substrate to the cell culture medium and at the same time small hydrophilic molecules such as estrogen can be absorbed by PDMS bulk from the culture medium. PDMS oligomers were found in membranes of NMuMG cells that were cultured in PDMS micro-channels for 24 hours. MCF-7 cells that are sensitive to both prolactin (a water-soluble hormone) and to estrogen (a hydrophilic hormone) were cultured on a PDMS substrate. Cells expressed less estrogen-triggered luciferase activity in the presence of PDMS, an indication of estrogen absorption by PDMS substrate; however, there was no obvious change in the prolactin-triggered luciferase activity (Regehr et al. 2009).

2.3.1 PDMS preparation

PDMS used in this study (Sylgard 184, Onecall, Leeds, UK) consists of two fluid components, the polymer base (silicone elastomer) and the curing agent or cross-linker (consists mostly of dimethyl, methyl hydrogen siloxane). Silicon elastomer and cross-linker were carefully weighed using a sensitive electrical scale and were mixed manually at a 10:1 (w/w) ratio. The mixture was covered with a parafilm

membrane (with small pores in it) and was put under a vacuum chamber at room temperature in order to degas the mixture. The vacuum pump was turned on until approximately 2/3 of the containing glass beaker was filled with bubbles. The pump was turned off at this point and the mixture was left in the vacuum chamber for about 30 minutes to let all the mini bubbles escape the mixture.

2.4 Soft Lithography

The template pattern to generate PDMS stamps for micro-contact printing was fabricated using a photolithography technique (Qin et al. 2010). First, the photoresist SU-8 2015 liquid (Chestech Ltd, Rugby, UK) was coated on a single side polished (SSP) type P silicon wafers (thickness: 320-350 μm , diameter: 50.8 mm, resistance: 0-100 ohm-cm) (University Wafers, Massachusetts, USA). The following program setting was set for the spin coating machine:

1- Initial spin coat at 500 rpm for 5 seconds.

2-Ramp up to 2,000 rpm within 35 seconds. Spin-coated wafers were then left for 10 minutes in order to allow SU-8 liquid to flow back from the edges and equilibrate.

Afterwards, SU-8 coated silicon wafers were baked on a hot plate at 60 °C for 1 minute and at 95 °C for 2 minutes subsequently. Wafers were left to cool down and placed in a mask aligner (Karl Suss MJB4, Garching, Germany) and put into soft contact with the chromium mask that contains desired strip pattern (Compugraphics, Glenrothes, UK) afterwards. Wafers were exposed to UV light for 4 seconds and baked on a hot plate for 1 minute at 60 °C and for 3 minutes at 95°C subsequently in order to crosslink the exposed SU-8. Cooled wafers were immersed in the SU-8 developer (Chestech Ltd, Rugby, UK) for 1 minute in order to remove un-cross linked SU-8 polymers. The prepared template (figure 2-5(a)) was rinsed twice with isopropyl alcohol, dried with pressurized nitrogen and baked at 150°C for 10 minutes (Figure 2-3).

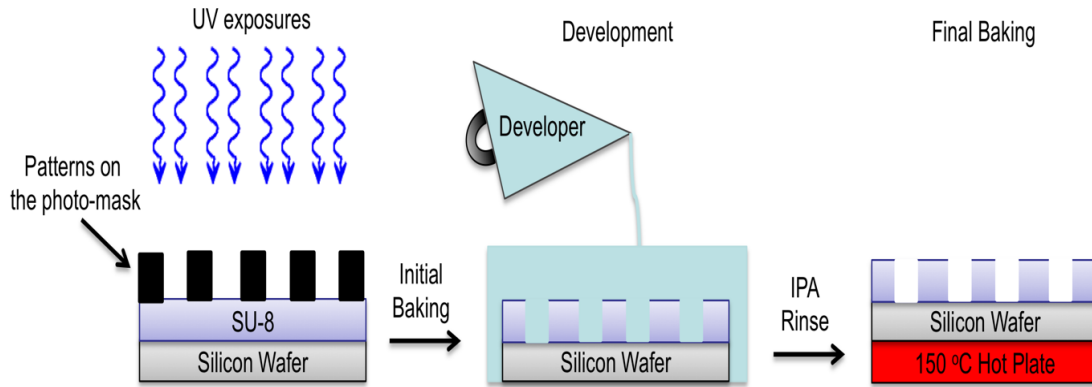


Figure 2-3: Schematic view of the fabrication process of pattern printing on the SU-8 film using soft lithography technique. Patterns were transferred from a photomask template to the SU-8 coated silicon wafer.

A layer with approximately 5 mm of PDMS prepared with the preparation method described in section 2.3.1 was poured onto prepared SU-8 patterns. Wafers were put into the vacuum chamber to remove trapped bubbles and baked at 150°C for about 15 minutes to cure PDMS. Patterned PDMS film (Figure 2-5(b)) was peeled off after completion of the process (Figure 2-4).

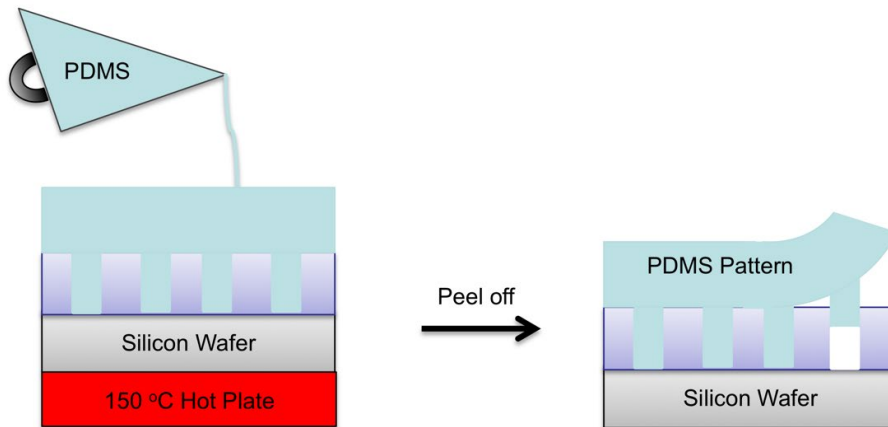


Figure 2-4: Fabrication of PDMS stamps from SU-8 patterns. The liquid PDMS was poured on the SU-8 coated silicon wafer template and the transferred pattern on PDMS was peeled off after curing.

2.5 Substrate preparation

Uncured PDMS prepared with the method described in section 2.3.1 was poured onto a circular coverslip (diameter: 22 mm, thickness: 0.19 mm). The coverslip was pre-rinsed with isopropanol,

sonicated for 10 minutes in an ionized water bath and blow-dried with pressurized air in order to clean it. Afterwards, the coverslip was spin coated at 1700 rpm for 35 seconds in order to fabricate a 55 μm layer of PDMS. The PDMS coated coverslip was baked at 150°C for 15 minutes for curing. A narrow circular line of uncured PDMS was streaked on the edge of a custom-made metal ring and the pre-prepared coverslip was mounted on the ring. The coverslip mounted ring was baked at 150°C for 15 minutes to cure the PDMS glue.

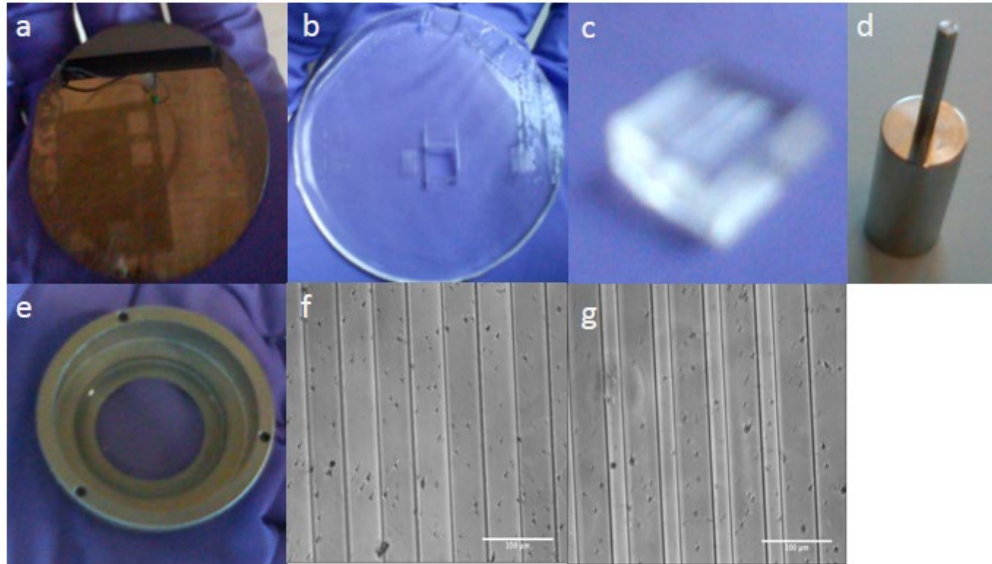


Figure 2-5: Materials used in the pattern preparation. (a) A patterned silicon wafer. (b) PDMS stamp from patterned silicon. (c) Cut PDMS pattern. (d) Standard weight (~100g) used for pattern transfer. (e) The custom-designed metal ring. (f),(g) Samples of PDMS ridge-groove patterns. (Ridge 50 μm , Groove 50 μm) (f) and (Ridge: 25 μm , Groove: 50 μm) (g). Scale bars are 100 μm .

2.6 Micro-contact printing

The desired PDMS stamp was cut from the patterned PDMS film that was made earlier (Figure 2-5(c)). The cut PDMS stamp was sterilized by immersion in 70% ethanol. Afterwards, the ethanol was washed away gently with 1x autoclaved PBS from the stamp. PDMS stamps were exposed to 50 $\mu\text{g}/\text{mL}$ fibronectin from bovine plasma (Sigma-Aldrich, Dorset, UK) and were incubated at 37°C for 1 hour. Stamps were gently rinsed three times with autoclaved 1x PBS and once with autoclaved ionized water subsequently. PDMS substrate embedded in the custom-made metal ring was treated with oxygen plasma treatment inside a plasma cleaner machine (FEMTO plasma cleaner, Diener Electronic, Ebhausen, Germany) at 90W and 25 Standard cubic centimetres per minute (sccm) flow rate for 20 seconds before being stamped with fibronectin inked PDMS stamp. Oxygen plasma treatment enhances pattern transfer in the stamping process by increasing the hydrophilicity of the PDMS substrate. The PDMS stamp was put in contact with the PDMS substrate and a gentle pressure, using a standard mass

(~ 100g) (Figure 2-5(d)), was applied in order to transfer the pattern to PDMS substrate. The substrate stamp complex was incubated at 37°C for 3 hours subsequently (Figure 2-6). Afterwards, the stamp was removed and the PDMS substrate was rinsed twice with 1x PBS and twice with ionized water. The

PDMS substrate was moved and kept in 4°C fridge at the end of the process. Cells were cultured on the patterns at a density of 6,000 cells/cm² and were cultured for 200 minutes in 37°C incubator.

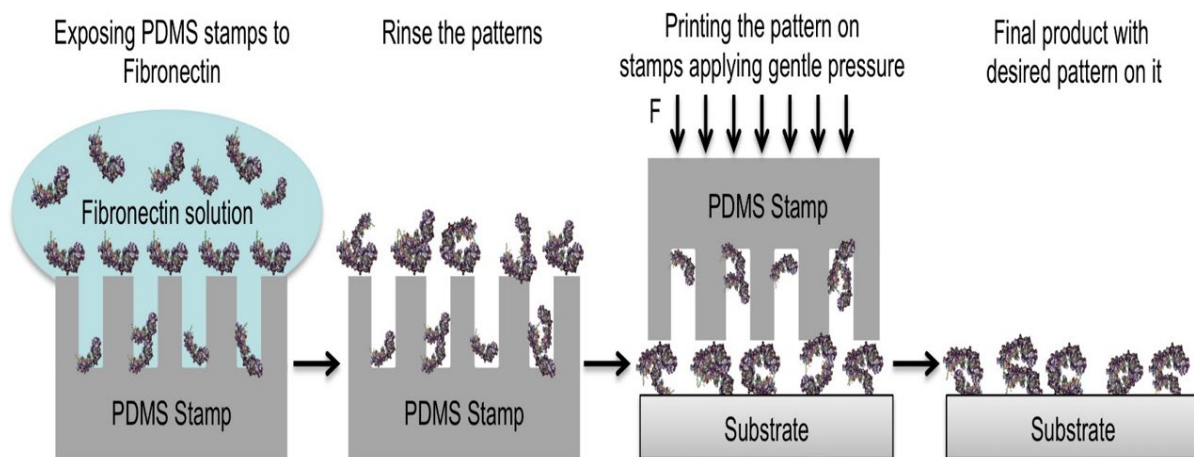


Figure 2-6: Micro-contact printing of the fibronectin stripe patterns from PDMS stamps.

Fibronectin was deposited on a ridge-groove patterned PDMS stamp and subsequently, the fibronectin stripe pattern was printed on the substrate by applying a gentle pressure on the stamp. The diagram is not to scale.

2.7 Fluorescent staining

2.7.1 Filamentous actin staining

16% formaldehyde stock (Polysciences Inc., Eppelheim, Germany) was diluted to 4% with 1xPBS. Cells were fixed with 4% formaldehyde for 10 minutes at room temperature and gently rinsed with PBS twice. Afterwards, the cells were soaked in 1x PBS with 0.1 % Triton X-100 (Sigma-Aldrich, Dorset, UK) for 3 minutes. The cells were again rinsed twice with 1x PBS and exposed to 1% BSA blocking solution (Sigma-Aldrich, Dorset, UK) for 30 minutes. The cells were stained with 6.6 µM Alexa Fluor 488 Phalloidin (Life Technologies, Paisley, UK), incubated for 30 minutes at room temperature and rinsed twice with 1x PBS afterwards. Stained cells were covered with aluminium foil and kept at 4°C. Phalloidin is a bicyclic peptide toxin that is isolated from a very toxic mushroom called *Amanita phalloides* or simply “death cap” and it has a very high affinity to filamentous actin. Therefore when it is conjugated with a fluorescent dye such as Alexa Fluor® 488 (excitation/emission: 495/518 nm), it

makes a highly selective stain for actin cytoskeleton of the cell (*Alexa Fluor 488 Phalloidin - Thermo Fisher Scientific*).

2.7.2 Nuclear staining

Cells were fixed with 4% formaldehyde and gently rinsed with 1xPBS three times. Cells were covered with 1 μ M of TO-PRO®-3 (Life Technologies, Paisley, UK) solution in 1xPBS and incubated for 30 minutes at room temperature protected from light. Subsequently, the staining solution was removed and cells were rinsed three times with 1xPBS. Fluorescent microscopy was performed using the same setup as filamentous actin with 632 nm He-Ne excitation laser and emitted light was captured around 661 nm. TO-PRO®-3 is a cell impermeant monomeric nucleic acid stain with far-red fluorescence (excitation/emission: 642/661 nm) and has a very strong affinity for double-strand DNA (dsDNA) (*TO-PRO-3 Iodide (642/661) - 1 mM Solution in DMSO - Thermo Fisher Scientific*).

For the visualization of suspended cells, the medium was removed after trypsinization (TrypLE for hMSCs) and cells were re-suspended in 1% PBS (for measurement of nuclei after relaxation time (see chapter 5.1 and 6.1), cells were re-suspended in their pre-warmed usual culture medium). Cells were stained with 5 μ g/mL Hoechst® 33342 (ThermoFisher scientific, Paisley, UK) for 10 minutes and quickly were imaged. Hoechst® 33342 is a fluorescent nuclear dye that emits blue fluorescence (excitation, emission: 350/461 nm) when is bound to the dsDNA and as it is a cell-permeable dye, it can be used to stain the nucleus of both fixed and live cells (*Hoechst 33342 Solution (20 mM) - Thermo Fisher Scientific*).

2.7.3 Image analysis

2.7.3.1 Maximum cell thickness measurement

Confocal images were taken with 0.5 μ m steps in the z-direction. Subsequently, the images were reconstructed using LAS X software (Leica Microsystems, Wetzlar, Germany). Comparing x-z and z-y cross sections, the approximate region of interest (ROI) was found and subsequently, the exact point that maximum thickness occurs were found enabling the thickness to be calculated.

2.7.3.2 Volume measurements

Captured images were analysed with Image J software. The area of each cell and nucleus has been

measured and subsequently volume measured by integrating the cell area multiplied by the z stack thickness.

$$V_{total} = \sum A_i d_i = d \sum A_i$$

In which A_i and d_i are the area and thickness of the z stack number i respectively. The z-stack micrographs for each cell or nucleus was imported to Image J and each z-stack image was carefully inspected and the area was approximated by freehand selection.

To estimate the error of area measurement by freehand selection for each z-stack image, we selected the area of a 3T3 fibroblasts for 10 times separately and measured the area (Figure 2-7). The ratio of standard deviation of these measurements to the average area ($\frac{\sigma}{A_{Average}}$) was $\frac{35.6 \mu m^2}{3527.2 \mu m^2} \sim 1\%$ and the ratio of the difference between the maximum and the minimum area to the average area ($\frac{A_{max} - A_{min}}{A_{Average}}$) was $\frac{131 \mu m^2}{3527.2 \mu m^2} \sim 3.7\%$. The stage of confocal microscope is sensitive to steps as small as $0.01 \mu m$ in the z direction.

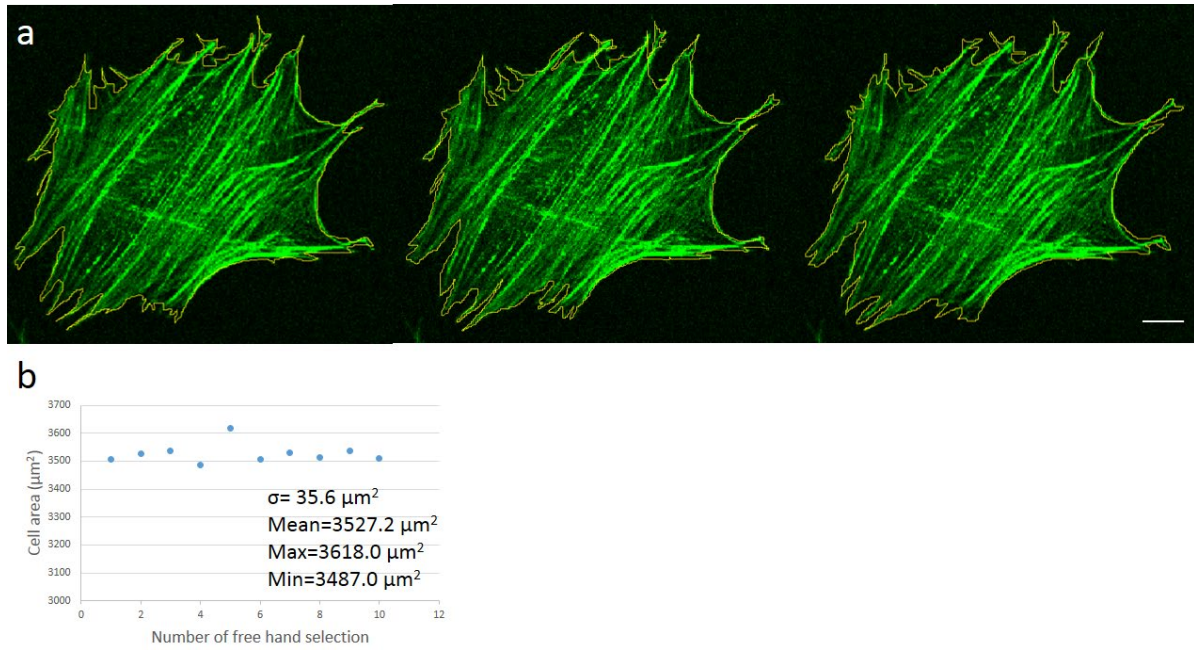


Figure 2-7: Error estimation for area measurement. (a) The area selected by freehand selection for a 3T3 fibroblasts on unpatterned fibronectin coated PDMS substrate (only 3 of 10 area selections is shown here). The distribution of area measurement for the same cell. The cell is fixed with formaldehyde and stained with Phalloidin for F-actin (green). Scale bar is 10 μm . (b) The distribution of cell area by different freehand selections. The vertical axis range is set to better show the difference between the selections.

2.8 Transfection

2.8.1 Principles of cell transfection

In order to genetically modify a cell to permit visualization of the desired cell structures, we used a technique called “transfection” which is a process of introducing a naked (unprotected) or purified foreign DNA to eukaryotic cells (*U.S. National library of Medicine 2016*). In this technique, a DNA plasmid is introduced to the host cell. This DNA plasmid usually is made of a DNA sequence that encodes a protein that binds to the target cell structure, the DNA sequence that encodes a fluorescent tag fused to the binding protein, a DNA sequence that encodes anti-bacterial resistance for selection of the cells that don’t express the introduced plasmid vector and a backbone that contains DNA sequence to facilitate expression of the introduced plasmid by the host cell (Figure 2-9(a)).

Usually, the negatively charged DNA plasmid is enclosed by a liposome. The process of DNA plasmid delivery to the host cells using liposomes is called “lipofection”, “lipid transfection” or “liposome-based transfection” (Matt carter, 2015). In this method, a DNA/liposome complex fuses

with the phospholipid bilayer of the host cell. The cell absorbs the DNA/liposome cargo via endocytosis and carries it within endosomes into the cell cytosol. The DNA plasmid is released upon lysing of the endosome inside the cytosol. The nuclear membrane dissolves during mitotic cell division and allows the plasmid DNA to enter the nucleus. The majority of the introduced DNA is expressed transiently in the transfected cell. However, a tiny proportion of the transfected cells absorbs the introduced DNA into their genome and pass it on to future generations (stable transfection), (Figure 2-8)

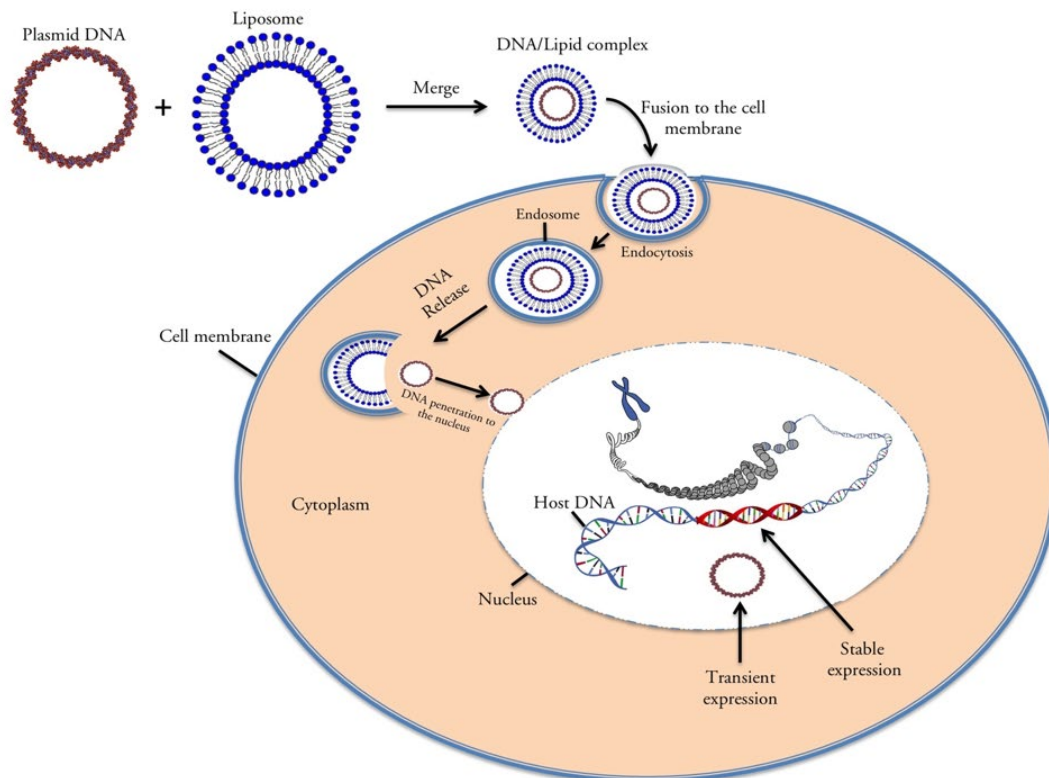


Figure 2-8: Liposome-based transfection schematic diagram. A foreign plasmid DNA is embedded in a liposome and is introduced to the host cell via endocytosis process. In a small number of the cases, the DNA plasmid gets stably integrated into the genome of the host cell.

2.8.2 Transfection for the visualization of the actin cytoskeleton

Cells were transfected with the plasmid p^{CMV}LifeAct-TagGFP2 (Thistle Scientific, Glasgow, UK) in order to visualize actin cytoskeleton in living cells. p^{CMV}LifeAct-TagGFP2 transfection genetically

modifies the cells to express a protein that binds to filamentous actin (F-actin) structure of the cells and express a GFP tag (Excitation/Emission: 483/506 nm) (Thistlescientific.co.uk).

The transfection was carried out according to a protocol from the plasmid supplier. A detailed protocol of the Lipofection transfection can be summarized by the following steps:

- 1- 3T3 cells were seeded in a 24-well plate (Cell star, Stonehouse, UK) for approximately 3 days to reach 80%-90% confluency.
- 2- 1 μ L of the transfection reagent Lipofectamine LTX (Life Technologies, Paisley, UK) was diluted in 25 μ L Opti-MEM medium (Life Technologies, Paisley, UK) in one vial.
- 3- 0.5 μ L of PLUS reagent (Life Technologies, Paisley, UK) and 500 ng of plasmid DNA were mixed in a separate vial. The plasmid DNA came in the form of a lyophilized plasmid. The DNA was resuspended in 20 μ L of TE buffer to obtain plasmid solution with the concentration of 1 μ g/ μ L. The resuspended DNA solution was stored at -20 °C.
- 4- These two vials were mixed in a 1:1 ratio and incubated for 10 minutes subsequently.
- 5- The old medium of the cells was aspirated off and 500 μ L of fresh growth medium was added to the multi-well plate.
- 6- Incubated DNA/lipid complex was added to the 24-well plate.
- 7- The cells were incubated for 48 hours.
- 8- The cells were subjected to selection pressure by adding 1.2 mg/mL of G418 sulfate antibiotic (Life Technologies, Paisley, UK), which kills those cells that do not express the antibiotic resistant gene.
- 9- Cell passage was performed every 3 days for two weeks with the addition of fresh medium and the antibiotic in order to achieve stable LifeAct-mTagGFP expressing 3T3 cells. Fluorescence microscopy on the cells was performed afterwards.

2.8.3 Transfection for the visualization of nuclear Lamin A

In order to visualize the nuclear structure in live cells, we transfected our cells with pBABE-puro-GFP-wt-lamin A DNA plasmid using liposomes (Addgene plasmid, Cambridge, Massachusetts). The plasmid originally was a gift from the Tom Misteli group which has designed the plasmid originally (Scaffidi & Misteli 2008a). The transfection was carried out using a protocol from the plasmid supplier.

pBABE-puro-GFP-wt-lamin A is a 8170 bp circular DNA sequence (plasmid vector) which has genes that encode N terminal enhanced green fluorescent protein (EGFP) (~600bp) as the tag protein (Excitation/Emission: 488/509 nm), pBABE-puro (5200bp) sequence as the backbone of the

sequence, GFP-Lamin A as the inserted gene and genes that make the cell resistant to Puromycin which acts as the selectable antibiotic marker (Figure 2-9(a)).

The plasmid vector was introduced to the host bacteria (*Escherichia coli*) in a process called bacterial transformation. The plasmid also contains genes to make sure that the host bacterium replicates the plasmid during bacterial growth and gives the same plasmids to the daughter bacterium. The pBABE-puro-GFP-wt-lamin A plasmid, therefore, was shipped as transformed bacteria in the form of a bacterial stab (Figure 2-9 (b)) which basically is a type of Lysogeny Broth (LB) Agar media that supports living of transformed bacteria. The bacterial stab was stored at 4°C upon arrival and then bacteria were streaked in a zigzag pattern using a sterile inoculating loop on an LB agar plate (Figure 2-9 (c)) and incubated at 37°C overnight in order to get a single colony of bacteria. Isolating a single colony for inoculating the bacterial culture to amplify the plasmids eliminates the risk of a heterogenous plasmid population growing after DNA purification.

2.8.3.1 LB agar plate and liquid LB preparation

35 g/L Broth with agar (Lennox) (Sigma-Aldrich, Dorset, UK) was diluted in distilled water in a glass container (usually 500 mL in each preparation). The solution was autoclaved at 121°C for 20 minutes to sterilize and was left for approximately 30 minutes until the solution was cold enough to handle and Ampicillin (100 µg/mL) antibiotic was added. The solution was shaken and approximately 25 mL was poured in 100mm Petri dishes (Greiner Bio-one, Kremsmünster, Austria). The bubbles were burst with a sterile tip and plates were left to cool. Plates were labelled and stored upside down in a 4°C fridge (Figure 2-9(d)).

For the preparation of liquid LB, 20g/L LB Broth (Sigma-Aldrich, Dorset, UK) were diluted in distilled water and the solution was autoclaved at 121°C for 20 minutes to sterilize and then allowed to cool before adding Ampicillin (100 µg/mL) antibiotic. The medium was stored at 4°C fridge.

The transformed bacteria have a gene that makes them resistant to the Ampicillin antibiotic and the LB agar plates have 100 µg/mL Ampicillin added to ensure that no foreign bacteria can grow on the agar plates. Using a sterile tip, the single colony was transferred from the agar plate to the LB liquid (Figure 2-9(e)) to incubate an overnight (~16 hours) bacterial culture in a shaking incubator (200 rpm) at 37°C in order to amplify the number of bacteria that contain the plasmid.

For longer-term storage, 25% (v/v) Glycerol (Sigma-Aldrich, Dorset, UK) was added to the bacteria culture and 1.5 mL of the mixture was added to labelled 2 mL cryovials (Starlab, Blakelands, UK) and stored in a -80°C freezer (Figure 2-9(g)). Plasmids are stable in such a -80°C glycerol stock for years (Addgene: Protocol - How to Create a Bacterial Glycerol Stock).

The bacteria culture which looks cloudy (Figure 2-9 (f)), was removed from the incubator and used for plasmid DNA isolation using a miniprep plasmid DNA kit (QIAGEN, Hilden, Germany)

according to the protocol of the supplier of the kit. A miniprep plasmid DNA kit (called also ‘miniprep’) is a fast and small-scale method to isolate plasmid DNA from the bacteria. In this method, first the bacteria culture medium is centrifuged and the bacterial pellet is removed in order to obtain a high concentration of bacteria. Afterwards, a strong lysing alkaline solution is used to disrupt the cell membrane of bacteria. The alkaline denatures both chromosomal DNA and plasmid DNA of bacteria. By acidifying the solution with potassium acetate, plasmid DNA reverts to its original shape while the chromosomal DNA remains denatured and gets filtered out by a gravity-derived column filter. A final centrifuge treatment removes remaining debris and gives a pure solution of plasmid DNA (Birnboim & Doly 1979).

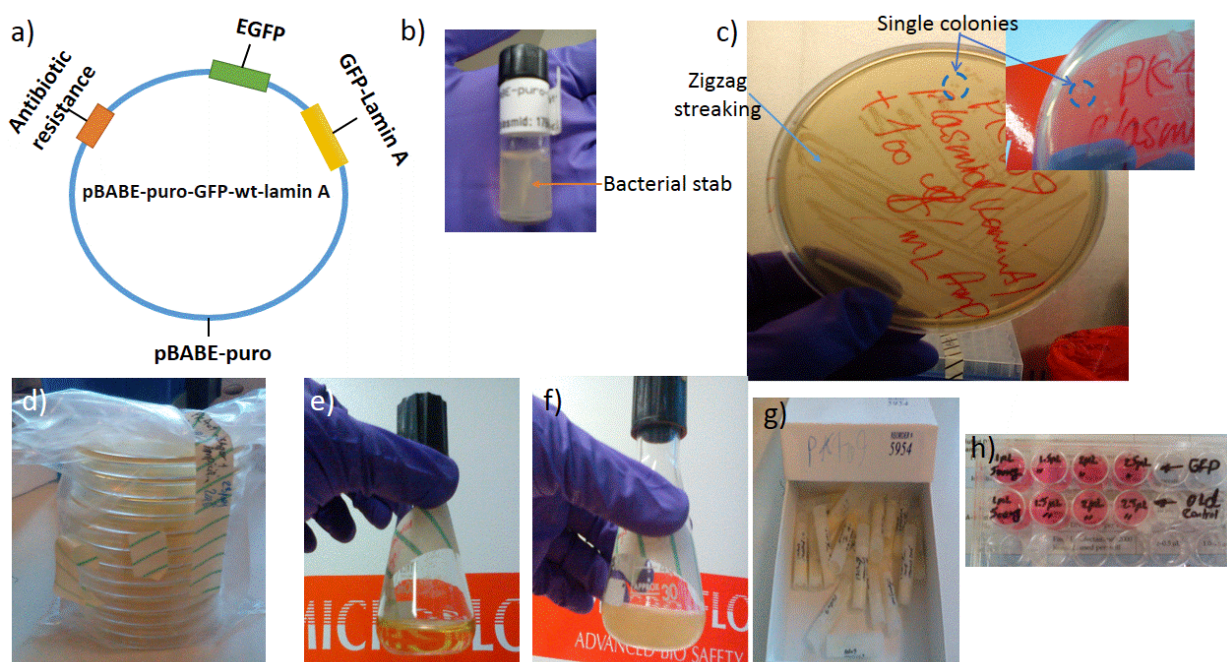


Figure 2-9: Structure and experimental items for storing, amplification, stocking and transfection of pBABE-puro-GFP-wt-lamin A plasmid DNA. (a) The genetic map of pBABE-puro-GFP-wt-lamin A DNA plasmid. (b) Bacterial stab containing transferred *E. coli* bacteria that carry the DNA plasmid. (c) Streaking the transferred bacteria to harvest a single bacterial colony. (d) Agar plates with 100 µg/mL Ampicillin antibiotic. (e) Liquid LB culture medium for *E. coli* amplification. (f) The cloudy culture of *E. coli* liquid culture after an overnight inoculation in a shaking incubator. (g) Transferred bacteria in 25% Glycerol solution stored in cryovials for long-term stocking. (h) Optimization of transfection of 3T3 fibroblasts with the DNA plasmid in different concentration of Lipofectamine® 2000 reagent.

The concentration of purified DNA was measured using a NanoDrop™ 2000 spectrophotometer (ThermoFisher Scientific, Loughborough, UK). 2 µL of tris(hydroxymethyl)aminomethane-Ethylenediaminetetraacetic acid (Tris-EDTA) buffer solution that contains purified plasmid DNA was

put on the spectrophotometers (Figure 2-10(a)) and DNA absorbance was measured (Figure 2-10(b)). The DNA absorbance of the buffer solution was measured as the background control signal (Figure 2-10 (c)). Results showed a yield of ~ 140 ng/ μ L purified DNA plasmid which means that we were able to isolate 40 μ g Plasmid DNA purified from 5 mL of LB bacterial culture. The transfection was carried out using Lipofectamine® 2000 (Thermofisher Scientific, Loughborough, UK) in a similar protocol used for transfection using Lipofectamine LTX (see 2.8.2). The following steps were changed accordingly:

2- 1,2,3,4 μ L of the transfection reagent Lipofectamine® 2000 was diluted in 4x50 μ L Opti-MEM medium (Life Technologies, Paisley, UK) in one vial to find out the optimum amount of the reagent (Figure 2-9(h)).

3- 50 μ L Opti-MEM medium and 1 μ g of plasmid DNA were mixed in a separate vial.

4- These two vials were mixed in a 1:1 ratio and incubated for 5 minutes subsequently.

6- 50 μ L Incubated DNA/lipid complex (500 ng DNA final use per well) was added to the 24-well plate.

8- The cells were subjected to selection pressure by adding 1 μ g/mL of Puromycin Dihydrochloride antibiotic (Life Technologies, Paisley, UK) for two weeks in order to select cells that express the transfected gene.

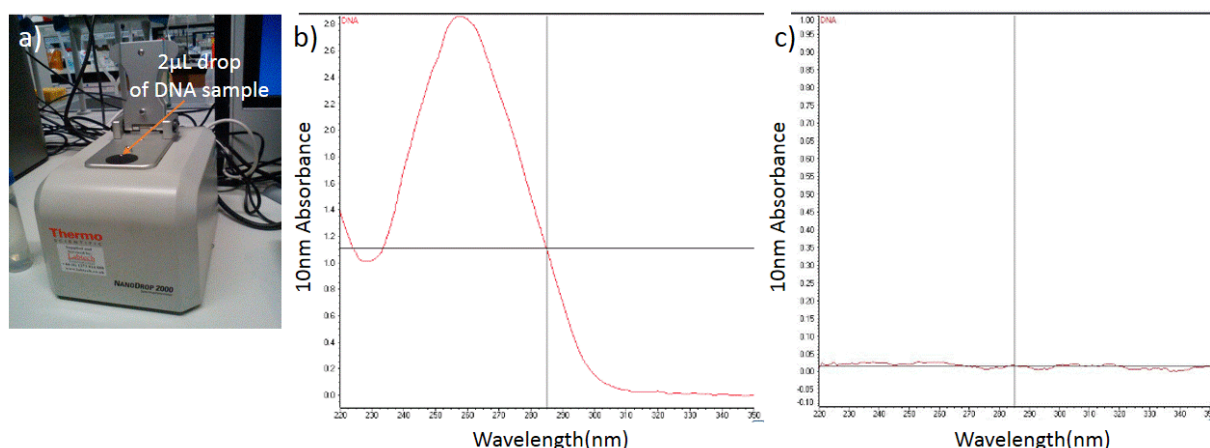


Figure 2-10: Measurement of purified DNA plasmid concentration. (a) A 2 μ L drop of DNA plasmid in Tris-EDTA buffer solution on the spectrophotometer. (b) A DNA plasmid absorbance curve. (c) The absorbance curve for Tris-EDTA buffer solution as the control.

2.9 Microscopy

An inverted confocal scanning laser microscope (Leica TCS SP5) was used for fluorescent microscopy, bright field microscopy and Interference reflection contrast microscopy (RICM). 40x, 63x and 100x oil immersion objectives of the microscope were typically used. Type F 1.518 oil from Leica was used as the immersion oil. Images were analyzed with the LAS AF Lite software suite from Leica. Bright field

microscopy for regular cell status checking during the cell passages, the cell counting by the haemocytometer and controlling the morphological effects of transfection process on the cells was performed on a Motic® AE31 Inverted Microscope. Captured images were analyzed with ImageJ software. In addition, we used this microscope for visualizing the nuclei that was stained with Hoechst® 33342 dye.

2.9.1 Live cell microscopy setup

To perform live cell microscopy without compromising the cell viability, temperature and pH should be maintained at 37°C and 7.4 respectively. As Figure 2-11 illustrates, the microscope stage is enclosed in a chamber and a feedback loop helps to maintain the temperature via an air circuit powered by a fan heater. A CO₂ tank combined with a carbon dioxide sensor and a control circuit helps to maintain the CO₂ level at 5%. This concentration of the carbon dioxide keeps pH of the growth medium at the desired 7.4.

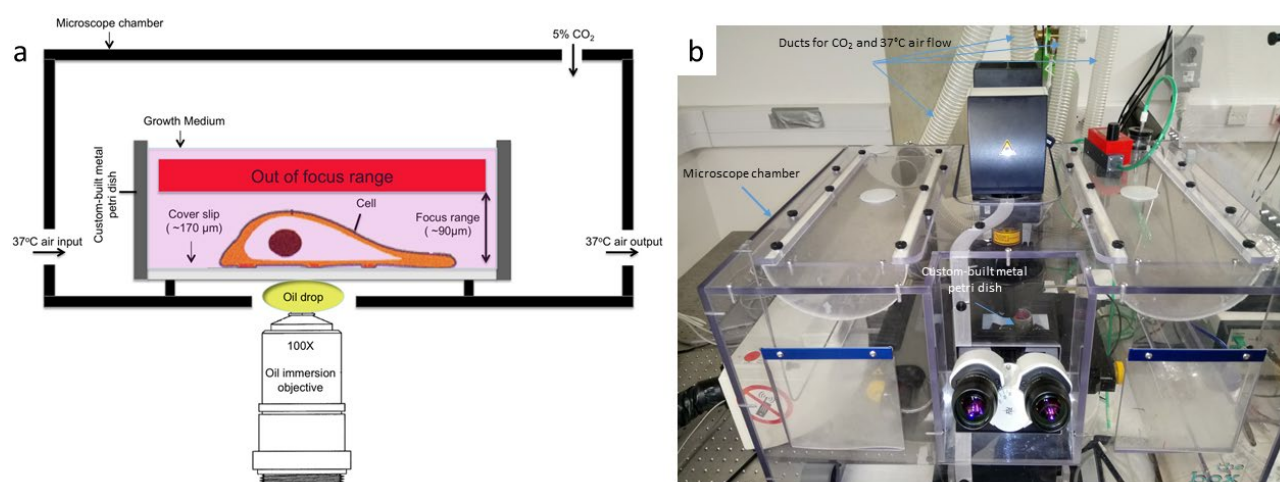


Figure 2-11: Microscope setting for live cell imaging. (a) Schematic view, the diagram is not up to scale. (b) The lab setup. The microscopic chamber provides the living cells with a constant flow of air at 37°C and 5% CO₂ level.

The working distance for different objective lenses varies from a few centimetres for 10X air to about 100 micrometres for the 100X oil immersion lens. Given the thickness of conventional coverslips added to the thickness of the PDMS patterned substrate, there can be limitations to the use of high magnification oil immersion lenses in the inverted microscope. The application of upright microscopy is not feasible for live cell imaging because of the possible contamination by the lens. To overcome the aforementioned challenges, we have designed a custom-built ring setup that consists of a thin

coverslip (0.19 mm) with a 55 μm layer of PDMS on top of it, which makes it possible to use a high magnitude lens to monitor the cells on the patterns. (Figure 2-5 (e)).

2.9.2 Confocal microscopy

Patented in 1957 by Marvin Mersky, this technique improves the resolution of the optical microscope by eliminating out of focus light (red beam in Figure 2-12) both laterally and vertically by means of a pinhole in front of the detector. The method enhances contrast by reducing noise at the cost of a reduction in intensity. The confocal setup gives a thin optical sectioning possibility, which makes it particularly useful in 3D imaging.

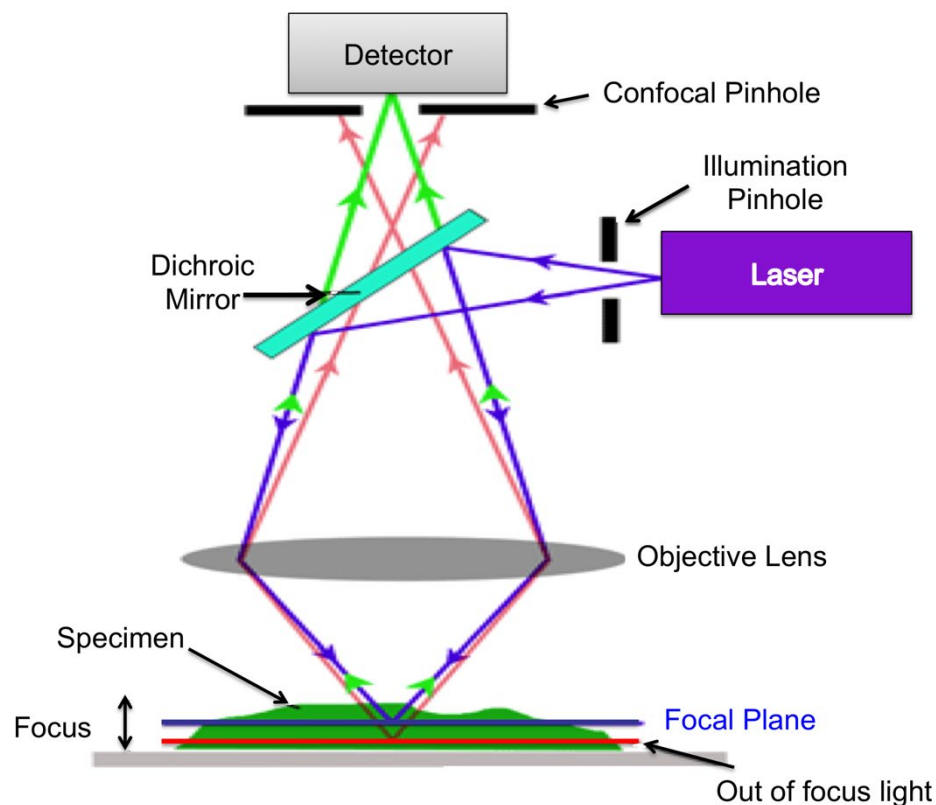


Figure 2-12: Schematic view of confocal microscopy. After (*Confocal microscopy*).

A pinhole in front of the illumination source increases the degree of collimation for the non-laser broadened light source. As laser beams have a very high degree of collimation, point illumination of the sample by them can enhance resolution and contrast of confocal microscopy by restricting the noise from outside the focus point. As the monochromatic beam of the laser is not subject to chromatic aberration, less light is excluded from the focal point compared to polychromatic sources. A minimized size of the illumination spot in confocal microscopy gives another advantage over wide-field fluorescent microscopy by reduction of the photobleaching in the specimen outside the focus point. The thickness

of the focal plane is calculated by the wavelength of illuminating light divided by the numerical aperture of the objective lens. However, it should be taken into account that the optical properties of the specimen are also important in the thickness of the focal point.

2.9.3 Differential Interference Contrast (DIC) microscopy

The method was patented in 1952 by Georges Nomarski; it is also known as Nomarski Interference Contrast (NIC) microscopy and operates on the principle of interferometry to acquire information from the specimen. As Figure 2-13 illustrates, unpolarized light gets polarized at 45° to the original direction as it passes through the primary polarizing filter. The light enters a Nomarski-Wollaston prism, which consists of two inclined slabs of a crystalline material, such as quartz, which has a refractive index dependence on the polarization of the light; it then gets split into two different rays polarized at 90° to each other (the sampling and reference rays). A condenser lens focuses the two rays on the specimen and they pass through the sample from two adjacent points with approximately $0.2\ \mu\text{m}$ separation (this separation distance approximately is the resolution of the microscope). As the optical thickness of the sample at these two adjacent points are different, the two rays experience different optical paths and the phase of one ray changes relative to the other one (phase shifting). The second condenser lens (objective lens) focuses two the rays into the second Nomarski-Wollaston prism. This prism recombines the two rays into one polarized beam at 135° . Interference between the two rays occurs during this recombination. Different phases translate to amplitude variations and result in darker

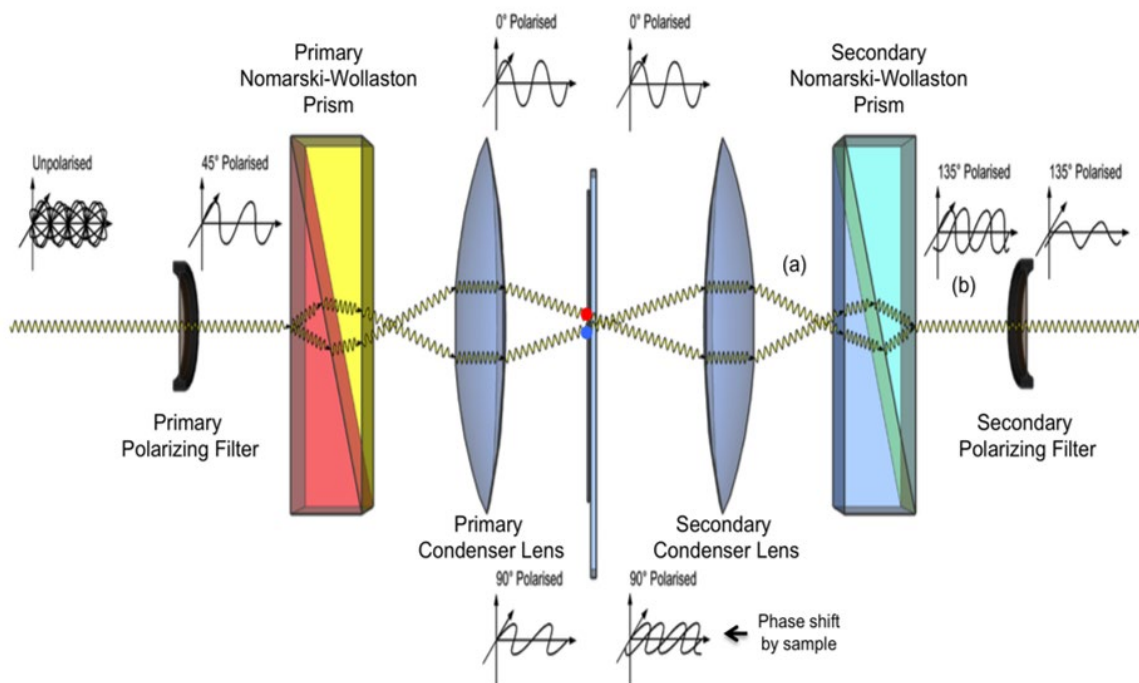


Figure 2-13: Schematic view of DIC microscopy. After Richard Wheeler (en.wikipedia.org).

This prism recombines the two rays into one polarized beam at 135° . Interference between the two rays occurs during this recombination. Different phases translate to amplitude variations and result in darker

or brighter pixels on the image. A secondary polarizing filter removes the directly transmitted light before the detector.

The dependency on the sample being transparent and oversensitivity on the phase polarization are the most important limiting factors for DIC microscopy. The method is not suitable for highly pigmented cells and thick specimens such as tissue slices. The method is much used in biological applications, in particular in the imaging of unstained samples as it enhances the resolution when the refractive index of the sample is fairly similar to the surroundings. However, it is not compatible with highly polarizing materials and this limits its non-biological applications.

DIC is blind to features of the sample that are parallel to the orientation of the Wollaston prism (apparent lighting direction). Imaging of the sample from different angles with the rotation of the specimen can help overcome this limitation.

2.9.4 Reflection Interference Contrast (RIC) microscopy

This technique was initially used to study oil layers and only in 1964 was it introduced for the first time to biological fields to study the contact points of an adhering cell on a glass substrate (Curtis 1964). In a typical RIC microscope, light from a polychromatic light source, such as a halogen lamp, passes through a monochromatic filter. Generated monochromatic light passes through a polarizer and subsequently gets reflected towards the objective lens via a dichroic mirror. A quarter-wave plate circularly polarizes the incident light before it hits the sample (Figure 2-14). The incident circularly polarized light (I_0) gets reflected by the transparent substrate, usually glass, to form the first reflected ray (I_1). Those parts of the incident beam that are not reflected, get refracted by the substrate and hit the sample. When the membrane of the sample (cells in our case) is attached to the substrate, the phase of reflected ray from the membrane is 180° shifted compared to the reflected light from the substrate. Therefore, these two rays of light cancel each other out by destructive interference and create a dark spot on the image. However, when the membrane is not attached to the substrate, the phase difference between reflected ray from the membrane (I_2) and I_1 is not 180° anymore and these two rays recombine together to make the final reflected ray (I), which gets captured by the detector, usually a CCD camera, as a lighter spot (Figure 2-15).

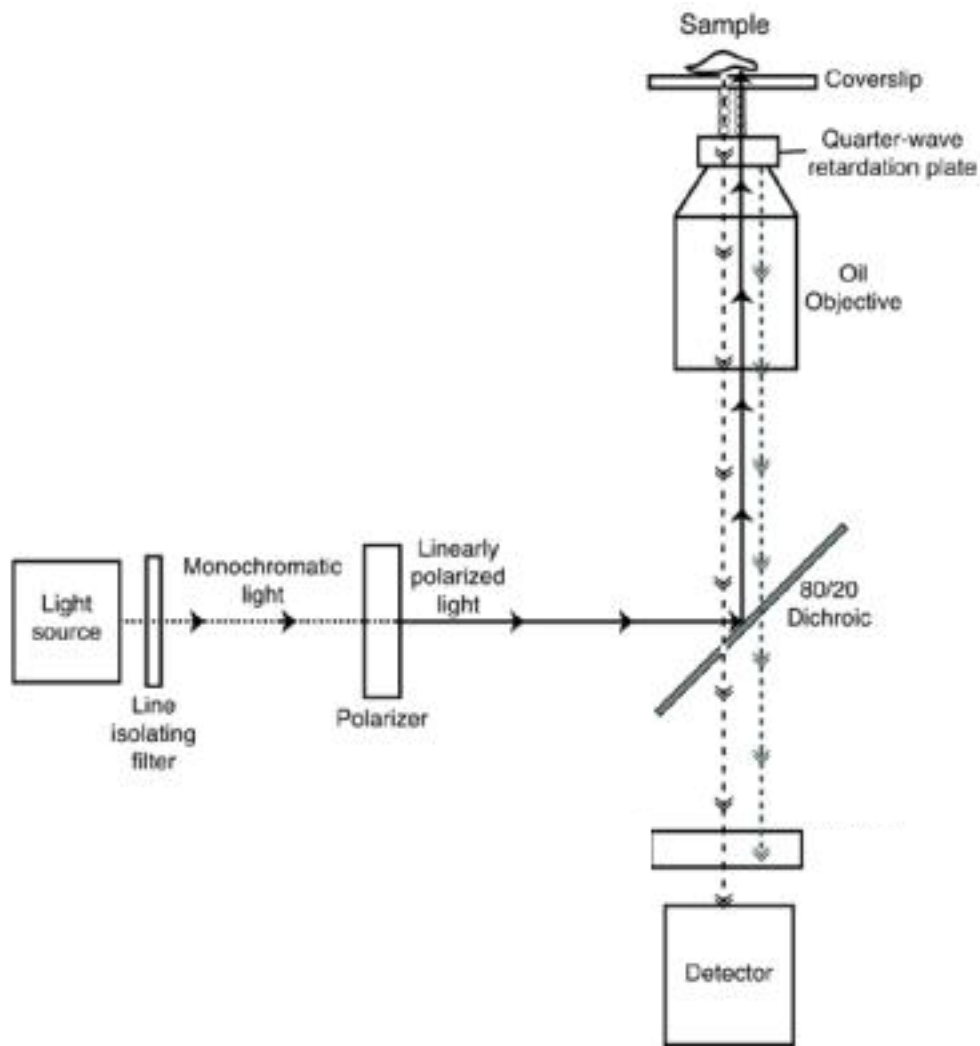


Figure 2-14: Schematic view of a RIC microscope. After (Barr & Bunnell 2009).

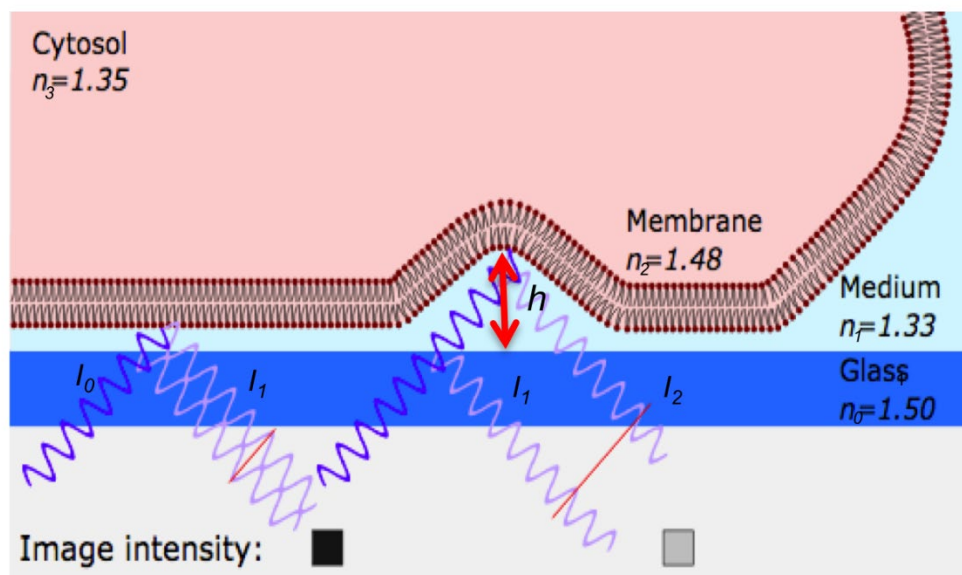


Figure 2-15: Conceptual illustration of image formation in RIC as a result of interference between reflected rays from the sample and the substrate. After Jhpbroeke (en.wikipedia.org)

The intensity of I is given by the following equation:

$$I = I_1 + I_2 + 2\sqrt{I_1 I_2} \cos(2kh + \pi) \quad \text{Equation 2-1}$$

Where $k = \frac{2\pi n_1}{\lambda}$, n_1 is the refractive index of the medium, λ is the wavelength of incident light and h is the distance between the sample membrane and the substrate.

Intensities of I_1 and I_2 are dependent on I_0 :

$$I_1 = r_{01}^2 I_0 \quad \text{Equation 2-2}$$

$$I_2 = (1 - r_{01}^2) r_{12}^2 I_0 \quad \text{Equation 2-3}$$

where r_{ij} are Fresnel reflection coefficients and depend on refractive indexes (n_0, n_1 and n_2).

$$r_{ij} = \frac{n_i - n_j}{n_i + n_j} \quad (i, j = 0, 1, 2) \quad \text{Equation 2-4}$$

As equation 2-1 illustrates I is a function of the distance h . Figure 2-16 depicts this dependency ($\frac{I}{I_0}$) for a light beam within the visible range (dashed curves shows the dependency of I on illumination Numerical Aperture (INA)). This way, the variations in the proximity of the sample to the substrate gives rise to image contrast. This image forming mechanism makes RIC microscopy an ideal option for the imaging of close contacts between sample and substrate (*i.e.* cell periphery and pseudopodia).

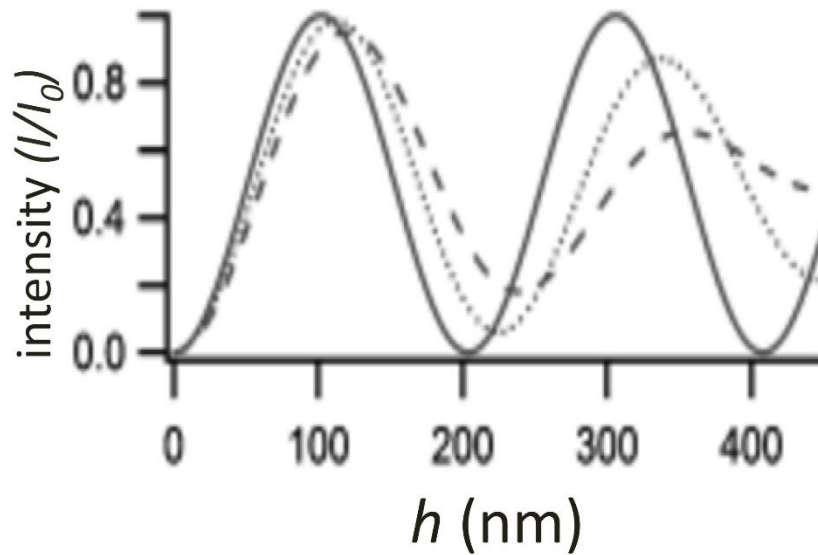


Figure 2-16: Dependency of the intensity of reflected ray to the distance between sample and substrate. After (Limozin & Sengupta 2009).

2.9.5 Phase contrast microscopy

Phase contrast microscopy was invented in the early 1930 by Frits Zernike and due to the importance of the techniques especially in the study of living cells, he was awarded the Nobel Prize in Physics in 1953 (Zernike 1955). The technique is widely used in microscopic observation of unstained biological samples.

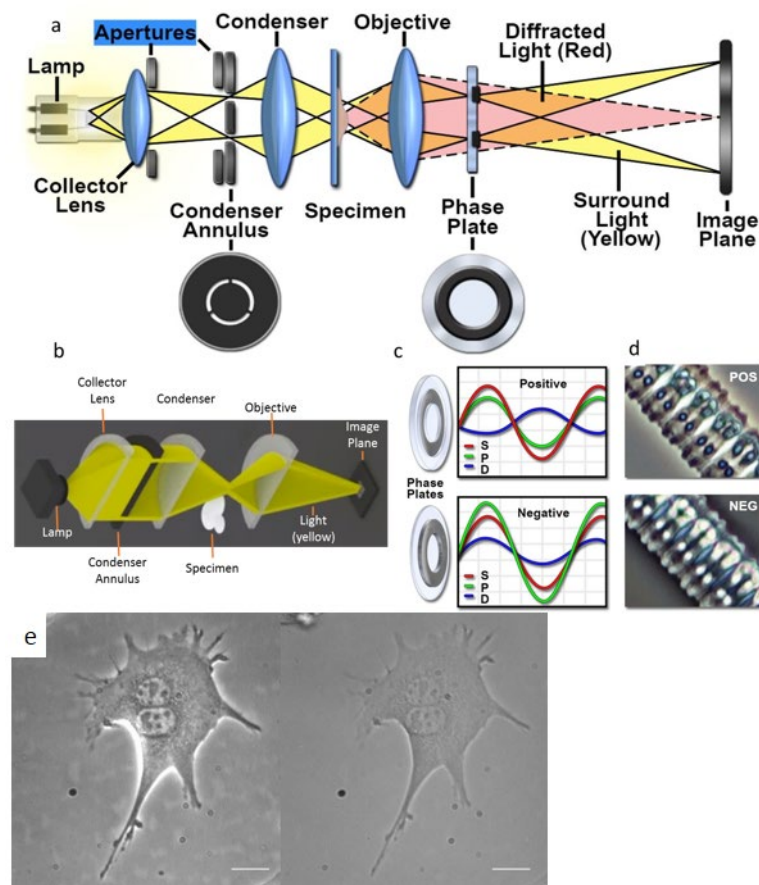


Figure 2-17: The phase contrast microscopy. (a) Schematic view of the ray path in a phase contrast microscope. (b) The formation of the hollow cone in the phase contrast microscope. (c) The phase plate with reduced/increase (positive/negative contrast microscope) thickness and destructive/constructive of surround waves (S) and diffracted waves from the specimen (D) to make the resultant particle waves (P) on the image plane in positive/negative phase contrast microscope. (d) The darker /brighter phase contrast image compared to the background in positive/negative phase contrast microscope. (e) Micrographs of a 3T3 fibroblast by bright field microscopy (left) and the bright field microscopy (right). Scale bars are 50 μm . (a), (c) & (d) after (Introduction to Phase Contrast Microscopy | MicroscopyU), (b) after (*File:Darkfield and phase contrast microscopies.ogv* - Wikipedia), (e) is a result of my personal work.

Unstained biological samples such as cells, usually are transparent and have a refractive index that is very similar to the surrounding medium and therefore they are not highly visible (low contrast) under bright field microscopy (Figure 2-17(e), right panel). Phase contrast microscopy is a technique that can translate small phase shifts of the light that passes through the specimen into changes in the brightness of the resulting image (Figure 2-17(e), left panel).

As Figure 2-17 shows, in a phase contrast microscope, a condenser annulus which is made of a black flat (opaque) disk with a transparent annular ring is put in front of the light source and makes it possible to illuminate the specimen by parallel wavefronts emanating from the annulus (usually described as a hollow cone with a dark centre). Usually, for most of biological specimens, the majority of the light passes through the specimen and around the specimen without interacting with it to create the background light in the image; it is referred as surround waves (S) which have a planar wavefront. However, a small portion of the light waves is diffracted by the specimen and comprise the diffracted waves (D) with a spherical wavefront. D waves have lower amplitude and are retarded (due to the thickness and refractive index difference between the specimen and surrounding medium) by about a quarter wavelength (-90 degrees) compared to S waves. Both D waves and S waves pass through the objective and are focused on the rear focal plane of the objective where the phase plate is placed. Because of the planar wavefront, the S waves occupy a small portion of the objective rear aperture (because they are focused) and therefore S waves and D waves occupy distinct portions of the objective rear focal plane. Therefore, the phase plate which is made of a ring with reduced (or increased for negative phase contrast microscopy) thickness etched into the glass can selectively shift the phase S wave by 90 degrees (an advance for positive phase contrast microscope or retardation for negative phase contrast microscopy) and therefore retard the D wave by 180 degrees compared to the S wave (positive phase contrast microscopy) or eliminates the phase difference between D and S waves (negative phase contrast microscopy). Usually, the ring on the phase plate has a light absorbing metal coating which reduces the amplitude of the S wave by 60-90%. Most phase contrast microscopes are positive phase contrast and therefore D waves and S waves combine in a destructive interference and lead to a resultant particle wave (P) with lower amplitude compared to the S wave. Therefore in these phase contrast microscopes, the cell appears darker than the surrounding medium (Introduction to Phase Contrast Microscopy | MicroscopyU)(Yin et al. 2012).

2.10 Raman spectroscopy

Raman microspectroscopy is a technique that gives comprehensive morpho-chemical information about the cell non-destructively and therefore it is highly used in cell science (see details of the technique in chapter 7.1).

A confocal Raman micro-spectroscopy system (Alpha 300, WITec, Ulm, Germany) was used for the acquisition of all Raman measurements. Spectra acquisition was performed at room temperature and samples were kept at 4 °C while they were not being analyzed under the microscope. A 20X objective lens (Zeiss Epiplan Neofluar, Cambridge, UK) with 12.1 mm working distance was used for cell imaging. Raman scattering was generated by a laser with 785 nm (visible red light) wavelength and 200 mW power. The laser was used with a groove density of 1200 g/mm grating (blaze wavelength was 750 nm). The spectral collection range was usually set from 400 cm^{-1} to 1150 cm^{-1} in order to optimize between spectra acquisition time and deriving the maximum possible biochemical information from the specimen. As Figure 2-18 shows, the calibration of the Raman microscope is performed prior to the start of data collection with standard silicon-based wafers designed for calibration purposes. Scattered Raman signal from silicon is centred at $\sim 521 \text{ cm}^{-1}$ Raman shift. All the tuning knobs were set to get maximum laser intensity in every experiment. The Raman microscope used in this study gives 200-300 nm lateral resolution (diffraction limited) and its ultra-fast scanning option makes it possible to acquire about 1300 spectra per second (0.76 milliseconds integration time per spectrum). This is particularly important in live cell imaging when time and laser toxicity are the main limiting factors.

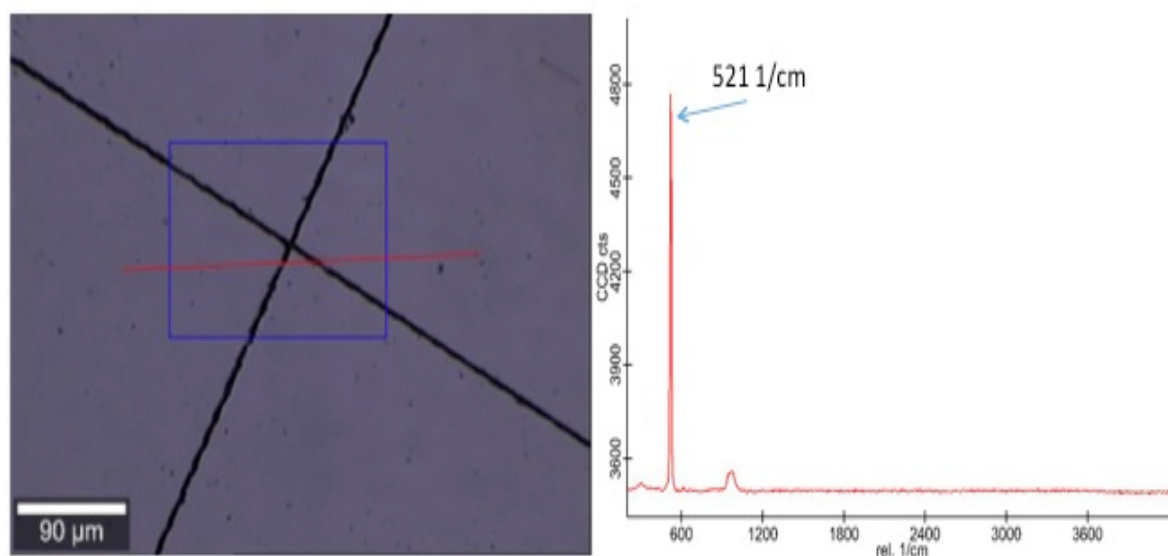


Figure 2-18: Calibration spectrum of Raman microscope using silicon wafer. The left panel is the bright field image of the calibration silicon wafer and the right panel is the calibration spectrum.

For the experiment in which we needed to perform Raman spectroscopy on a gold mirror (see chapter 7.1), we used a 19 mm Round Protected Gold mirror (Thor labs, Exeter, UK) (Figure 2-19(a)). These mirrors consist of a 6 mm quartz fused base with a 1-micron gold coated layer on top and an $\sim 80 \text{ nm}$ silica layer as protector (Figure 2-19(b)). Some part of the spectral acquisition of the cells on these

mirrors was performed with another Raman micro-spectroscopy system (InVia, Renishaw, Gloucestershire, UK).

2.10. 1 Sample preparation on the gold-coated mirrors

For methanol fixation, approximately 10^5 cells were collected from a given culture. The cells were centrifuged for 5 minutes at 1000 rpm and the supernatant was carefully removed and discarded. The cell pellet was re-suspended in 5 ml of PBS solution and shaken gently by hand. The cells were re-centrifuged for 5 minutes at 1000 rpm and the PBS removed carefully without disturbing the cell pellet (it is important to remove all the PBS to minimize interference with the Raman spectra). The cell pellet was re-suspended in 5 mL cold methanol (100%) at -20°C . The suspension was gently shaken and left at -20°C for 30 minutes. The solution was then centrifuged for 5 minutes at 1000 rpm and the methanol removed and discarded. Approximately 100 μl of wet cells were collected with a pipette and placed on a gold mirror and left until the methanol evaporated from the mirror surface. The cell samples on the gold carrier mirrors were then covered and stored at 4°C until analyzed (Figure 2-19 (d)).

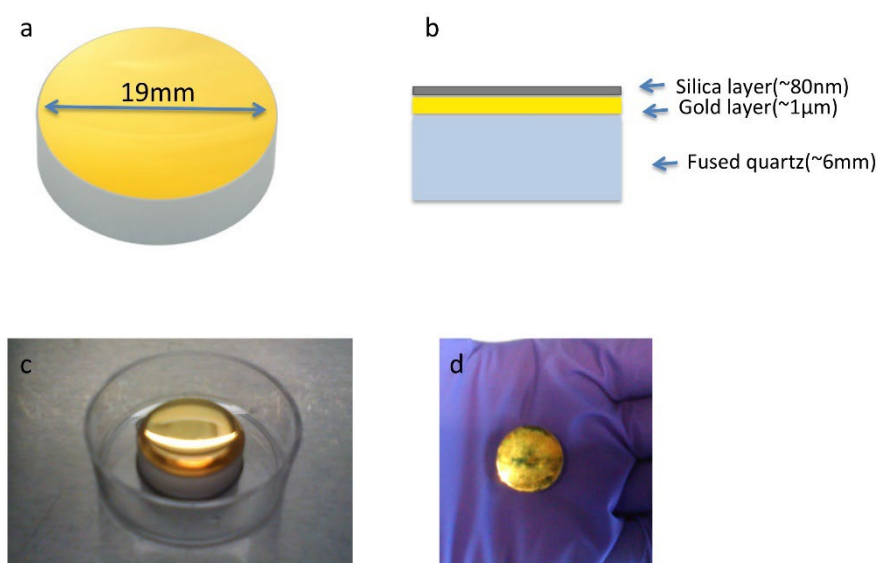


Figure 2-19: A gold mirror for Raman microscopy. (a) Schematic top view of the mirrors after (*Mid-Infrared Enhanced Protected Gold Mirrors*, www.thorlabs.com). (b) The material composition of the mirror. (c) Cell culture on the mirrors. (d) Methanol-fixed cells on the mirrors.

For adherent cells on the mirrors, $\sim 10^4$ were collected from a given sample and seeded on the mirrors. Approximately a 500 μl droplet of phenol-free DMEM/F12 (Life Technologies, Paisley, UK) was put

on cells (Figure 2-19 (c)). The old medium was removed every 4 hours and replaced with a fresh medium droplet.

Matlab 11.0 (The MathWorks, Natick, MA) was used for spectral processing and data analysis. Background spectra were collected from an empty site on the mirror close to the data collection region and subtracted from original spectra. Afterwards, all spectra were processed using a custom built Matlab software (Mamaghani 2015) by automated cosmic spike removal, baseline flattening using a moving average, peak sharpening, and automated smoothing steps.

2.10.2 Metal coating of the patterned substrate

For coating the patterns we used a physical vapour disposition (PVD) electron beam (E-beam) evaporator (KJ Lesker, Jefferson Hills, Pennsylvania) which is a thin film deposition system fitted with a four pocket electron beam source. The system can be used for deposition of thin films of Titanium (Ti), Gold (Au), Aluminum (Al), and silicon dioxide (SiO₂). The film thickness and rate of deposition are accurately computer-controlled using quartz crystal monitoring. In an electron beam evaporator, the anode source material gets bombarded with a beam of electrons and therefore evaporates under a very high vacuum. The beam is generated by a hot filament (usually made of tungsten) and gets accelerated by a high voltage and is targeted on the source material using a magnetic force. The evaporated particles of the sample rise and get deposited on the sample (Figure 2-20). The process allows precise control of the thickness of deposition and therefore is frequently used in the semiconductor industry (Mahan 2000).

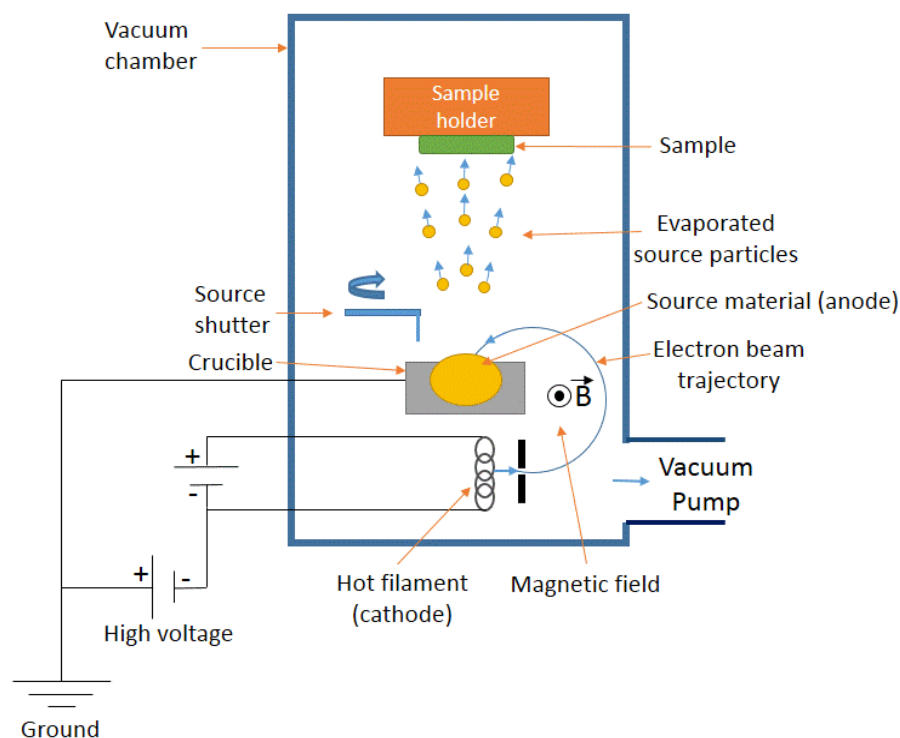


Figure 2-20: Schematic illustration of E-beam evaporator function's principle.

For coating, the pattern was transferred from the silicon template to PDMS (Figure 2-4 (b)) and was loaded into the centre of the sample holder and was attached using Kapton tape (Kapton tapes, Torrance, California). The venting process was started and the sample holder was loaded in the E-beam evaporator and was rotated clockwise to make it firm in its place. Afterwards, coating source materials (gold, silica and titanium) crucibles were loaded into the machine and the door was closed carefully and the vacuum pump was turned on and after approximately an hour the vacuum pressure reaches about $\sim 5 \times 10^{-5}$ Torr (6.6×10^{-3} Pa). The sample was set to rotate at a rate of 2 rotation/minute in order to achieve a uniform coating. The deposition rate was set to 1 angstrom/second for gold and 0.5 angstrom/second for titanium and silica. The crucible that contains the bottom layer (titanium) was selected and the E-beam evaporation was turned on by setting the acceleration high voltage (was set to 10kV or 8kV depending on the crucible's number) and waiting until the desired thickness was achieved. A gap of approximately 5 minutes between the deposition of two different materials was used and the second and third (gold and silica) deposition was carried out. Afterwards, the beam was turned off and the venting process was started to bring the chamber pressure back to ambient pressure and the sample was removed from the machine.

Chapter 3:

Review of the effects of topographical patterns on cell behaviour

In this chapter, we give a brief review of the utilization of topographical patterns to aid understanding and help to control cell behaviour. The review starts with a brief history of the early application of topographical cues in cell studies and continues by introducing different types of topographical patterns that are used in contemporary cell research.

Later we focus on the important works that have been carried out to use topographical patterns in the study of cytoskeletal and nuclear mechanics. We review studies that are comprehensive about the state of the art in the field and also contain results that we will need to understand subsequent result chapters. Finally, we narrow down our review to the effect of ridge groove and stripe patterns that are printed using ECM adhesive proteins such as fibronectin. The ridge-groove patterns are well-studied patterns and are the 3D template patterns used to print the fibronectin stripe patterns that we use in this study. Furthermore, both cytoskeleton and the nucleus of the cells on the ridge-groove patterns exhibit morphological responses that are similar to responses that are observed among cells on microprinted stripe patterns and therefore reviewing the works on the ridge groove patterns can help us to better understand our results.

3.1 Origin of the subject

In the early years of the 20th century, there was a huge rush and scientific excitement about the possibility of the cultivation of tissues of higher animals outside the body. There were successful attempts to isolate some vital tissues, nourish the tissue with a proper extraneous medium for hours or days while the tissue continued its impaired function and then regraft the tissue inside the original animal without seriously damaging the tissue. However, when they tried to isolate cells which were the constituent parts of those tissues, culture and expand them in order to regenerate the tissues, they soon realized that it is not just the composition of chemical reagents that influence the cell; but, physical cues such as the substrate material and morphology have an important impact on the cells (Harrison 1912). For example, they realized that locomotion, the polarity of the cells and direction of migration plays a key role in embryogenesis (Harrison 1914). In order to investigate the effect of the microenvironment on this process they set an experiment in which cells from chicken embryos were seeded on three

different microenvironments: clotted plasma which gives a fibril network to the cells, a solid surface of a glass coverslip which gives the cells symmetric solid support and a network of spider web fibers. As there was not mitotic cell division, membrane formation was due to cell migration and alignment to the substrate texture (Harrison 1914). Epithelium like cells from a chicken embryo that were cultured in clotted plasma featured a characteristic ring formation in which mesenchyme cells were presented and epithelium-like cells expressed a tendency to form a membrane (Figure 3-1 (a)). Cells on the coverslip surface spread and migrated on the surface and formed a monolayer cell membrane although union of the cells from adjacent parts of the membrane at some point made large holes in the structure.

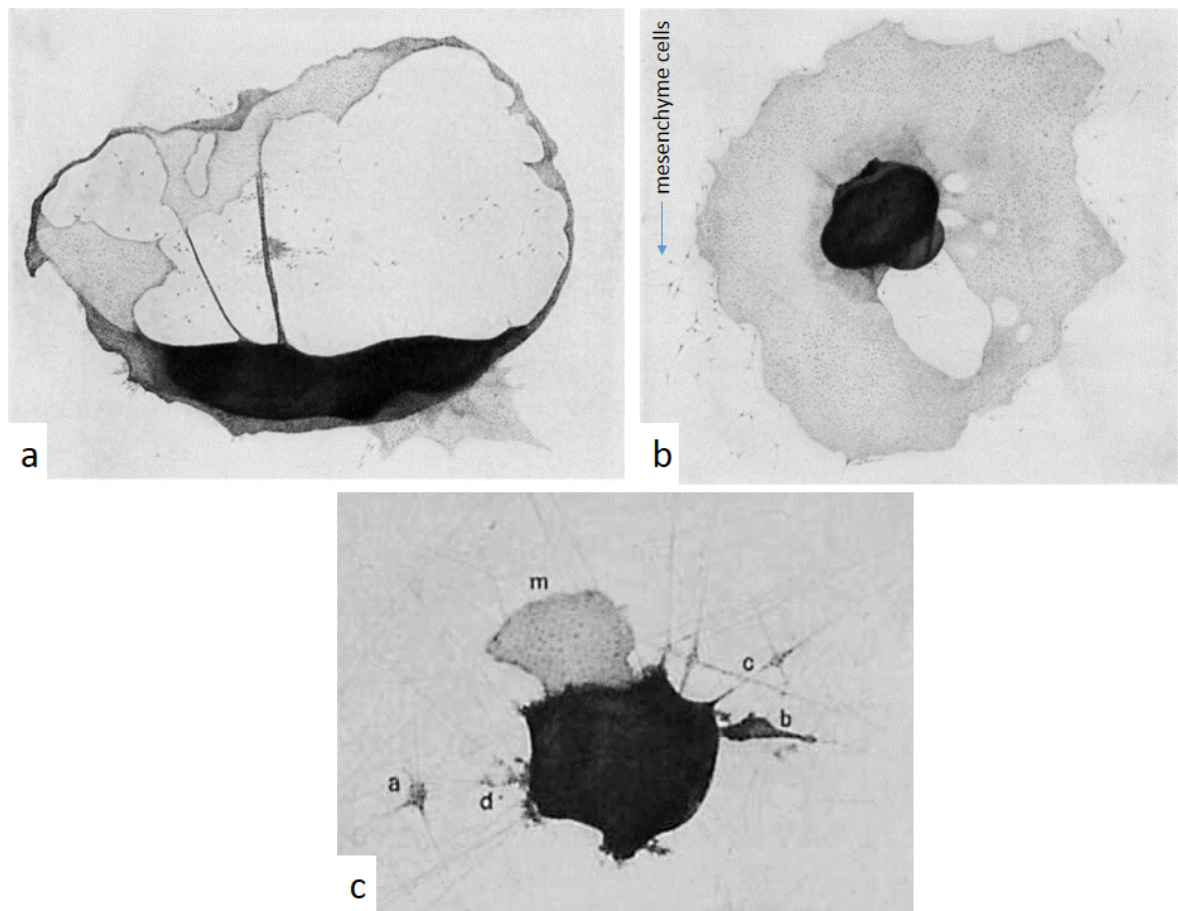


Figure 3-1. The effect of substrate texture on the chick embryonic cells (duodenum of 9-day chick embryo). (a) Cells were seeded in clotted plasma which has a fibril structure feature a ring-like structure. (b) Cells on a glass coverslip formed a monolayer membrane with some holes and large branched mesenchyme cells in the periphery. (c) A group of cells on spider-web formed a smaller membrane (m), a small group migrated along the fibres (a), a group attached to the web (b), a group polarized along the fibres (c), another group became necrotic (d). The magnification is x 39. (Harrison 1914).

Highly branched mesenchyme cells with big cell areas were observed in the periphery of the membrane (Figure 3-1(b)). Cells on the spider web formed a smaller membrane (m), a small group of cell migrated along the webs (a) a bigger group of the cells firmly attached to the web (b), a group of cells polarized along the webs and showed a spindle-like morphology that resembled embryonic nerve cells (c) and some cells became necrotic (d) (Figure 3-1 (c)).

To further investigate the polarization of the cells on the web, cells from medullary cord were seeded at lower density on the spider web and they showed a great degree of alignment to the webs creating spindle-like cells, bipolar cells, tripolar cells, cells adhering to the web with a right angle, and cells that cross over each other.

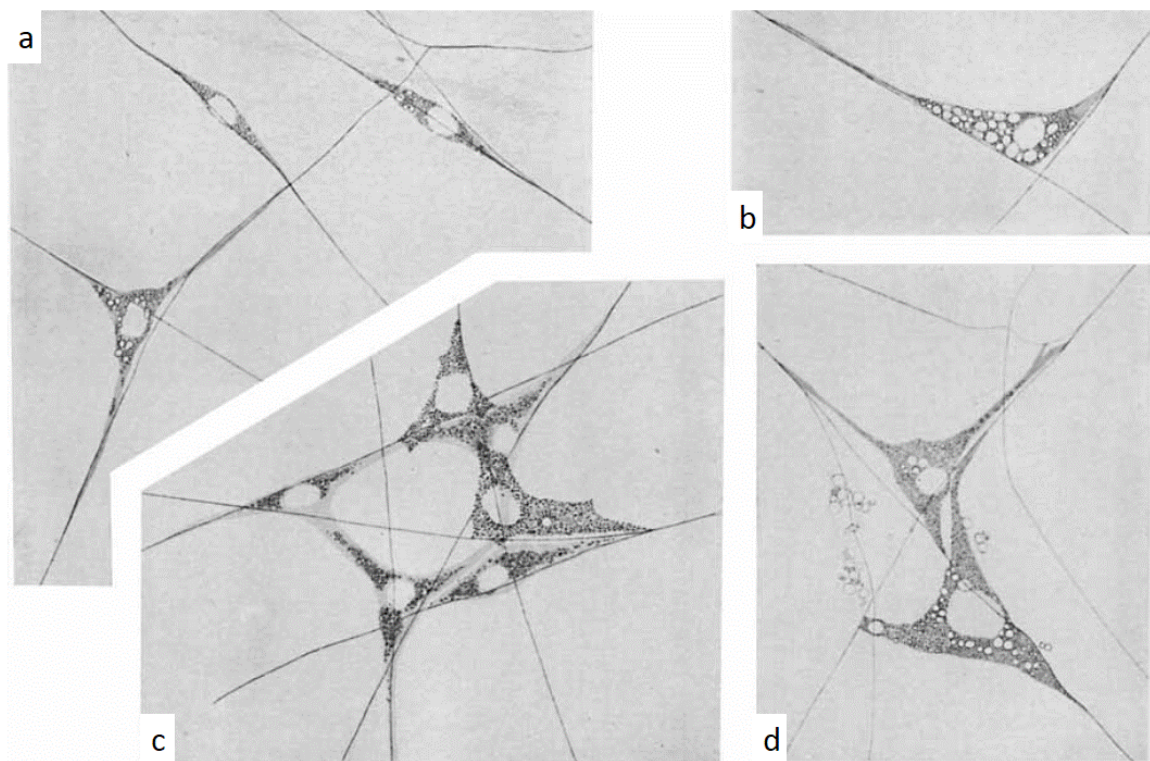


Figure 3-2: The polarization of medullary cord cells on the patterns made of a spider web. Cells polarized along the web fibres to form (a) spindle-like elongate bipolar and tripolar single cells, (b) bent and attached to a right angle crossed web fibres, (c) confined to a set of star-like web fibres, (d) two cells cross over each other on crossed fibre web. The magnification is x 39 (Harrison 1914).

After the early works that were carried out by Harrison in 1914, the effect of solid structures on cells were generally referred as the “thigmotaxis (from Greek thigma ‘touch’+ taxis ‘arrangement’)” or “stereotropism (from Greek stereos ‘solid’ + tropos ‘to turn’)” or “contact sensibility” or “tactile adhesion”. However, from 1941 onwards the phenomenon has got a different technical word of “contact guidance” when Paul Weiss observed that culturing of nerve fibres in a plasma clot that was stretched

by an external force, resulted in an oriented growth of neurons and therefore oriented growth of nerve processes (Weiss 1941)(Jacobson 1978).

By the middle of the century, researchers started to use non-organic materials or simple fabrication methods to create texture and patterns on the substrate in order to study cell and tissue polarization *in vitro*. A variety of pattern could be made by grooves that were created by scratching of mica substrates (Figure 3-3).

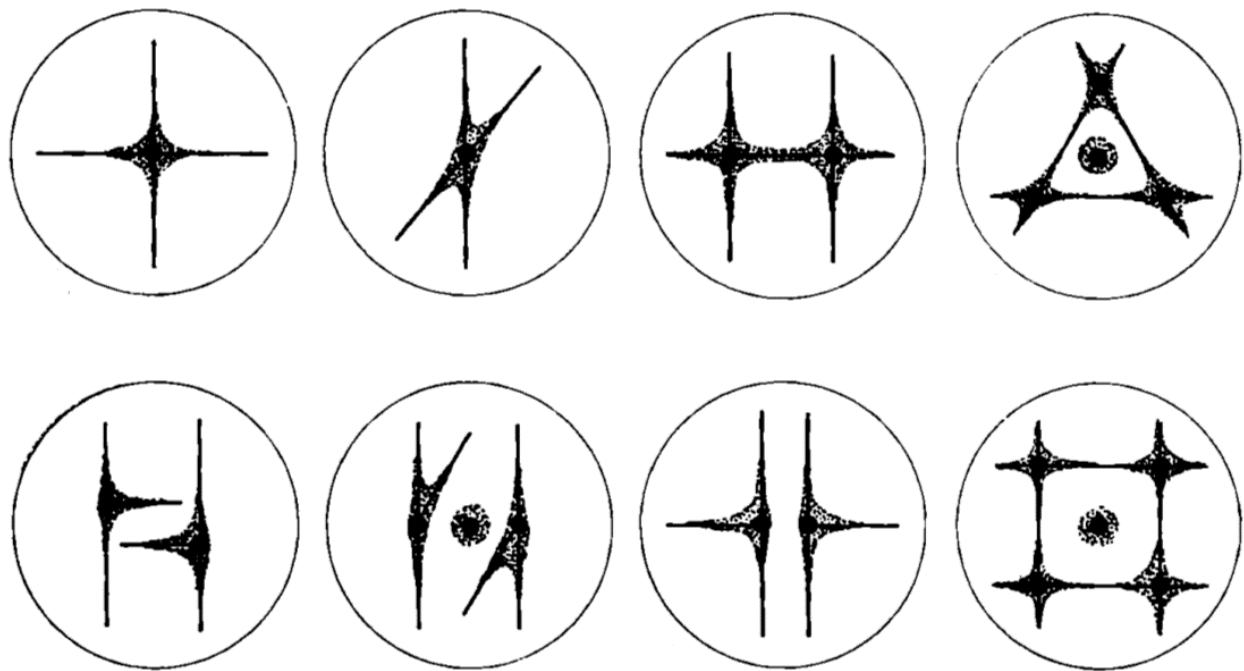


Figure 3-3: Diagram illustration of different groove patterns on mica substrate used by Weiss in 1945 to study nerve growth. Cells from embryonic spinal ganglia were cultured in the darker area on the grooves and cells were spread to the stippled area after several days. The circles indicate the area of culture medium (Weiss 1945).

In 1945, Paul Weiss examined more than 5000 tissue cultures and published one of the milestones in the field using grooved mica substrates which were used to study nerve growth using cells from embryonic spinal ganglia (Weiss 1945). He placed the cells in the crossing points of a pair of intersecting grooves and observed that the cells were spreading outwards in the form of a “tongue” along the direction of the grooves. The extending nerve tongue tapers towards an apex which lies in the groove (Figure 3-4(a)). The cells on two neighbouring nerve tongues can merge at their tips. He showed that the alignment of the cells to the patterns is more significant when the scratches are deeper.

He also used glass fibres with a size range from 8 to 26 μm to see the effect of the fibres on the polarization of nerve fibres. He observed that the cells build stronger adhesion to the surface of the glass fibres compared to the fibrin fibres of the surrounding plasma clot so that cells in the interface of plasma clot and glass fibres were attached and dragged from the plasma to elongate themselves along the fibres (Figure 3-4(b)). He previously had measured that the size of advancing cell filopodia of the nerve cells was approximately 0.2 μm and therefore he was not able to explain how the cells can sense the direction of the fibres with the width of 15 μm and align themselves with that direction. He set up experiments to examine the possible molecular orientation of glass fibre surface in the longitudinal direction of the fibres, the possibility of alignment of surrounding fibrin fibres to the direction of the glass fibres and the possibility of the sensitivity of advancing filopodia to the curvature of the fibres. However, in all cases, he was able to reject these hypotheses with experiments that he designed.

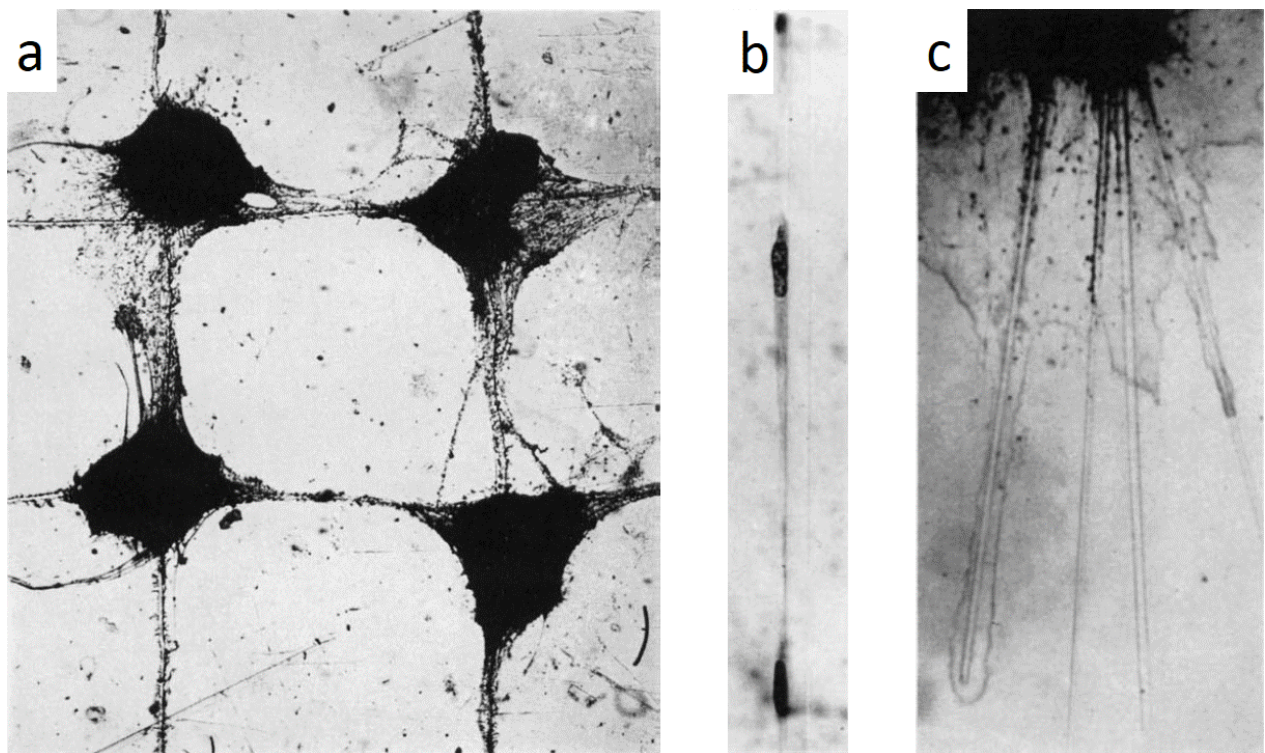


Figure 3-4: Contact guidance of cells on grooved mica and glass fibres. (a) Pattern alignment and orientation of cells from embryonic spinal ganglia that were cultured on right angle intersected grooves on mica substrate in the presence of liquid cell medium. X30. (b) Schwann cell (also called neurilemma cells) are elongated and aligning themselves to the interface of glass fibre and plasma clot. Nuclei are the dark dot on the cells. X360 (c) Extension of rat nerve exudates driven by capillary force along contact line between glass fibres and surface of the coverslip in the presence of plasma clot medium. Nerve cells are following the exudate in alignment to the glass fibres. X34. (Weiss 1945).

He finally concluded that the orientation of nerve fibres is derived by deformation of the exudates by the capillary force. Similar to surface wetting that allows water to wet a glass rod, the exudate also tends to coat the glass fibre. The capillary force makes the exudates to move along the fibres and this spreads a mesh of molecules that are secreted from the cells along the glass fibres which he calls the “ground mat”. The elongated ground mat which with today’s terminology consists of polarized ECM fibres guides the rest of cells in the tissue to elongate alongside the glass fibre (Figure 3-4 (c)). However, nowadays we know that the locomotion of the cell is a more complex active process that involves in the formation of the focal points and reorganization of the cytoplasm depending on the topographical and chemical cues of the substrate (see chapter 1.5 for more details).

3.2 Different types of topographical cues

Synthetic biomaterials have been used to mimic the ECM and also to build customized experimental setups with controlled geometrical and chemical (usually by changing the coating of the surface) parameters to study different aspects of cellular and tissue behaviour. Development in fabrication techniques has given the researchers options to create a diverse range of 2D and 3D topographical patterns at the nano and micrometre length scale to study cell migration, cell adhesion and alignment, stem cell differentiation (see chapter 4), quantified cell and nuclear deformation and quantified study of cellular forces. (Guillotin & Guillemot 2011)(Ermis et al. 2018).

A wide range of techniques which mostly originally were used in the electronics industry has been used to fabricate topographical cues on a surface to study mammalian cells. For nano-scale structure topographies, methods such as electron beam lithography, nanoimprint lithography, photolithography (interference), colloidal lithography, polymer demixing, acid etching, sintering of nanophase materials, anodisation, electrospinning, coating with nano-objects and for micro-scale structures methods such as photolithography, soft lithography and microprinting, Electrochemical micromachining, Laser ablation, Sandblasting or shot peening, Plasma spraying, Machining, Mechanical polishing, Electropolishing, Acid etching, Electroerosion and Electric glow discharging are used (Anselme & Biggerelle 2011).

The geometry of micropatterns is also diverse depending on the purpose of the study; however, it is possible to classify them into the following categories: microgrooves (with different groove cross-section and sizes) (Berry et al. 2004), micropillar arrays (Ghibaud et al. 2009), micro-pits (Berry et al. 2004), and microscale shapes printed with ECM adhesive proteins (Figure 3-5).

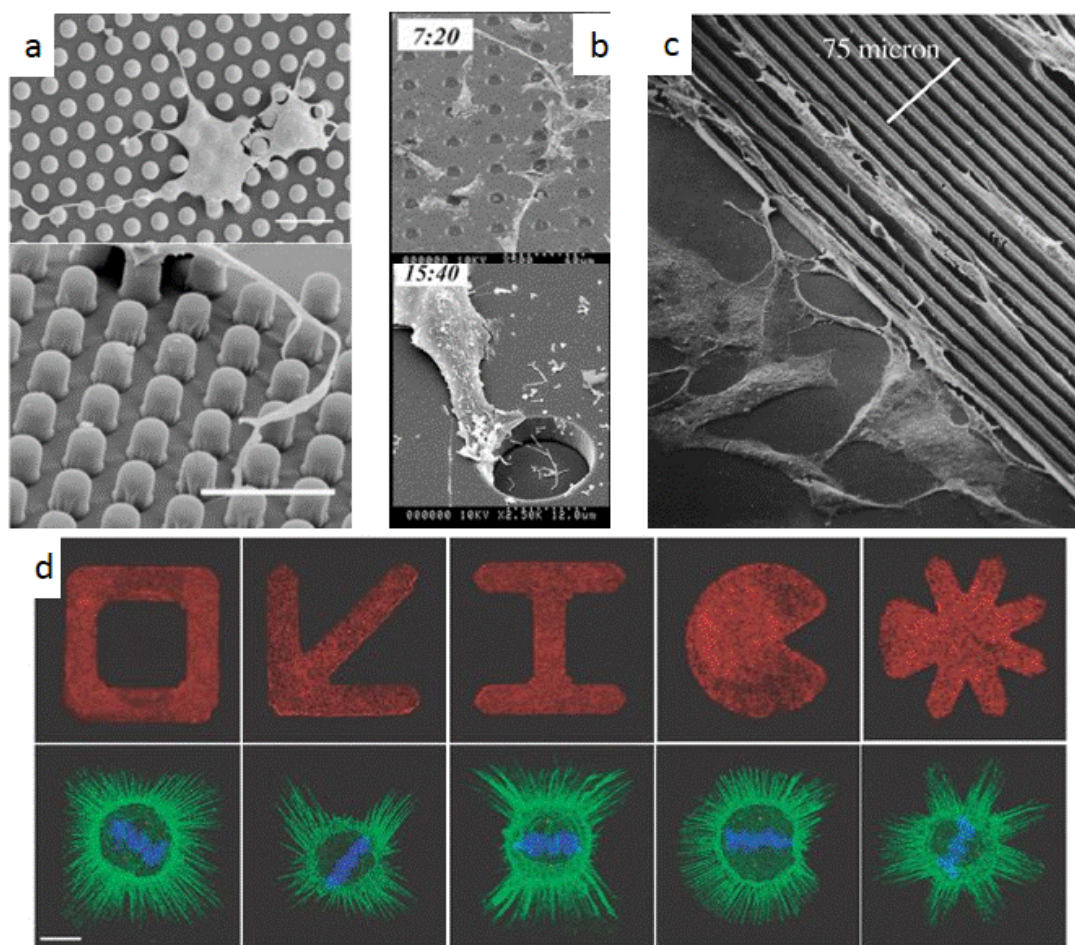


Figure 3-5: Typical geometries of micropatterns in biomaterials. (a) SEM images of 3T3 fibroblast on arrays of PDMS micropillars (height (H): 10 μm , diameter (D): 5 μm , spacing(S): 5 μm) from top-view (upper row) and side-view (lower row) of the micropillars (H: 6 μm , D: 5 μm , S: 5 μm) with an extended lamellipodium of an adhering cell. Scale bars are 20 μm . (Ghibaudo et al. 2009). (b) SEM images of primary human fibroblasts on a micro-pitted quartz substrate (depth: 4.8 μm , D: 7 μm , S: 20 μm , upper row) and (depth: 4.8 μm , D: 15 μm , S: 40 μm , lower row). (Berry et al. 2004) (c) SEM images of rat epitenon fibroblasts on polyurethane (Elastane) grooves showing substantial morphological differences of the cells on the patterns in comparison to the cells on the flat substratum (Curtis 2004). (d) Fluorescence microscopy of fibronectin micropatterns (red) with different shapes (upper row) to study the mitotic spindle orientation in human HeLa cells. Actin-rich retraction fibres (green, lower row), spindle poles (red) and chromosomes (blue) are shown. Scale bar is 10 μm (Théry et al. 2007).

3.3 Application of topographical patterns in study and control of cellular and nuclear mechanics

In the last 70 years, topographical patterns with different shapes have been used to study various properties and behaviour at both the cellular and tissue level (Anselme & Biggerelle 2011).

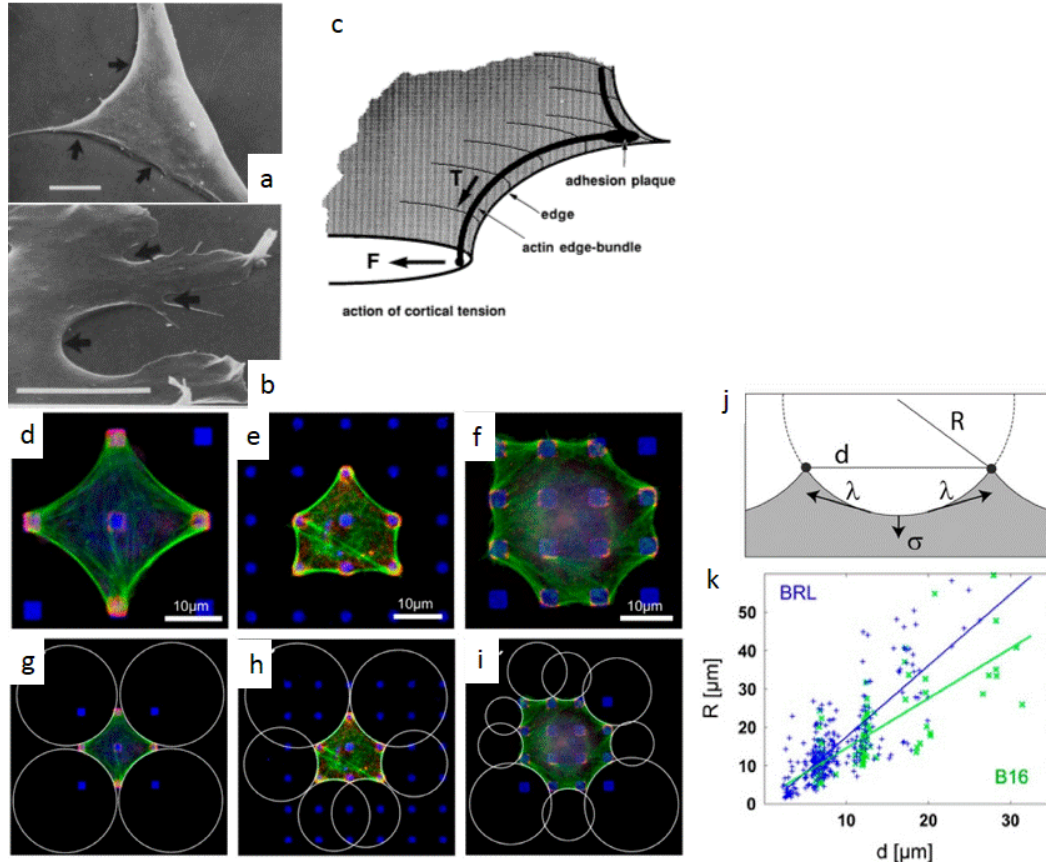


Figure 3-6: Fibronectin-dotted micropatterns for the quantitative study of actin edge bundles. (a)&(b) SEM images of 3T3 fibroblasts showing concave circular arcs (arrows) with varying sizes formed at their edge between adhesion points. Scale bars are 10 μm (Albrecht-Buehler 1987). (c) The original diagram of actin edge-bundles showing that the concave bundles form between two adhesion plaques (points) and the bundles develop a tension (T) to oppose the cortical tension (F) (Zand & Albrecht-Buehler 1989). Fluorescent microscopy of actin edge bundles arcs of cells on PDMS patterned with fibronectin dots (blue) showing F-actin (green) and Paxillin labelled focal adhesion (red), (d) &(e) buffalo rat liver (BRL) cells, (f) mouse melanoma cell line (B16) cells. (g),(h) & (i) show arc actin edge bundles fit circles respectively. (j) Schematic view of the simple tension model, the surface tension (σ) which pulls the cell membrane inwards balances the line tension (λ) which stretches the actin edge bundles between two adhesion points. (k) Arc radius increases (R) with spanning distance (d) for both BRL (blue) and (B16) cells. Scale bars are 10 μm (Bischofs et al. 2008).

One of the fields in which the patterns are most widely used is to understand, probe and control the mechanics of the cytoskeleton and nucleus. Micro-patterns gives a very strong tool to researchers to deform cells in a very well defined geometry and therefore the patterns act as an ideal platform to quantitatively observe and model mechanical structures of the cells and nucleus.

It has been known for a long time that adherent cells often form concave circular arcs in the webbed edges (Albrecht-Buehler 1987) (Figure 3-6(a)). The arcs later were called an “actin edge bundle” and it was shown that these bundles are composed mostly of actin, alpha-actinin and microtubules fibres. These bundles are more resistant to actin depolymerizing drug treatment compared to normal actin stress fibres. It was suggested that edge bundles are specialized cytoskeletal structures that support the webbed edges of interphase 3T3 fibroblasts (Zand & Albrecht-Buehler 1989)(Figure 3-6(b)). Micropatterns composed of fibronectin dots printed on PDMS substrate which mimic spatial distribution ECM ligands *in vivo* were used to study the actin edge bundles quantitatively (Bischofs et al. 2008). The results revealed that the arc morphology of actin edge bundles was universal regardless of the cell type, varying size of lattice constant (5, 10, 15, 20, and 25 μm) and dot sizes (0.5–3 μm) (Figure 3-6(c,d,e,f,g,h& i)).

Classically the radius of actin edge bundles is calculated using the Laplace law for cell adhesion which assumes both surface tension (σ) and line tension (λ) are local quantities. Therefore, the radius of the arc curvature (R) is constant ($R = \lambda/\sigma$) and independent from the spanning distance (d). This model is also called the simple tension model (Bischofs et al. 2008) (Figure 3-6 (j)) . However, the data from micropatterns showed that the curvature radius (R) increases with the spanning distance (d) and the experimental results were consistent only when the effect of elastic deformation of the arcs is considered in the line tension of the bundles (tension-elastic model) (Figure 3-7 (k)). By monitoring the distribution of arc radius (R) among the cells that were cultured on the micropatterns and were treated by actomyosin inhibition drugs, it was shown that the cell shape is regulated by both myosin motor contractility and structural changes in the actin filaments.

Vertical PDMS nanopillar arrays (radius= 50-350 nm, height= 0.7-2 μm) with micrometre spacing (2-10 μm) were used to study nuclear mechanics of 3T3 fibroblasts and to develop models for pressure exerted from the cytoskeleton on the nucleus (Hanson et al. 2015c) (Figure 3-7 (a)). Although there was no significant change in the cytoskeletal morphology (Figure 3-7 (b)), the nucleus was deformed significantly around the pillars (Figure 3-7(c)). Quantitative analysis of 3D confocal microscopy images of the nucleus showed that the nuclear deformation is highly dependent on nuclear stiffness, cell type, the integrity of cytoskeletal components and the geometry of patterns.

When 3T3 fibroblasts were genetically modified to express more lamina A (50-90% more compared to control 3T3s) and as a result got stiffer nuclei, their nuclei (deformed over 50% less on the patterns

compared to the control cells. Among different cell types, neurons have the most nuclear deformation on the patterns followed by MCF7 (a type of breast cancer cells), HL-1 cardiomyocytes and 3T3 fibroblasts. The difference between nuclear deformations of different cell lines is statistically significant and this makes the patterns useful as a potential method for studying nuclear deformability among various cell lines (Figure 3-7(d)).

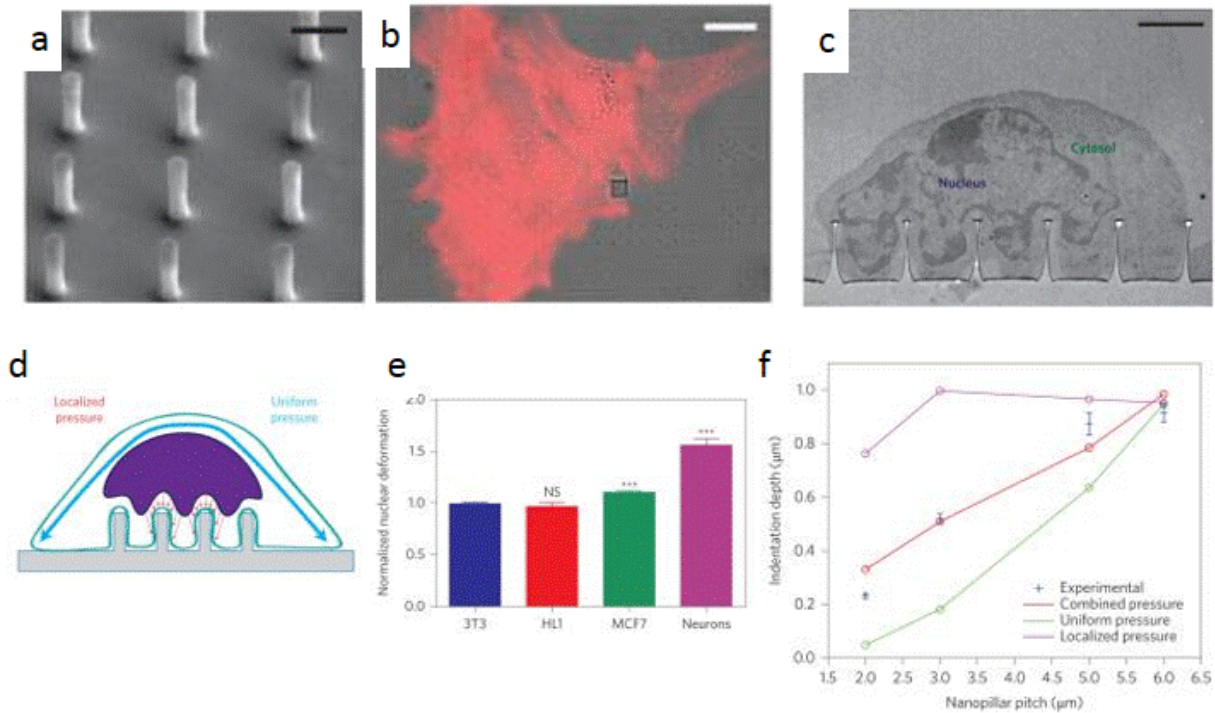


Figure 3-7: Using nanopillar arrays to probe the mechanics of the nucleus. (a) SEM images of PDMS made nanopillars (75 nm radius, 1.4 μm height and 2 μm pitch). Scale bar is 1 μm (b) Overlay of differential interference contrast (DIC) and fluorescence images actin cytoskeleton (red) of 3T3 fibroblasts on the patterns showing minor visible morphological effects of the nanopillar arrays on the cell cytoskeleton. Scale bar is 10 μm. (c) Transmission electron microscopy (TEM) of a 3T3 fibroblast on the nanopillar showing nuclear deformation of conforms to the surface of each pillar. Scale bar is 2 μm. (d) The diagram of main forces exerted on the nucleus, uniform pressure exerted by perinuclear actin cap fibers (blue) and localized pressure exerted by the fibers underneath the nucleus (red). (e) Average nuclear deformation of different cell types normalized to the 3T3 fibroblasts. Nuclei of neurons deform the most and are followed by MCF7 cancer cells and HL-1 cardiomyocytes and 3T3 fibroblasts. (f) Indentation depth of deformed nuclei of 3T3 as a function of nanopillar pitch measured by experiment and simulated by the pressure profile model, the graph shows the contribution of uniform pressure (green), localized pressure (purple) and the combination of the two pressures (red) (Hanson et al. 2015c).

This study shows the nuclear deformation is highly dependent on cytoskeletal filaments. The nuclear deformation of the cells that were treated with the actin depolymerization drug (low dose latrunculin B

or cytochalasin D) decreased drastically compared to control cells. However, when cells were treated with the microtubule depolymerization drug (colchicine), the nuclear deformation was not significantly different from the control cells and unexpectedly treatment of the cells with the intermediate filament depolymerization drug (acrylamide) increased the nuclear deformation (Figure 3-7 (e)). Based on these results, it was suggested that the actomyosin network generates the contractile force that pulls the nucleus towards the cell membrane while the intermediate filaments provide mechanical resistance against actin generated force.

Nuclear deformation also depends on the geometry of the patterns. The depth of nuclear deformation decreased with the increasing nanopillar radius and increased with increasing spacing between pillars (pitch) (Figure 3-7 (g)).

To model the observations, the nucleoplasm was considered as a soft material that is surrounded with a stiffer nuclear envelope and lamina and the actin force on the nucleus was considered to come either from perinuclear actin cap (actin stress fibres on the top of nucleus, see chapter 5) or basal actin fibres under the nucleus (Figure 3-7 (f)). The force from the perinuclear actin cap fibres generates a uniform pressure that pushes the nucleus towards the cell membrane and the force from actin fibres underneath the nucleus generates a localized pressure on the nucleus close to each pole. The modelling results gave the best fit to the experimental data when the effect of both uniform and localized pressure were considered on the nucleus. However, it was shown that the effect of localized pressure was dominant at the pillars with the smallest pitch (2 μm) and the relative contribution of the uniform pressure increased as the pitch of pillars increased (Figure 3-7(g)). This trend may indicate that the force of perinuclear actin cap has the dominant effect on the nuclear deformation for larger topographical cues.

3.4 The effect of ridge-groove and microprinted stripes on the cell

Ridge groove arrays are a family of topological patterns that have been used frequently for observation and interpretations of guiding effects of the substrate on the cell. The ridge groove patterns are also the master patterns for microprinting of the fibronectin stripes that we used in this study and act as the 3D counterpart for the stripes. Some of the cytoskeletal and nuclear morphological deformations such as elongation and alignment that are observed among cells on ridge-groove patterns have a similar counterpart among cells on the stripes printed with adhesive proteins. Therefore, in order to get an insight into the effects of micropatterned stripes on the cell, it will be useful to review the main effects of ridge-groove patterns on the cell morphology.

The patterns captured the interest of researchers as they mimic some of the frequently occurring structures in the living microenvironments of cells such as aligned collagen fibres. A majority of cell types that were cultured on these patterns were found to be aligned in the direction of the major axis

of the grooves (Nikkhah et al. 2012). O'hara and colleagues first introduced patterns in 1979 (Ohara & Buck 1979). They used these patterns to explain previously observed contact guidance among spreading chick heart fibroblast and kidney epithelial cells induced by fine grooves in plastic culture dishes. Their results revealed that the adherent fibroblasts and epithelium cells align more effectively on narrower structures as 75% of cells were aligned to grooves segregated by 5 μm ridges while only 60% of the cells were aligned to grooves separated with 30 μm ridges. They also observed that cells have the potency to bridge over the grooves without contacting their surface. They concluded that bridging is a characteristic behaviour of the cells as they observed the phenomenon in both grooves with different widths (2 μm and 10 μm) and regularly arranged collagen substrates made from fish scales. They hypothesized that the cell is stiff enough to bridge over the grooves even when only a limited area of the substrate is available for the establishment of cell to substrate contacts (focal contacts).

Later, Clark and colleagues used the ridge-groove pattern to compare the effect of lateral and vertical dimensions on the contact guidance of cells (Clark et al. 1990). They cultured three different cell lines (Baby Hamster Kidney cells (BHK), Madin-Darby Canine Kidney Epithelial cells (MDCK) and chick embryo cerebral neurons) on groove patterns with different depths (0.2, 0.56, 1.1 and 1.9 μm) separated with different ridge sizes (4, 6, 12 and 24 μm). Their results revealed that the ridge dimension has a small effect (alignment inversely proportional to the ridge size) on cell alignment (the direction of the maximum calliper diameter of each cell relative to the grooves); however, the groove depth is a much more important factor in the determination of the cell alignment. They observed about 99% alignment among the cells spreading on the grooves with 1.9 μm depth separated by 12 μm ridges (groove width: 12 μm) while only 20% of cells aligned to the groove with 0.2 μm depth separated by the same ridges. For all ridge sizes, they observed the same significant effect of the groove depth in cell alignment. In addition, they also observed a substantial variation among different cell lines in their reaction to the dimension of ridge-groove patterns. For example, BHK cells tend to align with the grooves that were deeper than 0.56 μm while MDCK cells aligned effectively on groove deeper than 1.1 μm . The alignment of MDCK cells depended on whether or not the cells were isolated or part of an epithelial cell island.

In a more recent study, Stevenson and colleagues observed three regimes of attachment depending on the ridge-groove dimensions: bridging, confinement and connection (Stevenson & Donald 2009) (Figure 3-8). They cultured 3T3 fibroblasts on the ridge-groove patterns with a range of groove width (10–80 μm), ridge widths (25–55 μm) and two ridge heights (15 and 21 μm). They observed that cells that were cultured on the patterns with the highest ridges (21 μm) and narrowest grooves (~10–20 μm) were able to bridge between grooves without touching the groove floor below (bridging). At the moderate groove sizes (~30–50 μm) cells were confined and aligned with either a single ridge or groove (confinement). The alignment happened in an increasing degree among the cells on the patterns with

narrower ridge widths. With the highest groove size ($> \sim 50 \mu\text{m}$) cells were able to transverse between a ridge and a groove (connection). These connections mostly happened at angles nearly perpendicular to the pattern. Decreasing ridge height to $15 \mu\text{m}$ allowed cells to connect on substrates with narrower grooves ($40 \mu\text{m}$) without affecting bridging or alignment. They proposed the existence of a critical length (roughly around the cellular size) for any cell protuberance that makes a ridge–ridge or ridge–groove connection.

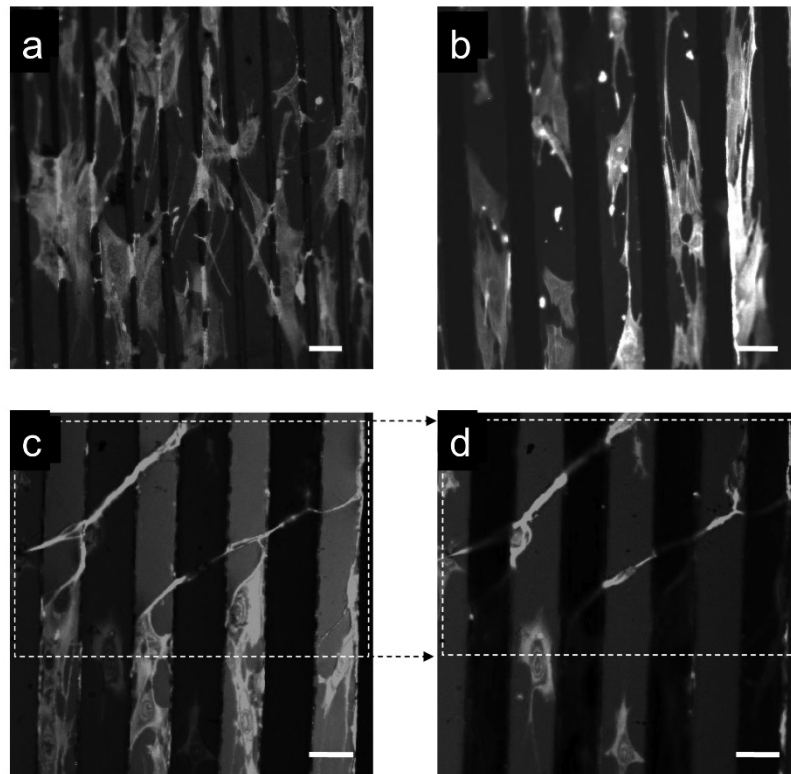


Figure 3-8: Three different attachment regime observed on 3T3 fibroblast spreading on ridge-groove substrates with different ridge/groove sizes. (a) Cell bridging between neighbouring ridges on the pattern with $10 \mu\text{m}$ grooves size. (b) Cells mostly confined and elongated along the ridges on the pattern with $30 \mu\text{m}$ groove size. (c)&(d), Cells traversing (connecting) between ridge and grooves when they are cultured on the pattern with $60 \mu\text{m}$ grooves. (c) is showing the ridges and (d) is confocal microscope focus of the same region (dashed region) to show grooves. The height and width of ridges in all images are 21 and $45 \mu\text{m}$ respectively. Scale bars are $50 \mu\text{m}$. (Stevenson & Donald 2009).

Development of microscopy techniques and the invention of novel live-cell staining methods has allowed the acquisition of deeper insight into cell adhesion dynamics on the patterns over time. In a study (Kung et al. 2011), 3T3 fibroblasts were stained with a live-cell dye with minimum cytotoxic effects and were cultured on ridge-groove patterns with two different ridge widths ($25 \mu\text{m}$ and $55 \mu\text{m}$). Cells were tracked individually using confocal microscopy for several hours. It was observed that there is a time scale ($\sim 2\text{--}4$ hours) over which cell morphology transitioned from the original

isotropy to anisotropy, where the preference was for cells to lie in a parallel direction to the patterns. In agreement with previous studies, they found that anisotropy occurred more rapidly and distinctly among the cells that were cultured on the narrower ridge. Furthermore, they observed a statistically significant correlation between cell orientation and morphology while there was no correlation between cell orientation and migratory direction.

The time scale introduced by Kung and colleagues is consistent with the timescale that has been observed for cytoskeletal filaments' alignment on ridge-groove patterns. Studies on the alignment and cytoskeletal organization of human gingival fibroblasts spreading on a ridge-grooved substrate with a range of groove width between 1-30 μm have revealed that microtubules were the first cytoskeletal filaments that were oriented to the parallel direction of grooves and were first aligned to the bottom of the grooves (~20 minutes after seeding) (Oakley & Brunette 1993). However, aligned actin filaments were observed 40-60 minutes after initial seeding and aligned focal contacts were not seen until 3 hours after initial seeding.

Recent studies have been focused on the quantitative study of the dynamic of cell migration and spreading on micropatterns made of CAMs in order to obtain a better understanding of the biological mechanism of cell adhesion and spreading. In a study, 3T3 fibroblasts were cultured on polydimethylsiloxane (PDMS) substrate fibronectin stripes with varying widths (50, 25 and 10 μm) (Huang & Donald 2014a). The kinetics of classical three-phase sigmoid spreading of the fibroblast cells within these three different size grooves were observed. It was revealed that during the early rapid expansion phase (E-phase) cells spread radially in a way that the total cell area is proportional with $t^{1.8}$ (t represents the time) until they reach the PDMS spacing (Figure 3-9). When they reach the PDMS spacing, cells start to spread lengthwise in a way that means the total area of the cell is proportional to t^1 . Assuming that the cell spreading in the early E-phase is directly linked to the F-actin elongation rate, that membrane tensions are negligible in the early stage of spreading and that molecular factors responsible for F-actin polymerization (such as G-actin, profilin, Arp2/3, etc.) are abundant and uniformly distributed, a model has been derived based on simple geometrical calculations that predict a t^2 law for the radial spreading cells and a t^1 law for the lengthwise spreading cells (Huang & Donald 2014a).

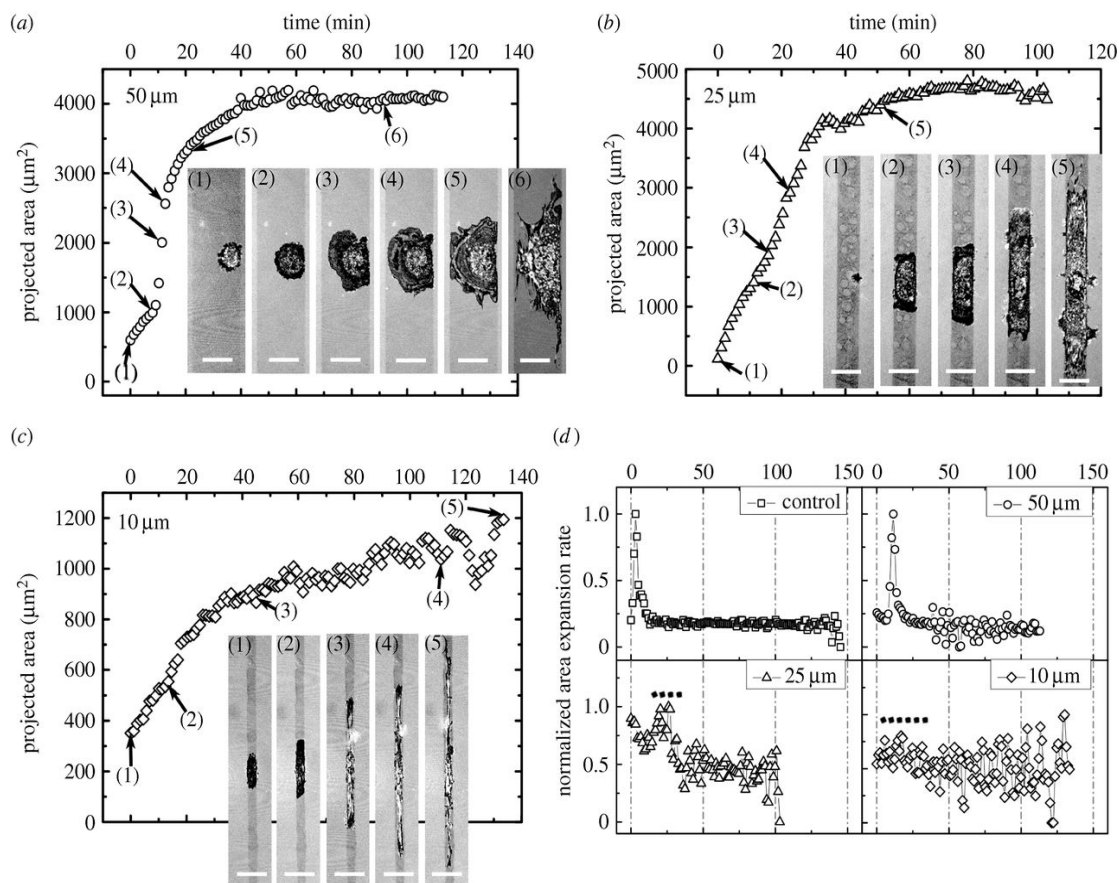


Figure 3-9: Dynamics of project cell area in 3T3 fibroblasts spreading on fibronectin printed stripes with different widths. (a),(b)&(c) Spread curves of fibroblasts cultured on the 50, 25 and 10 μm stripes, derived from reflection interference contrast microscopy of the cells. (d) A differentiated form of the spread curves of the four patterns. Revealing the dependence of cell spreading kinetics onits spreading morphology using micro-contact printed fibronectin patterns. (Huang & Donald 2014a).

Although previous studies have given us a substantial knowledge about the effect of ridge-groove and microprinted stripe patterns on the cellular behaviour; however, many aspects of these effects such the effect on cellular thickness, cellular volume and nuclear deformation remain poorly understood, which we aim to shed light on these aspects in this study.

Chapter 4:

A review on stem cells and how they are affected by physical cues

Stem cells are types of cells in multicellular organisms that are distinguished by two properties (Figure 4-1). Potency and self-renewal (Potten & Loeffler 1990).

Potency means that they can differentiate into other types of cells which can be either somatic cells or other types of stem cells (progenitors).

Self-renewal: Unlike fully differentiated somatic cells they have the ability to divide and produce more of the same stem cells. This ability is called self-renewal (Figure 4-1).

The exact history of stem cells discovery is a little bit ambiguous. In 1909, Alexander A. Maximow for the first time proposed the theory of stem cells in full-grown organisms by observation of ‘undifferentiated primitive blood cells’ that can differentiate to haemoglobin-rich and haemoglobin-free cells which resemble large lymphocytes (Maximow, 1909). Later, he discovered that in very young embryo elements of mesenchyme, the embryonic connective tissue, which arises from mesoderm form ‘blood islands’. The cells of the blood islands later differentiate in two directions. One type of cell formed are round and have been called ‘primitive blood cells’ which float in the plasma and the other type of cells are those which form the wall of the first blood vessels or the first endothelium (Maximow 1924).

In 1963, James Edgar Till and Ernes McCulloch who are mostly known for the discovery of stem cells nowadays discovered mouse bone marrow-derived hematopoietic cells that have the potential for self-renewal (Becker, McCulloch and Till, 1963). In 1965, it was discovered that undifferentiated neural cells in rats migrate postnatally from the forebrain ventricles to the hippocampus and become differentiated there (Becker, McCulloch and Till, 1963). The early knowledge about stem cells already was clinically used when the first successful bone marrow transplant in 1968 was performed to treat two siblings with combined immunodeficiency (Buckley 2011).

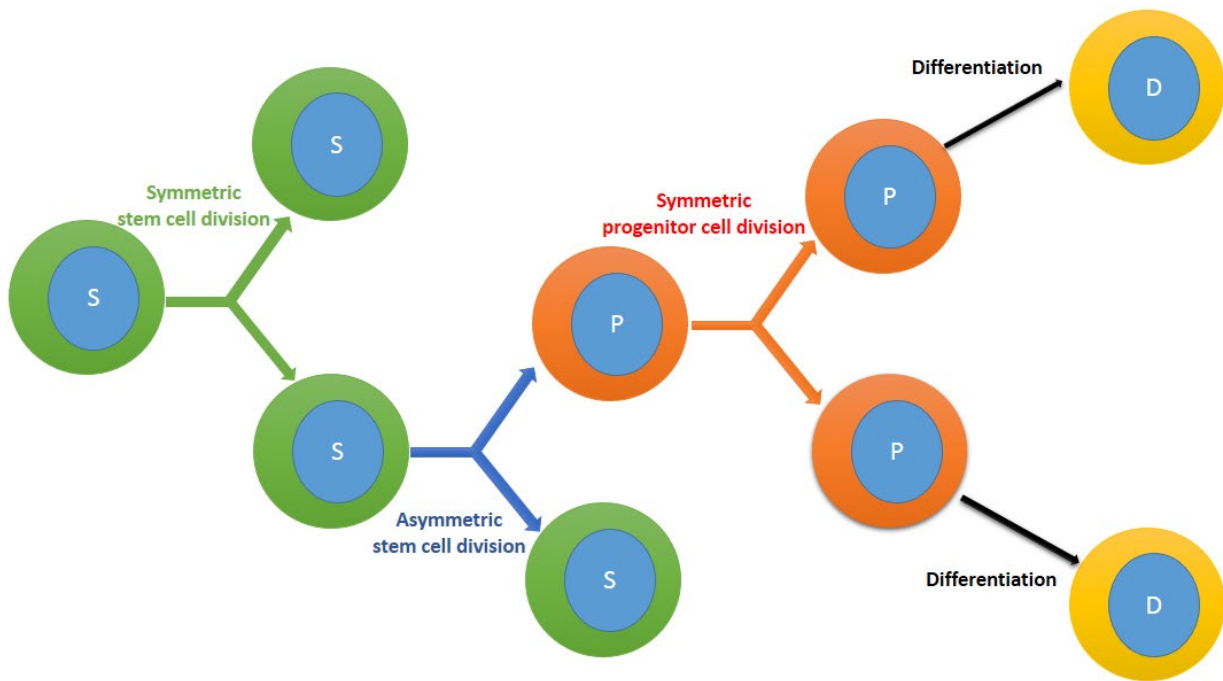


Figure 4-1: Division and differentiation of stem cells. Stem cells ((S), green) can renew themselves through many symmetric mitoses or they can undergo an asymmetric cell division to divide into one stem cell and one progenitor cell ((P), red). Progenitor cells can go through several symmetric mitoses and finally differentiate to a fate determined cell ((D), yellow).

Since then, there have been many landmarks in the field of stem cell research. Many different kinds of human stem cell lines have been successfully isolated and have been used for an ever-growing number of studies.

Indefinite (or effectively so) self-renewal and differentiation features of stem cells give them a huge potential in the future for regenerative medicine and restoration of malfunctioning tissues and organs (Mahla 2016a). Application of stem cells in repairing failed organs started in the early 21st century with trials on mostly animal models initiated by a successful repair of injured spinal cord of rats (Nandoe Tewarie et al. 2009). In 2008, the first tissue-engineered synthetic human organ was transplanted into a 30 years old woman. This organ was cultured in a bioreactor from denuclearized trachea who was donated from a human source as organ matrix and was seeded with patient's own epithelial cells and mesenchymal stem-cell-derived chondrocytes (Macchiarini et al. 2008). This transplant considered a breakthrough in medicine and got huge attention in public and scientific world. However, unfortunately, 7 out 9 patients that received the organ died and 2 were forced to replace it with an artificial one (Law et al. 2016). This failure made a long-standing controversy in the scientific society that resulted in the retraction of two main publications (Jungebluth et al. 2011)(Badylak et al. 2012) of the group. In addition, researchers involved in the study were convicted

of scientific misconduct (The Lancet 2018). This shows that we need much more knowledge about stem cells in order to unleash the huge potential of stem cell-based treatments. Nowadays, there are a growing number of clinical trials for stem-cell based treatments which cover many areas including cancer medicine, transplantation medicine (Trounson & McDonald 2015), anti-aging therapies (Honoki 2017), HIV cure (Hütter 2016) and etc.

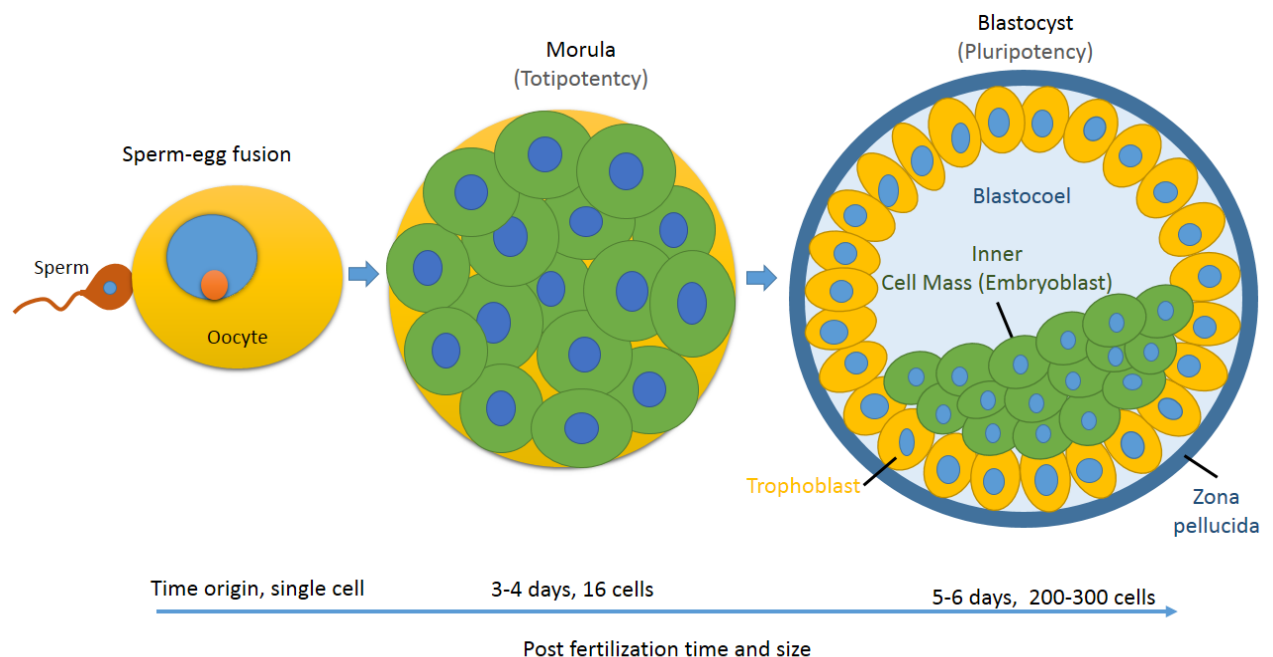


Figure 4-2: Zygote is the first totipotent stem cell created by the fusion of sperm and Oocyte cells. Cells in Morula cellular ball created by the first few division of the zygote remain still totipotent. The cells of inner cell mass inside blastocyst are pluripotent as they can differentiate to any cell within a germ layer.

4.1 Differentiation hierarchy of stem cells

Stem cells are usually labelled with their potential to differentiate or simply their potency. There are several classes of potency for stem cells.

4.1.1 Totipotent

Also known as omnipotent is defined as a stem cell that has the potential to differentiate into any other cell type with no exception (Schöler 2016). In other words, a totipotent stem cell is a cell that can give rise to a whole viable organism (Mitalipov & Wolf 2009). Some sources define totipotent stem cells as ‘‘ the true stem cell’’(Nandoe Tewarie et al. 2009). The zygote which is the first cell formed in the body as a result of a fusion between an oocyte and sperm is the first totipotent cell. In the first few cell division cycles in a forming embryo, cells still maintain their totipotency as they can still differentiate into both embryonic stem cells and extra-embryonic placenta cells (Figure 4-2). The number of division cycles that cells can undergo before losing totipotency is different between species. However, it is known that universally it is at least until the stage consisting of 4 cells (Mitalipov & Wolf 2009).

4.1.2 Pluripotent

After several cycles of cell division in the developing embryo and the formation of a blastocyst, totipotent cells either differentiate into embryonic stem cells in the inner cell mass or into trophoblasts (Figure 4-2). Trophoblasts form the outer layer of the blastocyst and provide nutrition to the embryo. Trophoblasts later develop to the placenta which gives the necessary support structure for embryonic development. The cells of Inner cell mass (known also as the embryoblast) are pluripotent stem cells that have the potential to differentiate into any cell type within any of the three germ layers (Figure 4-3).

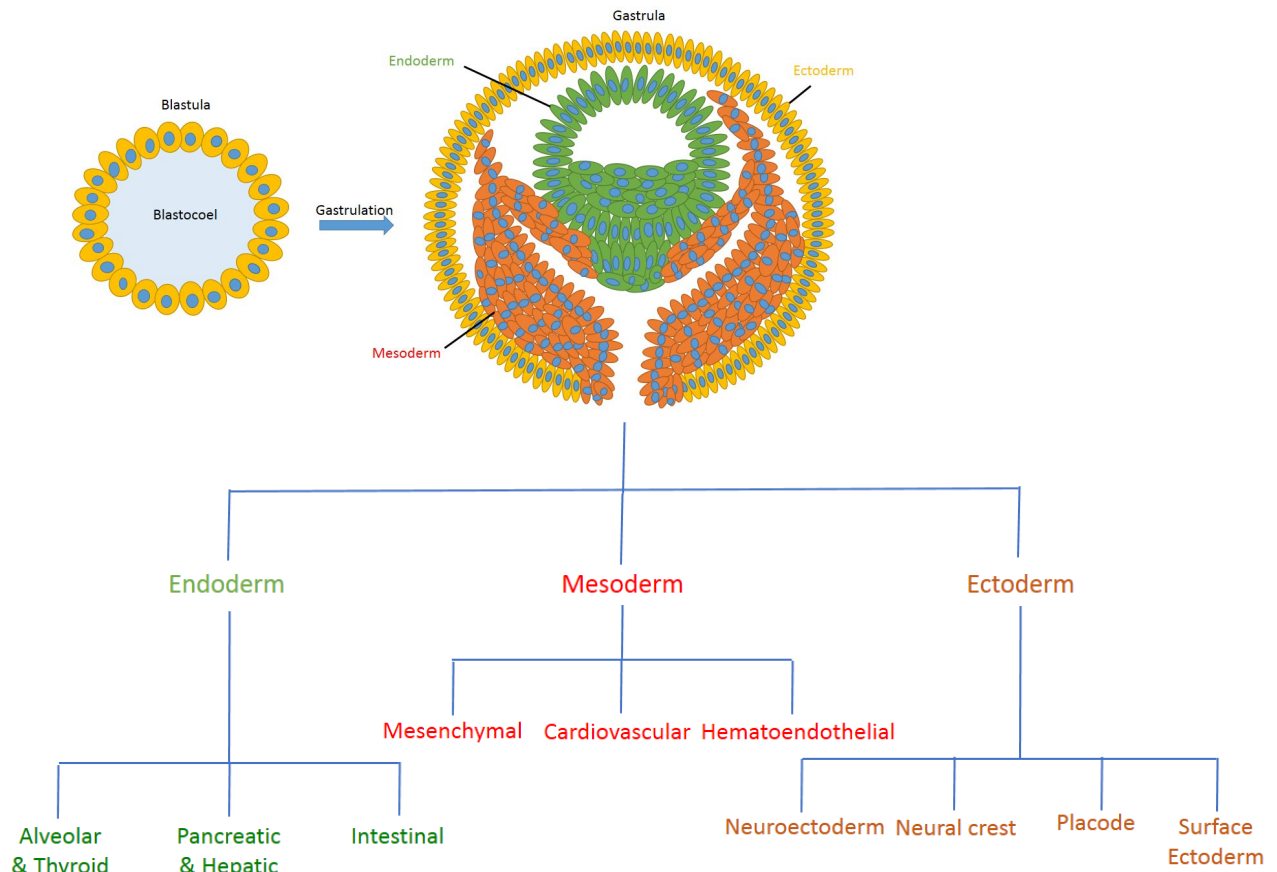


Figure 4-3: Blastula undergoes a gastrulation process and becomes a gastrula which consists of three groups of cells or three germ layers. Endoderm (green), Mesoderm (red) and Ectoderm (yellow). These three groups of cells later differentiate into multipotent stem cells that create all organs and tissues. Information in this graph was deduced from (Evseenko et al. 2010),(Cheng et al. 2013),(Tchieu et al. 2017).

4.1.3 Multipotent

Multipotent stem cells have the ability to differentiate into a number of cell types of a closely related cell family in a specific tissue or organ (Bindu A & B 2011). For example, Hematopoietic Stem Cells (HSCs) which are located in bone marrow can differentiate into various cell types in blood such as erythrocytes (red blood cells), T lymphocytes, Plasma cells, Natural killer cells, Macrophages, Neutrophils etc. (Figure 4-4)(Ng & Alexander 2017). Mesenchymal Stem Cells (MSCs)(Bianco 2014), Pancreatic Stem Cells (PSCs)(Noguchi 2010), Neural stem cells (NSCs)(Bianco 2014) are other major types of multipotent stem cells.

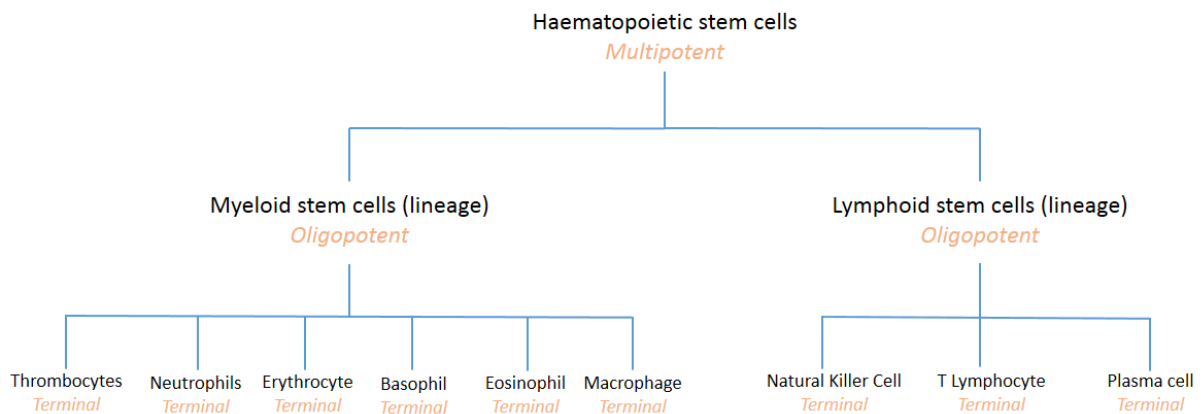


Figure 4-4: Differentiation hierarchy for HSCs as an illustration for multipotent, oligopotent and terminal mature blood cells.

4.1.4 Oligopotent

These cells can differentiate into a smaller number of cell types in comparison to multipotent stem cells (Wagers & Weissman 2004). For example, lymphoid or myeloid stem cells are oligopotent stem cells that have differentiated from HSCs and can differentiate into various different mature blood cell (Schöler 2016)(Figure 4-4).

4.1.5 Unipotent

These cells can only differentiate into one specific cell type. However, their self-renewal ability allows them to be classified as stem cells and distinguishes them from stromal cells. Unipotent stem cells are sometimes called precursor cells (4. *The Adult Stem Cell* | stemcells.nih.gov).

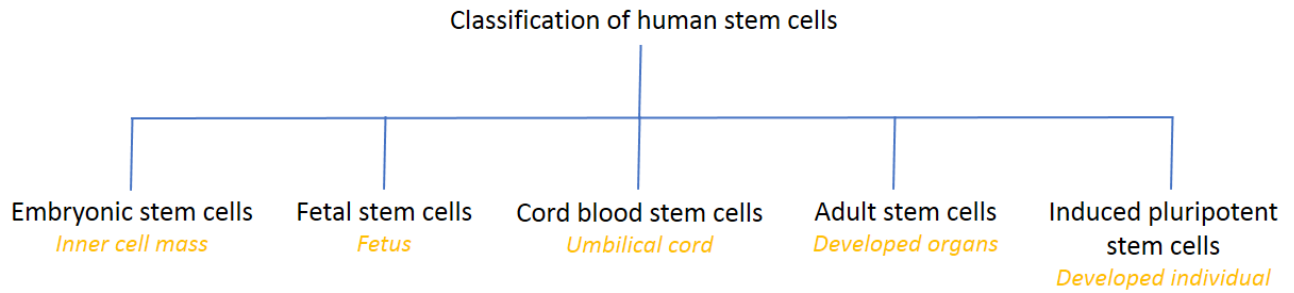


Figure 4-5: Classification of human stem cells and the origin of their isolation (yellow).

4.2 Human stem cell classification

Stem cells usually are classified based on their origin into several categories (Figure 4-5).

4.2.1 Embryonic stem cells (ESCs)

Embryonic stem cells are pluripotent stem cells that form the inner cell mass (ICM) in the blastocyst (Figure 4-2). In the human embryo, the blastocyst forms 5-6 days after fertilization during the pre-implantation stage and is made out of approximately 50-150 cells (Hardy et al. 1989). During the gastrulation process, embryonic stem cells form three germ layers. Endoderm, mesoderm and ectoderm (Figure 4-3). These three embryonic germ layers later differentiate into many cell types and form all the tissues and organs in the body. ESCs have a great potential for self-renewal and can go through many cell division cycles without differentiation. Because of this special property, they are also referred to as immortal cells (*Embryonic Stem Cells* | stemcells.nih.gov). Pluripotency and immortality of ESCs give them a unique potential in clinical, therapeutic and research applications. ESCs play a critical role in key research areas such as developmental biology, tissue engineering, regenerative medicine, functional genomics, pharmacological testing and cell therapy (Gepstein 2002). The ability for the infinite division of ESCs has made them a unique source for a large quantity of cells for therapeutic applications (L.M. Khoo et al. 2011). ESCs are being heavily used as models for prenatal screening for genetic disorders such as fragile-X syndrome and cystic fibrosis (Ben-Yehudah et al. 2012).

ESCs are harvested from 5-6 days old embryos by destroying the embryo during the pre-implantation stage. Therefore, there is a huge controversy about the ethical concerns of harvesting ESCs as some

people argue that the embryo could give rise to a fully developed human being. However, some researchers advocate using ESCs in contrast as they argue that a 5-6 day cellular mass is too young for possible consideration of personhood (King & Perrin 2014).

4.2.2 Foetal Stem cells

Foetal stem cells are isolated from various parts of a developing foetus such as foetal blood, bone marrow or foetal tissues such as the liver and kidney (O'Donoghue & Fisk 2004). A foetus is a prenatal human after the embryonic stage and before birth. The foetus stage is usually regarded as starting about 8 weeks after fertilization (Bindu A & B 2011). Foetal blood is a rich source of HSCs, MSCs, endothelial stem cells, epithelial stem cells and neural stem cells.

Foetal-derived stem cells have some advantages compared to stem cells isolated from an adult human source. Ageing of stem cells is a factor that limits the potential of stem cells. The quantitative and qualitative effects of ageing on stem cells is yet to be understood. However, there is a generally accepted belief in stem cell research that stem cells derived from younger individuals have better quality and potential (Van Zant & Liang 2003). As a result, foetal stem cells are assumed to have better quality in comparison to adult stem cells. Foetal HSCs have a higher proliferation rate in comparison to HSCs that are isolated from blood cord and adult bone marrow (O'Donoghue & Fisk 2004). MSCs that are isolated from human foetal pancreas also known to be highly proliferative (Hu et al. 2003).

The majority of foetal cells are harvested from aborted fetuses. Consequently, there are some ethical controversies about the use of foetal tissue because it is associated with the highly contentious abortion issue (Lo & Parham 2009).

4.2.3 Cord blood stem cells

Umbilical cord blood (CB) is a source for multipotent stem cells that are genetically identical to the new-born infant. This eliminates the problem of immune rejection when these cells are being used for therapeutic purposes in the body. Since umbilical cord is normally considered as medical waste, harvesting blood from the cord is simple and non-invasive. Because of this advantage, multiple public and private agencies and blood banks have been created for storing CB for possible future transplantation for the individual or closely related family members.

The first CB stem cell transplant was carried out in 1988 between two identical twins in order to cure Fanconi anaemia (Gluckman & Rocha 2005). As of 2007, 8,000 patients had benefited from CB transplant worldwide (Rubinstein 2006). These numbers have been rapidly increasing since then and only in the United States and as of 2017, it is estimated that 700,000 umbilical CB units have been donated, over 40,000 umbilical CB transplantations have been carried out and more than 25,000 patients have been cured using CB transplantation (Ballen 2017).

CB is mostly known as a rich source for highly proliferative HSCs that are able to form cellular colonies and consequently, an alternative to bone marrow-derived HSCs (Rubinstein 2006). MSCs have also been isolated from CB which gives an alternative for bone marrow-derived MSC (Gluckman & Rocha 2005). Liver and Neural stem cells also are successfully isolated from CB (Lee et al. 2004),(Rogers & Casper 2004).

4.2.4 Adult stem cells

Adult stem cells are undifferentiated cells that are found in various developed tissues and have the basic properties of stem cells, self-renewal and potency to differentiate into somatic cells. These cells make up only a small fraction of cells in developed tissues and are known also as somatic stem cells, tissue stem cells (Nature reviews, Molecular cell biology. 2000) or tissue-specific-stem cells (Pizzute et al. 2015). There are several tissues that have been used as a source for isolation of adult stem cells including bone marrow, central nervous system, retina, skeletal stem cells and dermis of mammalian skin (Toma et al. 2001), Adult stem cells are primarily responsible for maintaining and repairing the organ in which they are found. They remain in a quiescent state in their niche (*in vivo or in vitro* microenvironment that stem cells reside in and which interacts with the cell to regulate its fate) in the tissue in which they reside and start division and differentiation when they are activated by appropriate signals to start the repairing process. Therefore, these cells have a pivotal role in the future of regenerative medicine and organ synthesis for replacing failed, injured or aged organs (Mahla 2016b). Most adult stem cells are multipotent and they differentiate into cells within the organ that they reside. However, there are studies that indicate that some adult stem cells such as bone marrow stem cells may have the plasticity to differentiate into cells found in other organs, cardiac muscle cells in this case (Valarmathi & W. Fuseler 2011).

There are fewer ethical concerns about adult stem cells compared to ESCs as they are derived from developed individuals. As a result, there are fewer restriction and regulation about these cells which makes it easier for scientists to explore these cells as an alternative source of cells to ESCs (Pizzute et al. 2015). Because adult stem cells are harvested from the patient in most of the cases, there is no issue with transplant rejection which gives a big advantage for therapeutic methods based on these

cells (Aghazadeh & Nostro 2017). Due to the low ratio of adult stem cells number to total stromal cells, harvesting these cells for therapeutic or *in vitro* studies remains a challenging task (Greggio et al. 2013).

4.2.5 Induced pluripotent stem cells

Ethical concerns and immune rejection issues that are associated with ESCs set a race among stem cell researchers to find a method for making pluripotent stem cells from stromal cells of fully developed individuals. Soon it became clear that by transferring the nucleus of a stromal cell to a nucleus-removed oocyte, it is possible to reprogram the stromal cell to a pluripotent stem cell which is able to give rise to a fully developed viable offspring (Wilmut et al. 1997) 'cloning'. Later it was shown that by chemically fusing of stromal cells and ESCs, it is possible to make hybrid cells that are able to maintain tetraploid DNA content. These hybrid cells show characteristic features that are associated with ESCs such as morphology, growth rate and antigen expression patterns (Cowan et al. 2005). These studies suggested that oocytes and ESCs contain factors that can reprogram stromal cells to pluripotent stem cells. In 2006, a study published by the Takahashi group showed that by transducing (a process of introducing foreign DNA into a cell using a viral vector) adult mouse fibroblast with genes that express a set of four transcription factors which are known as Yamanaka factors (Oct3/4, Sox2, c-Myc, and Klf4), it is possible to reprogram them to pluripotent cells. These cells were called 'Induced pluripotent stem cells or iPSCs' and exhibited characteristic features of ESCs. When they were transplanted into nude mice, they created a variety of tissues from all three germ layers (Takahashi & Yamanaka 2006).

The ideal goal in the medical application of iPSCs is to produce desired cells or organs that are differentiated from iPSCs which are transduced from the patient's own cells (Figure 4-6). However, there are still many challenges in the field of cell reprogramming such as the low efficiency of the reprogramming process (Takahashi & Yamanaka 2006) or the risk of introducing genetic mutations (Selvaraj et al. 2010) or tumour generation as a side effect of transduction process (Câmara et al. 2016).

The first clinical application of iPSC was performed in 2017. In this trial, fibroblasts of two patients suffering from advanced Neovascular age-related macular degeneration were used to make iPSCs. These iPSCs were differentiated into retinal pigment epithelial cells (RPEs) and a sheet made of RPEs were transplanted into one of patient's eye. The transplanted retina remained intact after a year; however, no significant improvement or worsening symptoms was reported in the patient's vision (Mandai et al. 2017).

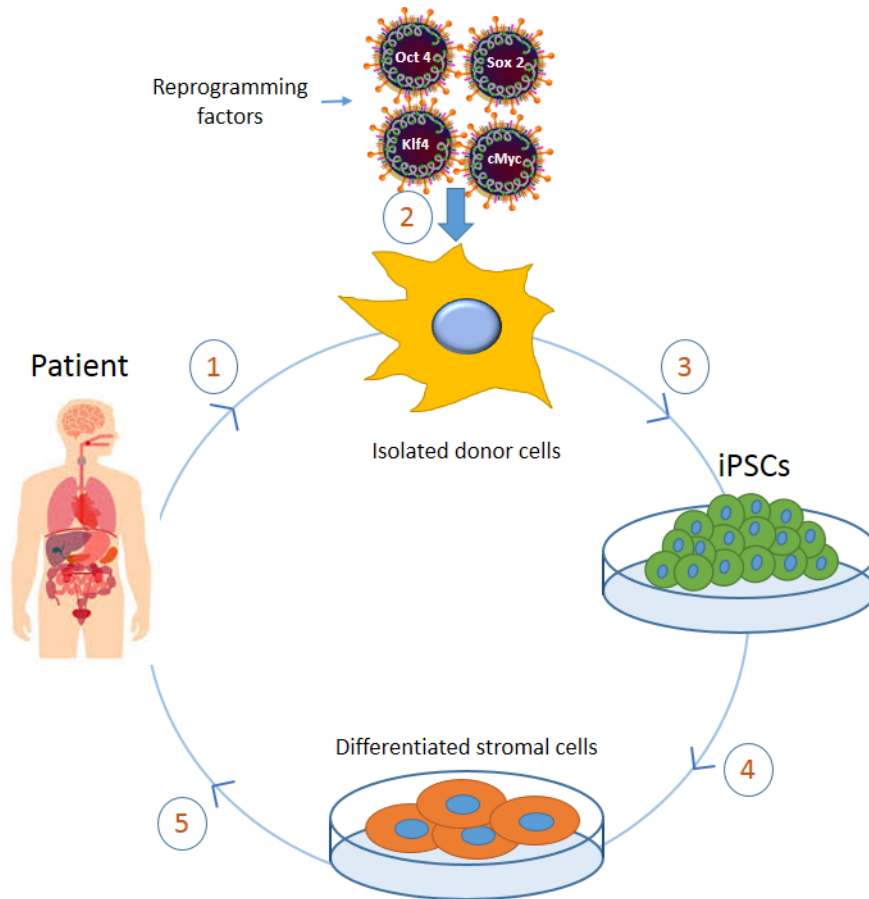


Figure 4-6: The proposed cycle of application of cell reprogramming in regenerative medicine.

1-Adult stromal cells are harvested from the patient. 2- Isolated donor cells get reprogrammed by transducing them with genes that encode reprogramming factors. 3- Resulted iPSCs get selected using antibiotic selections and amplified *in vitro*. 4- iPSCs get differentiated into desired stromal cells for the therapy. 5- The stromal cells/tissue transplanted into the patient.

4.3 Mesenchymal stem cells (MSCs)

MSCs are multipotent adult stem cells that are present in the bone marrow and most of the connective tissues (Augello & De Bari 2010). MSCs have been isolated primarily from bone marrow (Friedenstein et al. 1970). Bone marrow-derived MSCs are labelled as a gold standard for MSCs as they are the most studied type of MSCs (Hass et al. 2011). However more recently human Mesenchymal Stem cells (hMSCs) have been isolated from a variety of other developed tissues including adipose tissue (Araña et al. 2013), peripheral blood (Chong et al. 2012), lung (Jarvinen et al. 2008), brain (Paul et al. 2012) and dental pulp (Shi & Gronthos 2003). In addition, they have been

isolated from multiple organs the foetus including placenta (Vellasamy et al. 2012), amniotic fluid (in't Anker et al. 2003), umbilical cord blood (Lee et al. 2004) and foetal heart (Garikipati et al. 2018).

MSCs are known as common predecessors of mesenchymal tissues and initially are known to differentiate into mesodermal lineage cells such as adipocytes, chondrocytes and osteocytes both *in vitro* and *in vivo* after transplantation (Friedenstein et al. 1974). MSCs can differentiate into fibroblasts when they are exposed to various chemical or physical stimuli (Lee et al. 2006).

Later studies have shown that MSCs are capable of differentiation into cell lines from ectodermal and endodermal lineages in a process labelled as transdifferentiation (Uccelli et al. 2008) (Figure 4-7). It is reported that MSCs can differentiate into neurons (Scuteri et al. 2011), astrocytes (Wislet-Gendebien et al. 2005) and epithelial cells (Păunescu et al. 2007) from ectodermal lineage. Other studies have shown that MSCs can differentiate into cells from endoderm lineage including gut epithelial cells, lung cells (Uccelli et al. 2008), smooth muscle cells (Lee et al. 2006), cardiomyocytes (Shen et al. 2017) and skeletal myocytes (Hodgson et al. 2018).

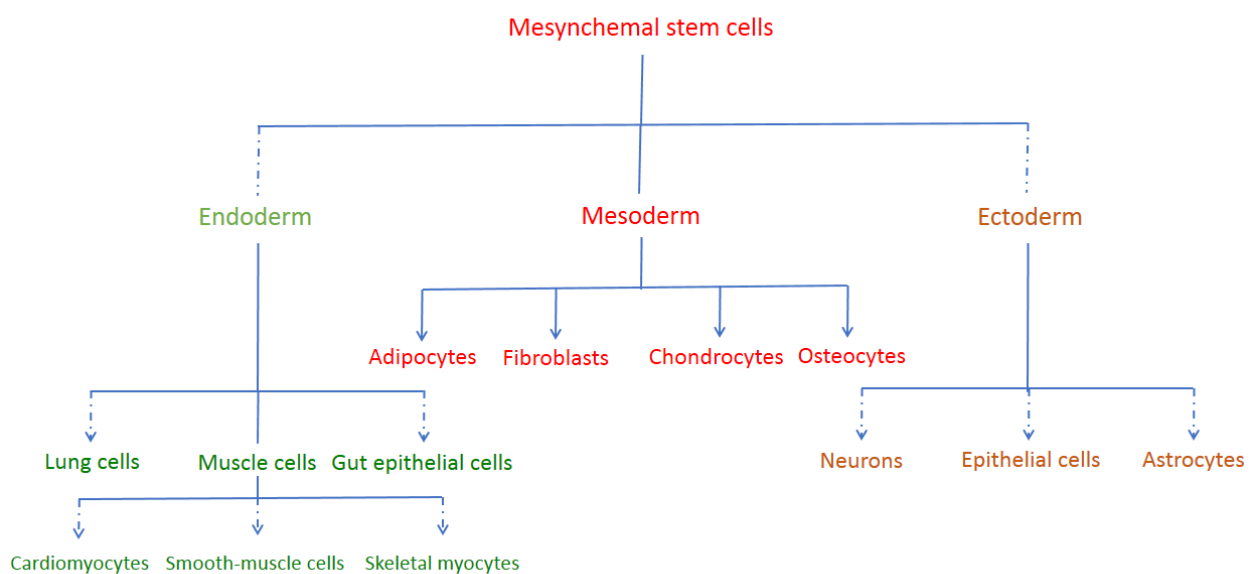


Figure 4-7: Differentiation of MSCs into cells with different lineages. MSCs mainly differentiate into mesenchyme tissue cells with mesodermal lineage (solid arrows). When exposed to specific physical or chemical signal cues, they can transdifferentiate into endodermal and ectodermal lineage cells (dashed arrows).

4.3.1 Mechanical and cytoskeletal properties of MSCs

Many of the effects that mechanical cues in the microenvironment or *in vitro* have on MSCs' growth, differential and morphology are understandable only when we know the mechanical and cytoskeletal characteristics of MSCs and the primary cell lines that are differentiated from MSCs. Therefore, many studies have been recently focusing on measuring and quantifying these properties (Mathieu & Lobo 2012).

The stiffness of hMSCs has been measured using different methods. AFM measurement shows that the Young's modulus of MSCs is about 2.5 kPa in detached spherical form and increases to 3.2 kPa when adhering to Poly-L-Lysine (PLL)-coated Petri dishes (Darling et al. 2008). The same study shows that among cell lines that are believed to be differentiated from MSCs, adipocytes are the softest with Young's modulus of 0.9 kPa. Chondrocytes are intermediate, with an elastic modulus of 1.4 kPa in the spherical detached shape and 1.8 kPa in the adherent configuration. Osteoblasts have almost the same stiffness as MSCs in the detached spherical form with an elastic modulus of 2.6 kPa. However, they become very stiff when they adhere to the substrate with a Young's modulus of 6.5 kPa. The AFM measurements for fibroblasts' elastic modulus lies in the range between 1-2 kPa when they adhere to glass coverslips which have been coated with collagen I (Jaasma et al. 2006) (Figure 4-8).

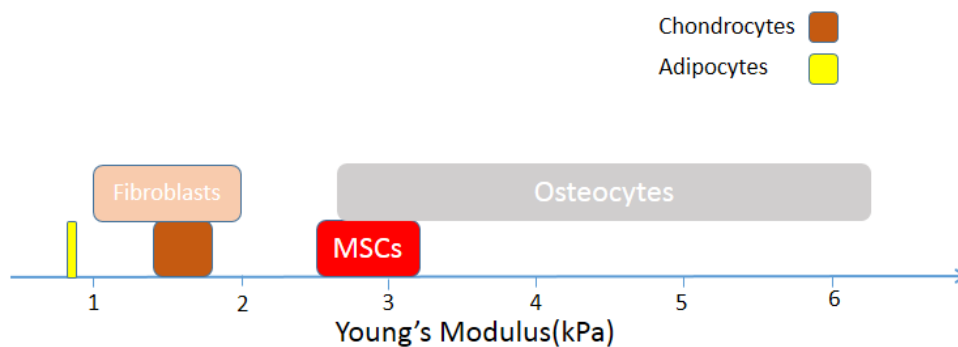


Figure 4-8: Stiffness range of MSCs and cell lineages that are differentiated from them measured by AFM.

Similar results have been observed when the stiffness of bone marrow-derived hMSCs was monitored during exposure to a differentiation-inducing medium using micropipette aspiration. Both the instantaneous (E_0) and equilibrium (E_∞) Young's modulus of hMSCs were almost doubled compared

to the control from 457 ± 88 Pa and 98 ± 37 Pa to 890 ± 219 Pa and 224 ± 40 Pa respectively when the cells were cultured in osteogenic induction medium for 3 weeks. On the other hand, both moduli decreased to 420 ± 52 Pa and 87 ± 23 Pa, respectively when hMSCs were cultured in adipogenic inducing medium for 3 weeks (Yu et al. 2010).

Cell stiffness of hMSCs is mostly dependent on the actin cytoskeleton. Studies have shown that inhibition of actin polymerization with cytochalasin D has significantly decreased the elastic modulus of both hMSCs and osteoblasts. The decrease was even more notable on the hMSCs stiffness. However, disruption of microtubule structure of the cytoskeleton using nocodazole have not any significant effect on the stiffness of hMSCs and osteoblasts (Titushkin & Cho 2009).

The stiffness difference between detached spherical and adherent form of a cell may indicate how dependent the stiffness is on the cytoskeletal actin structure. The elastic modulus of the cell varies considerably between adherent and detached form in osteocytes and fibroblasts. However, the variance is negligible among chondrocytes and adipocytes (Figure 4-8).

It has been shown that osteoblasts show more polygonal and flattened shapes and they are less prone to proliferate in comparison to the hMSCs. However, there are two categories of cells among hMSCs with distinct morphological features; rapidly self-renewing cells (RS) which are spindle-shaped cells and large flat cells (FC). FCs adhere strongly to the substrate and form more focal adhesions compared to RSs. FCs and osteoblasts express very similar thick stress fibres while RSs have thin actin filaments in the cytoskeleton and demonstrate some actin accumulation in the lamellipodia and many filopodia (Docheva et al. 2008).

Differentiated adipocytes are usually round (GREGOIRE et al. 1998). The round shape allows adipocytes to store lipid in fat tissue in a very effective way while the spreading form of osteoblasts allows them to effectively deposit bone matrix (Parfitt 1984). hMSCs that were cultured in adipogenic induction medium showed a significantly higher percentage of adipogenic differentiation when were cultured at higher cell density (25000 cells/cm²). In contrast, hMSCs that were cultured in osteogenic induction medium showed notably higher osteogenic differentiation when they were cultured at lower cell density (3000 cells/cm²) (McBeath et al. 2004) indicating that more space to spread is a positive factor in osteogenesis of hMSCs. A similar effect was observed on single hMSCs spread on microprinted fibronectin islands which shows that the effect of shape on the differentiation is not due to cell-cell interaction (McBeath et al. 2004).

Mature articular chondrocytes usually display a round morphology *in vivo*. However, when chondrocytes are cultured in a monolayer culture at low density *in vitro*, they adhere and spread on the substrate and their morphology changes from a polygonal or round shape to amoeboid-like flattened shape (Von der mark et al. 1977).

Both configuration of the actin cytoskeleton and microtubule filament in the cytoskeleton play a key role in chondrogenesis (the process of cartilage formation from condensed mesenchymal tissue). Initial studies have revealed that disruption of the actin cytoskeleton of monolayer cultured chick limb bud MSCs by cytochalasin D induces chondrogenesis (Lim et al. 2000). However, later studies supported the initial results when either inhibition of actin polymerization by cytochalasin D or stabilization of existing actin filaments by jasplakinolide in mesenchymal limb bud cells increased chondrogenic transcription factor Sox9. In contrast, disturbing of microtubule polymerization by colchicine totally blocks expression of Sox9 (Woods et al. 2005).

4.3.2 The effect of physical cues on MSCs

MSCs are isolated from various body tissues and can differentiate into multiple cell lines in the body. It happens that these cell lines build up frequently damaged tissues in an adult human being such as articular cartilage or fibrocartilage (Ma et al. 2012). Therefore, MSCs have great therapeutic potential in tissue engineering and regenerative medicine. Because of this promising potential, numerous studies have been dedicated to understanding and possibly controlling the role of biological and chemical signals in differentiation and optimization of pre-differentiation culture conditions of MSCs (Delaine-Smith & Reilly 2011). Mesenchymal tissues and subsequently MSCs in their niche are exposed to various mechanical stimuli. Therefore, it is not surprising that an increasing number of studies suggest that mechanical cues play an equally important role in the fate and behaviour of MSCs. *In vivo*, MSCs are exposed to mechanical forces in the forms of ECM mechanical and topographical properties, shear stress forces of surrounding bodily fluids, mechanical forces of cell-cell interactions (Nava et al. 2012). *In vitro*, these mechanical factors are simulated by models that study the effects of substrate stiffness (Xu et al. 2017) and topography (Nakamoto et al. 2014), fluidic shear stress (Yourek et al. 2010) and regulation of cellular and nuclear morphology using external hydrodynamic forces (Heo et al. 2016).

4.3.2.1 Effect of matrix stiffness of MSCs

Similar to other adult stem cells, MSCs egress from their niche and circulate around in the body until they finally get implanted in the microenvironment of destination tissue and differentiate (Katayama et al. 2006). The stiffness of destination tissue or matrix microenvironment for MSCs varies significantly from very soft tissues such as brain tissue (~1kPa) (Budday et al. 2015) and adipose tissue (~2kPa)(Yuan et al. 2015), or muscle tissue (~10kPa)(Gilbert et al. 2010) to stiffer tissues such

as cartilage (~1 MPa)(Chizhik et al. 2010) and hard tissues such as cortical bone (~10GPa) (Figure 4-9).

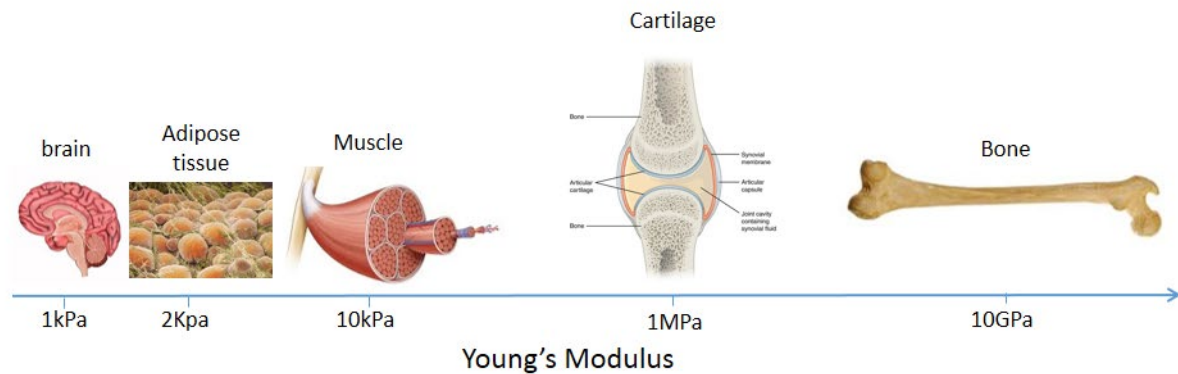


Figure 4-9: The approximate elastic modulus of tissues and matrix microenvironments that host different cell lines differentiated from MSCs.

Among differentiated cells, matrix stiffness can alter the cytoskeletal and focal adhesion structures (Discher et al. 2005) and consequently influence the cellular mechano-sensory and mechanotransduction machinery (Ingber 2006). Therefore, it was expected that substrate stiffness *in vitro* may have an effect on the commitment of MSCs to different lineages. In 2006, a study published by the Discher group demonstrated that MSCs differentiate into different lineages depending on the different stiffness of polyacrylamide gel substrates coated with collagen (Ingber 2006). The Young's modulus of the substrates was controlled through crosslinking and was set to soft (0.1-1kPa), stiff (8-17kPa) and rigid (25-40kPa) ranges in order to mimic the typical range of matrix stiffness in the brain, muscle and collagenous bone. It was shown that MSCs that are cultured on soft brain-mimicking substrates show branched and filopodia-rich neurogenic morphology; cells on stiffer muscle-mimicking substrates express myogenic spindle morphological features and MSCs on comparatively rigid bone-mimicking substrates manifest polygonal osteogenic characteristics (Figure 4-10). In addition, microarray profiling of MSCs transcription factors among cells cultured on soft, stiff and rigid substrates also clearly confirmed that cells on a soft substrate express a high level of neurogenic transcription factors while cells on stiff substrates express myogenic factors and cells on rigid substrates highly express osteogenic factors. The study showed that substrate stiffness-derived commitment is only reprogrammable in the first week and after several weeks of matrix-stiffness commitment the differentiation is stable, irreversible and consistent with the differentiation induced using biochemical factors. Furthermore, it was demonstrated that the matrix stiffness-derived

commitment is highly dependent on cytoskeletal actin-myosin machinery so that by inhibiting non-muscle myosin II using blebbistatin, all differentiation processes were completely blocked.

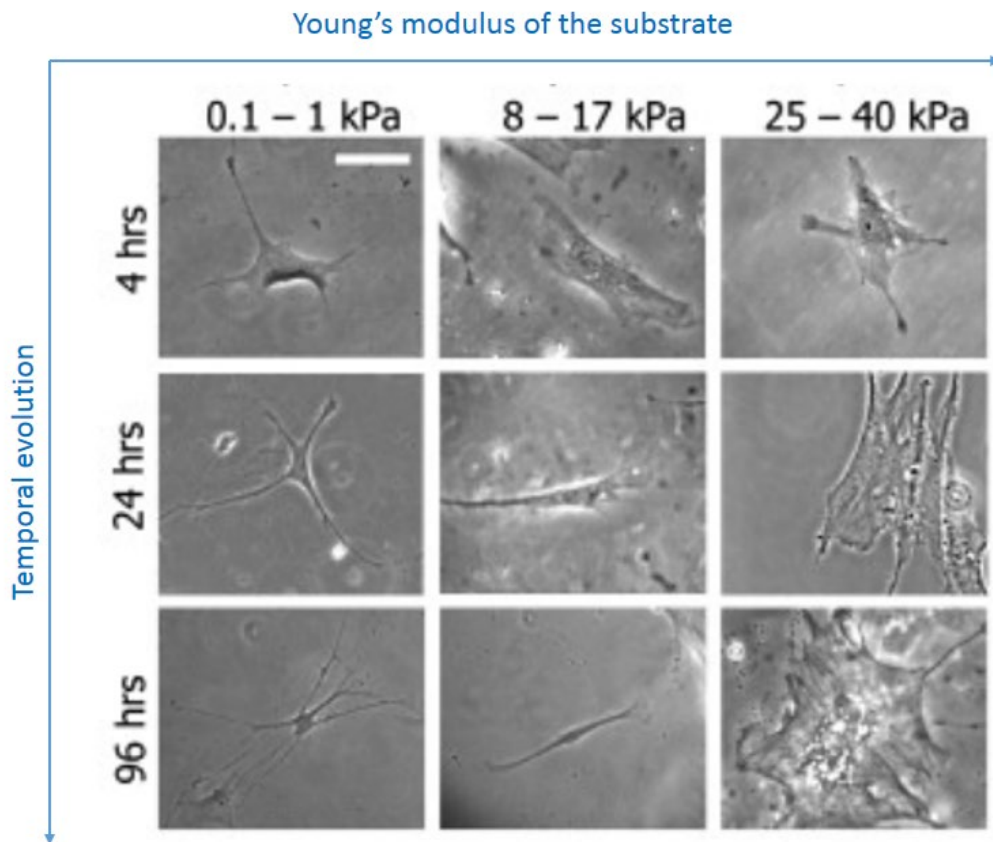


Figure 4-10: Bright field microscopy of morphological evolution of MSCs cultured on collagen type I coated polyacrylamide substrate with different stiffness. The soft substrate with Young's modulus of 0.1-1kPa mimics brain tissue stiffness and induces branching neurogenic cell shape. The substrate with Young's modulus of 8-17kPa mimics muscle tissue stiffness and induces spindle like elongated myogenic features and the rigid substrate with Young's modulus of 25-40kPa which mimics collagenous bone triggers polygonal osteogenic cellular morphology (Ingber 2006).

Later studies have tried to integrate the substrate–stiffness-derived differentiation with conventional biochemical differentiation factors in order to gain a more comprehensive control of the MSCs fate commitment process. Transforming growth factor β (TGF- β) is one of the best-known factors that promote the differentiation of MSCs into either chondrocytes or smooth muscle cells (SMCs). On the other hand, culturing MSCs on stiff collagen-I coated glass substrates increases expression of SMCs markers such as α -actin; while, culturing the MSCs on soft collagen-I coated substrate (~ 1 kPa) result in cells that express higher levels of chondrogenic markers such as collagen-II and adipogenic markers. These cells are also less prone to spread, have fewer stress fibers and lower rates of

proliferation compared to cells on the stiff substrate. When cells on the stiffer substrate were exposed to TGF- β , even higher levels of SMCs markers were observed. However, when cells on the soft substrate were exposed to TGF- β , only chondrogenic markers were boosted and adipogenic markers were completely surpassed (Park et al. 2011). The result shows that matrix stiffness can be a powerful tool in parallel to conventional biochemical factors to increase the yield of MSCs differentiation.

Sulphur-containing acidic groups are among the best known chemical factors that can induce chondrogenesis both *in vitro* and *in vivo* which is very important in cartilage regeneration. A study has shown that when MSCs are cultured on Sulphonate-coated polyacrylamide gels (S-PAAm gels) with lower Young's modulus ($\sim 1\text{kPa}$), cells express high chondrogenic markers and exhibit very low undifferentiation factors even in the absence of conventional chondrogenesis differentiation factors. However, cells that are cultured on the stiffer S-PAAm gels ($\sim 150\text{kPa}$), did not express chondrogenesis markers in the absence of a differentiation supplement. In addition, cells on the soft gels show morphological characteristics of chondrocytes such as high cortical actin, round shape and few stress fibers while the cells on the stiffer gels demonstrate strong expression of stress fibers and are more spread out. Similar to the previous studies, inhibition of myosin II by Blebbistatin completely suppressed the chondrogenesis on the soft gels (Joon Kwon & Yasuda 2013).

Although cytoskeletal actin-myosin has a very decisive role in the action mechanism of matrix stiffness on MSCs, the actual mechanotransduction mechanism involved has proved to be a more complex system of feedback and sensory loops.

Cytoskeletal stress fibers generate a contractile force which is balanced by the compressive resisting forces of cytoskeletal microtubules and the traction force that is exerted on the extracellular matrix (ECM) across focal adhesion points. As a result of this force transfer, the microtubule compression is directly determined by the substrate stiffness. Through cytoskeletal feedback loops mediated by several molecular chains, the cell stiffness changes its maximal sensitivity close to the microtubule compression value which is determined by ECM stiffness. In fact, computational models show that cell sensitivity is not a constant and has a bell-shaped behaviour over the range of physiological matrix elasticity and the position of sensitivity peak depends on the cytoskeletal organization and in particular F-actin structure. The model suggests that the reorganization that is observed in F-actin in MSCs when they are seeded on substrates with different elasticity is a cellular process that shifts the sensitivity peak towards the value of the substrate elasticity. If microtubule compression, which is determined by the matrix stiffness, is outside the range of cell sensitivity (or the cell is too soft or too stiff for the substrate in other words), the cell starts to either reinforce or dismantle the stress fibers through polymerization or depolymerization processes of actin bundles (De Santis et al. 2011).

Traction force on the ECM also triggers the integrin-mediated transduction pathway and the pathway influences the cytoskeletal actin polymerization which controls the contractility of stress fibers. Both

the contractile force of actin filaments and microtubule compression forces are transmitted to the nuclear Lamin-A and therefore are sensed by the nucleus and will influence transcriptional pathways. In addition, some direct signal from the integrin-mediated signal transduction cross-talks with Lamin-A transmitted signals in determining the transcriptional factors which govern stem cell differentiation and influence actin contractile stress fibers and Lamin-A structures (Figure 4-11)(Lv et al. 2015).

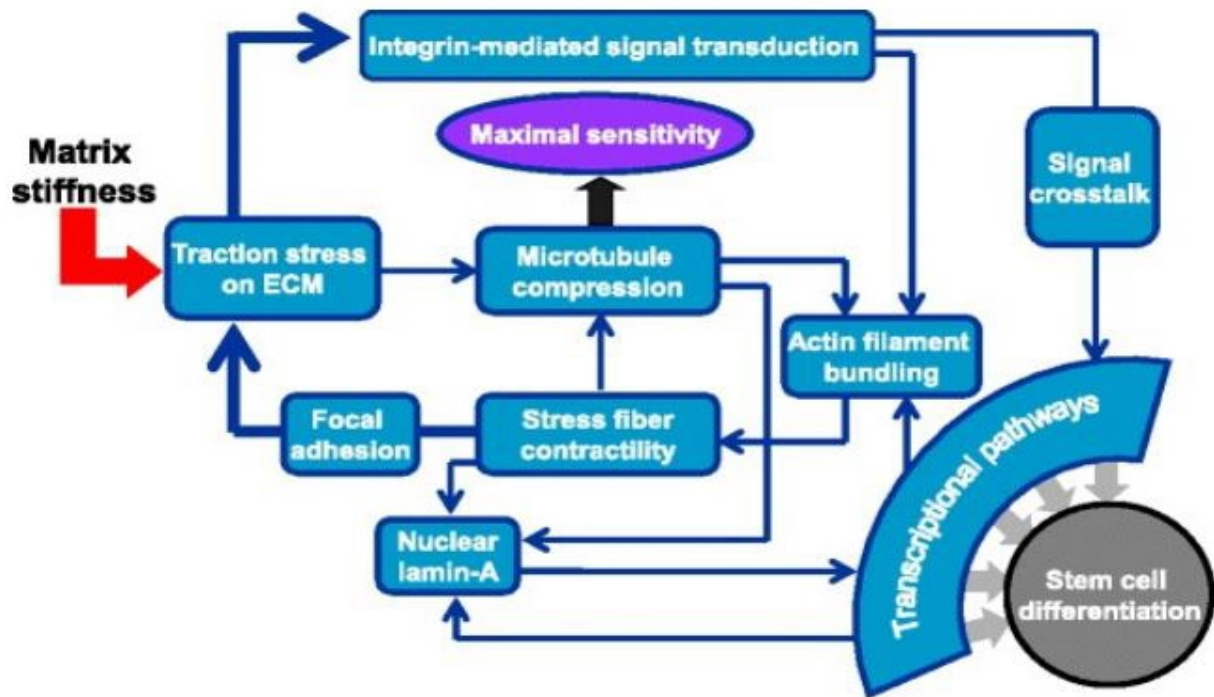


Figure 4-11: Mechanotransduction mechanism of matrix stiffness mediated stem cells differentiation. (Lv et al. 2015).

MSCs that are cultured on rigid substrates spread more, have well-aligned stress fibers and enhanced focal adhesion assembly which results in a cytoskeleton with high tensile stress. On the other hand, MSCs growing on the soft substrate, have a smaller cell projected area, diffuse and poorly defined actin cytoskeleton and fewer focal adhesions which result in an overall low tension cytoskeleton (Ingber 2006)(Figure 4-12). There is accumulating evidence that shows cytoskeletal based feedback loops are highly sensitive to the tensile stresses in the cytoskeletal elements (Swift et al. 2013)(Pajerowski et al. 2007)(Sun, Chi, Xu, et al. 2018) and therefore we can rationalise how the cell fate is highly dependent on the stiffness of the substrate matrix (Lv et al. 2015).

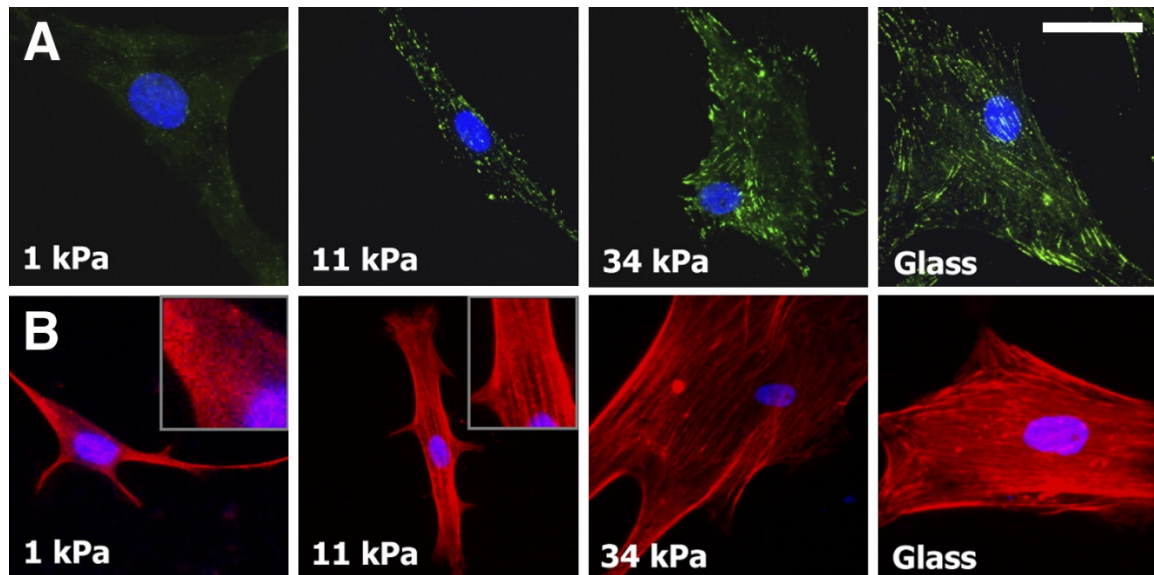


Figure 4-12: Cytoskeletal structure and adhesion state of MSCs cultured on substrates with different stiffness. (A): Paxillin labelled focal adhesions (green) are diffused and poorly defined in the neurogenic soft gel (1kPa) and they grow as the elasticity of the substrate increase in the myogenic gel (11kPa), osteogenic (34kPa) and the rigid glass substrate. (B) Projected cell area and F-actin (red) organization increase as the substrates become stiffer. Scale bar is 20 μm (Engler et al. 2006).

4.3.2.2 The effect of substrate patterns on the MSCs

In vivo, MSCs are exposed to a complex microenvironment in their niche. ECM is one of the most important elements of the microenvironments that provides physical support to the cell when they are adherent cells and mediates various mechanical and chemical signals to the MSCs. Therefore, it plays a crucial role in cellular behaviours such as cell differentiation, migration and proliferation (Kelleher & Vacanti 2010). Advances in the microfabrication and nanofabrication techniques have been used to fabricate biomaterials in order to mimic the topographic features of the ECM *in vivo* as well as the other mechanical and chemical ECM properties such as elasticity, porosity, surface charge, architecture, hydrophobicity, functional groups and protein composition (Kaivosoja et al. 2012). These biomaterials play a key role in understanding the role of mechanical cues on MSCs and also can be a powerful tool to control the MSCs behaviour which is crucial for the improvement of MSC-based tissue regeneration strategies (Li et al. 2017). It is difficult to control temporal and spatial concentration gradients for chemical factors; however, scaffold-based cues such as substrate patterns are easier to control. This gives a significant advantage to the pattern-based techniques to control the behaviour and fate of MSCs cells (Subramony et al. 2013).

Basically, it is possible to classify the 2D substrate effects on MSCs into the effect of substrate roughness and the effect of the patterns of the substrate. The substrate patterns that have been used also can be classified into two major categories: isotropic and anisotropic patterns (Metavarayuth et al. 2016) (Figure 4-13). Currently, different fabrication techniques are being used to fabricate these biomaterials including microcontact printing, photolithography, self-assembly systems, sandblasting, electrospinning, replica casting or molding and particle synthesis. These techniques synthesize nano and microscale topographic features on the substrate (Ross et al. 2012) while the length scale of the patterns that can affect MSCs is varied widely between tens of nanometers to tens of micrometres (Dalby et al. 2007),(Thery 2010).

Surface roughness is a quality of a surface that shows how smooth the surface is. The surface roughness is quantified by the measurement of the deviation of the normal vector of the real surface from a smooth curvature that has the same geometric shape and dimension (Ohtsuki et al. 2013). Therefore, surfaces with higher roughness are rough and with lower roughness are smooth. Surface roughness can be quantified with several parameters; however, the most frequently used roughness parameter in biomaterial field is the average value of filtered roughness R_a and is defined by following equation (Anselme & Biggerelle 2011):

$$R_a = \frac{1}{l} \int_0^l |Z_x| dx \quad \text{Equation 4-1}$$

Where Z_x is the profile ordinates (vertical distance from the mean line) of filtered roughness profile and l is the total abscissa (horizontal length) of the roughness profile. The profile of the rough surface is filtered to make small changes to the profile that smoothen it and make it integrable function. (Roughness Parameters - Rubert & Co Ltd).

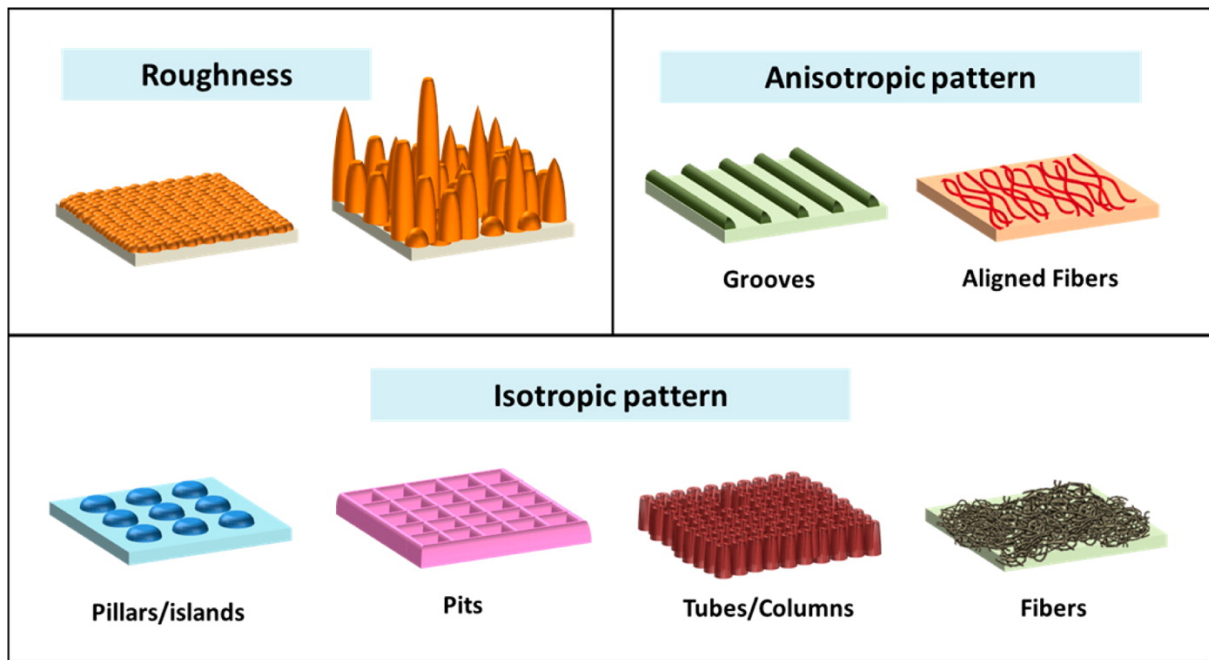


Figure 4-13: Classification of different topographic features of synthetic substrates (biomaterials) that affect MSCs behaviour and fate. (Metavarayuth et al. 2016).

The effect of surface roughness on MSCs is particularly important in the case of the response of the body to bone and dental implants (Wennerberg & Albrektsson 2009). Most of the studies have shown that substrates with an average roughness (Ra) about $1\mu\text{m}$ optimally enhances the osteogenic differentiation of the hMSCs (Yang et al. 2016). Other studies have shown that coating implants with an isotropic coating composed of a fibre network enhance cell proliferation, cell viability and osteogenic differentiation of the hMSCs. The enhancement was more significant among the MSCs that were seeded on the fibre networks with a spacing between the fibres that allowed them to penetrate deeply in the network (Symeonidou et al. 2013). This finding illustrates the importance of anchorage of the cell through their FAs which are significantly involved in mechanotransduction pathways of the cell (Shemesh et al. 2005).

A similar phenomenon of the optimized reaction of MSCs to a particular length scale was observed on isotropic aligned titanium dioxide (TiO_2) nanotubes. Aligned TiO_2 nanotubes with different diameters ranging from 15 nm to 100 nm have been fabricated (Figure 4-14 (a)) and MSCs were cultured on these nanotubes. In comparison to the smooth (TiO_2), surface and nanotubes with other sizes, the 15 nm nanotubes were found universally to promote MSCs cell adhesion, migration, proliferation and differentiation to osteoblasts (Park et al. 2009). Fluorescence microscopy of focal complexes that were stained by paxillin shows that osteoblasts express a more mature structure for focal adhesion complexes on the 15 nm nanotubes compared to 100 nm nanotubes, which is an

indication of stronger cell adhesion. As another indication of stronger adhesion of differentiated osteoblasts on 15 nm nanotubes, these cells deposit higher levels of fibronectin to ECM in comparison to the 100 nm nanotubes. Scanning electron microscopy (SEM) images revealed that differentiated osteoblasts on 15 nm nanotubes form extensive and thick filopodia and lamellopodia-forming is observable in fluorescence microscopy while there is no stable extension of filopodia among MSCs on 100nm nanotubes and lamellopodia are almost absent which together is an indication of impaired cell spreading (Figure 4-14(b)). It is hypothesized that the 15nm spacing may cause a more accelerated and compact clustering of integrin CAMs which have extracellular domain size of approximately 10nm (Giancotti 2003) into focal contacts and therefore result in more efficient signal transduction (Park et al. 2007) and consequently more enhanced cellular activities such as proliferation, differentiation, migration and adhesion (Park et al. 2009). Integrins are one of the most important CAMs that are connected to both cytoskeleton and the ECM and activate mechanotransduction cascades by mediating extracellular mechanical signals through focal adhesion complexes into the nucleus and cytoskeleton (Giancotti 2003).

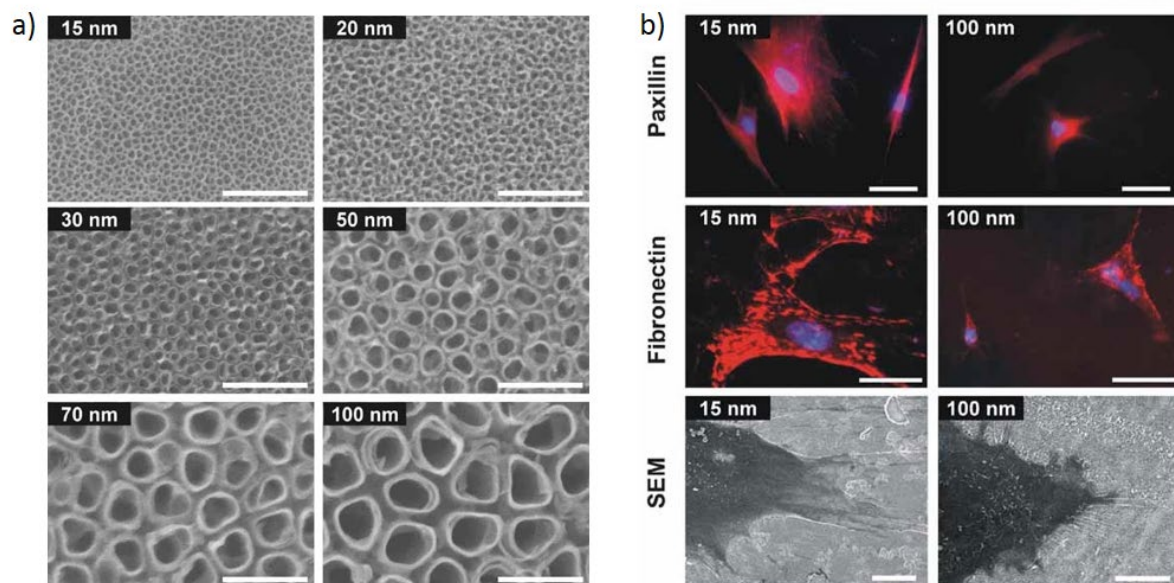


Figure 4-14: The effect of aligned TiO₂ nanotubes with different diameters on MSCs and osteoblasts. (a) SEM images of self-assembled layers TiO₂ nanotubes in the vertical orientation. Scale bars: 200nm. **(b)** Paxillin stained focal adhesion complexes (upper panel, scale bars: 100μm), extracellular fibronectin deposition on the substrate by osteoblasts (middle panel, scale bars: 50μm) and filopodia formation imaged by SEM (lower panel, scale bars: 10μm) (Park et al. 2009).

Size and shape of the patterns can enhance or inhibit MSCs differentiation into different lineages. Culturing MSCs on ridge/groove micropatterns (Figure 4-15(a)) on a Polyimide (PI) substrate enhance either osteogenic or adipogenic differentiation of MSCs depending on the size of the patterns (Abagnale et al. 2015). As was observed in other adhesive cells, the patterns contact guide MSCs parallel to the grooves (Figure 4-15(b)). It was shown that patterns with 15 μm ridges and 5 μm groove (2 μm deep) optimally enhances adipogenic differentiation compared to flat PI control surface and patterns with 2 μm ridges and 5 μm groove (2 μm deep). However, patterns with a 2 μm ridge (groove width: 5 μm) significantly increased osteogenic differentiation compared to 15 μm patterns and control PI substrate. Fluorescence microscopy revealed that the actin cytoskeleton was aligned to the patterns and patterned substrate reduce the area of cells. Focal adhesion (FA) complex stained by vinculin showed that patterns with 15 μm ridge reduce both the number per cell and area of FA compared to a control flat PI substrate; however, cells failed to form FAs on the patterns with the 2 μm ridge (Figure 4-15(e)). When they examined nano-scale patterns (Figure 4-15(d), nano-groove patterns with a periodicity of 650 nm and depth of 200 nm, the MSCs were still aligned to the patterns and migrated parallel to the grooves (Figure 4-15 (c), (f) and(g)). The 650 nm patterns increased both osteogenic and adipogenic differentiation of MSCs compared to the control unpatterned substrate when it was exposed to the oestrogenic and adipogenic differentiation medium. Fluorescence microscopy of the actin cytoskeleton revealed the partial polarization of actin fibres on the patterns and the cell areas almost did not change compared to the control flat substrate. Vinculin staining revealed that patterns slightly reduce the number and size of FAs; however, different from 2 μm ridge patterns, the visible FAs formed (Figure 4-15 (f)). In the absence of differentiation media, both micro and nano-scale ridge-groove patterns failed to detectably induce differentiation among MSCs.

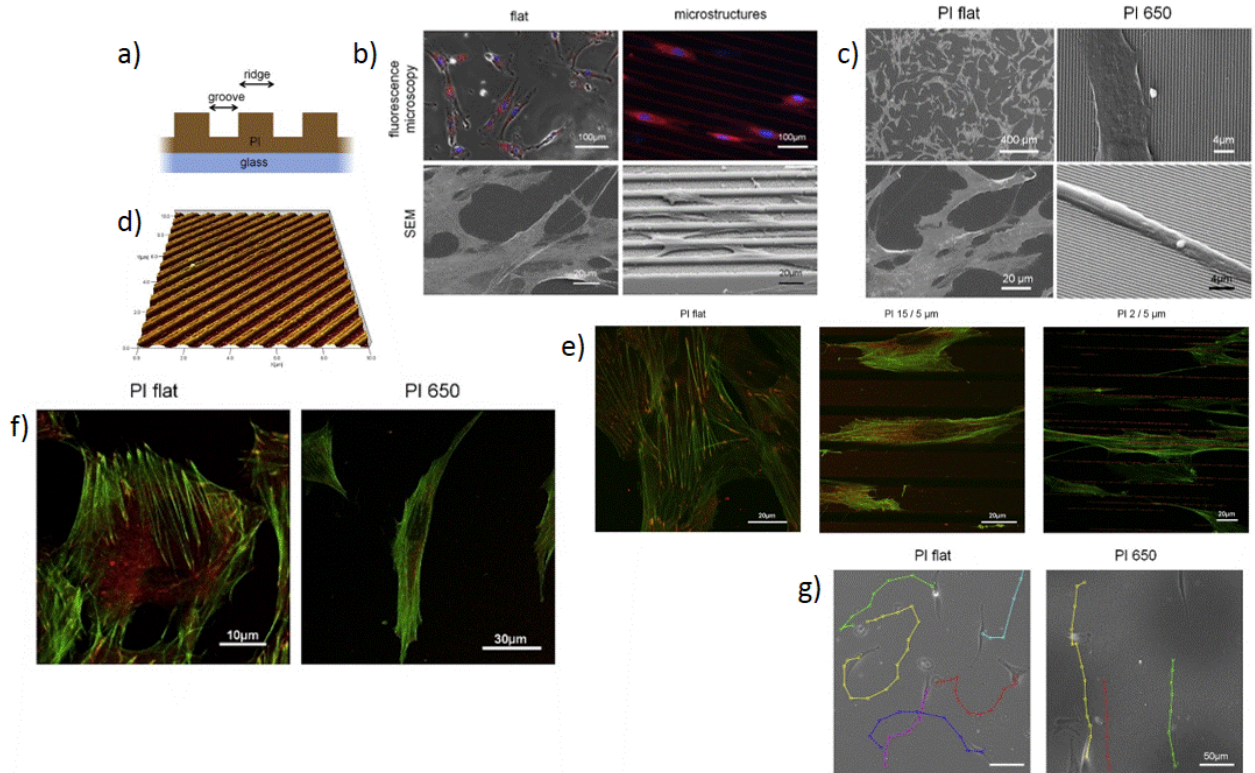


Figure 4-15: The effect of micro and nano-scale ridge-groove pattern on PI on MSCs. (a)

Schematic side view of micro-meter ridge patterns. (b) SEM and fluorescence microscopy of MSCs on flat and 15 μm ridge-groove patterns showing cell alignment. The nucleus was stained with DAPI (blue) and the cell membrane was stained with PKH26 (red). (c) SEM images of MSCs on flat PI and 650 nm ridge-groove pattern shown cell polarization on the patterns. (d) AFM measurement of nano-groove patterns with 650 nm showing the structure of the pattern. (e) MSCs on the micro ridge-groove patterns and flat PI were stained for actin cytoskeleton (green) and vinculin marked FA complexes (red). (f) MSCs on the 650nm ridge-groove patterns and flat PI were stained for actin cytoskeleton (green) and vinculin marked FA complexes. (g) The straight direction of cell motility of MSCs on the 650 nm ridge-groove PI patterns and random walk-type motility of cells on the flat PI substrate (Abagnale et al. 2015).

These results make it possible to conclude that the formation of FAs, which have a size of approximately $1 \mu\text{m}^2$, is mostly inhibited or minimized on a pattern with the size of the same order as the FAs; the formation process is almost indifferent to patterns with length scales bigger or smaller than their size.

The nano-scale topographical cues also have been used to study the dynamics of nuclei deformation of hMSCs (Chalut et al. 2010a). hMSCs were cultured on collagen-I coated nanogratings (350 nm width, 350 nm height, and 700 nm pitch) made of either PDMS or Polystyrene (PS) and deformation

of actin cytoskeleton and nucleus was monitored over time. The result revealed that the hMSC nuclei start to elongate along the direction of the gratings approximately 3 hours after seeding on the patterns and continue to elongate for 24 hours after seeding. In addition, it was shown that the alignment was more significant on stiffer PS patterns (Young's modulus $\sim 3\text{GPa}$) compared to softer PDMS counterparts (Young's modulus $\sim 400\text{ kPa}$). It was speculated that as the formation of stress fibres is more efficient on stiffer substrates, this may increase mechanical forces on the nucleus which is mechanically coupled with the actin cytoskeleton. (see chapter 1.4). The nuclear deformation was more pronounced 6-8 hours after the seeding when filamentous actin fibers oriented in the direction of the nanogratings.

The cellular shape can significantly influence the differentiation of MSCs independent from the soluble chemical and biological factors. MSCs were cultured on fibronectin-coated islands with different shapes and sizes on PDMS in a medium that had a mix of both osteogenic and adipogenic differentiation cues (Kilian et al. 2010). It has been shown that the medium induces a similar level of osteogenic and adipogenic differentiation among MSCs cultured on unpatterned substrates. However, when cells were cultured on islands of different sizes, they showed different differentiation tendencies. MSCs that were cultured on small patterns ($1000\text{ }\mu\text{m}^2$) primarily express adipocytes markers while cells on the patterns with a larger area ($5000\text{ }\mu\text{m}^2$) express markers of osteoblasts and cells on the patterns with an intermediate area ($2500\text{ }\mu\text{m}^2$) express a mixture of both osteoblasts and adipocytes. The results were consistent on rectangle, star and flower shapes. Immunofluorescence microscopy revealed a profound difference between cytoskeletal structures of MSCs on these patterns. MSCs on the $1000\text{ }\mu\text{m}^2$ patterns have a rounder morphology with a disrupted organization of actin and microtubule filaments, while cells that were allowed to spread on the $5000\text{ }\mu\text{m}^2$ patterns expressed much more and better-organized actin and microtubule filaments (Figure 4-16 (a), (b), (c) and (d)).

Pattern area is not the only geometric factor that influences the MSCs fate: the polarization of the patterns also plays an important role in the MSCs polarization and commitment to a specific lineage. MSCs were cultured on rectangular fibronectin patterns with different aspect ratios (1:1, 3:2 and 4:1) in the presence of a medium with a mix of adipogenic and osteogenic differentiation inducing reagents. It was shown that the rate of osteogenesis increases with the aspect ratio and the percentage of adipogenic cell differentiation reduces with the aspect ratio. Fluorescence microscopy revealed that cells on the rectangular patterns with higher aspect ratio have more organized actin filaments with long thick actin stress fibres along the edge of patterns (Figure 4-16 (e)). Furthermore, larger and more numerous FAs were formed at the corner and short edge of the cells on the rectangular patterns with a higher aspect ratio (Figure 4-16 (f)).

Symmetry and curvature of the shapes also can influence the MSCs' fate. MSCs which were cultured on flower shape patterns with large convex curves along each edge showed a higher level of adipocyte

differentiation while star-like shape patterns with concave edges and sharp points at the vertices showed a greater tendency towards osteogenesis. MSCs that were cultured on a pentagon shape with straight lines for the edges showed almost an equal tendency to osteogenic and adipogenic differentiation. Fluorescent microscopy showed that in flower patterns actin filaments are concentrated at acute corners between petals, whereas in star patterns the contractile filaments are concentrated at the concave regions between points of the star (Figure 4-16 (g)). Flower patterns have stronger and evenly distributed FAs across the cell, while FAs concentrated at the edges of MSCs on the star patterns (Figure 4-16 (h)). Immunofluorescent heatmaps that are the average of fluorescent images of many cells show that overall MSCs on star patterns form larger FAs and actin stress fibres compared to the cells on the flower patterns with the same pattern area (Figure 4-16(i),(j),(k),(l)).

Myosin II is a motor protein that primarily is responsible for cytoskeletal contractility. Although there is not a clear difference in the structure of myosin II of MSCs on star and flower patterns ((Figure 4-16(m)), average heatmaps revealed that there is a higher degree of actomyosin contractility in star patterns which is mostly concentrated in the edges of these patterns (Figure 4-16 (n)). It was concluded that local curvature which increases cytoskeletal actomyosin contractility increases osteogenic differentiation. In fact, the difference that was induced by pattern shape on the differentiation of MSCs was removed when cellular contractility was interrupted by chemical drugs such as Cytochalasin D and Blebbistatin which inhibit actin and myosin II polymerization respectively.

In an extreme case, cells were cultured on a pattern with both high aspect ratio and local curvature (holly leaf) and completely circular patterns. Cells on the circular pattern strongly favoured adipogenesis and have a very disrupted actin organization while the MCSs on the holly leaf pattern have more actomyosin contractility and strongly favoured osteogenesis (Figure 4-16 (o)). However, the yield of differentiation was almost similar to the star and flower patterns which may indicate that the influence of pattern shape on the fate decision of MSCs has its own limits.

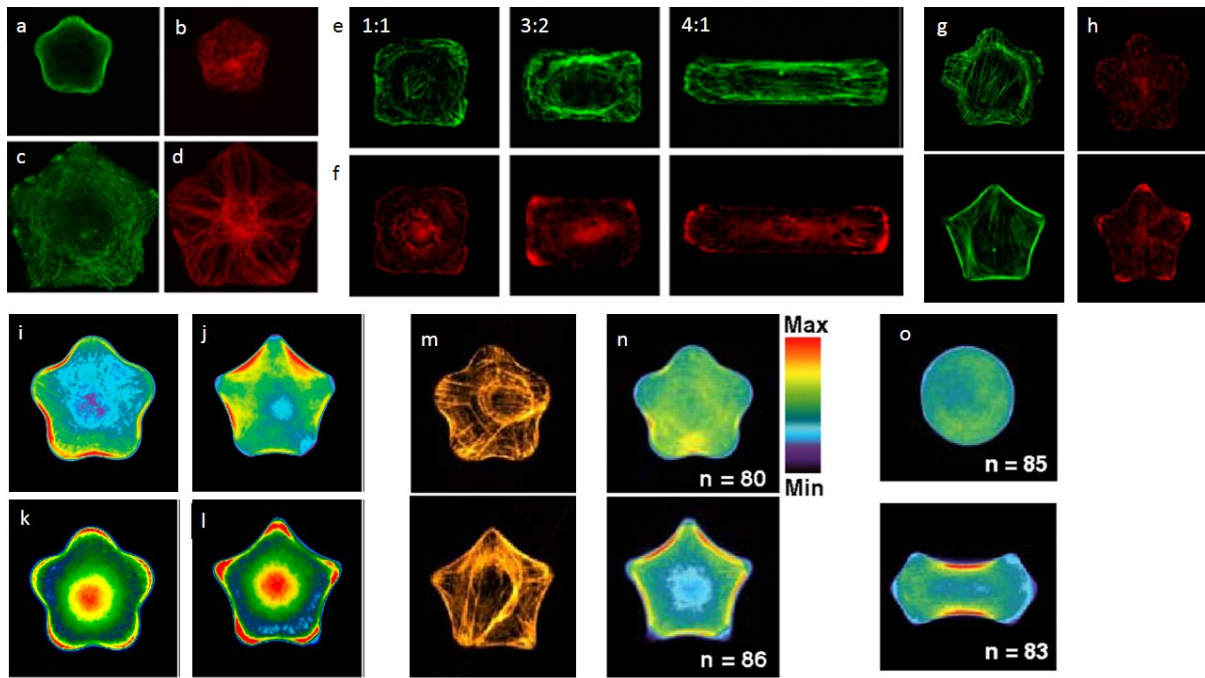


Figure 4-16: The influence of fibronectin patterns shape on the cytoskeletal structure of MSCs.

(a) Immunofluorescence image of round shape actin (Phalloidin, green) structure of MSCs on 1000 μm^2 pattern. (b) Round morphology of microtubulin (red) structure of MSCs on 1000 μm^2 pattern. (c)& (d) Organised structure of actin and microtubulin of MSCs that were allowed to spread on 5000 μm^2 patterns. (e) Increasing organization of actin cytoskeleton of MSCs on rectangular patterns with increasing aspect ratio. (f) FAs structure (red, vinculin) of the MSCs on rectangular patterns with different aspect ratios. (g) Structure of actin filaments of MASs on flower and star patterns stained for F-actin (green). (h) FAs distribution of MSCs on flower and star patterns stained for vinculin (red). (i) Immunofluorescence heatmaps of MSCs on flower pattern stained for F-actin, on star pattern stained for F-actin (j) Flower pattern stained for vinculin (k) And star pattern stained for vinculin (l). (m) Fluorescence image of MSCs on flower and star pattern stained for myosin IIa. (n) Immunofluorescence heatmaps of MSCs on flower and star patterns stained for myosin II quantitatively revealing the cellular actomyosin contractility. (o) Immunofluorescence heatmaps of MSCs on circular holly leaf patterns (Kilian et al. 2010).

Chapter 5:

The impact of fibronectin stripe patterns on the cellular and nuclear morphology of fibroblasts

5.1 Fibroblasts

Fibroblasts are differentiated from mesenchymal stem cells and are the most common cells of the connective tissue (see chapter 4) (Alberts et al. 2002b). Together with other connective tissue cells such as osteoblasts and chondrocytes, fibroblasts are mainly tasked to synthesize, secrete and maintain the ECM (Tschumperlin 2013). Fibroblasts produce the ground substance of the ECM and fibrous proteins such as collagen, fibronectin, elastin and glycosaminoglycan (GAGs) to form and maintain the ECM (Duncan & Berman 1989) (see chapter 1.6 for more details). Therefore, fibroblasts play a central role in wound healing and development of reparative extra fibrous connective tissue in response to injuries (fibrosis) (Tracy et al. 2016). Some fibroblasts such as mouse embryonic fibroblasts (MEFs) or human dermal fibroblasts (HDFs) also are used as “feeder cells” for stem cell cultures. These feeder fibroblasts support the stem cell culture by releasing growth factors to the culture media and synthesizing ECM for the stem cells (Llames et al. 2015).

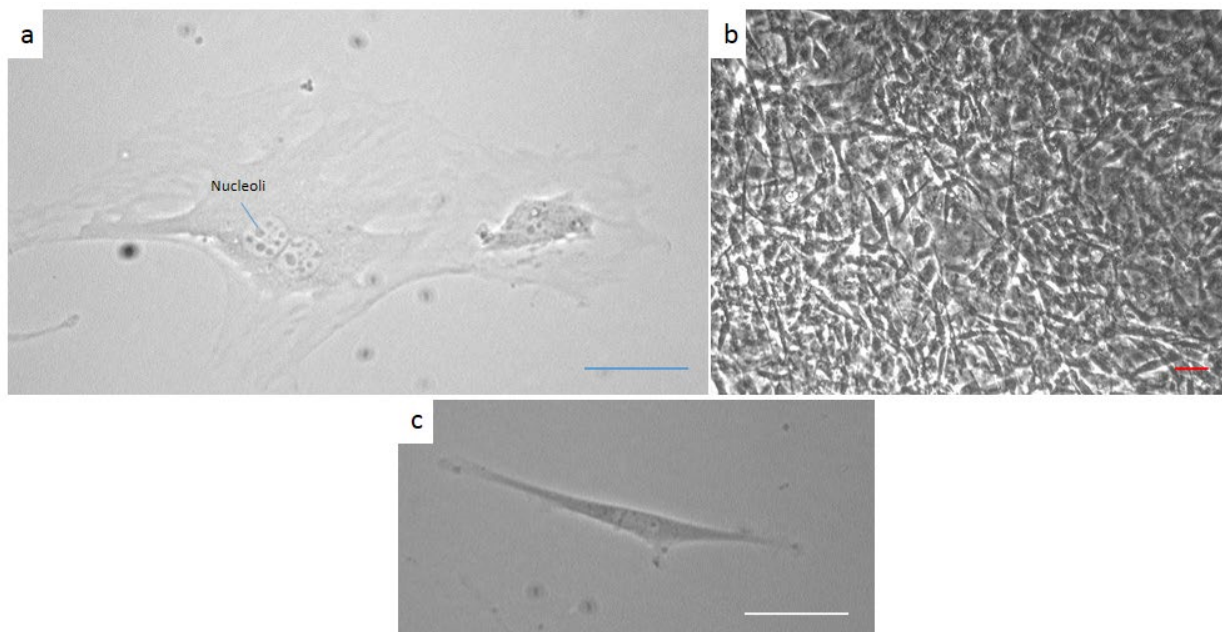


Figure 5-1: Morphological diversity of NIH/3T3 fibroblasts. (a) Bright field image of a dividing fibroblast with branched cytoplasm and multiple nucleoli (denser parts inside the nucleus) in a 25 cm² culture flask. (b) 3T3 fibroblasts in full confluency. (c) A spindle-like fibroblast in the culture of Figure 5-1(a).

Fibroblasts are adherent cells and express heterogeneous morphology such as branched well-spread cells (Figure 5-1(a)) or smaller spindle-shaped cells (Figure 5-1(c)) and have a nucleus with multiple nucleoli. When fibroblasts reach high confluency (Figure 5-1(b)) the majority of cells are fairly round. In addition, elongated cells don't show any aligned elongation in a certain direction in contrast to hMSCs (see Figure 6-1 (d)).

Some protease enzymes such as Trypsin (the most frequently used proteolytic enzyme in cell culturing) can cleave the peptide chains and cut away the focal adhesions of fibroblasts and dissociate them from the substrate (Huang et al. 2010) (Figure 5-2(a)). Adhesion is essential for the survival of adherent cells such as fibroblasts. Failure to adhere on the ECM or inadequate cell-ECM interaction, induce a type of programmed cell death (apoptosis) called anoikis (from “greek an: without” +” oik: house”) (Frisch & Francis 1994)(Vitale et al. 1999). The signalling for the anoikis is triggered by expression of unligated integrin (Stupack et al. 2001)(see chapter 1.5). When fibroblasts undergo apoptosis due to unfavourable culture condition such as apoptosis-inducing drugs, overgrowth in the culture or nutrition depletion, they start to disassociate from the surface as well and show hallmarks of apoptotic cell death such as blebbing (Huh et al. 2012)(Mills et al. 1998)(Figure 5-2 (b)&(c)). If the unfavourable condition continues, more cells detach from the substrate and undergo irreversible necrotic cell death (Figure 5-2(d)).

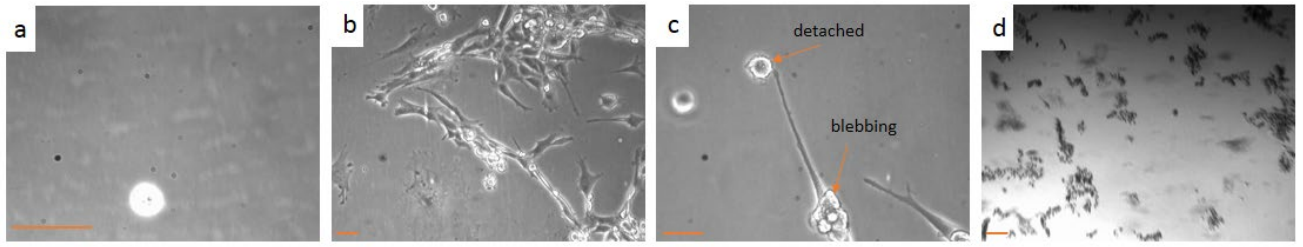


Figure 5-2: Phase contrast microscopy of 3T3 fibroblasts detachment from the substrate. (a) A cell is dissociated from the substrate (25 cm² culture flask) and form a spherical shape after treating with 0.25% trypsin-EDTA for 5 minutes. (b) Cells that were in culture for a week detach from the substrate and show hallmarks of apoptotic cell death such as blebbing (10x). (c) A closer look of apoptotic cells in Figure 5-2 (b) (20x). (d) Cells become necrotic and completely dissociated from the substrate in a long-running culture after two weeks, cell-cell attachment still keeps them in a patch. Scale bars are 50 μm.

To obtain information about the size of 3T3/NIH fibroblasts, the cells were treated with 0.25% trypsin-EDTA solution for 3 minutes at 37 °C and suspended later in fresh cell growth medium (see section 2.2.1). Phase contrast microscopy of the cells was done immediately when they were still in suspension (Figure 5-3(a)). Images were processed and the average diameter was determined by assuming a circular shape for the cells (Figure 5-3(b)). Figure 5-3 (c) shows the distribution of cell diameters coming from three different biological replicates (n=119 in total). A Gaussian curve with a mean value of 17.2 μm and a standard deviation of 3.23 μm has been fitted based on these values.

The cells are approximately round with a circularity of 0.889 ± 0.003 s.e.m. (n=119). Circularity or isoperimetric quotient is a dimensionless function of cell area (A) and cell perimeter (P) and is defined by equation 5-1 (Wayne Rasband 2000):

$$S = \frac{4\pi A}{P^2}, 0 < S \leq 1 \quad \text{Equation 5-1}$$

Circularity is between 0 and 1 for any given shape. It is 1 for a perfect circle and it can be much less for elongated polygons (Xiong et al. 2010a). It approaches zero for a straight line.

The results show that fibroblasts are among medium-size cells in the body. Typical somatic cells have a diameter between 10-20 μm; however in the human body, cells such as human ovum can be as big as 100 μm or be as small as erythrocytes with about 6.8-7.5 μm or human sperm which is the smallest human cell with a head dimension of $4.5 \times 2.8 \times 1.1$ μm (flagellar length of 56 μm) (Alberts et al. 2002a)(Turgeon 2004)(Smith et al. 2009).

The suspended live fibroblasts were stained with Hoechst dye to visualize the nucleus under fluorescence microscopy (Figure 5-3(d)) (see chapter 2.7.2 for more details). The nuclei of suspended fibroblasts are approximately round with a circularity of 0.845 ± 0.005 s.e.m. ($n=142$) although some oval shape nuclei also are visible with an average diameter of $13.2 \mu\text{m}$ and standard deviation of $2.61 \mu\text{m}$ (Figure 5-3(e)&(f)). Initially, we hypothesized the oval shape of some nuclei immediately after detachment maybe is because of physical memory from their adherent state. In order to examine this hypothesis, we put the cells in the media for 35 minutes on a shaking plate at 180 rpm and 37°C in order to inhibit possible adherence to the substrate. This period gives the nuclei enough time to forget their adherent shape. However, we could not observe a significant difference in the circularity (0.834 ± 0.005 s.e.m. ($n=161$)) of the relaxed nuclei compared to the nuclei of cells immediately after detachment (Figure 5-3(f)).

To rule out the possible effect of nucleus division among relaxed nuclei that can affect our observation, we considered the distribution of aspect ratio of the two groups of the nuclei.

The aspect ratio (AR) is defined as the ratio of the major axis to the minor axis of the best fit ellipse to a shape. The best fit ellipse has the same area, direction and centroid as the original outlined shape (Imagej.nih.gov 2012).

However, we observed relatively a similar distribution of aspect ratio for the two groups of nuclei with similar average and standard deviation (relaxed nuclei with a mean aspect ratio of 1.41 and standard deviation of 0.24 ($n=161$) compared to the nuclei immediately after detachment with mean aspect ratio of 1.45 and standard deviation of 0.27 ($n=142$) (Figure 5-3(h)). This indicates that there is no nuclear division during relaxation on the shaking plate. Furthermore, we observed that when nuclei were given time to relax, the average diameter of them was reduced to 11.80 ± 0.22 s.e.m. from 13.25 ± 0.21 s.e.m in the nuclei of the cells immediately after detachment. It has been shown that the nuclei of mouse fibroblasts reduce their volume during detachment from the substrate (Kim et al. 2015). The 3D finite element simulation in the same study has revealed that nucleus of the cell during detachment forms wrinkles on its surface in response to an increasing osmotic pressure outside of the nucleus (Figure 5-3(i)). We concluded that the formation of these surface wrinkles matures during relaxation time and therefore we observed homogenously decreasing size of the nuclei with a smaller diameter and relatively the same morphological features such as aspect ratio and circularity.

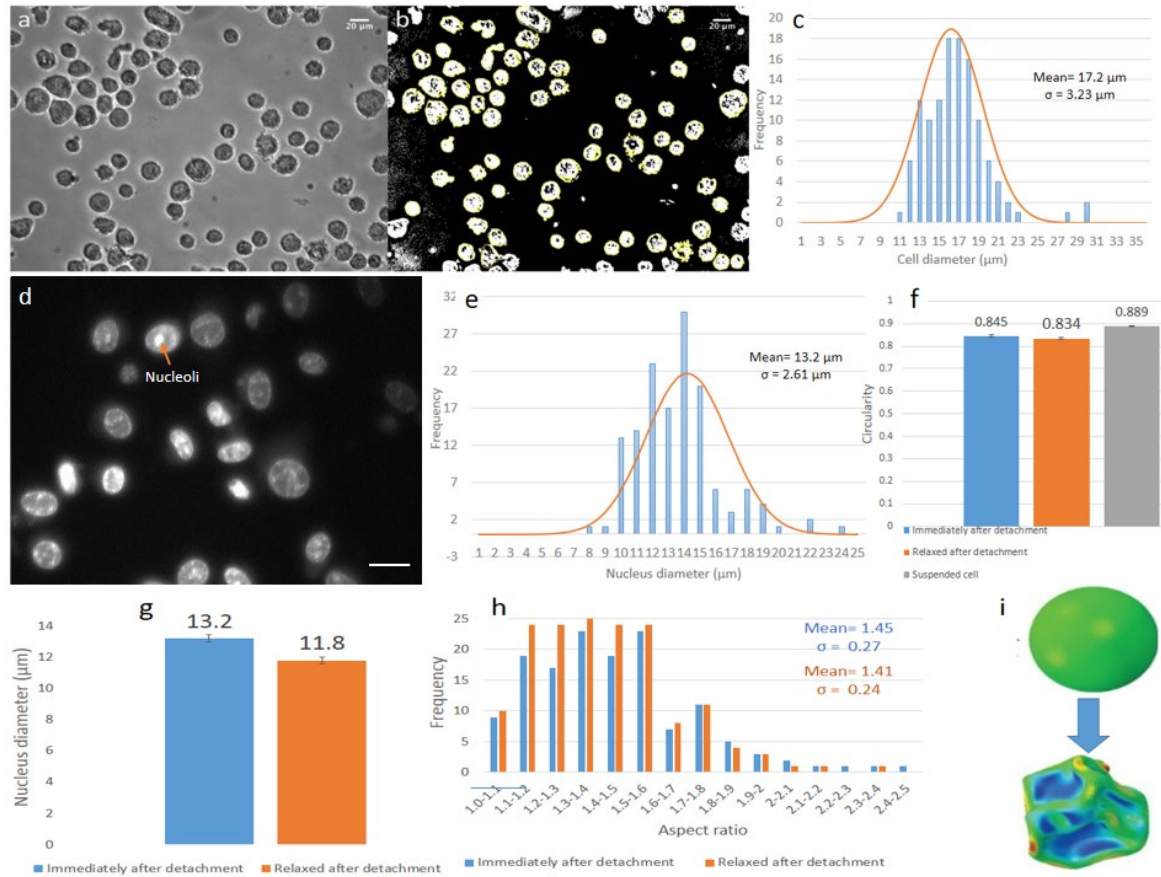


Figure 5-3: NIH/3T3 fibroblasts in the suspension. (a) Phase contrast microscopy (20x, NA=0.4) of suspended 3T3 cells in the 25 cm² flask disk. (b) Corresponding processed image. Marked regions (yellow-bordered regions) were automatically detected by Image J and were used to measure cell diameter. The cells adjacent to the images' edge were excluded from analysis to avoid software mistake. Small objects treated as debris and were rejected. (c) Histogram of NIH/3T3 cell diameter distribution. The diameter of suspended cells (n=119) was shown as the histogram with bin size=1 µm. A Gaussian curve (red curve) is fitted to the distribution using calculated mean and standard deviation. (d) Fluorescent micrograph (40x, NA=0.6) of detached nuclei of NIH/3T3 fibroblasts stained with Hoechst® 33342, denser (brighter) parts are the nucleoli. (e) Histogram of NIH/3T3 fibroblasts nuclei size distribution (n=142) (blue) with a Gaussian curve fitted to the distribution (red). (f) The circularity of NIH/3T3 fibroblasts immediately after detachment with 0.25% trypsin-EDTA solution (blue), after relaxation in suspension by being shaken for 35 minutes at 180 rpm (orange)(n=161) and suspended cells immediately after detachment with the trypsin-EDTA solution (grey). (g) The nucleus diameter of 3T3 fibroblast, immediately after detachment with 0.25% trypsin-EDTA solution (blue) and after relaxation in suspension by being shaken for 35 minutes at 180 rpm (orange) (h) The distribution of aspect ratio of 3T3 fibroblast nuclei immediately after detachment and after relaxation for 35 minutes. (i) Schematic illustration of the volume regulation of the

suspended nucleus during the relaxation process. Figure 5-3(i) is adapted by (Kim et al. 2015). Scale bars are 20 μm .

5.2 Adhesion process of fibroblasts

Some cell lines are capable of adhering to the surface (substrate), extracellular matrix (ECM) or the adjacent cells with the facilitation of a complex set of cell adhesion molecules (CAMs). Cell adhesion plays a critical role in the structural integrity of tissues, maintaining multicellular structures, pathogenesis of infectious organisms and signal transduction (Gumbiner 1996) (see chapter 1.5 for details). Previous temporal studies on the various adherent cells have shown that the projected cell area increases over time exhibiting a three-phase sigmoid curve((Döbereiner et al. 2004),(Cuvelier et al. 2007),(Mooney et al. 1995),(Fardin et al. 2010),(Xiong et al. 2010b)) which is very similar to the same temporal dynamic of cytoskeletal filamentous actin polymerization (Fujiwara et al. 2002), the critical mechanism behind cell spreading (Mooney et al. 1995). Detached 3T3 fibroblasts also show the same behaviour when they are seeded on the control unpatterned substrate (Figure 5-4). Projected area measurements of 3T3 fibroblast cells have illustrated that by 200 minutes after seeding on fibronectin-coated PDMS substrates the cell area reaches a steady state phase(S-phase) after an initial lag slow growth (L-phase) followed by a rapid area expansion phase (E-phase) (Huang & Donald 2014a).

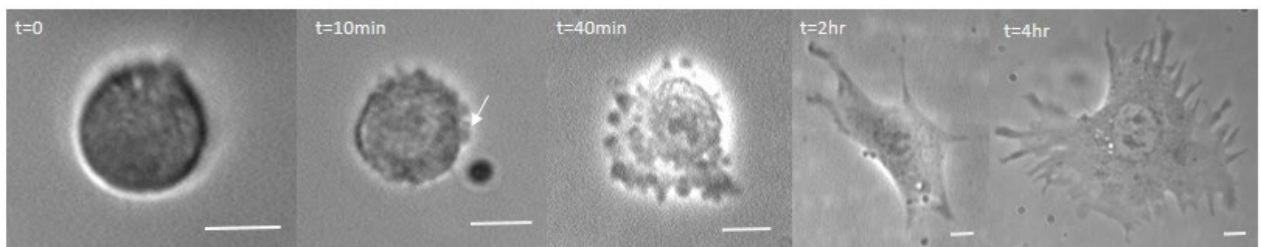


Figure 5-4: The adhesion evolution of NIH/3T3 fibroblasts on 25 cm^2 flask substrate. $t=0$ is a bright field image and the rest are phase contrast micrographs of fibroblasts spreading in different states of the adhesion process. The arrow shows early nascent filopodia in the leading edge of spreading fibroblast. Scale bars are 10 μm .

5.3 Fibroblasts on the fibronectin stripes

It is well known that when cells are seeded on substrates with topographical cues, the cytoskeletal and subcellular organelles of the cell are affected by the patterns. In other words, the patterns play a critical role in the control of the adhesion process and cellular behaviour (Curtis & Wilkinson 1997). Adherent cells, such as fibroblasts, demonstrate the ability to conform to the external topographical cues and move in accordance with the texture of the substrate. This phenomenon was first observed in 1912 (Harrison, 1912) and later was coined “contact guidance” (Weiss 1934) (see chapter 3.1 for more details). Contact guidance occurs not only *in vitro* when the cells are in contact with a two dimensional substrate texture, it also frequently happens in the native environment of the cells where they are constantly exposed to topographical cues in the form of the extracellular matrix (ECM) and surrounding cells ((Alberts 2008);(Cassimeris et al. 2011)). As a result, studying the phenomenon is of prominent importance in understanding several key processes such as wound healing, embryogenesis, nerve regeneration, angiogenesis and stem cell differentiation ((Marmaras et al. 2012);(Stuart & Moscona 1967);(Hoffman-Kim et al. 2010);(Bauer et al. 2009);(Song et al. 2015)).

2D topographic patterns printed by adhesive molecules such as fibronectin, are optimized models with precisely controlled parameters to mimic cell-ECM and cell-cell interaction in the native environment of cells. These *in vitro* models are increasingly capturing the attention of researchers, as accumulating evidence reaffirms that physical interaction of the cell and extracellular environment (either in the form of topography or matrix stiffness, or the combination of both) plays a critical role in modulating vital cell machineries such as cell proliferation, gene expression, differentiation and signal transduction and mechanosensing ((Yim et al. 2010);(Tilghman & Parsons 2008);(Geiger et al. 2009);(Vogel & Sheetz 2006)(Engler et al. 2006);(Delmas et al. 2011)).

In this study, we used fibronectin coated stripes on the PDMS substrate (Figure 5-5 (b)). By changing the width of the stripes in a wide range, we could observe different regime of the cellular response depending on the width. The stripe patterns mimic some of the frequently occurring situations in the living microenvironment of the adherent cells such as aligned collagen fibres. Micro stripe patterns printed by CAMs such as fibronectin or collagen have been employed for quantitative study of the dynamics of cell migration and adhesion, force coupling between the nucleus and adhesion complexes of the cytoskeleton, cytoskeletal filaments, adhesion morphology and mesenchymal stem cell differentiation ((Huang & Donald 2014a);(D.-H. Kim et al. 2014a);(Oakley & Brunette 1993);(Kung et al. 2011);(Kasten et al. 2014)).

Our fibronectin stripes were printed from ridge-groove patterns (Figure 5-5(a)) (see chapter 2.6 for details). Ridge-groove arrays are a family of topological patterns that have been frequently used for

studying contact guidance since 1979. The patterns were first introduced to explain previously observed contact guidance among chick heart fibroblast and kidney epithelial cells induced by fine grooves in plastic culture dishes (Ohara & Buck 1979). The majority of the cell lines that have been cultured on these patterns tend to align themselves along the major axis of the grooves (Nikkhah et al. 2012). Depending on the dimensions of the ridges and grooves, adherent cells show characteristic behaviour such as bridging over the grooves without contacting their surface (bridging), cell confinement, cell traversing (connecting) between ridge and grooves (Stevenson & Donald 2009) (see chapter 3.4 for details).

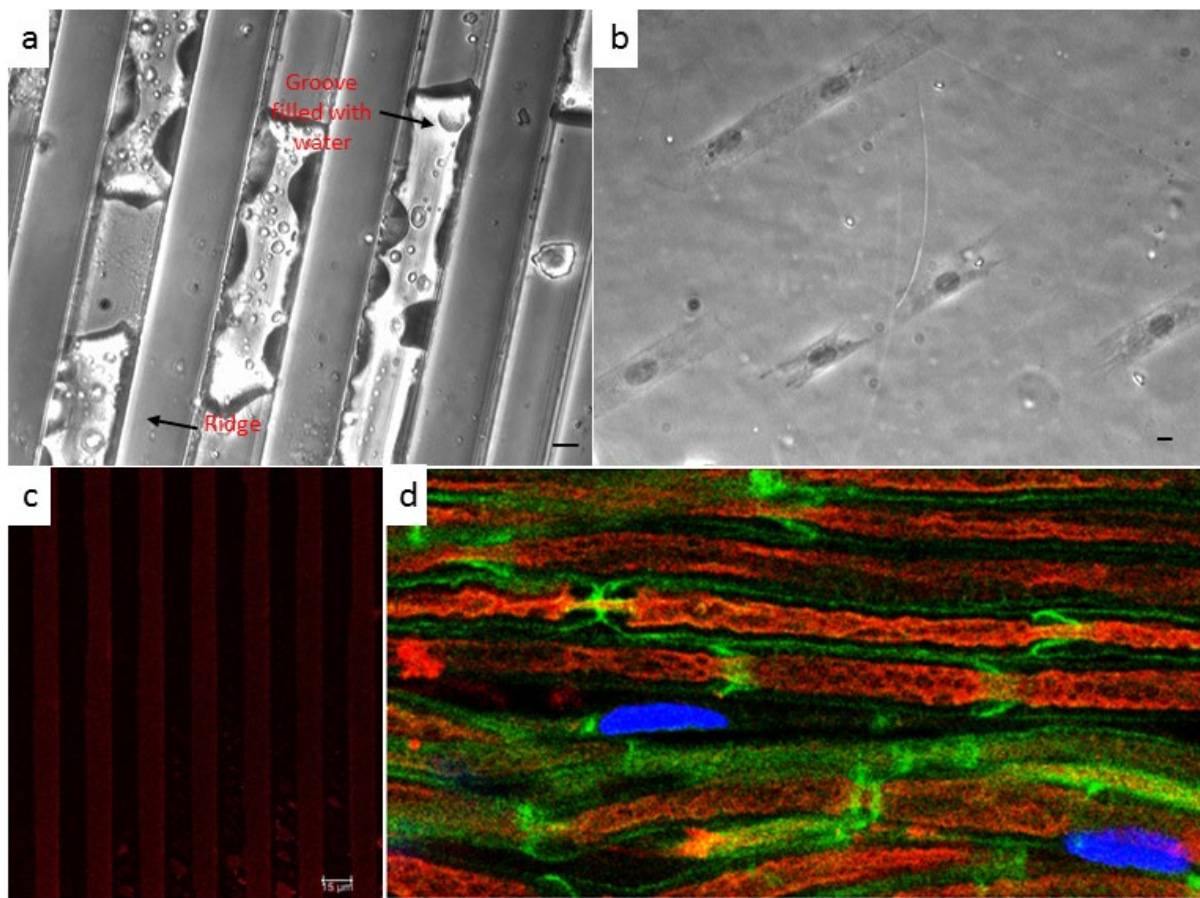


Figure 5-5: The fibronectin stripe patterns and their *in vivo* corresponding. (a) PDMS made ridge-groove patterns used to microprint the fibronectin stripes, this one is 25 μm groove with 25 μm ridge spacing. (b) Bright field micrograph of 3T3 Fibroblasts on the 25 μm fibronectin stripes spaced with 25 μm PDMS substrate. (c) The fibronectin stamp on the PDMS substrate visualized by TO-PRO-3 stain (red). (d) Fluorescent microscopy images showing *in vivo* configuration of axons (red) which are wrapped by Schwann cells (green) in sciatic nerves of mice. The nuclei of Schwann cells (blue) are elongated (Alvarez-Prats et al. 2018). Figure 5-5(a),(b)&(c) is result of my own work while Figure 5-5(d) is credited after NICHD/NIH.

When fibroblasts were seeded on the stripes, they are elongated along the major axis of the pattern (Figure 5-5(b)). On the control surface which is homogeneously coated with the fibronectin, Fibroblasts spread widely and the distance between the cell membrane and substrate varies in different parts of the cells. The RIC micrographs of spreading 3T3 which visualize this distance is consistent with the current understanding of different elements in an adhering cell (see Figure 1-9). The leading edges in the periphery of the adherent cell in RIC micrographs are darker which shows that filopodia of the cell are strongly anchored to the substrate and the cell membrane is very close to the substrate (see 2.9.4 for working principles of RIC microscopy). The distance between the substrate and the cell membrane starts to increase (RIC micrographs looks brighter) towards the centre of the cell where lamellipodium is formed. A dark ring is formed in the transition zone (the convergence of the lamellipodium and lamellum) where the focal complex anchor the cell membrane to the substrate. In the region that lamella and dorsal-ventral actomyosin bundles are formed, the distance between substrate and membrane is varying and this is evident by fluctuating image intensity of RIC micrographs in this region. In the central regions where the nucleus resides, a bright spot is observable in RIC images which shows that the cell membrane under nucleus has an almost constant distance with the substrate like a flat ground under the nucleus. This can be explained by the lack of focal complexes under the nucleus and the lower density of basal actin fibres underneath the nucleus (Figure 5-6(c)). It has been shown that basal fibres under the nucleus insert localized pressure to pull down the nucleus towards the substrate (Hanson et al. 2015c) (see Figure 3-7(d)). On narrow patterns, we observe an almost constant distance between the cell membrane and the substrate visualized by a bright profile in the RIC micrograph (Figure 5-6(a), lower panel). However, relatively dark parts are visible at two ends of the cell on the pattern where thin filopodia are formed. The filopodia are more visible in the regions that the cells locally escape the pattern and spread out of the pattern.

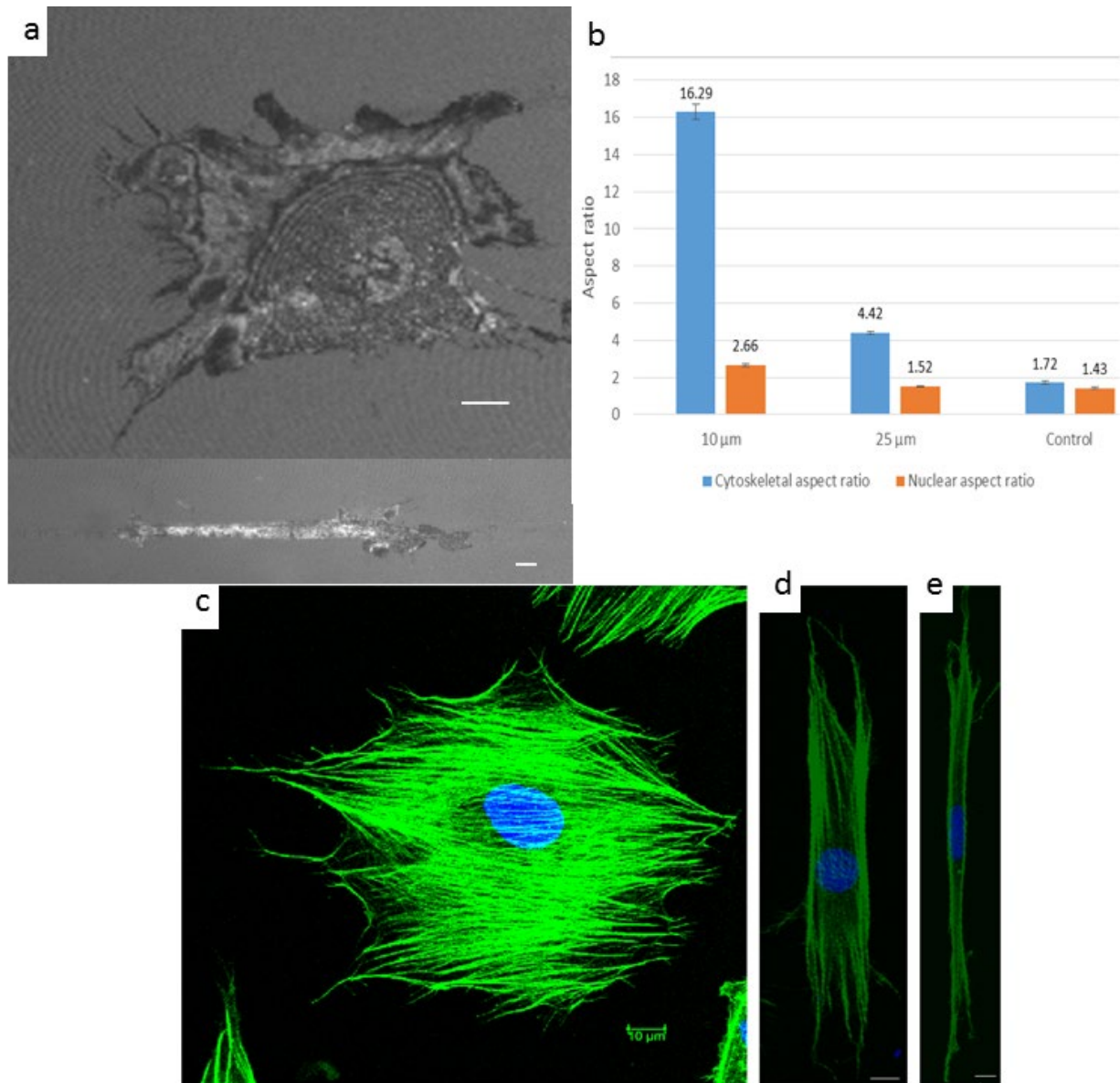


Figure 5-6: The fibronectin stripe patterns and morphological effects of them on the NIH/3T3 fibroblasts. (a) Upper panel is a RIC micrograph of a 3T3 Fibroblast on the evenly coated PDMS with fibronectin and lower panel is a RIC micrograph of a 3T3 fibroblast on the 10 μm fibronectin stripe. (b) The aspect ratio of nucleus and actin cytoskeleton on 10 μm ($n=83$, $n_{\text{nucleus}}=77$), 25 μm ($n=79$, $n_{\text{nucleus}}=82$) fibronectin stripes and evenly fibronectin coated control substrate ($n=81$, $n_{\text{nucleus}}=83$) on a PDMS substrate in the S-phase fixed with formaldehyde and stained with Phalloidin for F-actin (green) and TO-PRO-3 for the nucleus (blue). Error bars are SEM. (c)&(d)&(e) Fluorescence micrographs of 3T3 fibroblasts in the S-phase on PDMS substrate with even fibronectin coating (control), 25 μm and 10 μm fibronectin stripes respectively. The cells are fixed with formaldehyde and stained with Phalloidin for F-actin (green) and TO-PRO-3 for the nucleus (blue). Green and blue channels are overlaid by Image J. Scale bars are 10 μm .

The extent of confinement and elongation of the fibroblasts largely depends on the size of the stripes (Figure 5-6(a)). On an unpatterned substrate, the fibroblast is not confined and the cytoskeletal elements such as actin filaments don't have any preferred axis to align with ($AR = 1.72 \pm 0.07$ s.e.m. ($n=81$)). However, as Figure 5-1 shows, some cells elongate and migrate in random directions which change over time (Tang et al. 2015). The cells on the control substrate have an actin cytoskeleton that is covering all the projected area of the cell and the fibres are semi-orientated along the elongation axis of the cell. The actin edge bundles arcs (see 3.3 for more details) are visible at the edges of the fibroblasts and are slightly thicker compared to the actin bundles in the conventional actin stress fibres in the middle of the cell (Figure 5-6 (c)). On the 25 μm fibronectin stripes, fibroblasts are confined and cytoskeletal elements clearly align themselves with the direction of the stripe and the cell is elongated along the direction of stripes ($AR = 4.42 \pm 0.08$ s.e.m. ($n=79$)). The filopodia on the advancing edge of spreading cell, also are aligned with the patterns and are less numerous than the control cells (Figure 5-6(d)). There are clearly thicker and denser actin edge bundles in the intersection of cells and the patterns compared to the basal actin fibres in the middle of the cell. When cells are seeded on the 10 μm stripes which have a width smaller than the cell size ($17.2 \mu\text{m} \pm 0.3 \mu\text{m}$ s.e.m. ($n=119$)), the extent of elongation is greater ($AR = 16.29 \pm 0.39$ s.e.m. ($n=83$)) and the majority of actin fibres move to the edge of the cell at the border of the stripes and form a very dense straight actin edge bundle and therefore there is almost no visible well-structured basal actin fibre under the nucleus (Figure 5-6(e)).

Usually, the nuclei of the elongated cells also are elongated (S. B. Khatau et al. 2009a) due to the compressive force that is applied by actin stress fibres (Kim et al. 2015). The nuclei of fibroblasts on the control substrate with even fibronectin coating are slightly elongated ($AR: 1.43 \pm 0.04$ s.e.m. ($n=83$)). Previous studies have shown that among cells that are spread on unpatterned substrates, perinuclear actin fibres play an important role in the elongation of the nucleus (Bretscher et al. 2008). When cells are on the stripes (25 μm) with a bigger size than the nuclei of suspended cells ($13.5 \mu\text{m} \pm 0.2 \mu\text{m}$ s.e.m. ($n=142$)), the nuclei were not significantly more elongated ($AR: 1.52 \pm 0.03$ s.e.m. ($n=82$)) compared to the control cells despite the fact that the cytoskeleton is highly elongated and confined. The nuclei of fibroblasts on 10 μm which is smaller than the nucleus of fibroblasts on suspension are significantly more elongated ($AR: 2.66 \pm 0.06$ s.e.m. ($n=77$)) and are confined to the pattern compared to the control and 25 μm stripes (Figure 5-6(e)). Considering that fact that basal and perinuclear actin fibres are not densely present in the cells on 10 μm stripes, may indicate the key role of edge actin bundles in the deformation of the nucleus in highly elongated cells.

Because of the pivotal role that nuclear deformation plays in the behaviour and fate of cells, substantial interest has developed in exploring this opportunity to control the deformation using substrate topography((Hanson et al. 2015a);(Pan et al. 2012);(Badique et al. 2013)), particularly for control of proliferation and differentiation of stem cells ((Pan et al. 2012);(Yim et al. 2010);(Chalut et

al. 2010a)). More recent studies have even shown that certain topographical cues on the substrate can effectively be used to optimize the reprogramming of fibroblasts to induce neurons (Kulangara et al. 2014).

5.4 3D shape of fibroblasts on fibronectin stripes

Although 2D morphological features of adherent cells on these patterns have been well studied, due to the more complex nature of 3D microscopy, the 3D behaviour of these cells is poorly understood. We have designed a custom built setup (see Figure 2-11) which enables us to perform z-stack confocal microscopy to visualize all the body of cells on the patterns. The high precision stage control in the z-direction (10nm), leaves the diffraction-limit as the only resolution limiting factor. This is about $0.2\ \mu\text{m}$ for an objective numerical aperture (NA) of 1.4 and 488nm excitation light. With such a resolution we were easily able to visualize basal actin stress fibres (Figure 5-7(b)), nucleus region (Figure 5-7(c)) and perinuclear actin cap (Figure 5-7(d)).

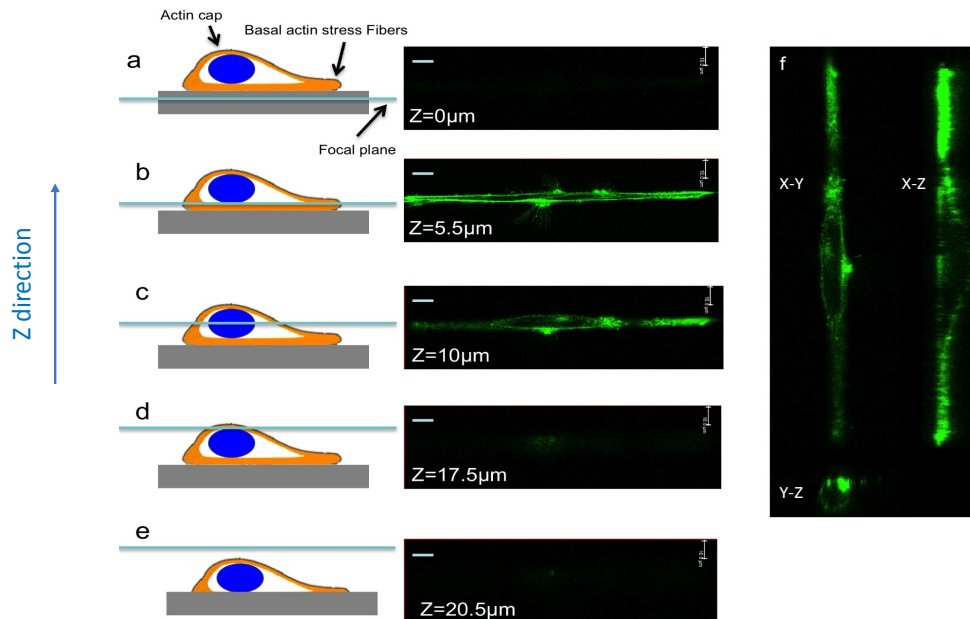


Figure 5-7: Confocal microscopy of cells on fibronectin stripes. Focal plane inside substrate (a), basal stress fibers (b) across the nucleus (c), perinuclear actin cap (d) and outside the cell(e). Cross sections of the same cell in x-y,x-z and y-z are shown (f). Scale bars are $10\ \mu\text{m}$.

5.4.1 Cell thickness measurement

One of the features that plays a critical role in cellular function *in vivo* is cellular thickness.

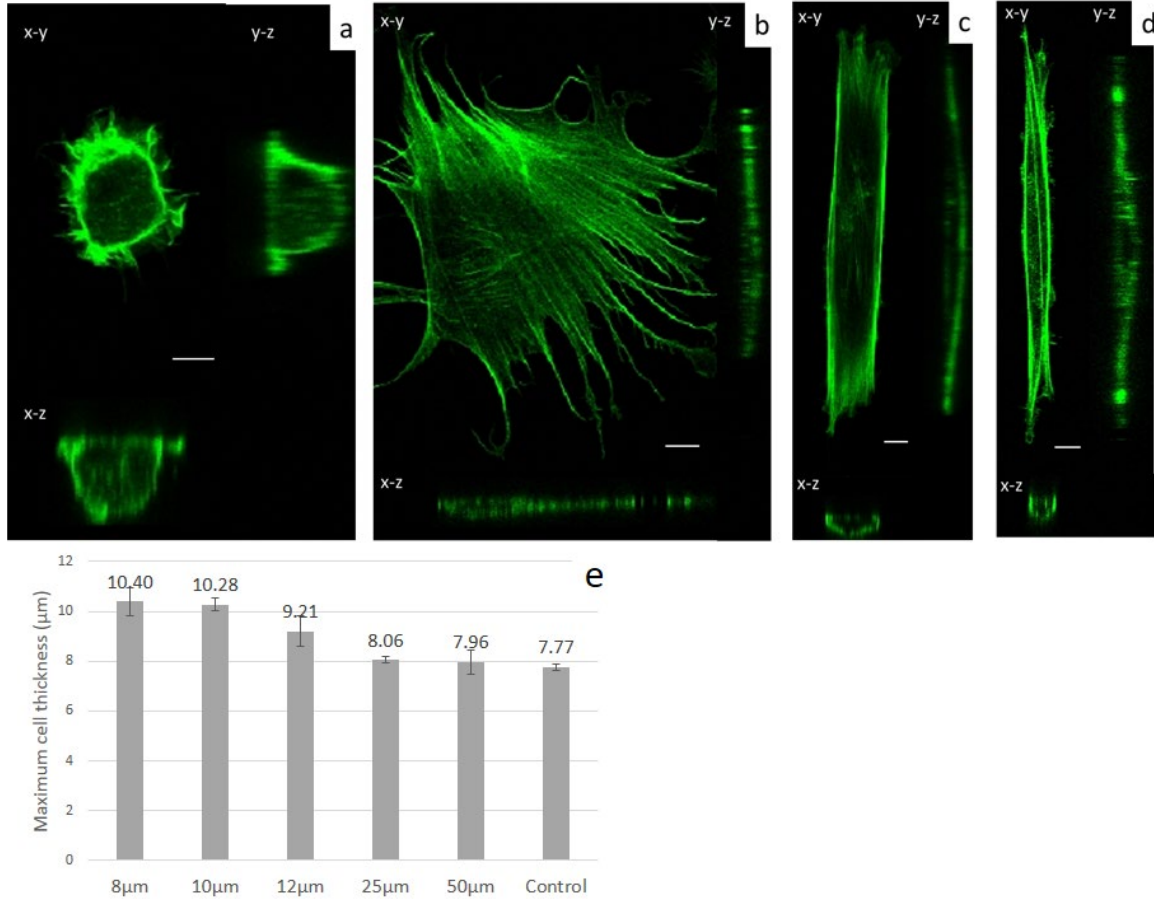


Figure 5-8: The 3D shape of fibroblasts on the fibronectin fibres with different geometry. (a) An almost unspread fibroblast on the PDMS substrate with small formed filopodia in basal x-y view and semi-spherical geometry of actin filaments in x-z and y-z cross-sections. (b) A 3D shape of fibroblast on the evenly coated fibronectin PDMS substrate in the S-phase fixed with formaldehyde and stained with Phalloidin for F-actin. (c) A 3D shape of fibroblast on a 25 μm fibronectin stripe on PDMS substrate. (d) A 3D shape of a fibroblast on a 10 μm fibronectin stripe on PDMS substrate. (e) Maximum cell thickness among 3T3 cells spreading on 8 μm (n=11 (spacing of 8 μm), 10 μm (n=79) (spacing of 80 μm), 12 μm (n=15) (spacing of 12 μm), 25 μm (n=83) (spacing of 50 μm) and 50 μm (n=33) (spacing of 50 μm) fibronectin stripes and evenly fibronectin-coated control substrate (n=87) on a PDMS substrate in the S-phase fixed with formaldehyde and stained with Phalloidin for F-actin. In our low seeding density and after washing away fixation and staining steps, few cells were observed to bridge the patterns or spread on uncoated PDMS and were not imaged. Error bars are SEM. Scale bars are 10 μm .

Cells don't function as a single layer of 2D sheets inside tissues; however, it is layer upon layer of the cells that form tissues and organs in the functioning body. As cells build up layers on top of each other, the dynamics of cellular thickness and how it depends on the substrate cues becomes important. *In vivo*, the substrate can consist of a layer of similar cells in the tissue, a layer of another formed by a different cell type in adjacent tissue, a layer of feeder cells, a substrate formed by extracellular matrix fibre proteins or even a layer of medical synthetic prosthesis or synthetic tissue embedded inside the body of a patient (see chapter 3.2). In all of these situations, understanding the dependency of cellular thickness dynamics on the underlying cue plays a vital role in understanding the whole tissue function and structure.

It has been shown that the projected area of fibroblasts adhering to the narrower fibronectin stripes, decreases significantly (Huang & Donald 2014a). Furthermore, total cellular volume and nuclear volume of fibroblasts do shrink when the cells fully spread on the substrate (Kim et al. 2015). However, a precise quantified study of the effect of adhesion on the cellular thickness and volume of cells on the fibronectin stripes pattern has not yet been performed. This is particularly important as we know that the geometry of cytoskeletal stress fibres plays a key role in deformation and bifurcation of the cell nucleus and this directly links to the gene regulatory machinery of the cell ((Kim et al. 2015);(D.-H. Kim et al. 2014b);(Hanson et al. 2015a)). As a result, it is crucial to acquire a clear 3D image of both cytoskeletal and nuclear deformation during the adhesion process in a model system as it will help us to gain a better understanding of possible gene regulatory effects of the extracellular microenvironment.

Figure 5-8 (e) shows the dependence of cell thickness on stripes of different width as well as a uniform control surface. This figure shows that the cell thickness in cells seeded on narrower fibronectin stripes (8 μm , 10 μm and 12 μm) is consistently higher than on wider stripes (25 μm , 50 μm and evenly fibronectin-coated substrate as the control). As it is expected and figure 5-8 shows, the maximum thickness in the cell happens in the region of the cell in which the nucleus resides. The nucleus is the stiffest organelle inside the cell and acts as a stiff ball in the middle of the cell that force-bearing elements of the cytoplasm help to regulate its shape (see chapter 1.4 for details). Therefore, to have a better insight into how different stripe sizes may change the maximum thickness of the cell, we need to know which forces are acting on the nucleus. Based on these results, we selected 10 μm , 25 μm and control patterns as representatives for three possible categories of (confined nucleus, confined cytoplasm), (non-confined nucleus, confined cytoplasm) and (non-confined nucleus, non-confined cytoplasm) in the rest of this study.

The forces that are exerted on the nucleus are either from conventional basal stress fibres or are from actin cap stress fibres ((Hanson et al. 2015b),(S. B. Khatau et al. 2009b)). Conventional stress fibres are terminated by conventional focal adhesions (FA) complexes whereas actin cap stress fibres are

terminated with actin cap associated fibres (ACAFs)(Kim et al. 2012). Actin cap stress fibres are composed of contractile bundles of actin filaments that are interconnected with phosphorylated myosin and α -actinin (D.-H. Kim et al. 2014a). These fibres are anchored to the top of the nucleus (Figure 5-9(b)) and physically connected to the nucleus through the linker of nucleoskeleton and cytoskeleton (LINC) complexes (Rothballer et al. 2013) and they, therefore, play a crucial role in nuclear deformation and transducing mechanical signals to the nucleus (D.-H. Kim, Allison B Chambliss, et al. 2013). In fact, among adherent cells, nuclear deformation is mainly governed by perinuclear actin contractile fibres rather than conventional basal stress fibres (Tamiello et al. 2015). It has been shown that for a significant proportion of the time, the actin cap is highly organized and elongated and strongly coupled to the nucleus; however for a small proportion of the time, the actin cap can be decoupled from the nucleus, allowing the nucleus to rotate and facilitate a migrating cell to re-orient itself in a new migratory direction (D.-H. Kim et al. 2014a).

The relation between deformation of the nucleus and the forces that are exerted on the nucleus is described by equation 5-2:

$$\frac{\sigma_{zz}}{\varepsilon_{zz}} = \frac{\frac{F_z}{A}}{\frac{d-d_0}{d_0}} = E \quad \text{Equation 5-2}$$

Where σ_{zz} is the applied vertical stress, ε_{zz} is the strain in the vertical direction, E is Young's modulus of the nucleus, F_z is the vertical component of applied force, A is the area on which F_z is applied, d_0 is the original vertical length of the nucleus, and d is the deformed nuclear vertical length.

Both modelling and traction force experiments have shown that actin cap contractile fibres can exert forces of the order of ~1-100 nN on the nucleus of adherent fibroblast cells ((Munevar et al. 2001),(Kim et al. 2015),(Sabass et al. 2008)). Considering the nuclear area of ~200 μm^2 (the nuclear-projected area of detached cells is $142 \mu\text{m}^2 \pm 5 \mu\text{m}^2$ s.e.m. (n=142) and projected area of the nuclei of fibroblasts on evenly coated fibronectin stripes is $322 \mu\text{m}^2 \pm 17 \mu\text{m}^2$ s.e.m. (n=94) (see Figure 5-15(b)), the perinuclear actin stress fibres can exert an effective pressure in the order of ~1kPa which is enough to regulate the shape of a fibroblast nucleus with an approximate Young's modulus of the order of ~1-10 kPa (Ferrera et al. 2014) considering that $\varepsilon_{zz} = \frac{d-d_0}{d_0} = \frac{13.5 \mu\text{m} - 7.77 \mu\text{m}}{13.5 \mu\text{m}} \approx 0.5$ (assuming the diameter of detached nuclei which is $13.5 \mu\text{m} \pm 0.2 \mu\text{m}$ s.e.m. (n=142) as the original vertical length of the nucleus and thickness of the fibroblasts on unpatterned control substrate ($7.77 \mu\text{m} \pm 0.13 \mu\text{m}$ s.e.m. (n=87)) as an estimation for vertical length of the deformed nucleus.)

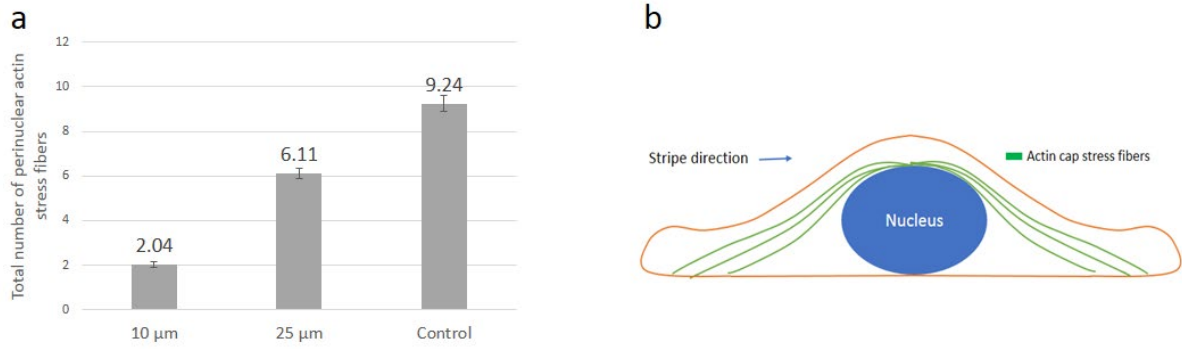


Figure 5-9: Perinuclear actin stress fibers of 3T3 fibroblasts on fibronectin patterns. (a) The total number of perinuclear actin stress fibres among 3T3 cells spreading on 10 μm (n=79), 25 μm (n=83) and fibronectin stripes and evenly fibronectin coated control substrate (n=87) on a PDMS substrate in the S-phase fixed with formaldehyde and stained with Phalloidin for F-actin. Error bars are SEM. (b) Schematic image showing the position of perinuclear actin cap stress fibres in a schematic cross-section of the cell.

To further explore the role of perinuclear actin stress fibres in determining cellular thickness adhering to different stripes, we counted the number of these fibres in each group of cells stained for filamentous actin (Figure 5-10).

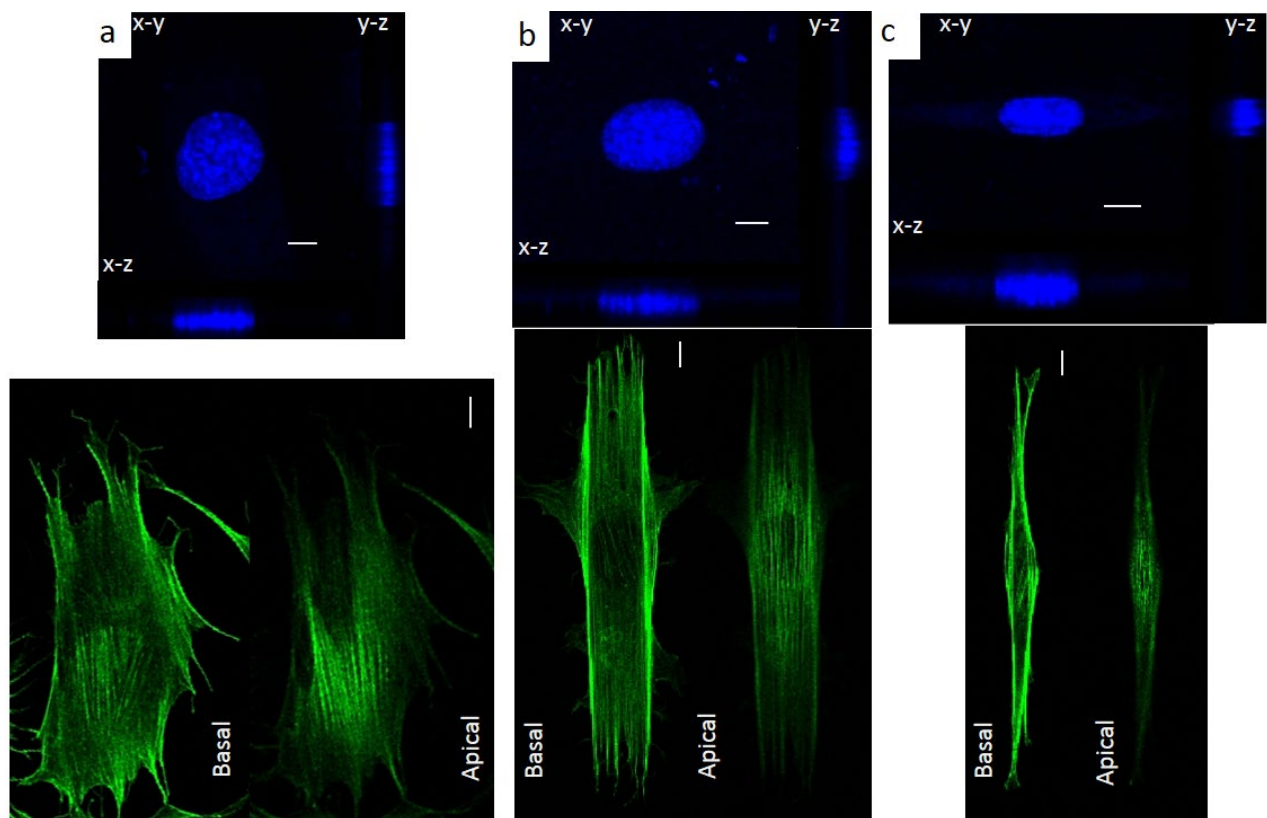


Figure 5-10: The 3D shape of the nucleus and organization of actin stress fibres of fibroblasts on the fibronectin stripes. (a)(b)&(c) upper panels: 3D fluorescence confocal micrographs of 3T3 fibroblast spreading on PDMS substrate evenly coated with fibronectin (control), 25 μm and 10 μm fibronectin stripes respectively. The nucleus is stained with TO-PRO-3 and false coloured blue. Lower panels: focal plane on basal surface reveals conventional basal stress fibres; whereas, focus on the apical plane on top of nucleus reveals highly organized perinuclear actin cap stress fibres among corresponding 3T3 fibroblast cells on control (a) and, 25 μm (b) and 10 μm (c) fibronectin stripes. The actin fibres are stained with phalloidin and false coloured green. Scale bars are 10 μm .

Figure 5-9 (a) shows that cells seeded on narrower 10 μm stripes have only about 20% of such contractile fibres compared to the cells spreading on control fibronectin-coated substrate. The fibres can be seen in Figure 5-10 (c), while cells on wider 25 μm stripes (Figure 5-10(b)) demonstrate almost about 65% of actin cap stress fibres were formed compared to cells adhering to the control fibronectin substrate. As 3D fluorescent micrographs of figure 5-10 shows, more perinuclear actin stress fibres on the nucleus of cells spreading on wider stripes flattens the nucleus further and therefore reduces the thickness of the cells. Among cells spreading on control fibronectin-coated substrates, we can clearly see the presence of semi-organized basal actin filaments under nucleus of fibroblasts on control substrate while they disappear as the cells elongated on the stripes which rule out their possible role in the regulation of nuclear shape on the stripes.

It is possible to conclude that in unpolarised adhering cells on the evenly coated substrates, conventional basal stress fibres terminated by FA (yellow) at the cell area and are not well organized; however, actin cap associated stress fibres terminated by ACAFAs (red) at the periphery of the adherent cell and are highly organized (Figure 5-11 (a)). However, in cells that are spreading on stripes, both conventional basal fibres and actin cap associated stress fibres are well organized and elongated in the direction of cell cytoskeleton (orange) and nucleus (blue) (Figure 5-11(b)). As Figure 5-11 reveals, actin bundles (brown) arcs are homogeneously present in the edges of cells on control substrate whereas in cells spreading on fibronectin stripes actin edge bundles are not present in the edges of the cells that are perpendicular to the pattern direction and are very thick in the periphery of the cell in direction of patterns.

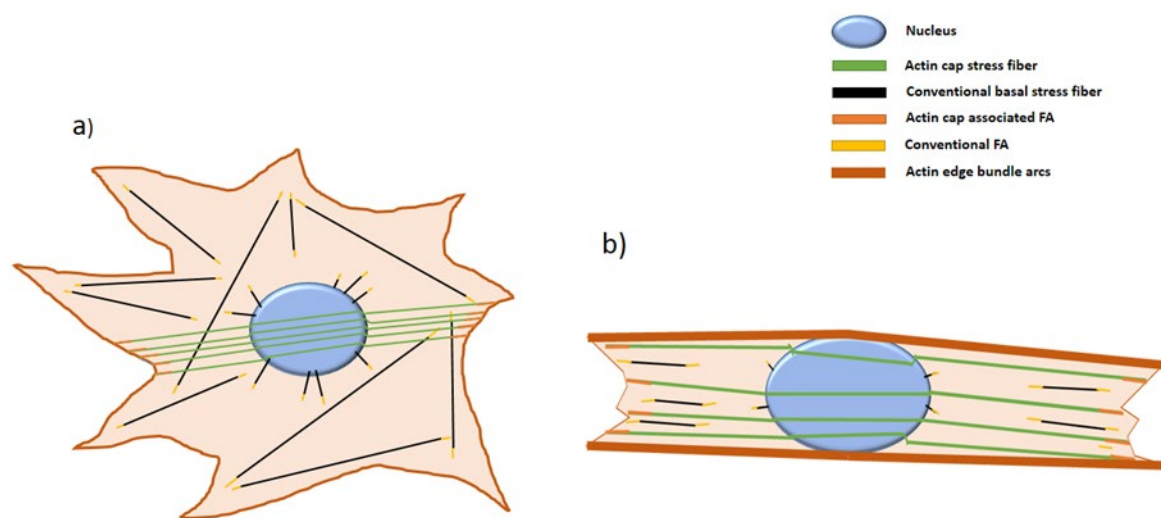


Figure 5-11: Schematic of the configuration of actin fibres and associated focal adhesions in adherent cells. (a) Schematic of stress fibres configuration in an unpolarised adhering cell spreading on a symmetrical unpatterned substrate. Figure 5-11(a) is inspired by (D.-H. Kim, Allison B. Chambliss, et al. 2013). (b) Schematic of stress fibres configuration in a polarized adherent cell elongated on a fibronectin stripe.

5.4.2 Volume regulation of the fibroblasts on fibronectin stripes

5.4.2.1 Cellular volume

The volume of cells is a critical parameter in the determination of organ and tissue morphology and therefore in the main function of living organisms. A cell's ability to regulate its volume plays a central role in cell function. Volume regulation gives the cell protective and adaptive advantages by

allowing cytoskeletal rearrangements (Hoffmann et al. 2009). In addition, changes in cellular volume trigger signalling pathways for cell proliferation, death, and migration (Jiang & Sun 2013). Vertebrate cells, with a few exceptions, are permeable to water and lack the stiff cellular wall of plants and bacteria (Hoffmann et al. 2009). The cell volume is controlled by the interplay of membrane tension, active contractility and water/ion influx (Jiang & Sun 2013). It has been shown previously that adherent mouse embryonic fibroblasts have a bigger volume compared to detached cells (Kim et al. 2015).

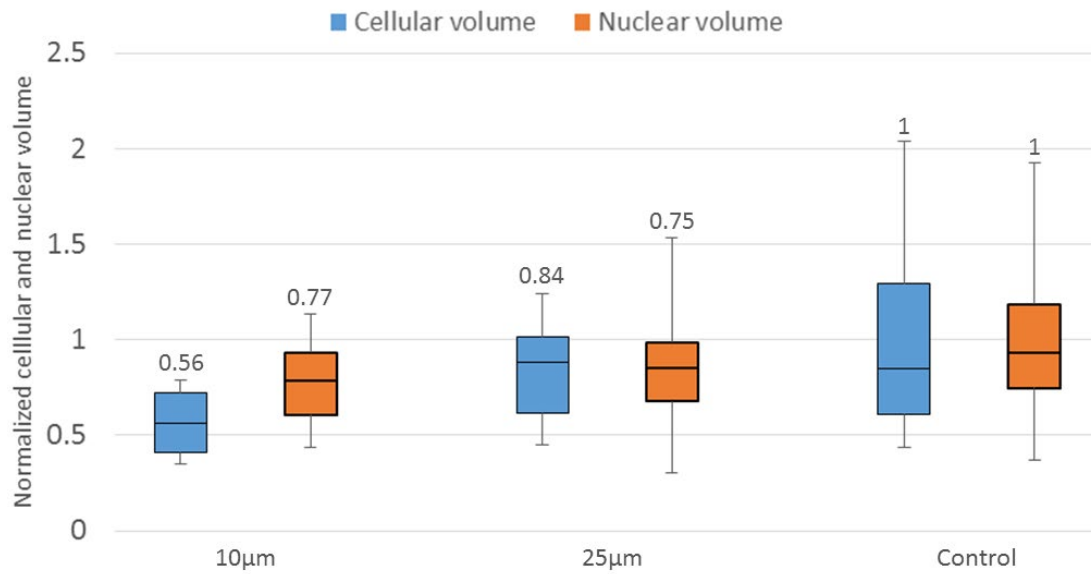


Figure 5-12: Cellular and nuclear volume change on fibronectin stripes. Plot box of relative volume of the fibroblasts (blue) and their nuclei (orange) on 10µm ($n=81$, $n_{\text{nucleus}}=82$), 25µm ($n=79$, $n_{\text{nucleus}}=84$) and fibronectin stripes and evenly fibronectin coated control substrate ($n=82$, $n_{\text{nucleus}}=91$) on a PDMS substrate in the S-phase fixed with formaldehyde and stained with phalloidin for F-actin and nucleus is stained with and TO-PRO-3 for 3D confocal fluorescent microscopy. Average value of each box are shown on top of the box.

Our results based on 3D fluorescent microscopy of the cells (see 2.7.3 for details of the method) shows that the volume of the cell in the steady state phase of adhesion (S-phase) (see 5.2 for details) on fibronectin stripes is dependent on the width of the stripe. The volume of the cells that spread on narrower 10 µm stripes ($2.6^\circ \pm 5.1^\circ$ s.e.m, ($n=81$)). is ~ 40% smaller compared to cells that adhere to unpatterned fibronectin-coated control substrate (Figure 5-12). The cellular volume on wider 25 µm stripes is ~15% smaller compared to unpatented control cells which shows that as the patterns get wider, the cellular volume becomes comparable to that of cells adhering to unpatterned fibronectin-coated surfaces.

It is well known that actin polymerizing is the main force driving morphological changes during cell spreading in the adhesion process (J Thomas Parsons et al. 2010b). We hypothesize that confining

cells to the patterns inhibits this actin polymerization process in the perpendicular direction to the stripe's direction and this way, reduces the total cellular volume.

5.4.2.2 Nuclear volume

The nucleus is the stiffest and largest organelle in eukaryotic cells and contains most of the genetic information of the cell (Dahl, Alexandre J S Ribeiro, et al. 2008a). It is the site for the major functions of a cell such as DNA replication, transcriptional regulation, and RNA processing and ribosome maturation (Kim et al. 2015). The lamina envelope of the nucleus is coupled with the cytoskeleton via a series of binding proteins to the actin and intermediate filaments (Herrmann et al. 2007). Therefore, the intracellular and extracellular forces affect the shape and structure of the nucleus and inevitably the cell signalling and gene transcription. In most of the eukaryotic cells, the nuclear volume and cytoplasmic volume are usually related and the ratio of nuclear volume to cytoplasmic ratio is called karyoplasmic ratio (Webster, Keren L. Witkin, et al. 2009). Cancer cells usually have disrupted karyoplasmic ratio by having unusually big or small nuclei which is suggested that gives them an advantage for metastatic invasion (Rizzotto & Schirmer 2017). It has been shown that cytoskeletal motors and actin stress fibers actively control the nucleus shape (Kim et al. 2015). Cytoplasmic mechanical forces and pressure difference across the nuclear envelope can change the nuclear volume of adherent cells (Kim et al. 2015). It has been shown that the substrate topography and stiffness can deform the nucleus (Hanson et al. 2015b), (Badique et al. 2013)).

Our results show that the volume of nuclei of the cells that adhere to the fibronectin stripes is ~ 25% smaller than the cells that adhere to unpatterned fibronectin-coated control substrates (Figure 5-12). However, the width of fibronectin stripes did not affect the nuclear volume considerably despite the clear morphological differences that we observed before such as difference in the nuclear aspect ratio of cells that adhere to 10 μm and 25 μm stripes. (Figure 5-6(b)). We think that this results from the fact that the force from basal contractile actin fibres has more effect on nucleus volume (Hanson et al. 2015b) and these fibres might act similarly on the patterns with different sizes as we observed few actin fibers in the central part of the cell where the nucleus resides among both cells that adhere to 10 μm and 25 μm stripes (Figure 5-8 (c)&(d), basal focus plane).

We also suspect that differences in the distribution of the cell cycle for different patterns can play a role in this result as we came across more dividing cells adhering to the control substrate. Previous studies have shown that cell volume change in different cell cycles and almost doubles during interphase of dividing cells (Maeshima et al. 2011). Unfortunately, it was not always easy to distinguish a dividing nucleus from a slightly elongated one. Furthermore, our staining was not

sufficient to correlate nuclear volume with the cell cycle. We think that further studies are needed to understand how the fibronectin stripes might affect the cell cycle (see chapter 8.2 for more).

5.5 Fibroblasts on sub-nuclear fibronectin stripes

5.5.1 Morphological features of the Fibroblasts on sub-nuclear stripes

In previous experiments, we studied the effect of fibronectin stripes that were bigger or comparable to the size of the nucleus of fibroblasts so that the nuclei either fully confined to the stripes or did not sense the stripes directly. To examine to what extent the nucleus of cells can elongate, we fabricated fibronectin stripes with a size of 5 μm (with a spacing of 11 μm) which is about 1/3 of the suspended nuclear size of a fibroblast. We call these “sub-nuclear” stripes as their size is smaller than the nucleus. Fibroblasts were seeded on the patterns and were given the same time (200 minutes) to spread on the patterns that were given to fibroblasts on fibronectin-coated substrates to reach the steady-state phase of adhesion (s-phase). Cells on this pattern of stripes showed three major morphologies: 1- some fibroblasts were almost not responding (confining in any extent) to the patterns and are spreading on the patterns as if they are on an evenly coated substrate (Figure 5-13(a)), 2- some fibroblasts are elongated along the stripes and confined to the patterns to a large extent (Figure 5-13(b)) and 3- the third group of fibroblasts were partially confined to the patterns mostly through the filopodia of the leading edge of the spreading cell while the main body of the cell in centre is not confined to one particular stripe and bridges over several adjacent stripes (Figure 5-13(c)).

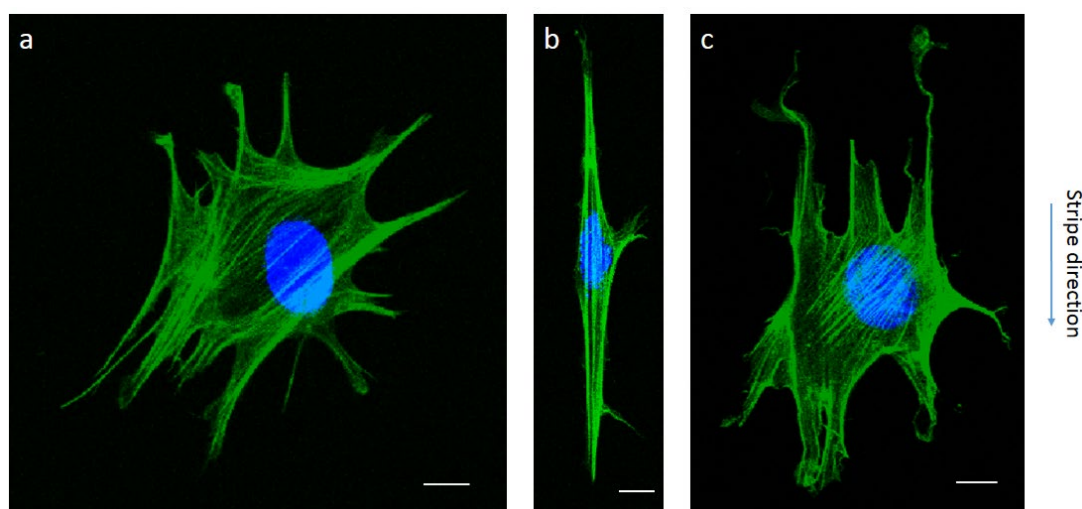


Figure 5-13: Fluorescent micrographs of different morphology of 3T3 fibroblasts on a sub-nuclear fibronectin pattern of stripes. (a) The cell is mostly not confined to the stripes. (b) The cell that confines to the pattern and is highly elongated along the stripes. (c) The filopodia in the leading edge of spreading cell are confined and elongated along the stripes and the main body of the cell in middles bridges over several stripes. The actin cytoskeleton of hMSCs is stained with phalloidin and false coloured in green and the nucleus is stained with TO-PRO-3 (false coloured in blue). Green and blue channels are overlaid by Image J. Scale bars are 10 μm .

The histogram of cytoskeletal aspect ratio also shows three classes of cells (Figure 5-14(a)). The majority of cells are almost not elongated by the patterns and so in other words, are minimally confining to the patterns. A group of cells are partly elongated along the fibronectin stripes and are partially confined to the patterns. A small group of the cells are highly elongated along the patterns and confined to the stripes. When we look at the histogram of the nuclear aspect ratio (Figure 5-14(b)), we see almost the same categories of fibroblasts. However, we see a bigger fraction of nuclei that is partly elongated and confined to the patterns. Furthermore, the populations of minimally elongated nuclei and partially elongated nuclei are more overlapping. The average aspect ratio values show that overall both the cytoskeleton and nucleus of fibroblasts on sub-nuclear stripe patterns are more elongated compared to the fibroblasts on evenly fibronectin coated control substrates, a result which confirms that patterns affect the cells and nuclei (Figure 5-14(c)). This increase in elongation is more significant in the cell cytoskeleton ($\sim 50\%$) compared to the nuclear elongation ($\sim 10\%$). However, we generally observe less elongation of the nucleus compared to the cytoskeleton in previous 10 μm and 25 μm stripes (Figure 5-6(b)). The elongation of the cytoskeleton of cells on the sub-nuclear stripe pattern is less significant compared to bigger patterns such as 10 μm and 25 μm which confine the cells to a larger extent. However, the nucleus elongation on the sub-nuclear stripe pattern is only slightly more compared to 25 μm stripe ($\sim 5\%$) where the nucleus almost doesn't touch

the pattern edges (Figure 5-6 (d)) and is significantly less (~40%) compared to the 10 μm which confine the nucleus in a bigger extent (Figure 5-6(e)).

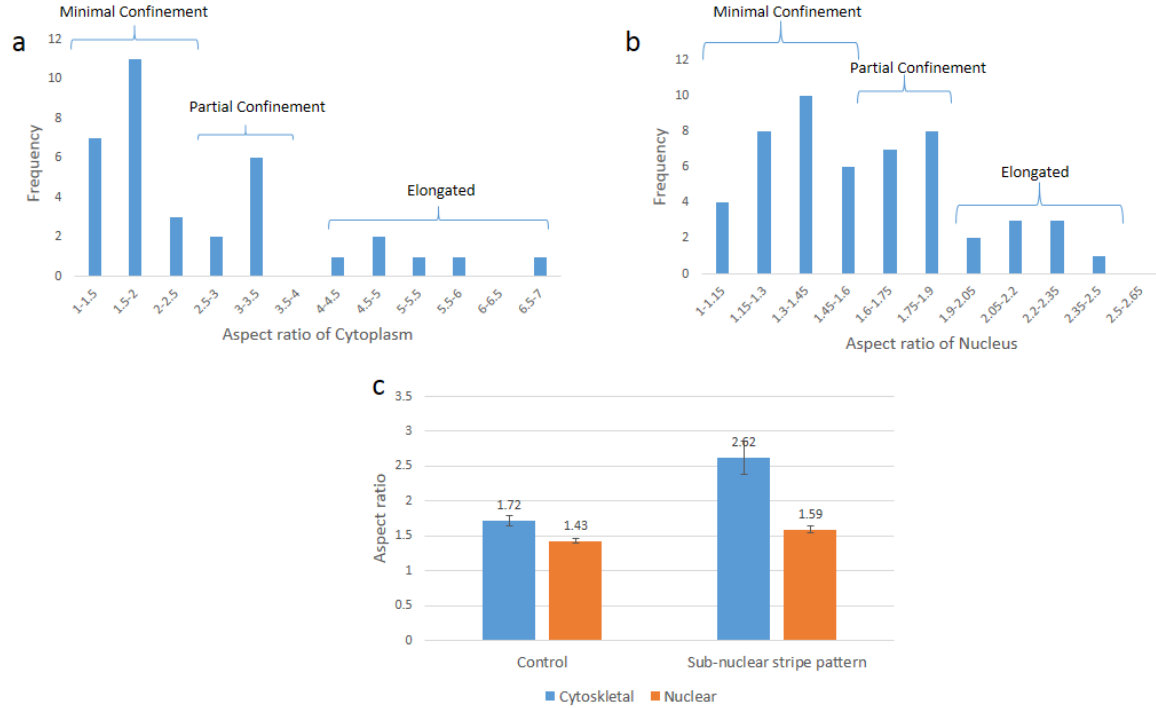


Figure 5-14: The aspect ratio of 3T3 fibroblasts on the sub-nuclear pattern. (a) The histogram of cytoskeletal aspect ratio on the patterns (n=35) showing three major categories minimally confined, partially confined and elongated fibroblasts. (b) The histogram of nuclear aspect ratio on the patterns (n=52). (c) The average cytoskeletal and nuclear aspect ratio of fibroblasts on evenly fibronectin-coated (control) ($n_{\text{cytoskeleton}}=81$, $n_{\text{nucleus}}=83$) and on the sub-nuclear pattern ($n_{\text{cytoskeleton}}=35$, $n_{\text{nucleus}}=52$). Error bars are s.e.m.

The PDMS substrate that is not coated with an ECM protein such as fibronectin is not very biocompatible which means that it is not favourable for adherent cells and largely inhibits cell spreading (Figure 5-8(a)). Studies have shown that the high surface hydrophobicity of PDMS is the main cause for the poor cell adhesion on the PDMS substrates (Chuah et al. 2016). Therefore it is expected that on the sub-nuclear stripe pattern which almost 70% of its total consists of uncoated PDMS will reduce the projected area of the spreading cells. Figure 5-15 (a) shows that fibroblasts on the sub-nuclear stripe pattern spread only to half the area that they spread on PDMS substrate that is evenly coated with the equal concentration of fibronectin. This shows that despite the fact that majority of cells were able to bridge over the uncoated PDMS stripes and reach to fibronectin-coated

stripes on sub-nuclear patterns, the total spreading potential of them to spread is largely inhibited. On the other hand, the projected area of the nuclei of fibroblasts on sub-nuclear stripes pattern was only slightly lower (~8%) compared to fibroblasts on evenly fibronectin-coated substrates (Figure 5-15(b)). The nucleus is not in direct contact with the substrate and its shape is regulated by mostly actin force bearing fibres which is largely present among the fibroblasts on sub-nuclear stripes pattern (Figure 5-13). Furthermore, the actin edge bundles which limit the spreading of the nucleus on patterns such 10 μm (Figure 5-6(e)) are only present in a small fraction of highly elongated fibroblasts on the sub-nuclear stripes pattern (Figure 5-13 (b)).

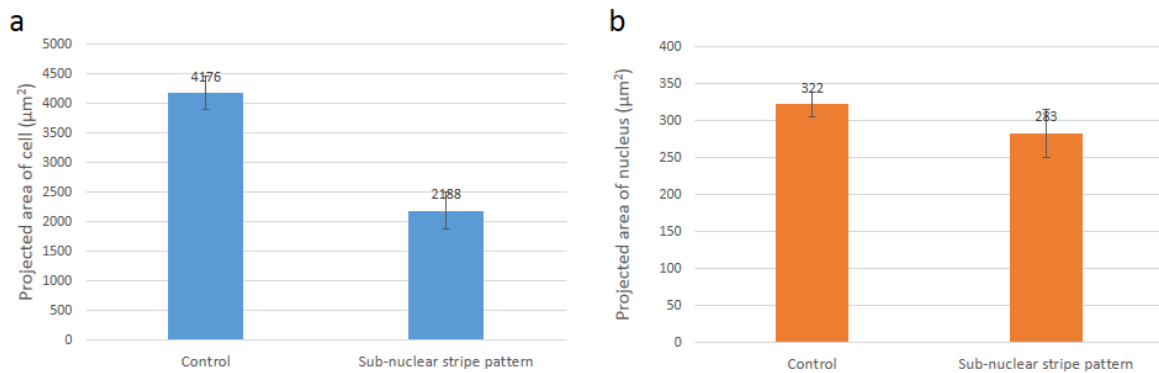


Figure 5-15: Projected area of 3T3 Fibroblasts on sub-nuclear pattern and control substrate. (a) The projected area of the cytoskeleton on the sub-nuclear stripe pattern (n=35) and fibronectin-coated control (n=65). **(b)** The projected area of the nucleus on the sub-nuclear stripe pattern (n=52) and fibronectin-coated control (n=94). Error bars are s.e.m.

5.5.2 Orientation of the Fibroblasts on sub-nuclear stripes

Sub-nuclear stripes impose a directional anisotropy on the substrate and therefore it is sensible to ask to what extent this anisotropy is imposed on the cells on the pattern. One way of studying the anisotropy among the cells on the pattern is to measure how the orientation of the cell cytoskeleton and nucleus is aligned with the direction of substrate patterns (Chalut et al. 2010b)(Clark et al. 1990)(Fujita et al. 2009).

To measure this, we fit the best fit ellipse to the nucleus and cell and measure the angle between the major axis of the fitted ellipse with the direction of stripes. We call this the deviation angle and show it as Θ . Figure 5-16 (a) shows the scatter of the deviation angles across the different cells. As it is expected, the angle is very symmetric to the pattern direction and therefore the average angle is close to zero ($\Theta_{\text{average}} = -2.6^\circ \pm 5.1^\circ$ s.e.m, (n=35)). However, when we look at the absolute value of Θ , we

can see more deviation from the direction of the stripes ($|\Theta|_{\text{average}} = 14.7^\circ \pm 3.6^\circ \text{ s.e.m. (n=35)}$). The histogram of the absolute value of deviation angle shows that the sub-nuclear stripes impose an anisotropy on the cells directionality and align them to the direction of the stripes (Figure 5-16 (b)). 50% of the cells are deviated from the direction of the stripes by less than 10° ($|\Theta| < 10^\circ$) while the percentage of the cells that are aligned with the stripes with deviation angle smaller than 20° is $\sim 66\%$ (Figure 5-16(b)).

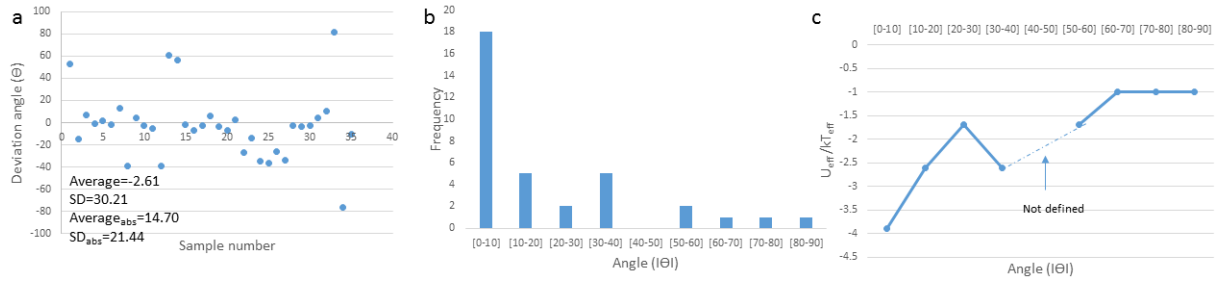


Figure 5-16: The orientation of 3T3 fibroblasts on the sub-nuclear stripes pattern. (a) The orientation of fibroblasts in respect to the direction of stripes ($n=35$) and average and standard deviation (SD) for the deviation angle (Θ) and its absolute value. **(b)** Histogram of the absolute deviation angle distribution ($|\Theta|$) of fibroblasts on the patterns. **(c)** Effective potential energy curve calculated using 5-16(b), the energy axis was shifted down by -1 in order to achieve better illustration.

From an energy point of view, the subnuclear stripe patterns create an effective potential energy (U_{eff}) that helps align the cells with the direction of patterns. There are multiple force bearing elements inside the cell; however, actomyosin-mediated contractility is the main source of the mechanical force inside the cell that generates this potential energy (Murrell et al. 2015).

To calculate the shape of the effective potential energy curve, we consider our system as a classical discrete system. Although our system is not a thermal system; however, our system can be analogous to a thermal system with an effective temperature (T_{eff}) instead of ambient temperature (T).

P_i denotes the probability of the system in the i th microstate (i th bin in the histogram of absolute value of deviation angle (Figure 5-16(b)) which as given in Equation 5-3 can be calculated by the ratio of the number of cells in the i th bin of histogram (n_i) to total number of cells in the histogram (N). If we assume that all attainable microstates of the system are equally probable, it can be shown that P_i is proportional to the $e^{-\beta E_i}$ where $\beta = \frac{1}{k_B T_{eff}}$ (k_B is the Boltzmann constant and T is the temperature) and E_i is energy of the the system in the respective microstate (Shell 2015).

$$P_i = \frac{n_i}{N} = A e^{-\beta E_i}$$

Equation 5-3

Since the sum of probabilities of all microstates should be equal to 1, we can calculate the constant A according to Equation 5-4 where Z is called the canonical partition function.

$$\sum_i p_i = \sum_i \frac{n_i}{N} = 1 \quad \rightarrow \quad A = \frac{1}{\sum_i e^{-\beta E_i}} = \frac{1}{Z} \quad \text{Equation 5-4}$$

Now we can calculate E_i based on measured n_i (from the histogram of the absolute value of deviation angle, Figure 5-16(b)) as expressed in equation 5-5:

$$E_i = \frac{-\ln\left(\frac{p_i}{A}\right)}{\beta} = K T_{eff} (\ln AN - \ln n_i) = C - K T_{eff} \ln n_i, \quad C = K T_{eff} \ln AN \quad \text{Equation 5-5}$$

Using equation 5-5 and our experimental data, we calculated the shape of the effective potential curve (Figure 5-16(c)). The alignment of the cells with the stripes direction shows itself as deep well around $\Theta = 0^\circ$ in the potential energy curve (Figure 5-16(c)).

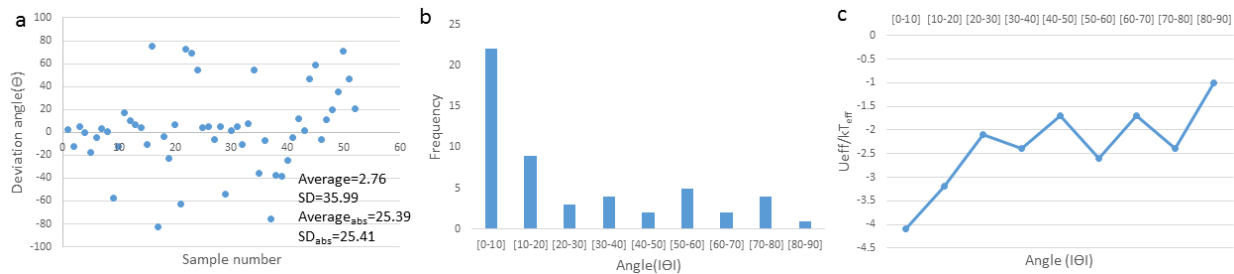


Figure 5-17: The orientation of 3T3 fibroblast nuclei on the sub-nuclear stripes pattern. (a) The orientation of fibroblast nuclei with respect to the direction of stripes ($n=52$) and average and standard deviation (SD) for the deviation angle (Θ) and its absolute value. **(b)** Histogram of the absolute deviation angle ($|\Theta|$) distribution of fibroblast nuclei on the patterns. **(c)** Effective potential energy curve calculated using 5-17(b), the energy axis was shifted down by -1 in order to achieve better illustration.

When we look at the deviation angle of fibroblast nuclei (Figure 5-17(a)), we again observe that a majority of nuclei of fibroblasts on sub-nuclear patterns are aligned with the direction of fibronectin stripes. However, the alignment of nuclei is slightly weaker in comparison to the alignment of the cytoskeleton of fibroblasts ($\Theta_{\text{average}} = 2.76^\circ \pm 4.99^\circ$ s.e.m, $|\Theta|_{\text{average}} = 25.39^\circ \pm 3.52^\circ$ s.e.m, ($n=52$)). ~42% of the nuclei deviate by less than 10° relative to the pattern direction and ~60% of nuclei deviate less than 20° from the direction of stripes. As mentioned earlier, the orientation of the nucleus in adherent cells is governed mostly by force-bearing actin filaments in the cytoskeleton and therefore we hypothesize that nuclear orientation is a secondary function of stripe orientation. In other words, cell cytoskeleton primarily contacts the stripes and aligns itself with them. This followed by a subsequent step when the aligned force-bearing actin filaments in the cytoskeleton exert an effective torque on the nucleus that rotates it along the direction of stripes. As Figure 5-6(d) & (e) shows, thick

edge actin bundles on 10 μm or 25 μm stripes are in touch or very close to the nucleus and effectively align the nucleus to the cytoskeleton and subsequently to the stripes. However, minimally confined or partially confined branched cells on the patterns which make the majority of the cells on subnuclear stripes pattern (Figure 5-14(a)) don't form actin edge bundles that touch the nucleus and align it with the direction of the stripes. Furthermore, as Figure 5-13 shows, there is not a perfect alignment between actin cytoskeleton of the fibroblasts and the stripes as it was among the cells on 10 μm or 25 μm stripes. Therefore, we think that these two factors, reduce the effectiveness of the cytoskeletal actin fibers in aligning of nuclei in the direction of stripes and we observed that the alignment of nuclei is slightly weaker compared to the alignment of the cytoskeleton of fibroblasts.

Chapter 6:

The impact of fibronectin stripe patterns on the cellular and nuclear morphology of mesenchymal stem cells

6.1 Mesenchymal stem cells in culture

As we discussed broadly in chapter 4, mesenchymal stem cells (MSCs) are a class of multipotent stem cells that are found in the connective tissue (mesenchyme) and bone marrow. When MSCs are exposed to suitable chemical and physical cues they differentiate mostly into cells from mesodermal lineages such as adipocytes, chondrocytes and osteocytes. Although recent studies show that they can differentiate into fibroblasts, neurons, lung cells and a wide range of muscle cells (see 4.2 for details). MSCs are widely used in stem cell research and can be isolated from different organs of an adult patient. However, the most frequent source of isolation is bone marrow. The MSCs that we used in this research were isolated from bilateral punctures of the posterior iliac crests of adult human volunteers which were screened for various possible health conditions and pathogens (see 2.1.2 for more details). Similar to fibroblasts, MSCs are adherent cells and express a heterogeneous morphology such as branched, well-spread cells (Figure 6-1(a)) or smaller spindle-shaped cells (Figure 6-1(b)) and have a visible nucleus with multiple nucleoli. In lower concentrations ($\sim 10^4$ cell/cm²), the hMSCs show a morphology similar to 3T3 fibroblasts (Figure 6-1(c)). However, when they are seeded in a high concentration ($\sim 5 \times 10^4$ cell/cm²) or reach full confluency, the proportion of spindle-shaped cells increases (Figure 6-1(d)), unlike 3T3 fibroblasts for which cells become more round and adjacent to each other (Figure 5-1(b)). In low confluency, when cells are not in contact with each other, a majority of hMSCs express a rounder shape on polystyrene culture flasks (Young's modulus ~ 3 GPa); however, there are also very elongated cells among the hMSCs ($AR_{\text{average}} = 3.3 \pm 0.24$ s.e.m) (Figure 6-1(e)). For the same hMSCs at low confluency, the spread of the aspect ratio distribution for nuclei is smaller. The majority of nuclei are slightly elongated and a minority show very elongated nuclei ($AR_{\text{average}} = 1.60 \pm 0.03$ s.e.m) (Figure 6-1(f)).

Unlike stromal cells, stem cells are prone to follow a differentiation pathway in response to chemical and physical stimuli. Therefore, in general, stem cell cultures need more gentle stress and handling techniques in order to keep them dividing symmetrically (see Figure 4-1 for details of stem cell division). The more careful handling techniques include gentle physical stress due to milder shear stress and centrifugal force during the maintenance of the culture and smaller temperature shocks during thawing of cryopreserved hMSCs (see 2.2 for more details). In addition, stem cells are more sensitive to chemical and biological agents that they are exposed to in culture and in the process of cell passages. Therefore in contrast to stromal cell lines which need classical DMEM medium enriched with foetal bovine serum (FBS) (see chapter 2.2.1 for details), hMSCs need to be cultured in an optimized medium that helps to maintain their potency to differentiate into main mesoderm lineages (see chapter 2.2.2 for more details).

The traditional buffer solutions that are used for the cell passage of stromal cell lines may have ingredients that promote the differentiation of hMSCs into a certain lineage. For example, studies have shown that magnesium chloride promotes osteogenesis of rat bone marrow-derived MSCs (Díaz-Tocados et al. 2017). Therefore to avoid the risk of unwanted differentiation, buffer solutions with chemical compositions that don't include these chemical elements (calcium chloride, magnesium chloride) are used in subculturing of hMSCs.

Trypsin is often used for dissociation of stromal adherent cells such as fibroblasts from the substrate (see chapter 5.1). However, studies have shown that trypsin is harmful for hMSCs as it degrades many surface antigens of these cells in a relatively short time after treatment (~30 minutes) while other enzymatic dissociation agents such as TrypLE which is often used for detachment of hMSCs from the substrate doesn't have same degrading effect on the surface antigens of hMSCs (Ojima et al. 2016). TrypLE is an enzyme that cleaves peptide bonds on the C-terminal sides of lysine and arginine amino acids (Tsuji et al. 2017) and therefore cuts the focal adhesions that help hMSCs to adhere to the substrate (see Figure 1-9 and Figure 1-10).

To measure the size of hMSCs in suspension, we treated the cells with TrypLE at 37°C for 5 minutes in order to detach hMSCs from the substrate. Detached hMSCs were immediately imaged while the cells are still in suspension and the adhesion process has not started (Figure 6-2(a)).

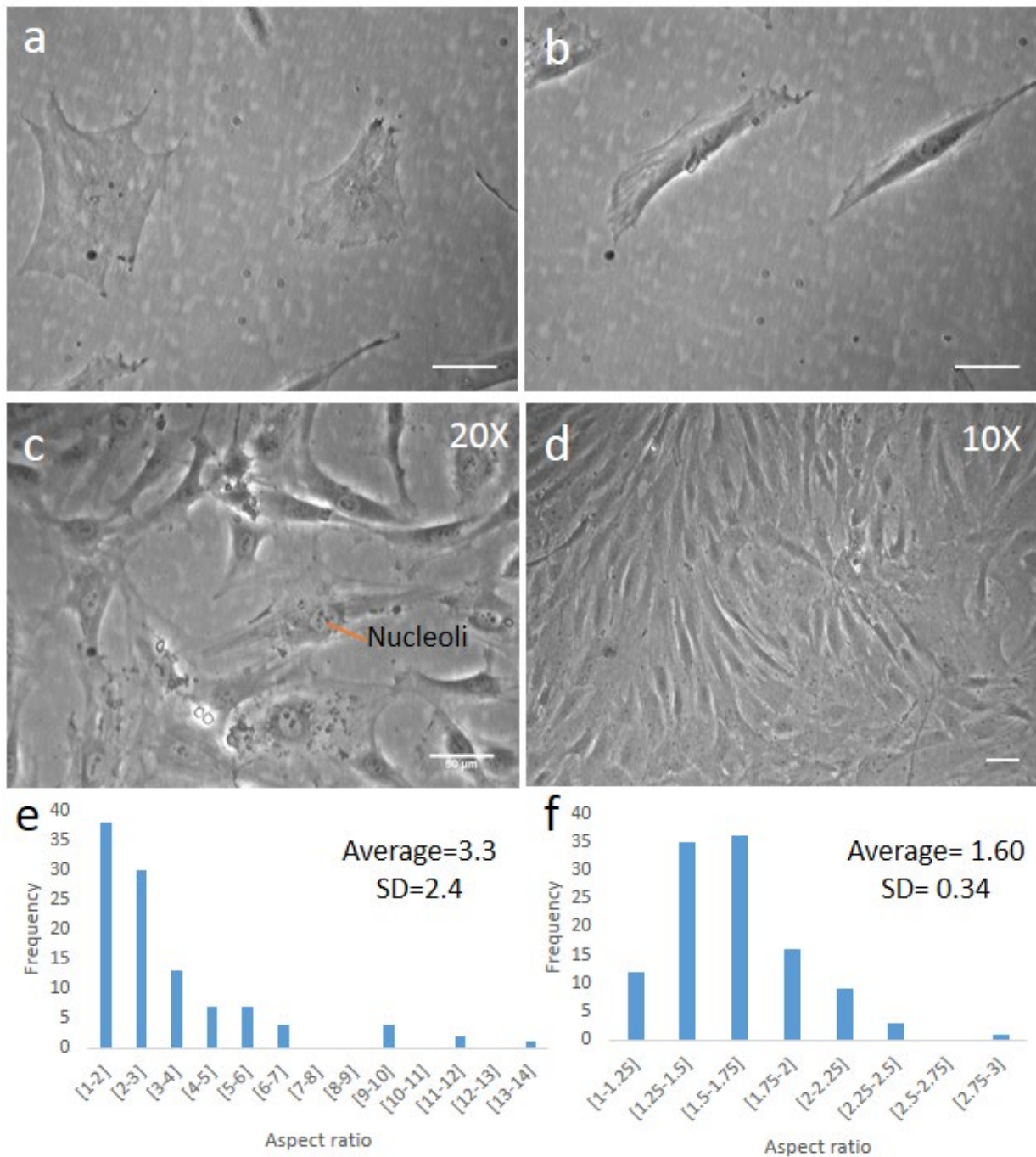


Figure 6-1: Phase contrast images of hMSCs on a 25 cm² cell culture flask. (a) Two hMSCs with branched and well-spread morphology (b) Two hMSCs exhibiting elongated spindle-like morphology. (c) hMSC culture in low concentration ($\sim 10^4$ cell/ cm²) resembles the morphology of fibroblasts, the arrow is showing the multiple nucleoli (denser parts inside the nucleus) of hMSCs. (d) hMSCs are elongated and polarized when seeded in higher concentrations ($\sim 5 \times 10^4$ cell/cm²). (e) The histogram of the aspect ratio of hMSCs cells seeded in low concentration after 24 hours culture in on a 25 cm² cell culture flask (n=106). (f) The histogram of the aspect ratio of hMSCs nuclei seeded in low concentration after 24 hours culture in on a 25 cm² cell culture flask (n=112) and stained with 5 μ g/mL Hoechst® 33342. Scale bars are 50 μ m.

While cells are still in suspension, the cells are fairly round with a circularity (see chapter 5.1 for the definition) of 0.839 ± 0.005 s.e.m. ($n=189$) (Figure 6-2(f)) and not significantly elongated, with an aspect ratio of 1.21 ± 0.012 s.e.m. ($n=189$) (Figure 6-2(g)). Relying on this, we assumed a spherical shape for the suspended hMSCs to allow a calculation of the diameter of the cells using the measured cell area (Figure 6-2(b)). The histogram of the diameter of suspended hMSCs shows a distribution close to a normal distribution with a mean value of $21.7 \mu\text{m}$ with a standard deviation of $4.5 \mu\text{m}$. Therefore, the diameter of hMSCs is $21.7 \pm 0.3 \mu\text{m}$ s.e.m. ($n=189$) which shows that hMSCs are in the middle of the size range among other human cells (~ 7 to $100 \mu\text{m}$) and are slightly bigger than 3T3 fibroblasts (see chapter 5.1).

The nuclei of cells in suspension were visualized by staining the live cells with $5 \mu\text{g/mL}$ Hoechst® 33342 which labels the nucleus by binding preferentially to adenine-thymine (A-T) regions of DNA and emits blue fluorescence (460-490 nm) when it is excited by ultraviolet light (peak excitation at 350-361 nm) (see more detail in 2.7.2 for details) (Figure 6-2(c)).

Similar to the fibroblasts, we measured the nucleus diameter both immediately after detachment and 30 minutes after the detachment in order to give the stiff nucleus time to relax and mechanically forget its adherent shape. During this relaxation time, cells were shaken on a shaking plate at 180 rpm and 37°C in order to prevent possible adhesion to the substrate and deformation of the nuclei. The normal distribution that was fitted to the nucleus diameter has a mean value of $11.4 \mu\text{m}$ and standard deviation of $1.6 \mu\text{m}$ which means that the nucleus diameter is $11.4 \pm 0.15 \mu\text{m}$ s.e.m. ($n=107$) which is smaller than the 3T3 fibroblast nucleus immediately after detachment (13.25 ± 0.21 s.e.m.) (see chapter 5.1). Therefore, the ratio of cell diameter to nucleus diameter is $\frac{21.7}{11.4} = 1.90 \pm 0.03$ while it is $\frac{17.2}{13.2} = 1.30 \pm 0.03$ for 3T3 fibroblasts, which means that the nucleus occupies a bigger portion of the cell in suspension in 3T3 fibroblasts (The uncertainty of the ratio is calculated based on errors of the measured cell and nucleus size measurements).

The size of hMSCs nuclei reduces by approximately 10% after relaxation to $10.2 \pm 0.11 \mu\text{m}$ s.e.m. ($n=141$). Considering a similar reduction of approximately 10% was observed in 3T3 fibroblasts nuclei after relaxation, shows that a similar phenomenon is observable in different cell lines.

As mentioned before, previous studies have shown that a nucleus forms wrinkles on its surface during the detachment process, which allows the change in the nucleus size (Kim et al. 2015) (see Figure 5-3(i)). As time passes, more wrinkles on the nucleus permit increasing reduction in the size of the nucleus. The circularity of the nucleus reduces slightly from 0.832 ± 0.006 s.e.m. ($n=107$) to 0.777 ± 0.007 s.e.m. ($n=141$). This effect may arise from the increasing wrinkles which increase the effective perimeter of the nucleus (Figure 6-2(f)).

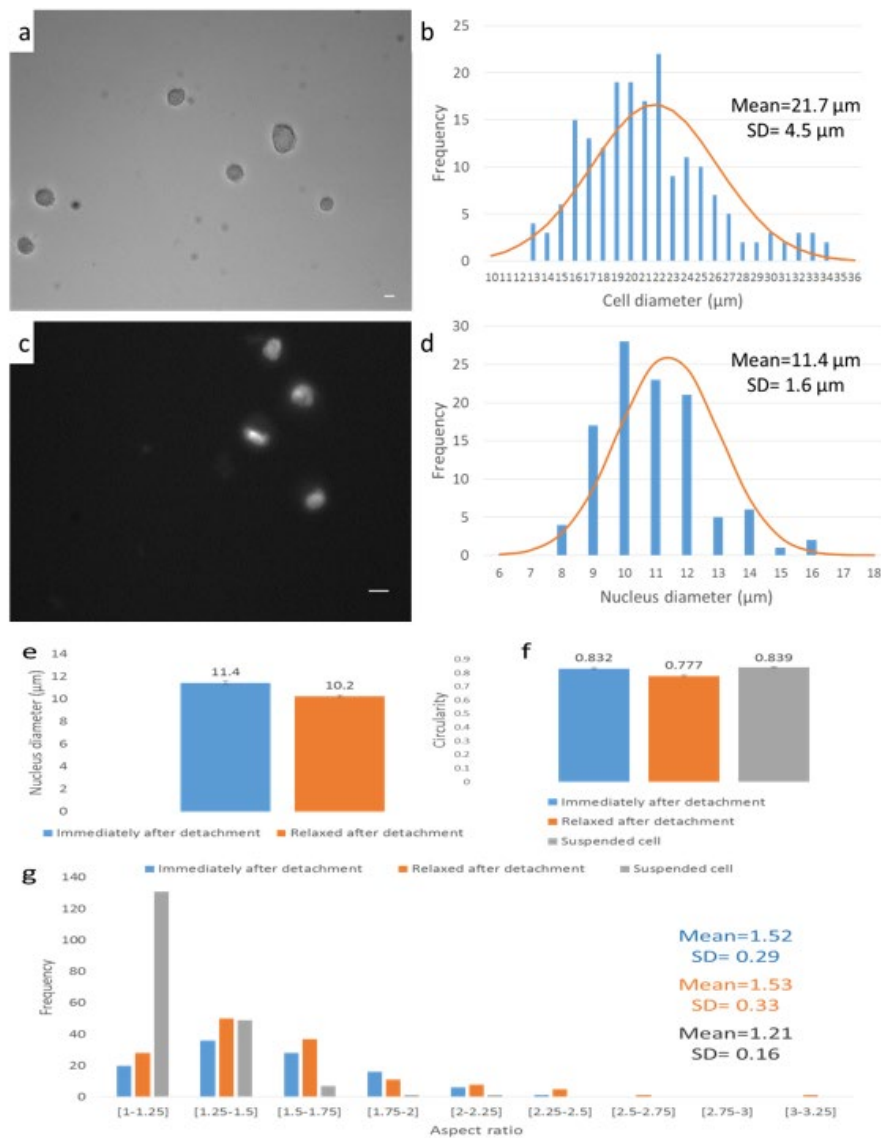


Figure 6-2: hMSCs in suspension. (a) Phase contrast microscopy of suspended hMSCs in a 25 cm² flask disk. (b) Histogram of hMSCs cell diameter distribution. The diameter of suspended cells (n=189) was shown as the histogram with bin size=1 μm. A Gaussian curve (red curve) is fitted to the distribution using calculated mean and standard deviation. (c) Fluorescent micrograph of detached nuclei of hMSCs stained with Hoechst® 33342, denser (brighter) parts are the nucleoli. (d) Histogram of hMSCs nuclei size distribution (n=107) (blue) with a Gaussian curve fitted to the distribution (red). Scale bars are 10 μm. (e) The nucleus diameter of hMSCs, immediately after detachment with TrypLE solution (blue) and after relaxation in suspension by being shaken for 30 minutes at 180 rpm (orange). (f) The circularity of hMSCs immediately after detachment with TrypLE solution (blue), after relaxation in suspension by being shaken for 30 minutes at 180 rpm (orange)(n=141) and suspended cells immediately after detachment with the TrypLE (grey). (g) The distribution of aspect ratio of hMSCs nuclei immediately after detachment, after relaxation for 30 minutes and the aspect ratio of suspended hMSCs immediately after detachment.

The distribution of the aspect ratio in relaxed nuclei ($AR_{\text{average}} = 1.53 \pm 0.02$ s.e.m. (n=141)) and nuclei immediately after detachment ($AR_{\text{average}} = 1.52 \pm 0.02$ s.e.m. (n=107)) is fairly similar which shows that the reduction in nucleus size happens in an isotropic way. The aspect ratio histogram of the suspended cell shows that the cell quickly returns to its spherical shape ($AR_{\text{average}} = 1.21 \pm 0.01$ s.e.m. (n=189)) while the nucleus remains slightly elongated after the detachment. Although nuclear lamina maintains the nuclear shape (Webster, Keren L Witkin, et al. 2009), it is the actin fibres that are mainly responsible for the deformation of nuclear shape (Hanson et al. 2015c). Therefore, we hypothesize that cytoskeletal fibres that regulate nuclear shape depolymerize during detachment and this lack of external force on the nucleus of suspended cells causes a delay in returning the nucleus to its spherical shape from its slightly elongated adherent state ($AR_{\text{average}} = 1.60 \pm 0.03$ s.e.m.).

Similar to stromal cell lines such 3T3 fibroblasts, failure to adhere to the substrate *in vitro* or extracellular matrix *in vivo* induces anoikis which is a programmed cell death (apoptotic cell death) in hMSCs (see chapter 5.1 for details). Anoikis is a major challenge in MSCs based clinical treatment, in which loss of adherence in transplanted MSCs reduces the efficiency of the treatment (Lee et al. 2015). We observed some of the classical apoptotic features such as blebbing in the hMSC culture both in cells that completely failed to adhere (Figure 6-3 (a)) or the adherence was weak (Figure 6-3 (b)). In the case of stromal cell lines such as fibroblasts, the cells grow to high confluency density (see Figure 5-1(b)) and become necrotic in approximately 10-14 days after the start of culturing and detach from the surface (Figure 5-2(d)). However, in some hMSC cultures, especially when many passages were carried out on the same cells, the cells can almost stop proliferation at some point while the majority of cells remain adherent to the substrate for a long period of time without losing their morphological shape (Figure 6-3(c) & (d)). Some authors have suggested that it very likely that these hMSCs in long-running cultures undergo senescence and lose their potency for self-renewal and differentiation due to the accumulation of oxidative stress and dysregulation of important differentiation regulatory factors (Turinetto et al. 2016). In addition, the cell migration capacity of senescent hMSCs may get impaired (Turinetto et al. 2016).

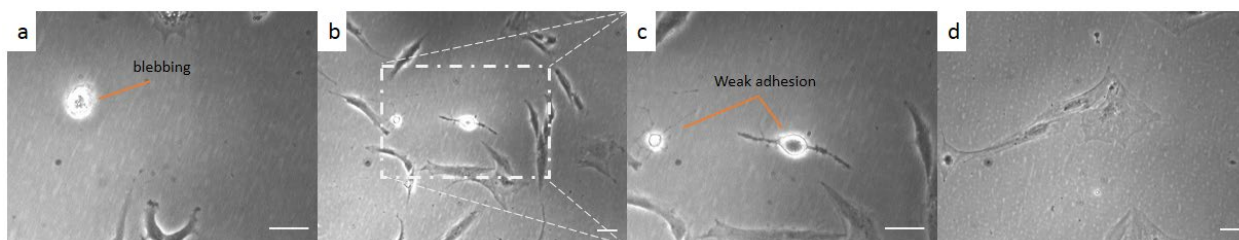


Figure 6-3: Anoikis and long-term culture of hMSCs. (a) Phase contrast micrograph of an hMSC showing blebbing, a classic hallmark of apoptotic cell death due to complete failure to adhere to 25 cm² culture flask while nearby cells are spreading normally on the substrate approximately 12 hours after seeding. (b) Blebbing of two hMSCs among normal adherent adjacent cells approximately 12 hours after seeding (10 x). (c) The high magnification (20X) of 6-3(b) shows that these two apoptotic hMSCs are weakly adherent to the substrate. (d) hMSCs culture 42 days after seeding on a 25 cm² culture flask at 37°C showing a normal morphology for hMSCs without signs of apoptotic or necrotic cell death. Scale bars are 50 µm.

6.2 Mesenchymal stem cells on fibronectin stripe patterns

MSCs are subject to different topographical and mechanical cues in their niche *in vivo* that are provided by the ECM and the behaviour of MSCs change by conformation to these cues (Anderson et al. 2016). *In vitro* studies have shown that micro or nano-scale topographical cues can significantly influence cellular behaviour including the differentiation potency of the MSCs (Metavarayuth et al. 2016). MSCs are relatively easy to isolate as they are sourced from various organs and differentiate into multiple cell line in the body and therefore have a significant role in stem cell-based therapeutic technique (Ma et al. 2012). As a consequence, engineering biomaterials with designed topographical features in order to control the behaviour of stem cells has gained significant importance in the fields of regenerative medicine and tissue engineering (Mahla 2016b). These bioengineered materials either aim to increase the efficiency of tissue transplanting by improving the scaffold of transplanted organs *in vivo* or improve the differentiation and growth performance of stem cells *in vitro* which is crucial for achieving higher quality and quantity for the cells that are used for the clinical applications (Tamiello et al. 2015). (See chapter 5.2 for more details).

We used fibronectin, which is a crucial element in the structure of ECM, to fabricate our patterns. Fibronectin enhances the cell adhesion to the substrate and is widely used for the fabrication of micropatterns for the study of cell function and morphogenesis (Thery 2010).

Previous studies have shown that the shape of MSCs significantly influences their tendency to differentiate into different cell lines in their lineage (Kilian et al. 2010). More elongated MSCs have

the tendency to differentiate into osteoblasts, while less elongated cells have a greater tendency towards adipogenic differentiation (Kilian et al. 2010) (see chapter 4.3.2.2 for details). Therefore, in order to study the effect of the shape of the substrate pattern on the hMSCs, we chose to use fibronectin coated stripes of different sizes. Stripe micropatterns occur *in vivo* in the form of cells that are surrounded by adjacent cells and are elongated in a stripe shape (Alvarez-Prats et al. 2018) (Figure 5-5(d)). Similar patterns have been used *in vitro* to study cell morphology (Huang & Donald 2014b) (See chapter 2 for more details). We chose to seed cells on evenly fibronectin-coated substrates, plus 25 μm and 10 μm fibronectin coated stripes. The cells were allowed to spread on the surface for 200 minutes at a density of 6000 cells/ cm^2 (see 2.6 for more details). Previous studies show that the adhesion process of hMSCs take place approximately in the first 2 hours after seeding and deformation of the nucleus in response to patterned PDMS substrate happens 3 hours after seeding (Chalut et al. 2010b).

An evenly fibronectin-coated substrate acts as the control since cells don't feel any anisotropy from the substrate (Figure 6-4(a)). The cells spread widely on the control pattern (5377 ± 455 (s.e.m) μm^2 (n=58)) (Figure 6-4(e)). The actin filaments are abundantly formed across the cell. However, the density of basal actin filaments reduces in the centre of the cell where the nucleus resides (Figure 6-4(a)). The actin edge bundles are formed in the periphery of the cell and form concave circular arcs in the webbed edges of the cell (Figure 6-4(a)). These actin bundles are cytoskeletal structures that are specialized to support webbed edges of the cell (Zand & Albrecht-Buehler 1989) (see chapter 3.3 for details).

As mentioned earlier (see chapter 6.1), hMSCs may adopt a spindle-like elongated morphology or a well-spread polygonal morphology (see Figure 6-1). The same phenomenon was observed among hMSCs on the fibronectin control substrate. However, the aspect ratio of hMSCs on fibronectin-coated control substrate (2.15 ± 0.13 (s.e.m) (n=58)) was less compared to the hMSCs seeded on the tissue culture polystyrene (TCP) flask (3.3 ± 0.23 (s.e.m) (n=106)). The Young's modulus of polystyrene culture flask is approximately 3 GPa (Miyake et al. 2006) while the Young's modulus of PDMS (mixing ratio of 10:1 (base: elastomer)) is 580 kPa (Park et al. 2010). Previous studies have shown that the morphology and differentiation preferences of hMSCs are largely influenced by the stiffness of the substrate *in vitro*. Most of these studies have focused on the substrate stiffness between 1-100 kPa (Ingber 2006)(Sun, Chi, Li, et al. 2018). These studies generally found out that MSCs on a very soft substrate ($\sim 1\text{kPa}$) express branched neurogenic shape. On the intermediate substrates ($\sim 10\text{kPa}$), they show spindle like elongated myogenic features and on the stiffer range (25-70kPa) they show polygonal osteogenic cell shape (Ingber 2006)(Sun, Chi, Li, et al. 2018). It has been shown that on the stiffer substrate ($\sim 230\text{ kPa}$), the differentiation of hMSCs is biased toward osteogenesis and cells express more features of osteoblasts (Piroli & Jabbarzadeh 2018). Therefore it is generally

believed on high stiffness substrates, hMSCs mostly express osteogenic cell features and as the substrate gets stiffer, cells elongate further.

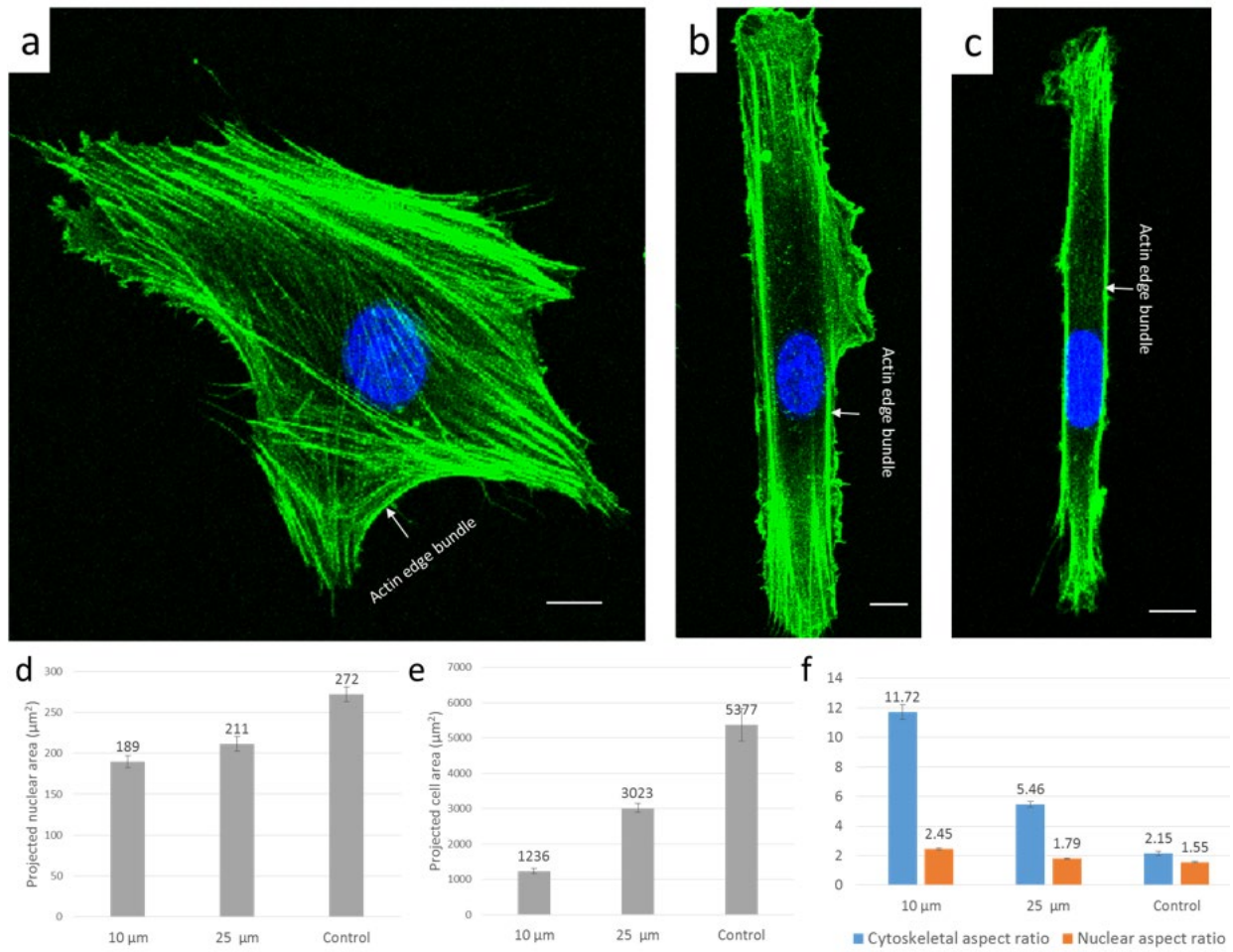


Figure 6-4: The morphological effects of fibronectin stripe patterns on the hMSCs. (a)(b)&(c) Fluorescence micrographs of hMSCs in the S-phase on PDMS substrate with even fibronectin coating (control), 25 μm and 10 μm fibronectin stripes respectively. The cells are fixed with formaldehyde and stained with Phalloidin for F-actin (green) and TO-PRO-3 for the nucleus (blue). Green and blue channels are overlaid by Image J. Scale bars are 10 μm. (d)&(e) Projected area of nucleus and cytoskeleton of the hMSCs on 10μm (n=53, n_{nucleus}=53), 25μm (n=54, n_{nucleus}=54) fibronectin stripes and evenly fibronectin coated control substrate (n=58, n_{nucleus}=58) on a PDMS substrate (f) The aspect ratio of nucleus and actin cytoskeleton on 10μm (n=53, n_{nucleus}=53), 25μm (n=54, n_{nucleus}=54) fibronectin stripes and evenly fibronectin coated control substrate (n=58, n_{nucleus}=58) on a PDMS substrate. Error bars are SEM.

As an example, hMSCs on very stiff titanium substrate with Young's modulus of 113 GPa, get more elongated compared to cells on TCP substrate (Loye et al. 2018). *In vivo*, the elastic modulus of tissues that are made up from cell lines that are differentiated from hMSCs varies widely from soft brain tissue (~1kPa) (Budday et al. 2015) to adipose tissue (~2kPa)(Yuan et al. 2015), or muscle

tissue (~10kPa)(Gilbert et al. 2010) to stiffer tissues such as cartilage (~1 MPa)(Chizhik et al. 2010) and hard tissues such as cortical bone (~10GPa) (see Figure 4-9). Therefore, we hypothesize that stiffer TCP substrate shifts our cells toward osteogenesis and allows cells to elongate more compared to the softer PDMS substrate as it would occur in the native microenvironment of hMSCs niches in different tissues.

25 μm stripes clearly make the cytoskeleton and cytoskeletal actin stress fibres to align parallel to the patterns (Figure 6-4(b)). Very strong straight actin edge bundles are formed parallel to the patterns; however, some actin edge bundles arcs formed at the two ends of the cells or in the places that filopodia manage to escape the patterns. There is a substantial amount of actin polymerization at the two ends of the cell which result in a higher density of basal stress fibres in these regions (very green regions at two ends of the cell. However, there is a very small number of basal actin fibres in the region in the middle of the cell underneath the nucleus (Figure 6-4(b)). Cells on 25 μm stripes are less spread (3023 ± 131 (s.e.m) μm^2 (n=54)) compared to cells on the control substrate (Figure 6-4(e)) and the cells are more elongated (5.46 ± 0.19 (s.e.m) (n=54)) compared to control cells (Figure 6-4(f)). The nuclei of hMSCs on 25 μm stripes (211 ± 9.1 (s.e.m) μm^2 (n=54)) spread compared to the cells on the control substrate (272 ± 9.0 (s.e.m) μm^2 (n=54)) and are slightly more elongated with the aspect ratio of 1.79 ± 0.04 (s.e.m) (n=54) compared to the control cells (1.55 ± 0.04 (s.e.m) μm^2 (n=58)).

On the narrower 10 μm stripes, the cytoskeleton and the internal actin filaments of the cell align themselves with the patterns and elongate on the stripes (AR: 11.72 ± 0.48 (s.e.m) (n=53)). The nucleus is tightly pushed between two thick actin edge bundles that are formed in the edge of the cell and parallel to the pattern direction (Figure 6-4(c)) and therefore is more elongated (AR: 2.45 ± 0.07 (s.e.m) (n=53)) compared to the nuclei on control and 25 μm stripes (Figure 6-4(f)). On the 10 μm stripes, most of the actin polymerization inside the cell takes place at the two ends of the cell and a small number of actin stress fibres are visible only in this region while there are almost no basal actin fibres in a big portion of the cell in the middle of the cell. Both the cytoskeleton (1236 ± 70 (s.e.m) μm^2 (n=53)) and nucleus (189 ± 7.4 (s.e.m) μm^2 (n=53)) spread less on the 10 μm stripes compared to the control substrate and 25 μm stripes (Figure 6-4(d)&(e)) .

Although the patterns largely alter cell spreading and shape, the Feret's diameter doesn't differ largely among the cells spreading on different patterns. Feret's diameter or maximum calliper is defined as the largest distance between any two given point along the boundary of a shape (Imagej.nih.gov). Feret's diameter has been used as one of the key parameters to describe overall morphology evaluation in the microscopic objects (WALTON 1948).

We measured the Feret's diameter of cells on the control substrate at (130.6 ± 4.6 (s.e.m) μm (n=58)) while our measured it at (149.0 ± 4.9 (s.e.m) μm (n=53)) and (146.0 ± 4.3 (s.e.m) μm (n=54)) for hMSCs on 10 μm and 25 μm stripes respectively. It seems that despite the high adaptability of the cell

to confine itself to different patterns, there is an internal control mechanism that put a restriction on how far two points of a cell can get apart from each other during the cell adhesion.

6.2.1 How patterns influence the orientation of the nucleus inside the cell

It is well known that force bearing actin fibres inside the cell can deform the nucleus shape (Hanson et al. 2015c)(Shyam B Khatau et al. 2009). As figure 6-4 reveals, the fibronectin stripes with different widths, significantly change the architecture of the actin fibres and therefore change the shape of the nucleus.

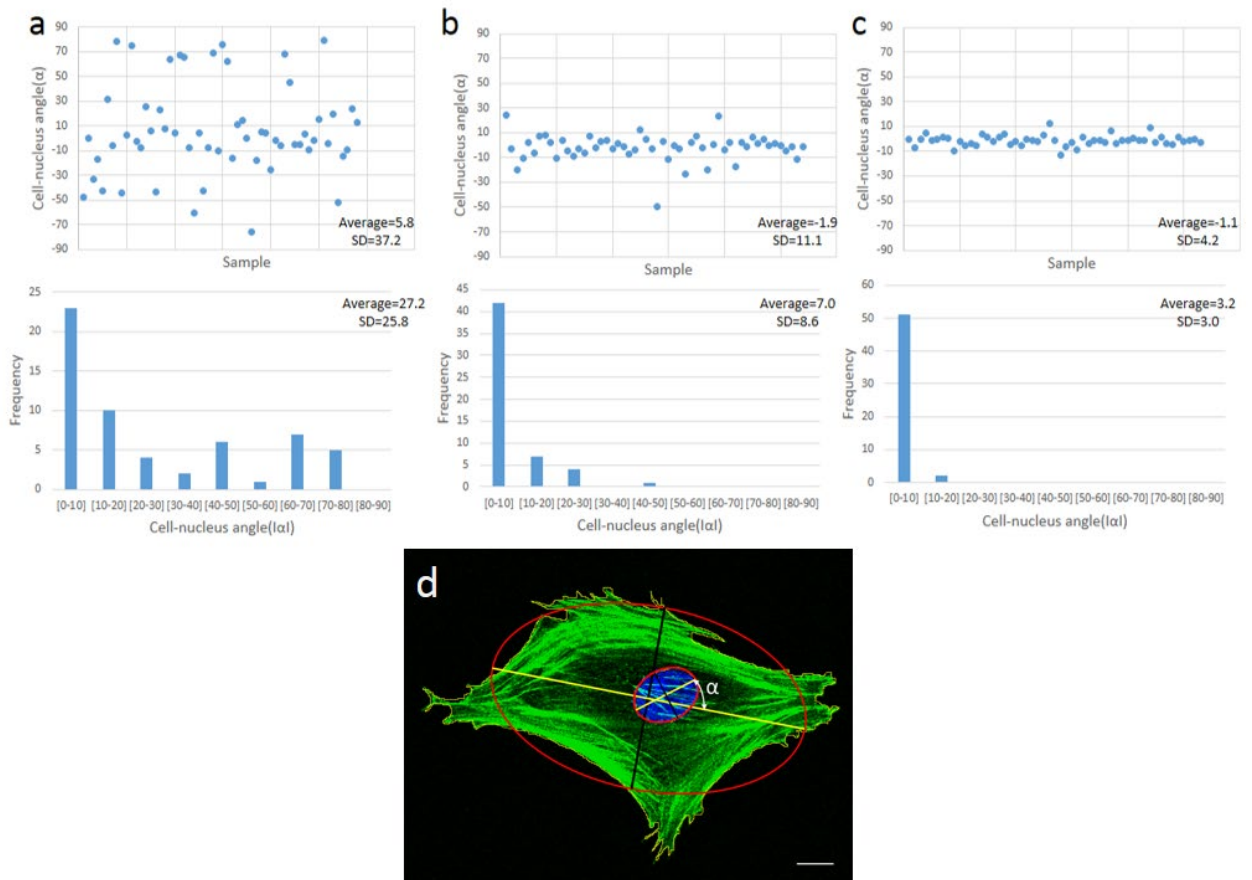


Figure 6-5: The orientation of nuclei of hMSCs relative to cytoskeleton on fibronectin stripes.

(a)(b)&(c) the angle(α) between the major axis of the best fit ellipse to the cytoskeleton and nucleus of hMSCs on fibronectin-coated control (n=58), 25 μm (n=54) and 10 μm (n=53) fibronectin stripes on the upper panel. The lower panel is the histogram of the absolute value of the nuclear orientation angle ($|\alpha|$) on the control, 25 μm , and 10 μm fibronectin stripes respectively. (d) The angle between the major axis (yellow) of best fitting ellipses (red) to the cytoskeleton and nucleus (α) of an hMSC on unpatterned fibronectin coated PDMS substrate. The cell is fixed with formaldehyde and stained with Phalloidin for F-actin (green) and TO-PRO-3 for the nucleus (blue). Green and blue channels are overlaid by Image J. Scale bar is 10 μm .

We looked at how the orientation of the cytoskeleton on different patterns affects the orientation of the nucleus. In order to quantify this, we measured the angle (α) between the major axis of best fitting ellipses to the cytoskeleton and nucleus (Figure 6-5 (d)). This measurement shows how the nucleus direction is correlated with the major axis of cell shape. Among the cells on the control pattern, the nucleus is less aligned with the cytoskeleton ($|\alpha|_{\text{average}}=27.2^\circ$) compared to the cells on 25 μm ($|\alpha|_{\text{average}}=7.0^\circ$) and 10 μm stripes ($|\alpha|_{\text{average}}=3.2^\circ$). The standard deviation of the cell-nucleus angle also significantly reduces with decreasing fibronectin width, so that it drops from 25.8° for control cells to 8.6° and 3.0° for cells on 25 μm and 10 μm stripes respectively (Figure 6-5).

The histogram of cell-nucleus angle ($|\alpha|$) for hMSCs on control substrate (Figure 6-5(a)), shows that in a relatively big portion of cells ($\sim 40\%$), the nucleus is aligned with the cytoskeleton ($|\alpha| < 10^\circ$), while there a considerable number of nuclei that are not aligned with the cytoskeleton. On the 25 μm patterns, the alignment percentage increase to 78% and we almost could not witness nuclei that are not significantly orientated with respect to the cytoskeleton. Almost all (96%) cells on 10 μm stripes are closely aligned with the cytoskeleton.

In adherent cells, it has been shown that perinuclear stress fibres which are coupled with nucleus through nuclear Lamin A/C and LINC complexes (see chapter 1.4 for details). In the absence of the perinuclear actin cap, the nucleus is free to rotate inside the cell while in the presence of actin cap fibres, the angular rotation of nucleus is stopped (Dong-Hwee Kim et al. 2014). Therefore, we hypothesize that among hMSCs, the perinuclear actin cap which is usually aligned with the cytoskeleton (see Figure 6-7), aligns the nucleus with the cytoskeleton in a substantial portion of the cells (Figure 6-5(c)). While, the disruption of organized actin nuclear cap or weaker alignment of the fibres with the cytoskeleton in some cells, allows the nucleus to rotate and reduces the cell-nucleus alignment. As cells adhere to the narrower strips, both perinuclear actin stress fibres which are more aligned with cell body (see Figure 6-7) on the strips and actin edge bundles, force the nucleus to align with the cytoskeleton. As Figure 6-4 shows, the effect of actin edge bundle on the further alignment of the nucleus with the cytoskeleton is more evident on 10 μm stripes compared to 25 μm stripes.

6.2.2 Interaction between the cytoskeleton and the nucleus of hMSCs on fibronectin stripe patterns in the single cell level

As previously was shown, the projected area of hMSCs on fibronectin stripes is positively correlated with the width of stripes (Figure 6-4(d) & (e)). In order to see if the same positive relationship between cell and nuclear size exists among the cells on each of the fibronectin patterns, we studied the nuclear and cell projected area at the single cell level (Figure 6-6).

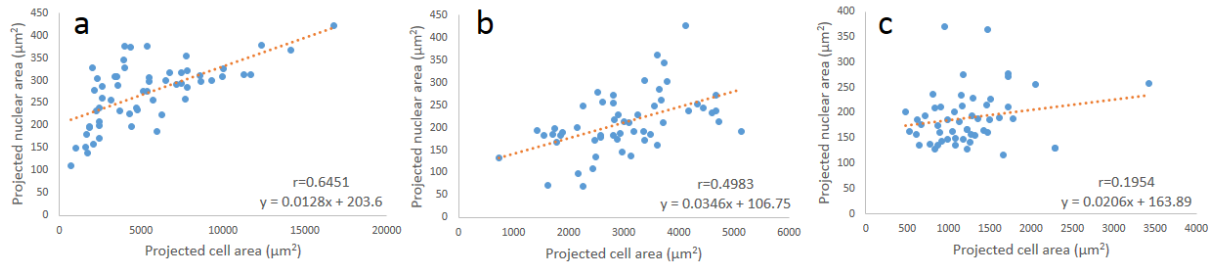


Figure 6-6: Single cell-based relationship between nucleus size and cell size of hMSCs on fibronectin stripes. (a)(b)&(c) Correlation between nuclear and cellular projected area of hMSCs on fibronectin-coated control (n=58), 25 μm (n=54) and 10 μm (n=53) fibronectin stripes. The linear equations and Sample Pearson correlation coefficients (r) are describing the line (orange) that is fitted to the data using the least square method.

In order to quantify the correlation between cell and nuclear projected area, we used the Pearson correlation coefficient. The coefficient, which is also referred to as Pearson's r , measures the correlation between two variables (X and Y) and is defined as the ratio of covariance of two variables ($cov(X, Y)$) to the product of standard deviations of the two variables ($\sigma(X)\sigma(Y)$) (Yeager 2019). For a sample, the correlation between two variable is denoted $r_{x,y}$ or simply r is calculated using equation 6-1 (Mukaka 2012) where E is showing the expected value, x_i and y_i are the i 'th value of variable x and y , μ_x and μ_y are the sample mean of variable x and y and n is the number of paired data.

$$r_{x,y} = \frac{cov(X,Y)}{\sigma(X)\sigma(Y)} = \frac{E((X-\mu_x)(Y-\mu_y))}{\sigma(X)\sigma(Y)} = \frac{\sum_{i=1}^n (x_i - \mu_x)(y_i - \mu_y)}{\sqrt{\sum_{i=1}^n (x_i - \mu_x)^2 \sum_{i=1}^n (y_i - \mu_y)^2}} \quad \text{Equation 6-1}$$

The Pearson correlation coefficient is always between -1 and 1 (Mukaka 2012). $r=1$ occurs when two variables are perfectly positively correlated (they form a line with a positive slope) whereas $r=-1$ happens when two variables are perfectly negatively correlated (they form a line with a negative slope). $r=0$ happens when there is no correlation between the two variables. Other values for r between 1 and -1, shows how close is the correlation between two variables to these three situations.

Our measurement showed that there is a positive correlation between the projected area of the nucleus and cell among all patterns. However, the correlation is stronger among hMSCs on evenly fibronectin coated control substrate ($r=0.64$) and it gets weaker among cells on 25 μm fibronectin stripes ($r=0.49$) and is very weak among cells on 10 μm stripes ($r=0.19$). It has been shown that basal actin fibres under the nucleus, insert a localized pressure on the nucleus that plays an important role in

deformation of the nucleus (Hanson et al. 2015c) and are the main providers of force in adherent cells during cell migration (Dong-Hwee Kim et al. 2014). As Figure 6-4 shows, the number of basal actin fibres under the nucleus significantly reduces as the fibronectin stripes get narrower. Therefore, we hypothesize that the decreasing number of basal actin fibres among cells on narrower stripes dissociates cell more from the nucleus. This dissociation prevents the effective transfer of force from the cytoskeleton of cells that are increasing in size to stretch and increase the nuclear size.

6.3 3D shape of hMSCs on fibronectin stripes

Most of the morphological studies of hMSCs and the effects of substrate patterns have been focused on the 2D architecture of cell, nucleus and subcellular organelles (Engler et al. 2006), (Kilian et al. 2010), (Yim et al. 2010). However, it is necessary to study these cells in 3D in order to get a better understanding of their morphological response to the substrate topography and how they might behave in the body. Our experimental setup allows us to perform z-stack confocal microscopy (see Figure 5-7) and get a 3D image of the cell and nucleus. Similar to 3T3 fibroblasts, we observed that hMSCs on both the evenly fibronectin-coated control substrate and on fibronectin stripes form actin filaments on top of their nucleus which is usually highly organized and aligned with the direction of the cell (Figure 6-7). Furthermore, we observed that cells form different 3D shapes on different patterns.

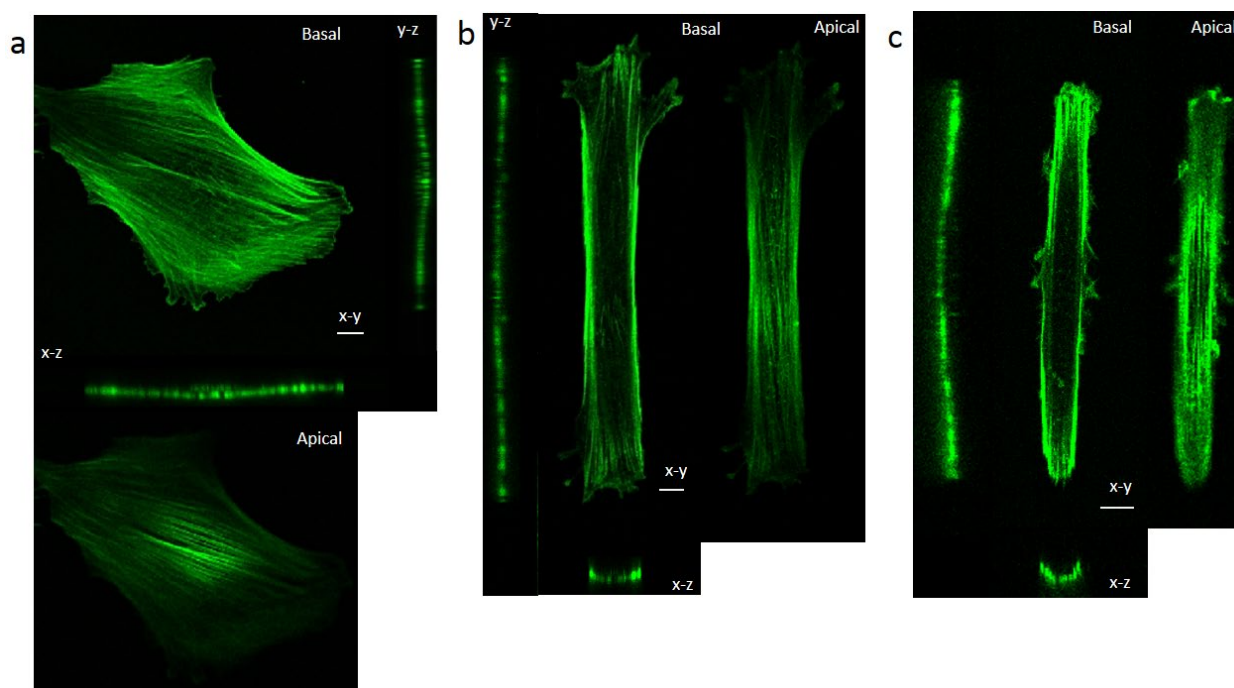


Figure 6-7: The 3D shape of hMSCs on the fibronectin fibres with different geometry. (a)(b) & (c), A 3D shape of hMSCs in the S-phase of spreading fixed with formaldehyde and stained with Phalloidin for F-actin on the evenly coated fibronectin PDMS substrate, 25 μm and 10 μm fibronectin stripes respectively. With the focal plane on the basal surface conventional basal stress fibres are revealed; whereas, focus on the apical plane on top of the nucleus reveals a highly organized perinuclear actin cap stress fibres. Scale bars are 10 μm .

In order to quantify the morphology of the cell, we measured the maximum cell thickness which occurs somewhere on the top of the nucleus (Figure 6-8(a)). Our results, shows that cell thickness is negatively correlated with the width of the fibronectin stripes so that cells on 10 μm stripes (10.46 ± 0.29 (s.e.m) μm (n=53)) are the thickest while the cell height reduces on wider 25 μm stripes (7.93 ± 0.17 (s.e.m) μm (n=54)) and control substrate (6.87 ± 0.13 (s.e.m) μm (n=58)). However, the number of perinuclear actin fibers is positively correlated with the width of fibronectin stripes so that hMSCs on unpatterned control substrate form the greatest number of perinuclear stress fibers (8.91 ± 0.38 (s.e.m) μm (n=58)) while the number reduces for the cells on 25 μm stripes (5.38 ± 0.28 (s.e.m) μm (n=54)) and is the least for cells on 10 μm stripes (1.94 ± 0.16 (s.e.m) μm (n=54)). The perinuclear actin fibers put uniform pressure on top of the nucleus (Hanson et al. 2015c) (see Figure 5-9(b)) and compress the nucleus towards the substrate. Therefore, we think that the higher number of actin fibers on top of the nucleus will put a greater compressive force on the nucleus and flatten it more (Figure 6-10), consistent with the results that we observed for fibroblasts (see chapter 5.4).

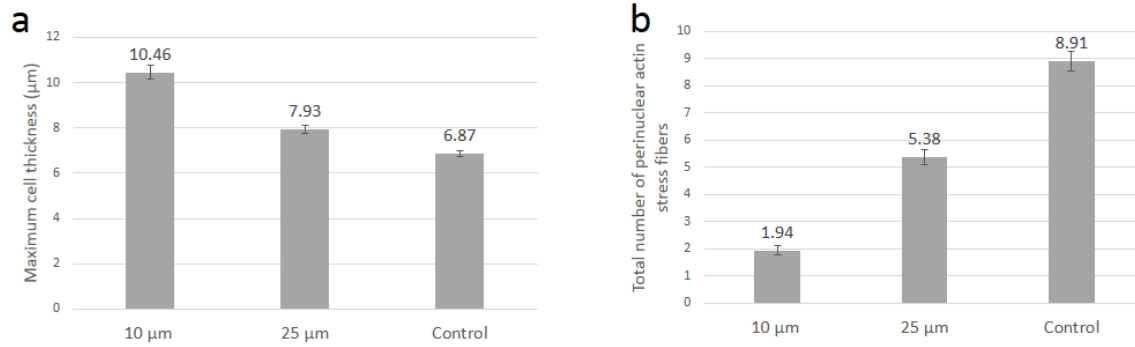


Figure 6-8: Maximum cell thickness and number of perinuclear actin stress fibers of hMSCs on fibronectin patterns. (a)&(b) Maximum cell thickness and the total number of perinuclear actin stress fibres among hMSCs spreading on 10μm (n=53), 25 μm (n=54) and fibronectin stripes and evenly fibronectin coated control substrate (n=58) on a PDMS substrate in the S-phase fixed with formaldehyde and stained with phalloidin for F-actin. Error bars are SEM.

The role of perinuclear actin fibers in compressing the nucleus leading to an impact on cellular height is evident also on the correlation of maximum cell thickness and number of perinuclear actin fibers at the single-cell level among cells on different fibronectin stripes (Figure 6-9). The correlation analysis shows that the maximum cell thickness is negatively correlated with the number of perinuclear actin fibers for both control and fibronectin stripes. However, the correlation is weakest among cells on control substrate ($r = -0.3840$) and significantly increases as the width of stripes decrease among cells on 25 μm ($r = -0.6041$) and 10 μm stripes ($r = -0.7758$).

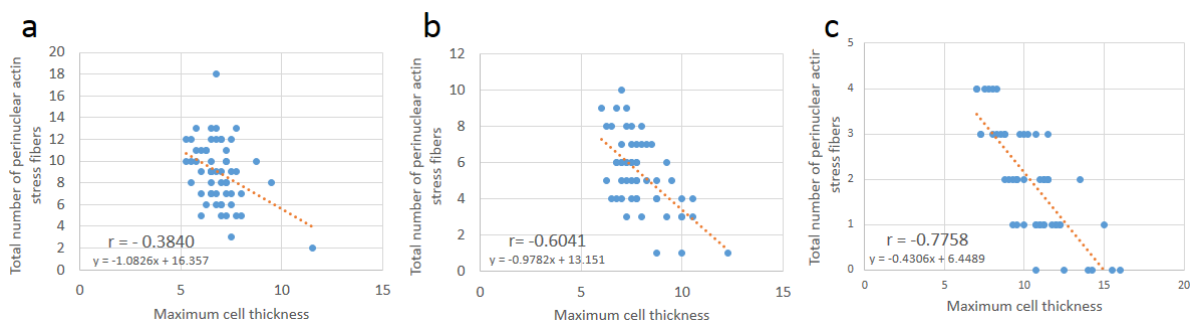


Figure 6-9 Single cell-based relationship between maximum cell thickness and number of perinuclear actin fibers of hMSCs on fibronectin stripes. (a)(b)&(c) Correlation between maximum cell thickness and total number of perinuclear actin fibers of hMSCs on fibronectin-coated control (n=58), 25 μm (n=54) and 10 μm (n=53) fibronectin stripes. The linear equations and sample Pearson correlation coefficients (r) are shown by the line (orange) that is fitted to the data using the least square method.

Atomic Force Microscopy (AFM) analysis on rat MSCs cells has shown that the Young's modulus of the cell on nuclear region exponentially increases as cell thickness decreases (Kihara et al. 2011). Therefore we hypothesize that this variation in stiffness may mean that thicker cells on the 10 μm stripes are more sensitive to the number of actin stress fibres.

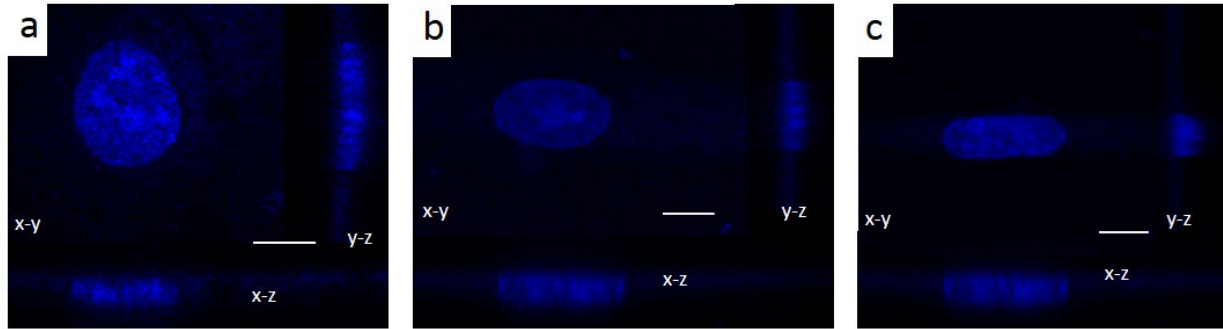


Figure 6-10: The 3D shape of the nucleus of hMSCs on the fibronectin stripes. (a)(b)&(c), 3D fluorescence confocal micrographs of hMSCs spreading on PDMS substrate evenly coated with fibronectin (control), 25 μm and 10 μm fibronectin stripes respectively. The nucleus is stained with TO-PRO-3 and false coloured blue.

6.4 hMSCs on sub-nuclear fibronectin stripes

6.4.1 Morphological features of the hMSCs on sub-nuclear stripes

hMSCs are to a large extent confined to the 10 μm and 25 μm fibronectin stripes and the morphology of both cytoskeleton and nucleus is significantly altered by the stripes (see section 6.2). However, when hMSCs were cultured on 5 μm fibronectin stripes (11 μm PDMS spacing between stripes) which are about 40 % of the detached hMSCs nucleus size ($11.4 \pm 0.15 \mu\text{m}$ s.e.m. (n=107)), we observed different morphological features among the cells (Figure 6-11). Some cells spread widely on the patterns with only small signs of local alignment in some regions in the periphery of the cell (Figure 6-11 (a)). The conventional basal actin fibers were abundantly formed in these cells; however, the alignment of these fibers with the patterns was not very obvious except for some local alignment in the middle of the cell (Figure 6-16(b)).

In a small minority of cases, cells were elongated and tried to confine themselves to the patterns although they could not completely elongate along the patterns and escaped out of the patterns particularly in the centre of the cell where the nucleus resides (Figure 6-11(b)). In these cells, we

could observe that the nucleus was partly confined to the pattern but finally escaped out of the pattern and stretched out until it was held by two thick edge actin bundles that are formed parallel to the direction of stripes in the periphery of the cell. The basal actin fibers were rarely formed in the central parts of the cell and most of the actin polymerization occurred at the two ends of the cell (Figure 6-11(b)).

Other groups of cells were widely spread on the cells; however, they were partially confined to the patterns and clearly followed the patterns by creating “branches” that were spread along the patterns. They also formed clear thick edge actin bundles parallel to the stripes on the periphery of the cell (Figure 6-10(c). However, the cell also spread over non-coated regions at its centre and the nucleus was not touched by visible actin edge bundles created by the patterns. Conventional actin fibers were formed throughout the cell and the fibers were clearly aligned with the direction of patterns. Some of these basal actin fibers which were connecting two branches of the cell on the patterns were visibly thicker compared to other basal actin fibers.

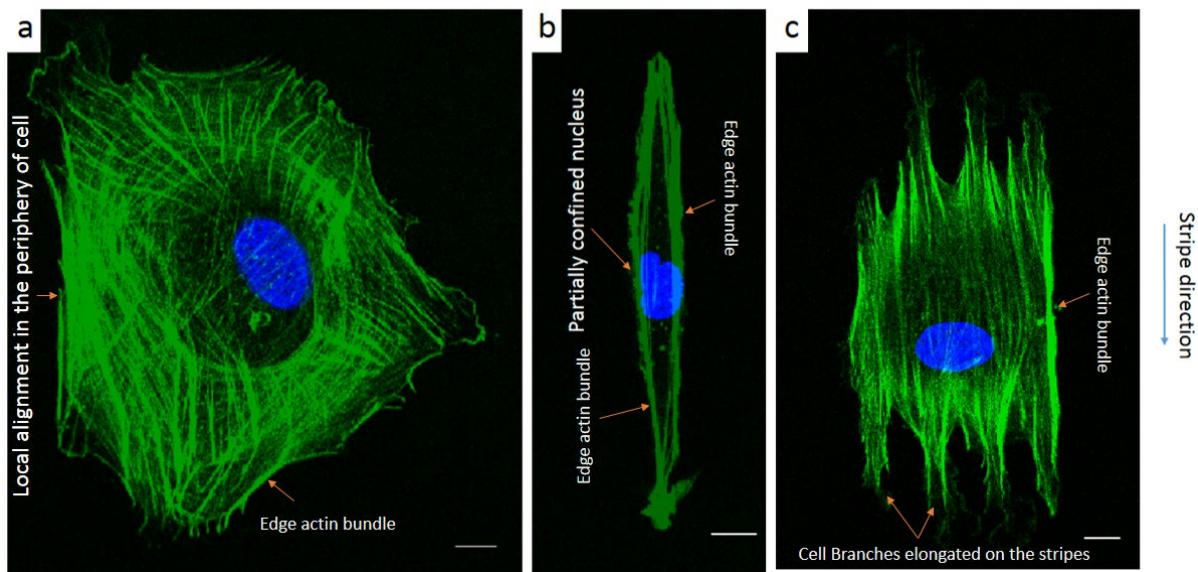


Figure 6-11: Fluorescent micrographs of the different morphologies of hMSCs on a sub-nuclear fibronectin pattern of stripes. (a) The cell is mostly not confined to the stripes. (b) The cell is confined to the stripes and is highly elongated along them. (c) The filopodia in the leading edge of spreading cell are confined and elongated along the stripes and the main body of the cell in the middle bridges over several stripes. The actin cytoskeleton of hMSCs is stained with phalloidin and false coloured in green and the nucleus is stained with TO-PRO-3(false coloured in blue). Scale bars are 10 μm .

We think that these groups of cells are also partially visible in the histogram of the aspect ratio of the cells (Figure 6-12(a)). Cells that were well spread on the patterns and were round (not elongated) are the cells that largely contributing to a peak in the histogram with the lower aspect ratio, whereas the partially elongated cells which form branches along the patterns contribute to the smaller peak in the histogram with the higher aspect ratio. However, there is an overlap between these two populations as the size, extent, and elongation of branches vary between cells. There are also rare very elongated cells on the pattern with a bigger aspect ratio. In overall, we did not see a significant change in the aspect ratio of hMSCs on sub-nuclear stripes pattern (2.12 ± 0.17 s.e.m. (n=71)) compared to hMSCs on fibronectin-coated control substrate (2.15 ± 0.13 s.e.m. (n=58)). We hypothesize that the minimally aligned round cells on the sub-nuclear patterns are representative of large and well-spread hMSCs (Figure 6-1) on the isotropic substrate and partially confined branched cells representing elongated hMSCs on the unpatterned substrate. However, the sub-nuclear stripe pattern changes the morphology of elongation by directing the nascent filopodia of the spreading cell on the stripes instead of letting the cell elongate to form an oval shape.

The histogram of nuclei of hMSCs on the sub-nuclear-sized patterns showed a behaviour close to the normal distribution with some rare elongated nuclei. From section 6.2, we know that the most intense changes to the shape of the nucleus are induced by edge actin bundles. In the case of sub-nuclear stripe patterns, the edge actin bundles either were not completely aligned with the patterns (Figure 6-11(a)) or they were not directly in contact with the nucleus (Figure 6-11(c) and only in rare elongated cells, the nucleus was in touch with the actin bundles (Figure 6-11(b)). Therefore, it is expected not to see a substantial change in the morphology of the nucleus. However, there is a minor increase in the average aspect ratio of hMSCs nuclei on sub-nuclear stripe pattern (1.63 ± 0.04 s.e.m. (n=65)) compared to the nuclei of hMSCs on the fibronectin-coated control (1.55 ± 0.04 s.e.m. (n=58)) which we think is due to basal actin fibers that are aligned with the stripes among partially confined branched hMSCs (Figure 6-11(c)) and locally aligned with the patterns underneath the nucleus in some well spread hMSCs on sub-nuclear stripes patterns (see Figure 6-16(b)).

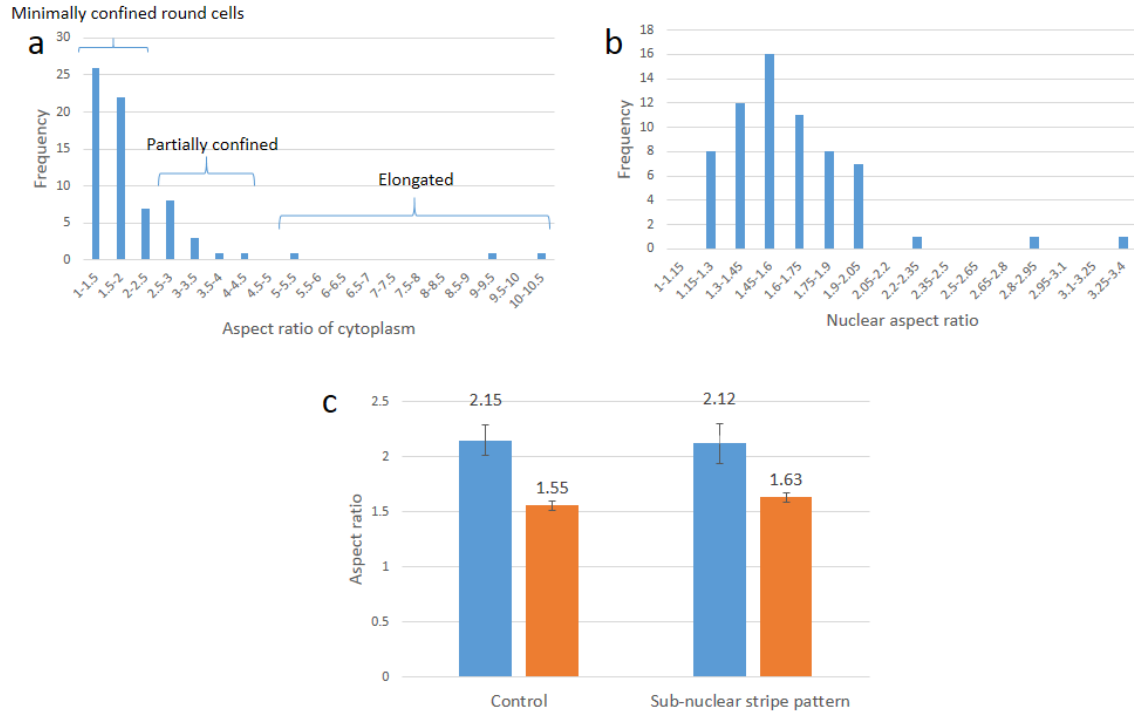


Figure 6-12: The aspect ratio of hMSCs on the sub-nuclear pattern. (a) The histogram of cytoskeletal aspect ratio on the patterns (n=71) showing three major categories minimally confined round cells, partially confined and elongated hMSCs. (b) The histogram of the nuclear aspect ratio on the patterns (n=65). (c) The average cytoskeletal (blue) and nuclear (orange) aspect ratio of hMSCs on evenly fibronectin-coated (control) ($n_{\text{cytoskeleton}} = 58$, $n_{\text{nucleus}} = 58$) and on the sub-nuclear pattern ($n_{\text{cytoskeleton}} = 71$, $n_{\text{nucleus}} = 65$). Error bars are s.e.m.

The projected area of hMSCs on the sub-nuclear stripe pattern ($4327 \pm 323 \mu\text{m}^2$ s.e.m. (n=71)) is reduced compared to hMSCs on the fibronectin-coated substrates ($5377 \pm 455 \mu\text{m}^2$ s.e.m. (n=58)) (Figure 6-13(a)). This is expected because of the PDMS spacings located between the fibronectin stripes. PDMS is not a biocompatible substrate and hinders the cell spreading significantly because of its high surface hydrophobicity (Chuah et al. 2016). The projected area of nuclei of hMSCs on the sub-nuclear pattern ($215 \pm 6 \mu\text{m}^2$ s.e.m. (n=65)) is also reduced compared to hMSCs on fibronectin-coated control substrate ($272 \pm 9 \mu\text{m}^2$ s.e.m. (n=58)).

Previously we showed that there is a positive correlation between cell and nucleus size (Figure 6-6)) and the correlation increases among that the cells that form a substantial number of basal actin fibers. As previously mentioned, both minimally confined round hMSCs and partially confined branched cells on the sub-nuclear patterns, which constitute a great portion of the hMSCs on the patterns, develop substantial number of basal actin stress fibers and therefore we think that for this reason, the

size of nuclei of hMSCs on sub-nuclear pattern is highly correlated with the cell size of hMSCs which reduces on the sub-nuclear patterns compared to control substrate.

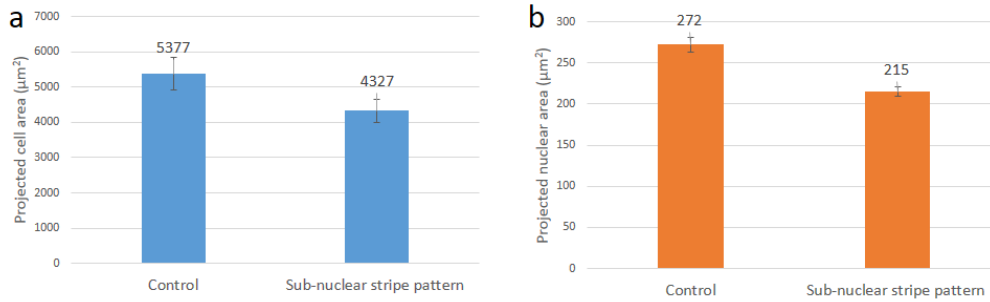


Figure 6-13: Projected area of hMSCs on sub-nuclear pattern and control substrate. (a) The projected area of the cytoskeleton on the sub-nuclear stripe pattern (n=71) and fibronectin-coated control (n=58). (b) The projected area of the nuclei of hMSCs on the sub-nuclear stripe pattern (n=65) and on fibronectin-coated control (n=58). Error bars are s.e.m.

6.4.2 Orientation of the hMSCs on sub-nuclear stripes

Previously we showed that hMSCs elongate along the 10 μm and 25 μm stripes. Other studies have shown that some cytoskeletal structures of hMSCs, such as focal adhesions, can align with a grating as narrow as 350 nm (550nm in depth and 700 nm in pitch) (Chalut et al. 2010b). From an energy point of view, the patterns create an effective potential energy (U_{eff}) that helps align the cell and its different organelles to the direction of patterns. The main source of the mechanical force that generates this potential is coming from actomyosin-mediated contractility (Murrell et al. 2015). In order to quantify this effective potential of alignment to the direction of patterns, we measured the deviation angle of the major axis of the best fitting ellipse and direction of the stripes (Θ) (Figure 6-14(a)). If we create the histogram of the deviation angle of the cells (Figure 6-14(b)), we can then calculate the probability of a cell belonging to each interval of deviation angle and using equation 5-5 (see chapter 5.5) we can calculate the shape of the effective potential energy curve (Figure 6-14(c)).

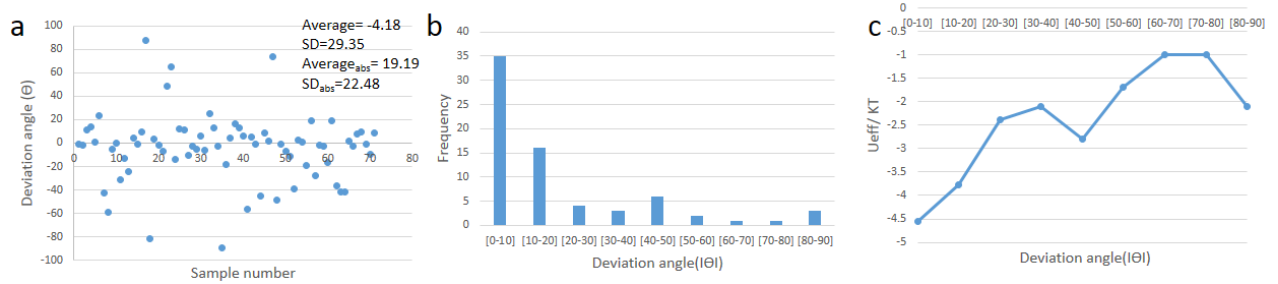


Figure 6-14: The orientation of hMSCs' cytoskeleton on sub-nuclear stripes pattern. (a) The Orientation of hMSCs' cell body with respect to the direction of stripes (n=71) and average and standard deviation (SD) for the deviation angle (Θ) and its absolute value. (b) Histogram of the absolute value of deviation angle ($|\Theta|$) distribution of hMSCs' cytoskeleton on the patterns. (c) Effective potential energy curve (normalized by $k_B T_{eff}$) calculated using the 6-13(b), the energy axis was shifted down by -1 in order to achieve a better illustration.

As Figure 6-14 shows, the cytoskeleton of hMSCs on sub-nuclear patterns are aligned with the pattern ($|\Theta|_{\text{average}} = 19.19^\circ \pm 2.6^\circ \text{ s.e.m (n=71)}$) (Figure 6-14 (a)). Almost half of the cells deviate by less than 10° relative to the pattern direction and more than 70% of cells deviate less than 20° from the direction of stripes. This effect shows itself as a deep well in the potential energy landscape around $\Theta = 0^\circ$ which forces the cell to align itself with the direction of patterns (Figure 6-14(c)). The alignment of elongated and branched hMSCs is more evident; however, the alignment manifests itself as the aligned parts of cell periphery even in most round well-spread cells (Figure 6-11(a)) which secures a smaller angle between the major axis of the best fitting ellipse and the pattern direction.

The nuclei of hMSCs are aligned to the direction of patterns to a lesser extent ($|\Theta|_{\text{average}} = 35.78^\circ \pm 3.62^\circ \text{ s.e.m (n=65)}$) compared to the cytoskeleton alignment (Figure 6-15(a)). Only 27% of nuclei showed a deviation less than 10° relative to the stripe direction and the percentage of nuclei that exhibited a deviation angle less than 20° was 40% (Figure 6-15(b)). The lack of actin edge bundles that can substantially align the nucleus with the cytoskeleton leaves only the perinuclear and basal actin fibers as the sources of mechanical force to align the nucleus with the cytoskeleton similar to cells on the control substrate; as we showed earlier (see 6.2.2). The alignment of the nucleus with the cytoskeleton using only these two sets of fibers is not as strong as with actin edge bundles. The lower probability of alignment of nuclei compared to cytoskeletal alignment means that in the energy landscape, the depth of the effective potential well around $\Theta = 0^\circ$ is smaller (Figure 6-15(c)).

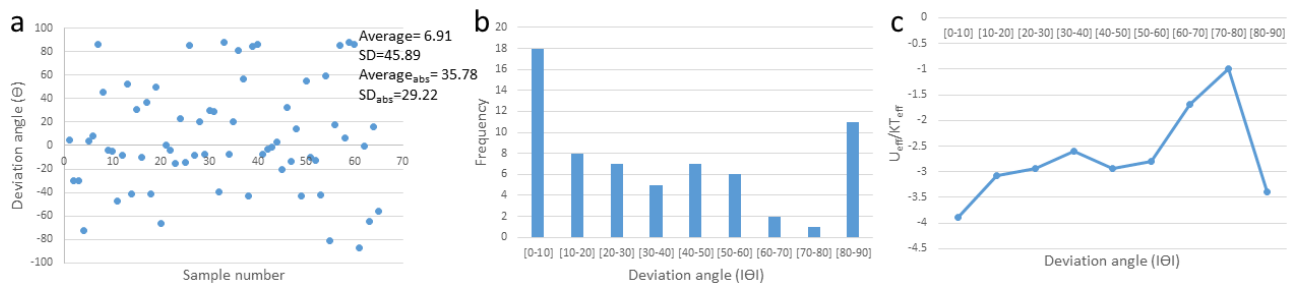


Figure 6-15: The orientation of hMSCs nuclei on the sub-nuclear stripes pattern. (a) The orientation of hMSCs nuclei with respect to the direction of stripes ($n=65$) and average and standard deviation (SD) for the deviation angle (Θ) and its absolute value. **(b)** Histogram of the absolute deviation angle ($|\Theta|$) distribution of hMSCs nuclei on the patterns. **(c)** Effective potential energy curve calculated using 6-14(b), the energy axis was shifted down by -1 in order to achieve better illustration.

We also observed a relatively large number of nuclei (17% of total nuclei) that are almost perpendicular to the direction of patterns ($80^\circ < |\Theta| < 90^\circ$). This shows up as a local maximum around $|\Theta| = 90^\circ$ in the orientation histogram of hMSCs nuclei (Figure 6-15(b)) and consequently as a second but smaller minimum in the potential energy curve (Figure 6-15(c)).

As we observed earlier about hMSCs on 10 μm and 25 μm stripes, the actin cap is highly aligned with the direction of the elongated cell and nucleus. Studies have shown that the actin cap is mostly aligned with a migrating nucleus in mouse embryonic fibroblasts on unpatterned substrates and plays the key role in determining the direction of nucleus elongation and translocation (Dong-Hwee Kim et al. 2014). The role of perinuclear actin stress fibers in regulating the orientation of the nucleus also was confirmed among Rat2 fibroblasts on isotropic substrates (Maninová & Vomastek 2016). However, among those nuclei of hMSCs that are perpendicular to the stripe directions, we observed nuclei that defied the direction of highly organized perinuclear actin stress fibers both among the cells that were branched and the more rounded cells (Figure 6-16).

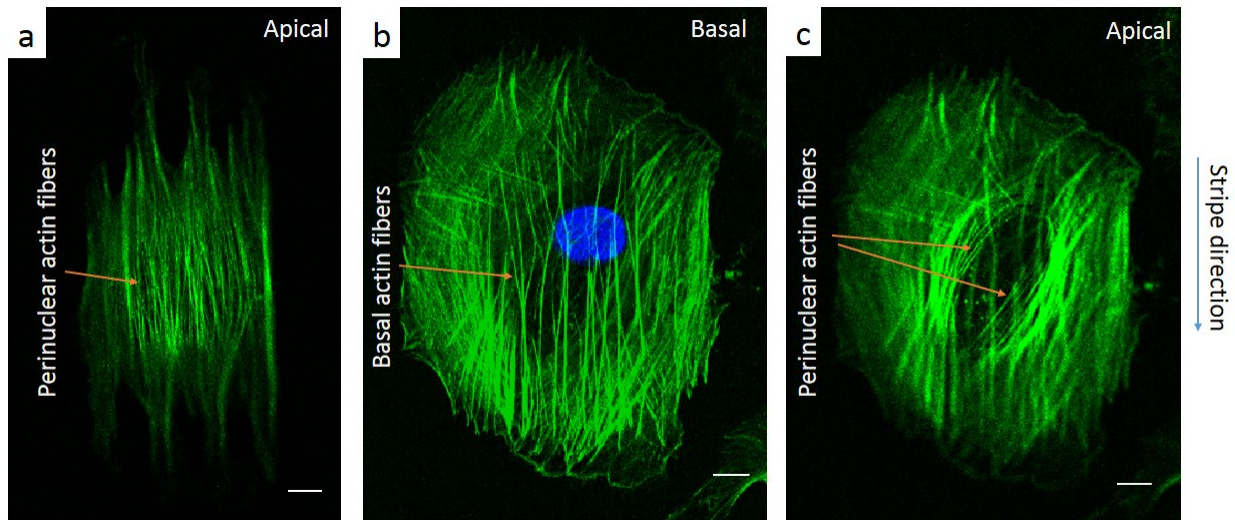


Figure 6-16: Perpendicular hMSCs nuclei that defy basal and perinuclear actin fibers on sub-nuclear strip patterns. (a) Apical focus plane of an hMSC that is confining to sub forming branches on the sub-nuclear strip patterns, the basal focus plane and nucleus is shown in Figure 6-11 (c). (b) Basal focus plane of a round shape hMSC that spreading wide on the sub-nuclear pattern, the basal actin fibers are thick, long and aligned with the stripe direction. The nucleus (blue) is almost perpendicular to the direction of stripe and basal stress fibers (c) Apical focus plane of the cell in Figure 6-16 (c), the perinuclear actin stress fibers on top of the nucleus are organised (aligned with each other) and not aligned with the direction of the nucleus. The actin cytoskeleton of hMSCs is stained with phalloidin and false coloured in green and nucleus is stained with and TO-PRO-3(false coloured in blue). Scale bars are 10 μm .

We hypothesise that the observation of perpendicular nuclei to the patterns can be explained by the basal actin fibers underneath and in the periphery of the nucleus (see Figure 5-11). These relatively short fibers end with focal adhesions (D.-H. Kim, Allison B. Chambliss, et al. 2013) and generate a force to push the nucleus towards the substrate (Hanson et al. 2015c).

As Figure 6-17 (a) shows, we think that if the cell initially lands on the substrate in a way so that it sits on two adjacent stripes, focal adhesions and consequently the actin fibers underneath and in the periphery of the nucleus can anchor the nucleus to the substrate and lock the orientation of the nucleus so that it is harder to change it using the force from perinuclear actin fibers. Figure 6-17(b) shows that the cell will land on two adjacent stripes only if the centre of the cell, assumed to be spherical before adhesion, remains in the purple band with the width of $d-s$. Therefore, the probability for the centre of the cell landing on this band (P_{double}), is given by the equation 6-1:

$$p_{double} = \frac{d-s}{s+l}$$

Equation 6-1

Where d is the diameter of the cell, s is the PDMS spacing between fibronectin stripes and l is the width of fibronectin stripes.

Using our measurement results for the diameter of detached hMSCs ($21.7 \pm 0.3 \mu\text{m}$ s.e.m. ($n=189$)) (see chapter 6.1), the probability for the hMSCs will be $\frac{21.7-11}{11+5} = \sim 66\%$, while for the 3T3 fibroblasts with their average diameter of ($17.2 \mu\text{m} \pm 0.3 \mu\text{m}$ s.e.m. ($n=119$)) (see chapter 5.1) will be $\frac{17.2-11}{11+5} = \sim 38\%$ which is much smaller. Furthermore, the likelihood of keeping the nucleus in a perpendicular orientation and resistance to the force coming from the actin cap fibers is higher if more focal adhesions can be formed on the stripes in the periphery and underneath the nucleus. Figure 6-17 (C) which is to scale for the size of hMSCs and 3T3 fibroblasts and the size of the pattern, clearly shows that there is more area on the stripes for hMSCs to form focal adhesions and consequently higher number of focal adhesion can be formed to support the nucleus in the perpendicular orientation. Therefore, we think this is the reason, we observed a high number of cells that are almost perpendicular to the stripe direction only among hMSCs.

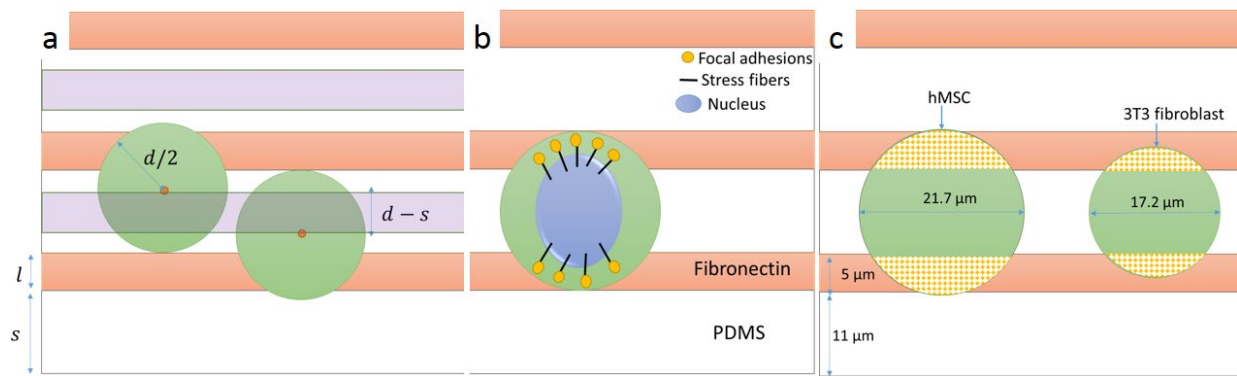


Figure 6-17: Schematic illustration for orientation of nucleus perpendicular to sub-nuclear stripes pattern. (a) Initial landing sites for the cell on the pattern in order to settle on two adjacent stripes. If the centre of the cell is in the purple band, the cell can touch two adjacent stripes. (b) Formation of basal actin fibers supported by focal adhesions underneath and in the periphery of the nucleus in order to lock the nucleus in a perpendicular position relative to strip direction. (c) Up to scale schematic illustration on available area for the cell (yellow dotted regions) to form focal adhesions on two adjacent fibronectin stripes.

In conclusion, we observe that fibroblasts and hMSCs show relatively similar behaviour on control, $25 \mu\text{m}$ and $10 \mu\text{m}$ fibronectin stripes. However, certain configurations of the stripes such as sub-nuclear patterns trigger radically different behaviours between the two cell lines.

Chapter 7:

Potential further avenues for studying substrate topography effects on cells

7.1 Raman micro-spectroscopy as a tool for studying the effect substrate topography on cells

7.1.1 Principles of Raman spectroscopy

Discovered by Sir C.V. Raman in 1928, Raman spectroscopy is a laser-based technique that can monitor vibrational, rotational and low-frequency modes of molecules. This technique relies on a form of inelastic scattering that is known as Raman scattering (Schäfer & Schmidt 2012). When monochromatic laser light interacts with a molecular structure, the vast majority of the incident photons scatter without any change in their energy and frequency. This type of elastic scattering is called Rayleigh scattering. In fact, during Rayleigh scattering, the sample absorbs one photon and releases another photon with the same energy and frequency (an elastic interaction) but most likely in a different direction from the incident photon (Figure 7-1). Because in this interaction, the molecule in the sample does not gain energy, it returns to its initial energy level after jumping to a higher energy level during the interaction (Figure 7-2). Approximately one of every 10^6 - 10^8 photons, scatters with a changed energy and frequency (an inelastic scattering event). These photons are known as Raman scattered photons. Most Raman scattered photons have less energy than the incoming photon: this is called Stokes Raman scattering and the frequency change of the incoming photon is the 'Stokes frequency shift'. In rare cases, the sample scatters photons producing with higher energy. This type of scattering is called 'Anti-Stokes' Raman scattering and the frequency increase is known as the 'Anti-Stokes frequency shift'.

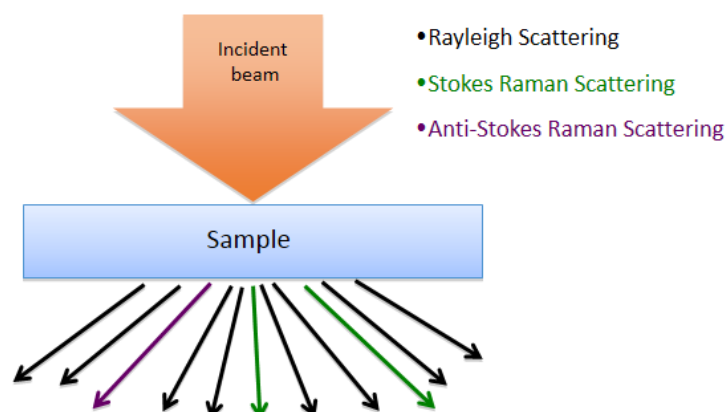


Figure 7-1: Different scattering modes. The red arrow representing incident monochromatic beam, black arrows representing more frequent elastic Rayleigh scattering photon, green arrows representing Stokes Raman scattered photons and purple representing rare Anti-Stokes Raman scattered photons. The arrow numbers are not up to scale. (Mamaghani 2015).

It is convenient to express the Raman shift in term of wavenumbers ($\tilde{\nu}$) instead of frequency shifts. The wavenumber is defined as the number of waves per centimetre and is given in terms of cm^{-1} while the frequency (ν) is the number of vibrations per second (Szymanski 1967). Therefore, the wavenumber is related to the frequency by the equation of $\tilde{\nu} = \nu / c$. If we suppose that the wavelength of an incident photon is λ_0 and the wavelength of a scattered photon is λ_1 , then the Raman wavenumber ($\Delta\tilde{\nu}$) can be obtained with the following formula:

$$\Delta\tilde{\nu} = \frac{1}{\lambda_0} - \frac{1}{\lambda_1} \quad \text{Equation 7-1}$$

Since usually, the wavelength of a scattered photon is longer than the incident photon, the wave number is usually positive. We can use the Einstein formula for the energy of a photon and derive the following relation between changes in energy (ΔE) and the frequency ($\Delta\nu$) change for the scattered photon (where c is the light speed $3 \times 10^8 \text{ m/s}$; h is the Plank constant $6.62 \times 10^{-34} \text{ m}^2\text{kg/s}$):

$$\nu = \frac{c}{\lambda} \Rightarrow \Delta\nu = \nu_0 - \nu_1 = c\Delta\tilde{\nu} \quad \text{Equation 7-2}$$

$$E = h\nu \Rightarrow \Delta E = E_0 - E_1 = hc\Delta\tilde{\nu} \quad \text{Equation 7-3}$$

As the conservation of energy law predicts, the energy gain or loss of scattered photons is equal to the energy loss or gain of the sample molecule and this is equal to the change in the vibrational ground states before and after the interaction with the photon (Figure 7-2). The vibrational ground states are unique for each chemical bond, such that the energy differences between the incident and scattered photon act as a fingerprint for each chemical bond. The fingerprint Raman shift of a band is highly

consistent. However, extreme changes in the environment in which the environment actively interacts with the molecule of interest can change the position of the fingerprint by a few cm^{-1} by altering symmetrical properties of stretching modes of certain chemical bonds (Giorgini et al. 2005).

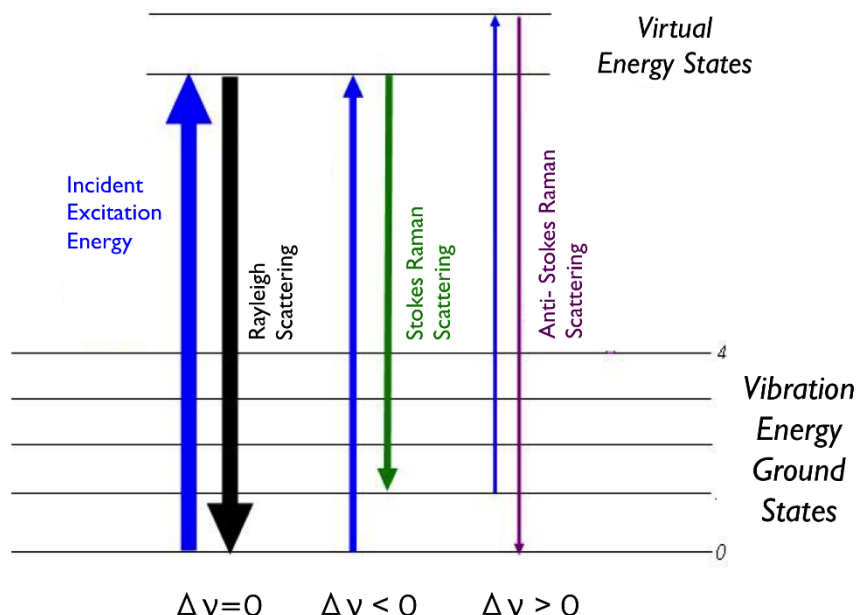


Figure 7-2: Energy level diagram of Raman and Rayleigh scattering. The frequency (ν) of an incident photon can increase, decrease or remain constant in Anti-Stokes Raman scattering, Stokes Raman Scattering and Rayleigh scattering respectively. After (Mamaghani 2015).

As Figure 7-2 shows, by monitoring the frequency of scattered photons and determining the intensity of them for every wave number (proportional to the Raman frequency shift), a spectrum is generated that can give a unique and precise indication of the chemical composition of the sample. The intensity of photons with certain Raman shifts is an indicator of the level of the corresponding chemical bond. For abundant biological components such as DNA, RNA or proteins, the Raman spectrum and dominant wave numbers are well known. As a result, we can monitor the common components of biological samples.

A band-pass optical filter, known as a maxline laser transmitting filter (Figure 7-3), narrows down laser light around its peak wavelength. A dichroic beam splitter, long wave pass filter reflects the laser beam. It is transparent to scattered photons and guides the light to the objective lens, which focuses the light onto the point of interest on the sample and collects scattered photons from the sample. The photons with a longer wavelength than the incident photons pass through the long wave pass filter and are focused by an optical lens onto a narrow slit ($\sim 25\mu\text{m}$) spectrometer. The frequency of the

collected photons is measured by a spectrometer and converted to a digital signal by a CCD camera. A computer saves and analyses the recorded data.

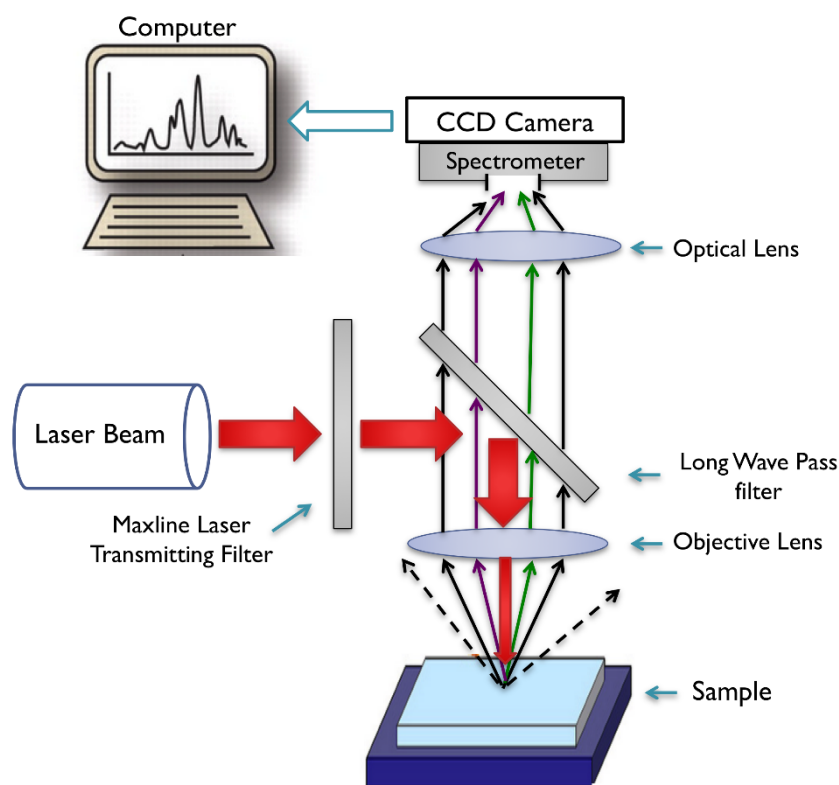


Figure 7-3: Schematic diagram of spontaneous confocal Raman micro-spectroscopy. After (Mamaghani 2015).

7.1.2 Raman micro-spectroscopy for cells

Raman micro-spectroscopy of cells is a powerful tool to study the cells as it simultaneously can be used for the study of cell morphology and imaging of subcellular organelles such as the nucleus (Okotrub et al. 2015), Golgi apparatus, mitochondria and cytosol (Klein et al. 2012)(Ichimura et al. 2014). A full Raman scan of a cell gives a comprehensive morpho-chemical insight into it. Once the spectra are acquired from the cell, it is possible to extract the desired chemical and morphological data. For example, when the spectra are being recorded for the visualization of the nucleus, other subcellular organelles or the spatial distribution of actin elements can be studied using the same spectra. However, in the conventional fluorescent microscopy, only stained elements can be probed and there is no opportunity to extract more information about non-stained cellular elements from the same data later. Staining or cell transfection is required for the fluorescent microscopy. Either of these

methods is invasive (by fixing) or can have some impact on cell behaviour (transfection). (See chapter 7.2). However, Raman micro-spectroscopy is capable of both fixed and live cell imaging as it is a non-invasive, non-destructive and non-contact method (Liu et al. 2014), particularly when the laser that has been used for the spectroscopy emits only low energy photons within the visible spectrum ($E \approx 1.6\text{-}2.4\text{ eV}$).

7.1.2.1 Raman spectroscopy of cell on the PDMS substrate

In our first attempt to use Raman micro-spectroscopy to study the effect of patterned substrates on adherent fibroblast cells, Raman spectra were acquired from cells cultured on unpatterned PDMS substrates and fixed with formaldehyde (4%) using a 785 nm laser as the light source (Figure 7-4).

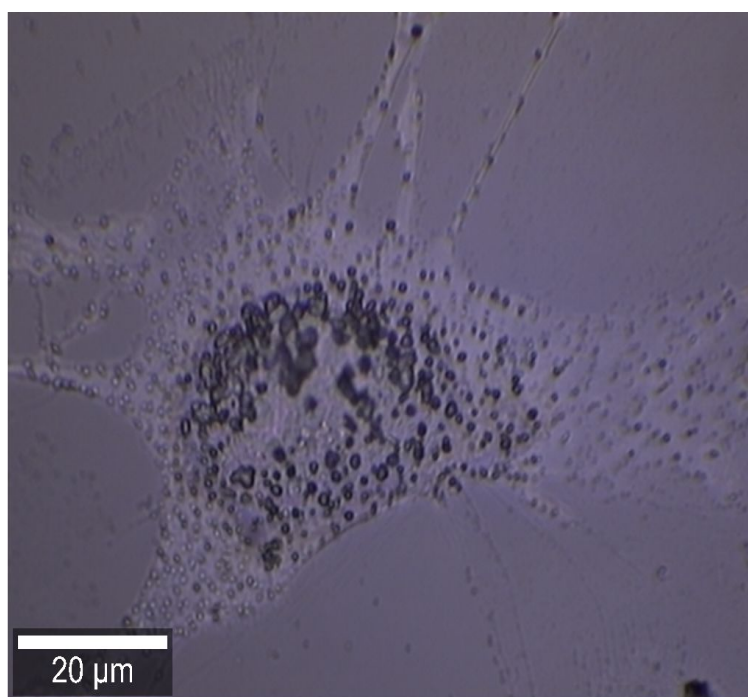


Figure 7-4: Bright field image of a 4% formaldehyde fixed adherent 3T3 cell on fibronectin-coated PDMS surface prepared for the Raman micro-spectroscopy.

The spectra were gathered from the cell area with a resolution of $1\mu\text{m}$ (pixel size= $1\mu\text{m} \times 1\mu\text{m}$). The spectra contained three major peaks centred at 492 cm^{-1} , 617 cm^{-1} and 712 cm^{-1} . The Raman shift centred at 492 cm^{-1} (Figure 7-5(a)) depends on the stretching mode of Si-O-Si bonds. The shift located at the 617 cm^{-1} (Figure 7-5(b)) is associated with the symmetric stretching and rocking mode of Si-CH₃ bond. The shift located at 712 cm^{-1} (Figure 7-5(c)) is associated with the symmetric stretching mode of Si-C bonds. These peaks have been observed previously in the spectrum of PDMS

(Cai et al. 2010). The spatial distribution of these three peaks across the formaldehyde-fixed cell clearly reveals the shape of the cell (Figure 7-5) in a darker colour compared to the substrate, which means that the CCD camera of the Raman microscope is receiving fewer scattered photons from these regions. This shows that the dominant Raman scattered photons are coming from the PDMS substrate and the cell body is acting as a shield for these scattered photons.

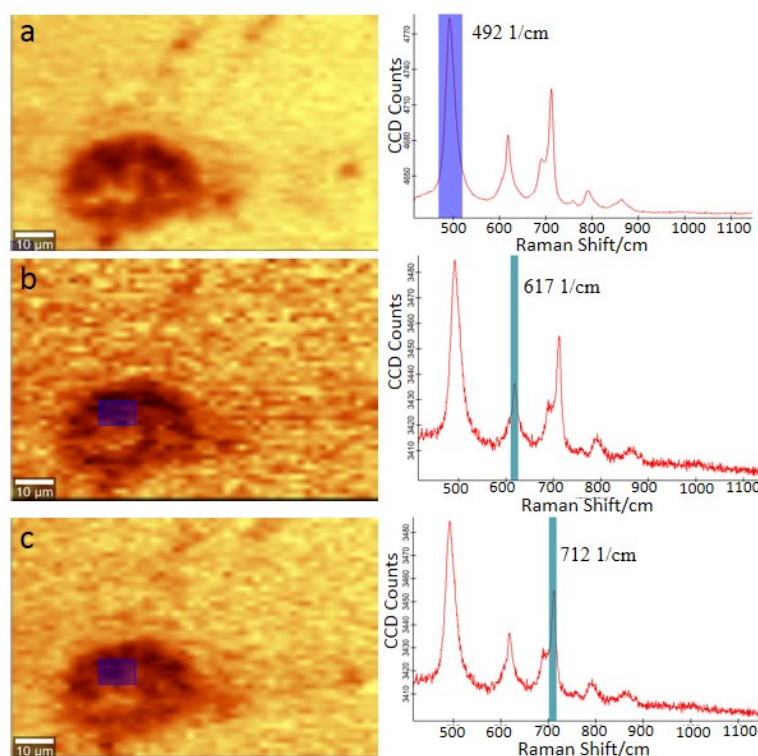


Figure 7-5: Spatial Raman micro-spectroscopic map of a formaldehyde 3T3 cells spreading on fibronectin-coated PDMS substrate. Three dominant peaks have been observed in the spectra, 492, 617 and 712 cm^{-1} . (a) Spatial map of a dominant peak centred at 492 cm^{-1} , which is associated with the Si-O-Si covalent bond. (b) Spatial map of a peak centred at 617 cm^{-1} , which is associated with the symmetric stretching and rocking mode of Si-CH₃ bond. (c) Spatial map of the peak centred at 712 cm^{-1} , which is associated with the symmetric stretching mode of Si-C bonds. These three bonds are significantly present in the PDMS substrate.

Despite the fact that PDMS scattering is stronger than the scattering from the cell, it is still possible to observe small peaks that belong to the biological molecules of the cell. The spatial distribution of the intensity of the peak located at 730 cm^{-1} (Figure 7-6(a)) shows that the peak is more intense within the cell area. This peak is associated with the ring breathing mode of adenine in DNA and RNA bases (Da Costa et al. 2018). Comparing the spatial distribution of the 730 cm^{-1} peak (Figure 7-6(a)) with the bright field image of the cell (Figure 7-4) shows that despite the high background signal from the PDMS substrate, the spatial distribution of the peak still is indicative of the nucleus of the cell.

Because of the strong background from the PDMS substrate, vital information from many important peaks that are associated with biological materials is missing. The peak centred in 1005 cm^{-1} is one of these peaks. The background noise from PDMS makes it hard to see the spatial distribution of the phenylalanine peak (Figure 7-6(b)). The peak is associated with the symmetric aromatic ring-breathing mode of the phenylalanine molecule. The phenylalanine peak is usually a visible strong peak and is one of the hallmarks for the spectra of all eukaryotic cells.

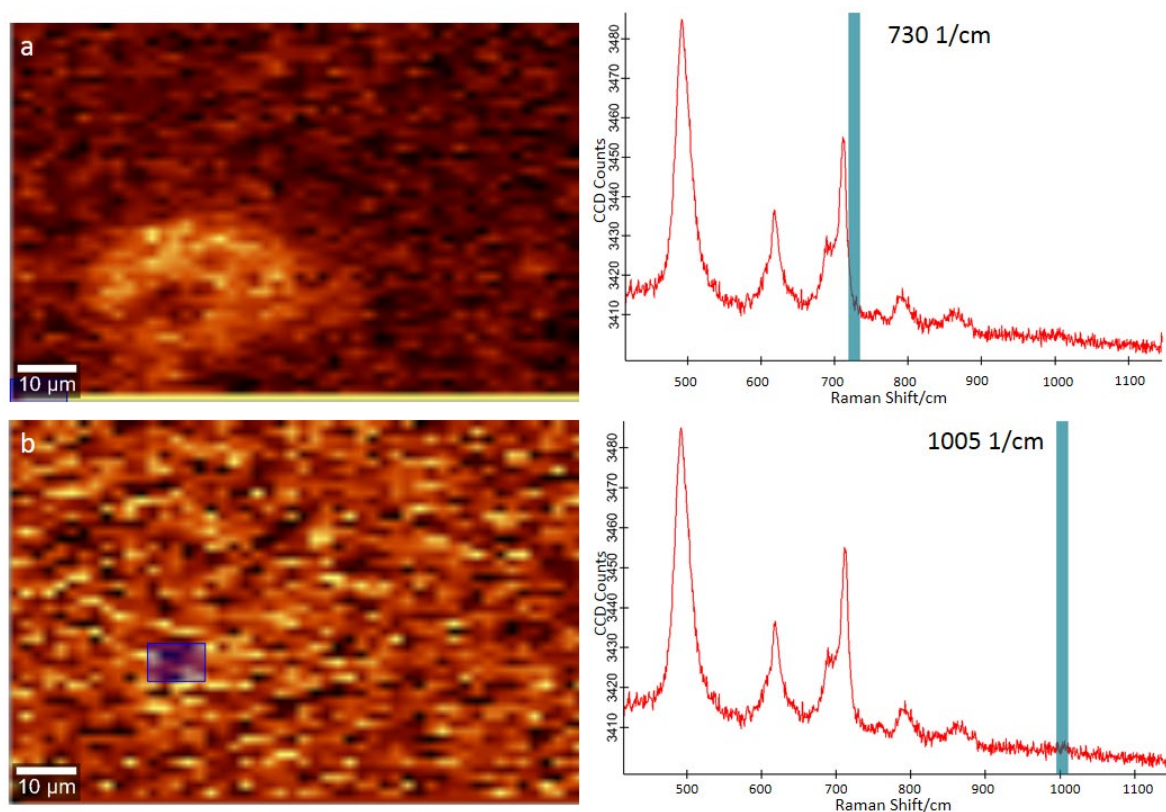


Figure 7-6: Spatial Raman micro-spectroscopic map of a protein and DNA/RNA associated with a formaldehyde-fixed 3T3 cell spreading on the fibronectin PDMS substrate. (a)& (b) Spatial Raman micro-spectroscopic maps of a DNA/RNA associated peak (730 cm^{-1}) and protein associated peak (1005 cm^{-1}).

7.1.2.2 Raman Setup for 2D patterns

PDMS substrates are some of the most common substrates among micro-patterned substrates to study the topological and chemical effects of substrates on the cell or tissue. However as shown in the previous section, the fact that this polymer generates a strong Raman signal has always been a discouraging factor for the researcher to use Raman micro-spectroscopy in these studies. This deprives the field of a highly versatile technique of Raman spectroscopy. To overcome the noise from

PDMS, we have used a commercially available prototype of gold-coated mirrors with an 80nm protective silica layer on them (see Figure 2-19 for details of mirror structure). The mirror reflects about 96% of light at 785 nm (Mid-Infrared Enhanced Protected Gold Mirrors, www.thorlabs.com). In the first attempt, detached cells were fixed with methanol and the spatial distribution of Raman spectra was acquired from the cells with a resolution of $1.1\mu\text{m}$ (pixel size= $1.1\mu\text{m} \times 1.1\mu\text{m}$). As methanol evaporates quickly from the cells, it is believed to not have a significant contribution to the Raman signal. The background noise was subtracted from the raw spectra from the cell (Figure 7-7 (a)). Afterwards, all spectra were processed by automated cosmic spike removal, baseline-flattening using a moving average, peak sharpening and automated smoothing steps (Mamaghani 2015).

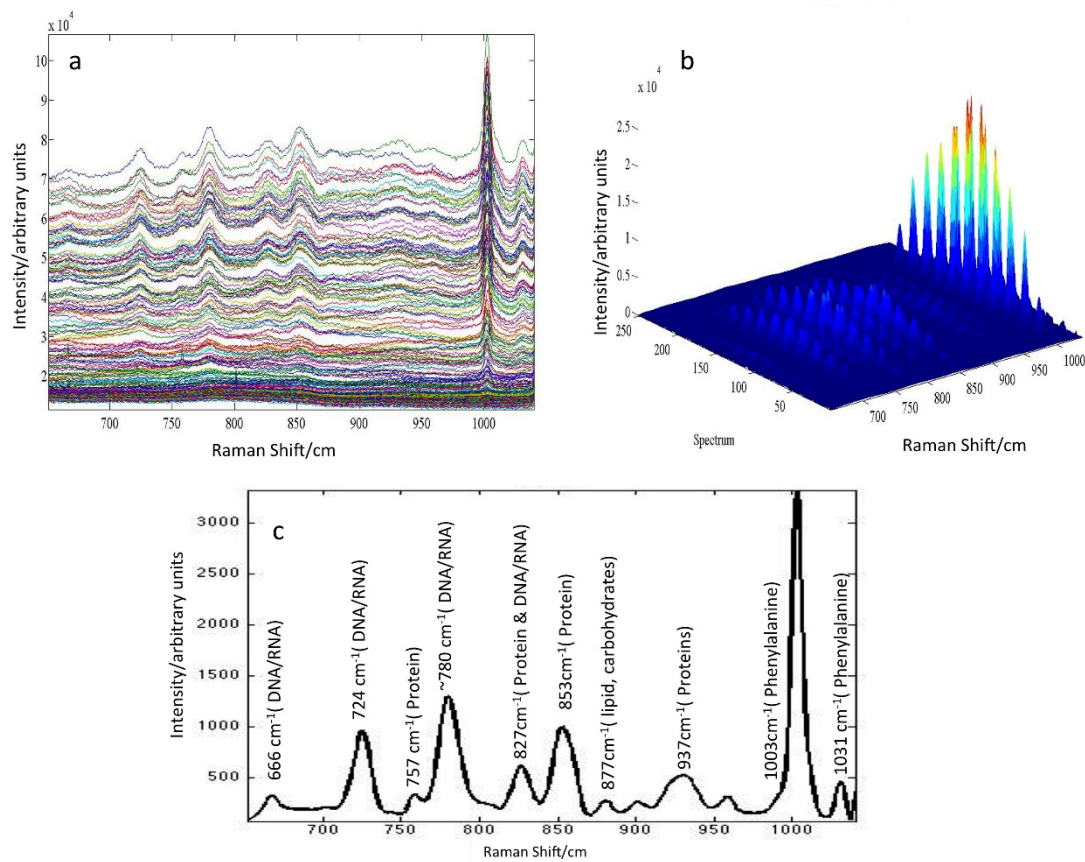


Figure 7-7: Raman spectra from a methanol fixed 3T3 cell. (a) Raw data from the cell area gathered from $1.1\mu\text{m} \times 1.1\mu\text{m}$ pixels. (b) 3D representation of the raw spectra, highlighting dominant peaks across the cell area. (c) The average processed spectra across the cell area after subtraction of baseline and cosmic spikes and application of smoothing function. Important peaks and their biological assignments are highlighted.

The processed spectra (Figure 7-7 (c)) have very distinct and strong Raman peaks that are associated only with the biological components of the cells. This confirms the effectiveness of our proposed setup in spectra acquisition from the cells. In the spectra, we have observed many peaks resulting from the

biological molecules (Figure 7-7 (c)). We have peaks representing nucleic acids (666 cm^{-1} , 724 cm^{-1} and 780 cm^{-1}), some representing proteins (757 cm^{-1} , 853 cm^{-1} and 937 cm^{-1}), and some are a mixture of two elements such as lipid and proteins. Table 7-1 gives a summary of the assignments for these peaks in the literature. Unlike the bare PDMS substrate, there is no stray peak from the substrate. This confirms the potential effectiveness of the setup that we propose for shielding the PDMS substrate with 3D patterns later in this chapter.

Table 7-1: Raman peak assignments of dominant peaks. (Movasaghi *et al.* 2007).

Raman peak	Assignment
666 cm^{-1}	G, T (ring-breathing modes in the DNA bases)-tyrosine-G backbone in RNA
724 cm^{-1}	DNA/RNA (adenine ring breathing)
757 cm^{-1}	Proteins (tryptophan symmetric ring breathing)
780 cm^{-1}	778 cm^{-1} : DNA/RNA (pyrimidin, ring breathing); 784 cm^{-1} : DNA (backbone O-P-O stretching)
827 cm^{-1}	Proteins (proline, hydroxyproline, out-of-plane ring breathing in tyrosine); DNA/RNA (asymmetric O-P-O stretching)
853 cm^{-1}	Proteins (proline C-C stretch in collagen; also tyrosine ring breathing in other proteins); carbohydrates (glycogen, polysaccharides C-O-C stretching)
877 cm^{-1}	C-C-N ⁺ symmetric stretching (lipids), C-O-C ring (carbohydrate)
937 cm^{-1}	Proteins (collagen type I C-C stretching, α -helix C-C stretching); carbohydrates (glycogen), Proline (collagen type I), Amino acid side chain vibrations of proline and hydroxyproline, as well as a (C-C) vibration of the collagen backbone C-C backbone (collagen assignment)
1003 cm^{-1}	Proteins (symmetric ring breathing in phenylalanine)
1031 cm^{-1}	Proteins (collagen, keratin, C-N stretching in proteins, C-H in-plane bending of phenylalanine); lipids (phospholipids); carbohydrates (polysaccharides)

Although every peak has valuable information about the cellular structure, we are more interested in the peaks representing nuclear structure. Nuclear mechanotransduction plays a crucial role in many biological processes of the cell, including migration, adhesion, polarization and proliferation (Dahl, Alexandre J.S. Ribeiro, et al. 2008). The knowledge that can be obtained about nuclear mechanics and

deformation from current techniques including Atomic Force Microscopy and fluorescent microscopy remains at the nuclear level (Hanson et al. 2015a). However, the possibility of looking at the sub-nuclear level with Raman micro-spectroscopy is a unique opportunity for us to shed light on the nuclear morphology and chemical composition with an unprecedented level of detail. Combination of the Raman micro-spectroscopy with the patterned substrate can give us a powerful tool to put a desired deformation to the cytoskeleton and nucleus and probe it with its tiniest chemical and morphological details using Raman micro-spectroscopy.

We have looked at the spatial distribution of the strong peak centred at 780 cm^{-1} to determine the nuclear structure (Figure 7-8). The peak located at 780 cm^{-1} is actually the superposition of two overlapping peaks. A peak at 778 cm^{-1} that is associated with ring breathing mode of pyrimidine derivative molecules (cytosine (C), thymine (T), and uracil (U)) and a second peak that is centred at 784 cm^{-1} which is associated with the symmetric stretching mode of O-P-O bond in the DNA backbone (Movasaghi *et al.* 2007). As a result, the peak around 780 cm^{-1} is representative of both the DNA and RNA content of the cell. As we can see, the intensity of the peak is highest in the middle of the cell (dark red); we believe that region is the nucleus and the lower concentration around this corresponds to the RNA content in the cytoskeleton (dark red). Due to the effects of the fixation method, there is a small amount of cellular material around the cell (light green). However, this problem has been solved for attached cells, as it is possible to fix the cells on the mirror without suspending them in the fixing solution (Figure 7-8).

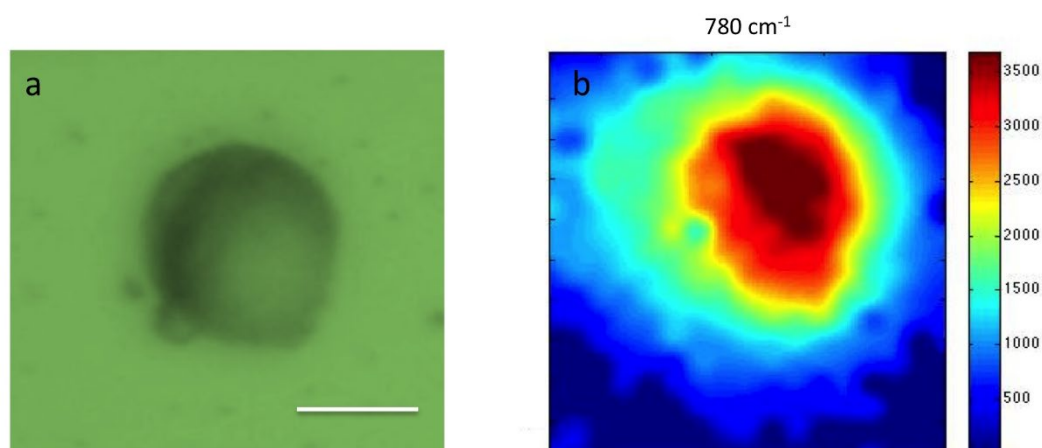


Figure 7-8: Spatial Raman micro-spectroscopic map of a DNA/RNA associated peak (780 cm^{-1}) of a methanol-fixed 3T3 cell on the silica-coated gold mirror. (a) Bright field image of the cell on the mirror. (b) Spatial Raman map of the peak representing a high concentration of nucleic acids in the nucleus (dark red), RNA content of the cytoplasm (light red), cellular content around residual due to the fixation process (light green) and absence of DNA/RNA peaks on the gold mirror (blue). Scale bar is $10\mu\text{m}$.

7.1.2.3 Cell adhesion to the silica protected gold mirrors

As we aim to study the effect of micropatterned substrates on the adherent cells such as 3T3 fibroblasts or hMSCs, we need to quantify the spreading of these cells on our proposed setup. 3T3 cells were grown on the mirror for 12 hours and then fixed with formaldehyde to perform the microscopy. The silica protecting layer on the gold mirror has provided enough stiffness for spreading of the cells and shielded the toxic effect of gold on cells (Figure 7-9).

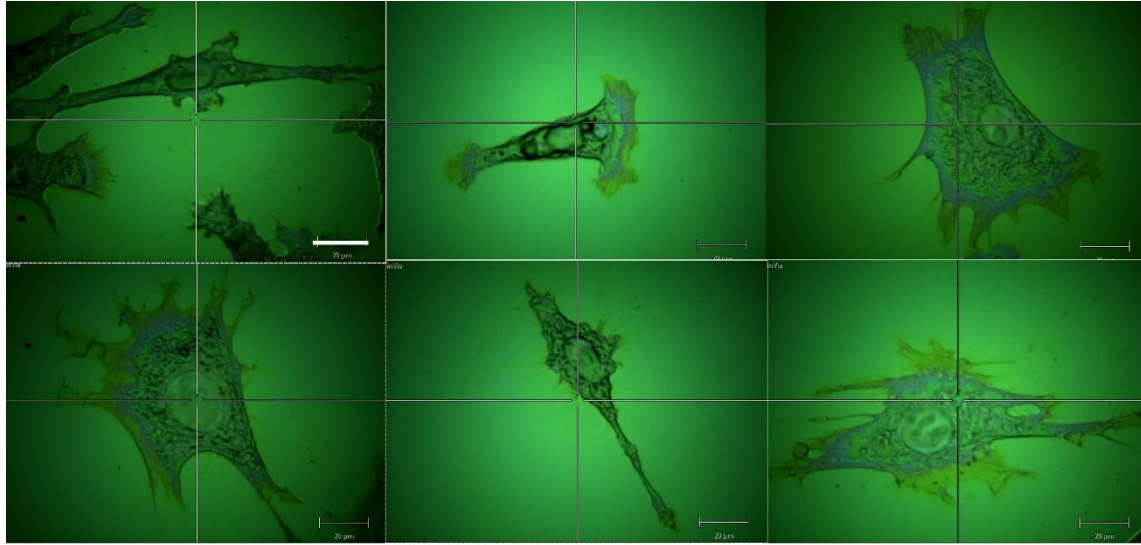


Figure 7-9: Formaldehyde fixed NIH/3T3 cells after 12 hours spreading on the silica protected the gold mirror. The silica layer has enough stiffness to support the spreading of the cells. Diverse patterns of the spreading and elongation are observed among the cells as it has been observed among the cells spreading on the fibronectin-coated substrates. Scale bars are 20 μ m.

The cells spread less on the mirrors ($1670 \pm 130.1 \mu\text{m}^2$ s.e.m. (n=67)) compared to the cells grown on the fibronectin-coated substrate ($4176 \pm 187.4 \mu\text{m}^2$ s.e.m. (n=65)) (Figure 7-10(a)). This is expected as fibronectin is a strong enhancing molecule for the cell adhesion complexes and promotes cell adhesion (see chapter 1-6).

For the fibroblasts on the silica-coated mirror, the aspect ratio of the cells (2.69 ± 0.21 s.e.m (n=67)) was increased compared to the cells on a fibronectin-coated substrate (1.72 ± 0.07 (n=81)) (Figure 7-10(b)). The Young's modulus of silica (in its amorphous form) is reported as around 70 GPa (Dahmani et al. 1998); the Young's modulus of polystyrene culture flask is approximately 3 GPa (Miyake et al. 2006) while the Young's modulus of PDMS (mixing ratio of 10:1 (base: elastomer)) is 580 kPa (Park et al. 2010). Previous studies have shown that the 3T3 fibroblasts elongate more on

stiffer 2D substrates (Lee et al. 2013). Therefore, we think that the higher aspect ratio on silica coated mirrors results from the higher stiffness of these mirrors compared to PDMS substrates.

We think that using the micro-contact printing techniques to fabricate our fibronectin coated patterns (see chapter 2.6 for details), it is possible to print 2D fibronectin patterns on this setup. And as we showed earlier in this chapter, the Raman micro-spectroscopy of cells can be performed on this setup in order to visualize the sub-cellular structure of the cells on these patterns (see chapter 8.2 for more suggestion).

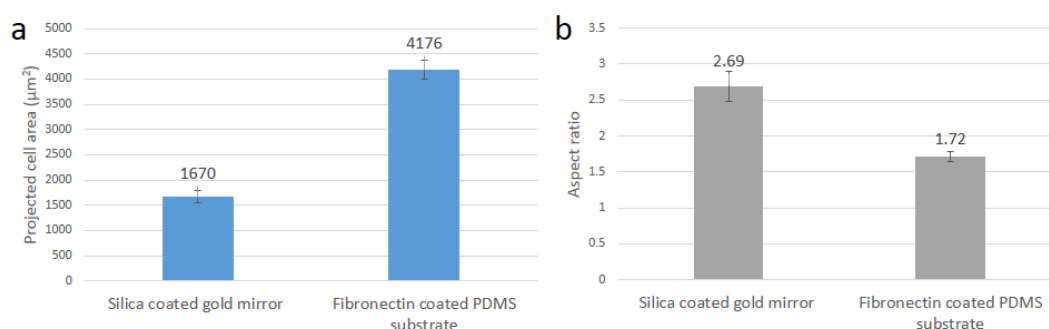


Figure 7-10: Morphological parameters of 3T3 cells spreading on a silica-coated gold mirror and on the fibronectin-coated PDMS substrate. (a)& (b) Projected cell area and aspect ratio of the cells in their steady-state adhesion phase on silica-coated gold mirrors and the fibronectin-coated substrate. Error bars are s.e.m.

7.1.2.4 Raman Setup for 3D patterns

PDMS is widely used in biomedical applications for substrate fabrication, microfluidics etc. (Toh et al. 2007). A wide range of patterns that are fabricated for cell study is 3D patterns (see chapter 3 for more details). This motivated us to fabricate a setup in order to overcome the PDMS background signal issue for 3D patterns. Inspired by the structure of the gold-coated mirror that we used earlier (see chapter 7.1.2.1), we proposed a new setup that can open new avenues in the application of Raman spectroscopy for micro-patterned substrates and in the field of microfluidics. Figure 7-11 (a) shows a schematic illustration of our novel setup.

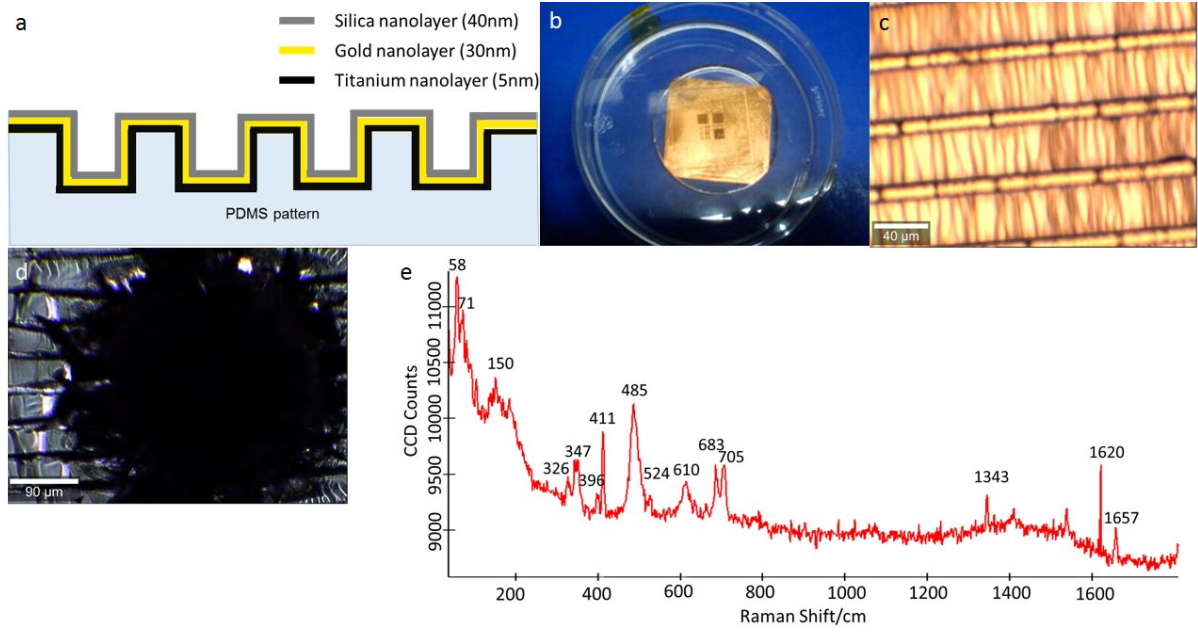


Figure 7-11: Proposed novel setup to shield the Raman signal of the 3D PDMS patterns. (a) Schematic view of different nano-layer deposition on the 3D PDMS pattern. **(b)** Macroscopic view of a ridge-groove pattern coated using e-beam evaporator. **(c)** Top microscopic view of the ridge (10 μm) - groove (40 μm) PDMS patterns. **(d)** The proposed pattern burnt by 488 nm laser. **(e)** Raman spectrum collected from the proposed pattern with 785 nm laser.

In this setup, we use an e-beam evaporator (see chapter 2.10.2 for details of the technique) to deposit nano-layers of metal in order to shield the background signal from the PDMS for ridge-groove 3D patterns (Figure 7-11(b)). A layer of silica will increase the biocompatibility of the pattern for cell adhesion. A bare gold substrate has shown weak biocompatibility for the NIH3T3 cells adhesion (Yoon & Mofrad 2011). However, a silica layer can act as a protective layer to improve cell adhesion (Yoon & Mofrad 2011). In addition, the silica layer stabilizes the gold layer on the patterns and prevents it from erosion or being washed away during handling steps for culturing the cell on the patterns.

To calculate the exact range of the metal layer thickness that is required for shielding the Raman signal from the underlying PDMS substrate, we need to calculate the skin depth of the metal layer.

The amplitude of the incident electrical magnetic wave (E) as it propagates through a conductor changes by time and by the depth of penetration (z). By solving Maxwell equations inside the conductor, we can calculate the amplitude dependent on time and depth using equation 7-4 (Fitzpatrick, 2006):

$$E = E_0 e^{i(kz - \omega t)} \quad \text{Equation 7-4}$$

Where E_0 is the amplitude of the incident wave on the surface of the conductor, $\omega=2\pi\nu$ is the angular frequency and k is the complex wave number, which is given by equation 7-5 (Fitzpatrick, 2006):

$$k^2 = \mu\omega (\varepsilon\omega + i\sigma) \quad \text{Equation 7-5}$$

where μ is the absolute magnetic permeability of the conductor ($\mu = \mu_0 \mu_r$), ε is the absolute permittivity of the conductor ($\varepsilon = \varepsilon_r \varepsilon_0$) and σ is the conductivity of the conductor. In the quasi-static regime ($\sigma \gg \varepsilon\omega$), we can approximate k using Equation 7-6:

$$k \approx \sqrt{i\mu\omega\sigma} = \sqrt{\frac{\mu\omega\sigma}{2}} (1 + i) = k_r + ik_i \quad \text{Equation 7-6}$$

where k_r and k_i are real and imaginary parts of k . Therefore, we can approximate the amplitude of the propagating wave using equation 7-7:

$$E = E_0 e^{-\frac{z}{\delta}} e^{i(k_r z - \omega t)} \quad \text{Equation 7-7}$$

The first term ($E_0 e^{-\frac{z}{\delta}}$) shows an exponential decay in the amplitude of the wave while the second term showing a pure oscillation. Based on this, we define δ as the skin depth of the conductor which literally means the depth in which the amplitude of the incident electromagnetic wave reduces by 1/e. Equation 7-8 gives the formula for skin depth for a conductor.

$$\delta = \frac{1}{k_i} = \sqrt{\frac{2}{\mu\omega\sigma}} = \sqrt{\frac{\rho\lambda}{\pi c \mu}} \quad \text{Equation 7-8}$$

Where ρ is the resistivity of the conductor, ν is the frequency of the emitted light, λ is the wavelength of the emitting light and $c = \frac{1}{\sqrt{\mu_0 \varepsilon_0}}$ is the speed of light in vacuum. Substituting 785 nm for the wavelength and other constants for the gold (MIT Material Property Database/Gold) and titanium (MIT Material Property Database/Titanium, 1999) the skin depths are approximately 3.9 nm and 16.5 nm for gold and titanium respectively. Considering the fact that the optical path for scattered photons from PDMS is twice the thickness of the shielding metal (d), the effective depth of the metal will be double. Therefore, 30 nm of the gold coating will attenuate the background signal by approximately $e^{-\frac{2d}{\delta}} = e^{-\frac{60 \text{ nm}}{3.9 \text{ nm}}} \cong 2 \times 10^{-7}$ and the 5nm titanium layer will attenuate the signal by $e^{-\frac{2d}{\delta}} = e^{-\frac{10 \text{ nm}}{16.5 \text{ nm}}} \cong 0.5$. Consequently, the whole metal coating will approximately attenuated the background signal of PDMS by 10^{-7} compared to the situation when the PDMS was directly hit by the laser beam. It worth mentioning that due to the reflection at the boundary of two conductors with different optical properties, the exact calculation of effective attenuation is a little bit more complicated than simply multiplying the attenuation of two layers (Deng et al. 2009). However, we believe that this doesn't change our general conclusion about the effectiveness of the nanolayers in shielding the PDMS background as the beam is attenuated significantly ($\sim 2 \times 10^{-7}$) when it reaches the titanium layer.

Furthermore, the metal coating will act as a mirror for the emitted laser beam to double the Raman scattering in comparison to a transparent substrate. In fact, from the incoming photons, only a tiny portion (10^{-6} - 10^{-8}) of them get scattered inelastically; others either don't interact with the specimen or scatter elastically in an isotropic pattern (Rayleigh scattering). The gold layer acts as a mirror by reflecting these photons. The reflected photons act as a virtual light source and it interacts again with the specimen to produce a new set of Raman scattered photons. The reflection coefficient of the gold layer depends on the laser wavelength. The exact reflection coefficient (amplitude) is given by Equation 7-9:

$$r = \frac{\eta_2 - \eta_1}{\eta_2 + \eta_1} = \frac{\sqrt{\frac{\mu_2(v)}{\epsilon_2(v)}} - \sqrt{\frac{\mu_1(v)}{\epsilon_1(v)}}}{\sqrt{\frac{\mu_2(v)}{\epsilon_2(v)}} + \sqrt{\frac{\mu_1(v)}{\epsilon_1(v)}}} \quad \text{Equation 7-9}$$

For lasers in the visible range of the spectrum is between 70% to 97% for gold-coated mirrors (*Mid-Infrared Enhanced Protected Gold Mirrors*, www.thorlabs.com). This is a big advantage for our proposed setup particularly for which live cell micro-spectroscopy which low laser power is needed to avoid toxic effects on cells (Liu et al. 2008).

Deposition of silica on a nanolayer gold film at the temperature that is not distorting for cured PDMS pattern is also a well-established method and the thickness of silica can be as thin as 5 nm (WIKTOR et al. 2015). However, we observed microscopic wrinkles formed in our patterns after deposition of nanolayers. (Figure 7-11(c)). In this preliminary work, we have not attempted to address the problem. However, we suggest that the problem can partly be solved by decreasing electron beam current which results in a lower deposition rate of the nanolayers and less heating of the PDMS pattern in the coating process (see chapter 2.10.2 for more details).

In contrast to the theory, the Raman spectra (Figure 7-11(e)) of nano-layered PDMS patterns showed that the peaks we observed for PDMS (peaks centred at 492 cm^{-1} , 617 cm^{-1} and 712 cm^{-1}) are not completely removed. However, the peaks were shifted to 485 cm^{-1} , 610 cm^{-1} and 705 cm^{-1} from the nano-layered PDMS substrates. We think the reason for the shift is because of rising temperature as the result of heating as temperature change can shift Raman peaks (Kingma & Hemley 1994).

The heating issue showed itself more when we used the high power of the laser beam particularly with 488 nm laser which allowed only 15 mW of power before burning down the coating and locally distortion of the pattern (Figure 7-11(d)). However, we were able to perform microscopy with power as high as 120 mW with a 785 nm laser beam.

The fact that we did not observe silica peaks that have been observed in thin films ($\sim 60 \text{ nm}$) silica samples such as 438 cm^{-1} , 1200 cm^{-1} and 1084 cm^{-1} (Borowicz et al. 2012) shows that our Raman signal comes mostly from the PDMS underneath the coating. As we showed earlier theoretically, the

nanolayer has to attenuate the signal from PDMS; however, we hypothesize that the laser beam locally melts the coating and reaches the PDMS. We think that keeping medium on the top of the cells can facilitate heat dissipation and consequently address the heating issue of the patterns.

Using the setups that we have designed that allows us to perform Raman microscopy of cells on both 2D and 3D substrate patterns, we can acquire unprecedented insight about cellular response to the patterns in a micrometre scale non-invasively. We can answer important questions about the morpho-chemical changes to the cells and their nuclei on the topographical patterns both among live and fixed cells which means that we can study the dynamics of cell behaviour on the patterns. We have discussed further the important questions about the effect of substrate patterns that can be addressed by Raman microscopy in suggested future work in chapter 8.

7.2 Genetic modification of cells for live cell imaging

Some synthetic or organic fluorescent stains that can pass through a live cell membrane can be used to permit time-lapse fluorescent microscopy of different organelles inside the cell. However, these dyes usually have toxic effects on the cell as they usually need a long exposure time during the staining process (Ge et al. 2013). Furthermore, application of fluorophores imposes serious photobleaching limitations for microscopy over an extended period of times (Stephens & Allan 2003). One of the popular approaches to address this problem is introducing a section of foreign DNA (plasmid) that incorporates to the genome of the cell and enables the cells to produce a bioluminescent protein that fuses into the desired structure of the cell and therefore helps to visualize the structure under the fluorescent microscope. One of the main advantages of this method is that it can be used for time-lapse fluorescent microscopy as the internal machinery of the cell continues to produce the bioluminescent protein during imaging.

7.2.1 Cell transfection for visualization of the actin cytoskeleton

As was mentioned in the first chapter, the actin cytoskeleton plays a pivotal role in the mechanical machinery of the cell (see chapter 1.2). In order to visualize the cytoskeleton of live cells, we transfected 3T3 cell lines with pCMVLifeAct-TagGFP2 plasmid vector. The vector encodes the LifeAct which is a 17-amino acid peptide derived from a yeast (*Saccharomyces cerevisiae*) protein called Abp140 (Riedl et al. 2008). The peptide has a high affinity to filamentous actin (F-actin) and

therefore when the peptide is fused to the c-terminus of a GFP tag (TagGFP2) (Figure 7-12(a)), it stains the actin cytoskeleton of eukaryotic cells (Riedl et al. 2008) (Figure 7-12(b)(c)& (d)).

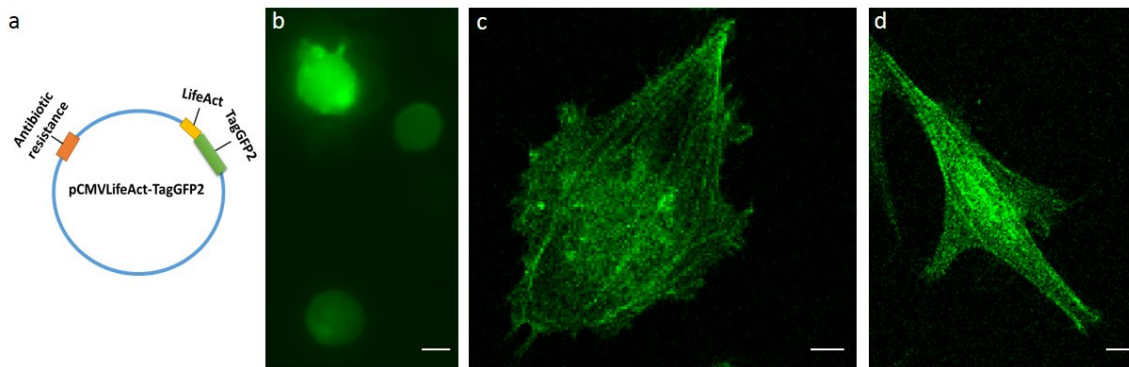


Figure 7-12: Actin visualization using pCMVLifeAct-TagGFP2 transfection. (a) Genetic map of the pCMVLifeAct-TagGFP2 plasmid vector. The information for this schematic is deduced from (ibidi®-cells in focus). (b) Fluorescent microscopy of suspended 3T3 fibroblasts transfected by pCMVLifeAct-TagGFP2 illuminated by a mercury lamp. (c)&(d) Fluorescent microscopy of adherent 3T3 fibroblasts transfected by pCMVLifeAct-TagGFP2 illuminated by 488 nm laser light (false-colored green). Scale bars are 10 μm.

7.2.1.1 The effect of LifeAct-GFP transfection on cellular morphology

Incorporation of a relatively large foreign DNA (4.7 kb) with the genome of the cell can significantly influence the machinery of the cell. Furthermore, we observed that the process of introduction of the DNA plasmid contained in liposome vesicles puts stress on the cell. As Figure 7-13 shows with increasing concentration of liposomes used for transfection, we observed more blebbed cells, which are a classical sign of apoptotic cell death. Studies also have shown that liposome intake can induce apoptotic cell death (Aramaki et al. 1999).

Previously it has been qualitatively reported that transfection of cells with fluorescent proteins can cause some abnormality in the morphology of the cell (Jensen 2013). We quantified the morphological changes that the transfection procedure induces on the cell. Our results show that the 3T3 cells that have undergone a transfection process spread less on the culture flask compared to unmodified control 3T3 cells. Both projected cell area ($2738 \pm 169 \mu\text{m}^2$ s.e.m (n=86)) and Feret's diameter ($111.6 \pm 3.6 \mu\text{m}$ s.e.m ((n=86)) of transfected cells were smaller compared to projected cell area ($3331 \pm 196 \mu\text{m}^2$ s.e.m (n=81)) and Feret's diameter ($131.0 \pm 3.9 \mu\text{m}$ s.e.m (n=81)) of control fibroblasts (Figure 7-14(a) &(b)).

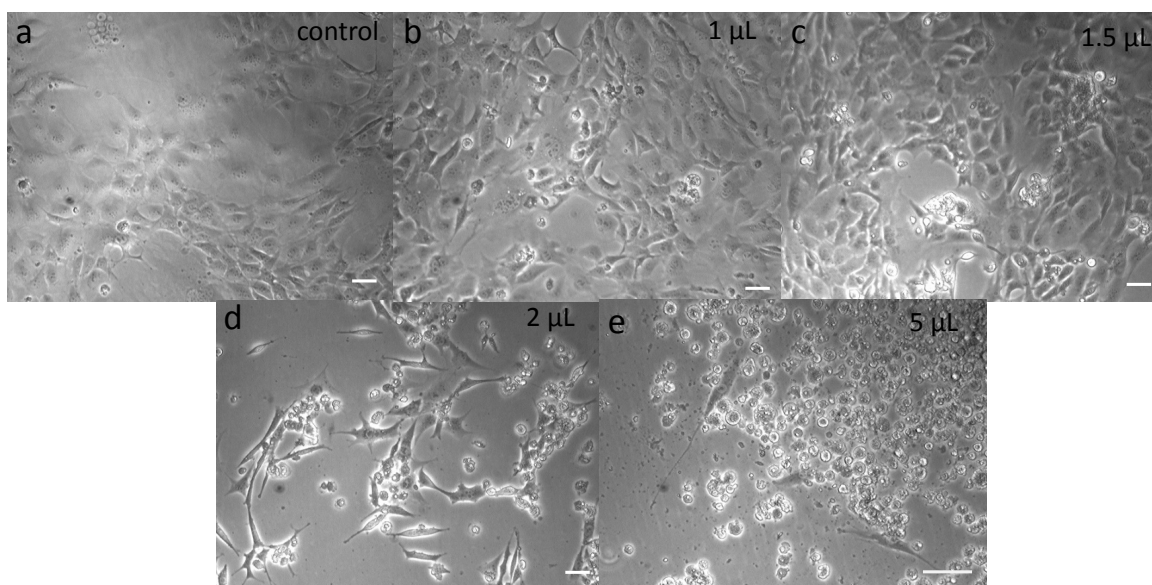


Figure 7-13: Liposome intake effect on the 3T3 fibroblasts. (a) Control 3T3 fibroblasts. (b),(c),(d)&(e) 3T3 fibroblasts exposed to 1 μL , 1.5 μL , 2 μL and 5 μL of liposomes (Lipofectamine® 2000) in 50 μL Opti-MEM medium for approximately 15 minutes. Scale bars are 50 μm .

Furthermore, the aspect ratio (2.96 ± 0.22 s.e.m (n=86)) of transfected cells was smaller compared to control 3T3 cells (3.13 ± 0.27 s.e.m (n=81)) which means that transfected cells are less elongated compared to 3T3 cells (Figure 7-14(c)). The circularity (see chapter 5 for the definition) histogram (Figure 7-14(d)) also shows that transfected cells are more round (0.356 ± 0.011 s.e.m. (n=86)) compared to (0.316 ± 0.017 s.e.m. (n=81)) which is an indication of less branching and elongation.

Therefore, we think that transfection of cells with a plasmid that express molecules that binds to the actin cytoskeleton affects actin polymerization process to some extent.

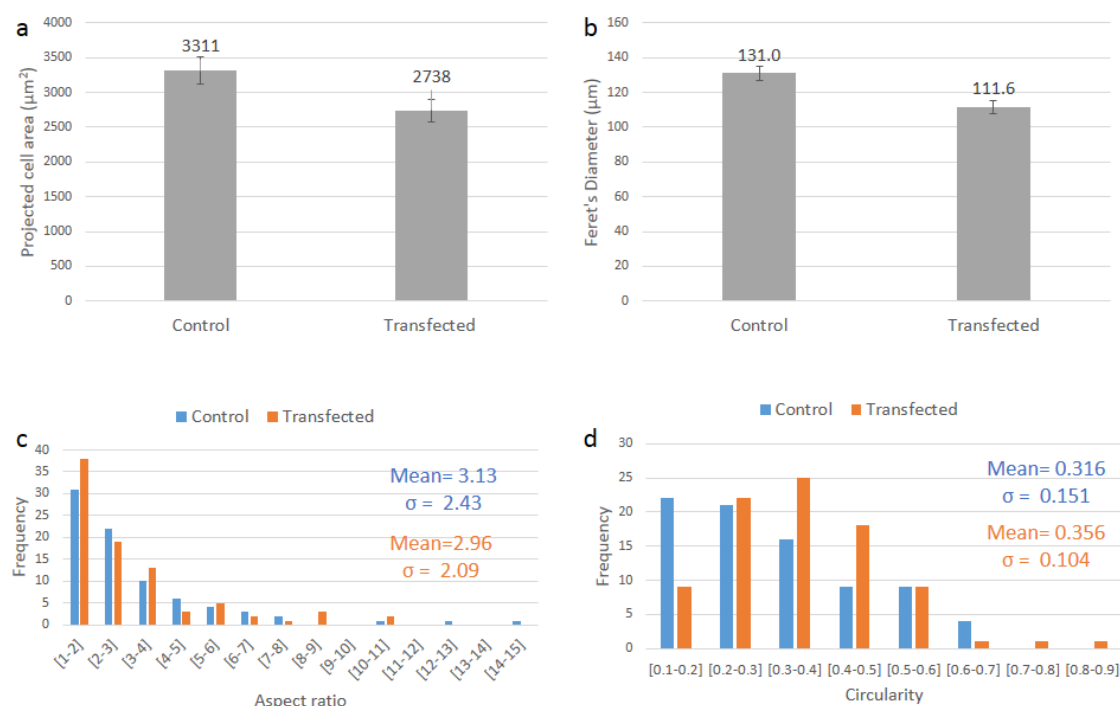


Figure 7-14: Morphological effects of transfection on 3T3 fibroblasts. (a)& (b) Projected cell area and Feret's diameter of transfected (n=86) and control (n=81) NIH/3T3 fibroblasts spreading on the 25cm² culture flask for 12 hours. (c)&(d) Histogram of the aspect ratio and circularity of the transfected and control fibroblasts. The mean and standard deviation are shown for control (blue) and transfected cells (orange). The results are based on bright field slides of the cells. Error bars are s.e.m.

7.2.2 Cell transfection for visualization of the nucleus

Nuclear lamin forms a dense network which is located in the inner nuclear membrane and peripheral chromatin (see Figure 1-7). The nuclear lamina is fairly thick (30 nm to 300 nm) (Höger et al. 1991) and provides mechanical support to the nucleus and plays a key role in several vital cellular functions such as DNA replication, cell cycle regulation, cell development and differentiation, RNA transcription, apoptotic cell death, nuclear growth and nuclear migration (Gruenbaum et al. 2003). Furthermore, the nuclear lamina is connected through a chain of protein such as the SUN protein, Nesperins and Plectin to cytoskeletal actin and intermediate filaments and therefore plays a key role in the mechanotransduction and mechanosensing machinery of the cell and it is heavily involved in response of the cell to mechanical forces in the microenvironment (Dahl, Alexandre J S Ribeiro, et al. 2008b). The nuclear lamina consists of the lamins and lamin-associated proteins. Lamins are intermediate filaments and can be categorized in two major class, Type A and Type B. Lamin A is a nuclear architectural protein and classified as Type A lamina which originates from LMNA gene

(Stuurman et al. 1998). Mutation in Lamin A protein can lead to serious health conditions and genetic disorders such as Hutchinson-Gilford progeria syndrome (HGPS) which shows itself as reminiscent premature ageing (Eriksson et al. 2003).

In order to visualize the nuclear structure in live cells, we transfected our cells with pBABE-puro-GFP-wt-lamin A (see 2.8.3 for more details) (Figure 7-15). This plasmid has been used frequently for visualization of the live cell nucleus for various cell lines (Sorokin et al. 2014)(Toh et al. 2015) (Barilari et al. 2017).

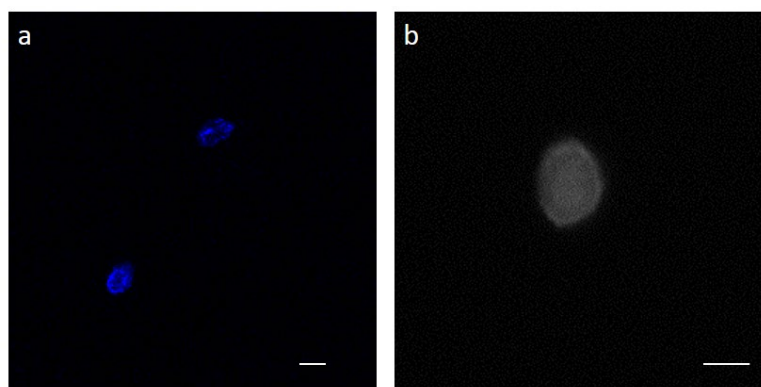


Figure 7-15: Nucleus visualization using pBABE-puro-GFP-wt-lamin A transfection. (a)

Fluorescent microscopy of the nucleus of adherent 3T3 fibroblasts transfected by pBABE-puro-GFP-wt-lamin A illuminated by 488 nm laser light.(false coloured blue) **(b)** Fluorescent microscopy of the nucleus of 3T3 fibroblasts transfected pBABE-puro-GFP-wt-lamin illuminated by a mercury lamp. Scale bars are 10 μm .

pBABE-puro-GFP-wt-lamin A is a circular DNA sequence (Figure 2-9(a)) which has genes that enable the transfected cells to express GFP in the presence of Lamin A which allows us to visualize the nuclei of live cells.(Scaffidi & Misteli 2008b) (See 2.8.3 for details).

The original paper that introduced the plasmid has reported that expression of fluorescent-tagged GFP-wt-lamin A has a mild effect on the nuclear shape and gene expression (Scaffidi & Misteli 2008b). However, as the nuclear lamin acts as the scaffold of the nucleus and plays the key role in the mechanical behaviour of the nucleus (see chapter 1.4 for more details), the effect of the plasmid expression needs to be evaluated further particularly if it is used for studies that are related to the mechanical properties of the cell.

Using genetically modified cells that allow us to perform live cell imaging on both actin cytoskeleton and nucleus we can study the dynamics of cellular response to our topographical patterns. Studying the dynamic response of the cells and their nuclei will help us to get a better understanding of the results of this study and cellular response to the topographical cues in general. We further discussed some of the

important questions that can be addressed using genetically modified cells in suggested future work in chapter 8. In addition, our quantified study of the effects of transfection on cellular morphology is helpful in understanding the limits of this technique and correct analysing the experimental results that we acquire using transfected cells.

Chapter 8:

Conclusion and future works

8.1 Conclusion

The classical approaches to study living cells which were predominantly created by biologists and chemists started to change towards the middle of the 20th century. One of the main works that challenged the classical methodology of cell science was ‘What Is Life? The Physical Aspect of the Living Cell’ which was written by the prominent physicist, Erwin Schrödinger, in 1944. The book introduced the cell membrane as a boundary that separates ‘order from disorder’; order has emerged inside the cell and this ordered system inside the boundary is governed by ‘laws of Physics’. This approach to cellular studies created a bedrock for the new field of ‘biophysics’ and later heavily influenced scientists who did revolutionary discoveries in molecular biology such as the discovery of DNA in the 1950s (Crow 1992).

The cell as a system that is governed by the laws of physics, is not a closed system and maintains its order and function by interacting with its surrounding which results in the interchange of energy and matter with the surrounding environment. In adherent cells, the substrate is the main part of the surrounding environment which exchanges mechanical forces with the cell and therefore physical and geometrical parameters of the substrate have a significant impact on the cellular behaviour.

Development of micro and nano-fabrication techniques in recent decades have enabled scientists to study the interaction between the substrate and cell at an unprecedented level of detail. In this study, we use micro-fabrication techniques to create topographical cues covered in extracellular molecules to shed new light on the interaction of the substrate and cell and how the patterns on the substrate influence the cellular and nuclear structure.

In the first chapter, we introduced the main organelles that are found in eukaryotic cells and their functions. Later we focused on the cytoskeleton structure and the main cytoskeletal polymers actin filaments, intermediate filaments (IFs) and microtubules. For each of these polymers, we reviewed their physical structure and the role that they play in the mechanical function of the cell. We tried to give an idea about the scale of size, elastic modulus and forces that exist inside the cytoskeleton. We also had a close look at the structure of the nucleus and the elements that play a key role in the

mechanical behaviour of the nucleus such as nuclear lamina and how the nucleus is mechanically coupled with the cytoskeleton. Furthermore, we gave a detailed review of the adhesion and spreading mechanism of the cell on the substrate. We focused on the structure that helps attachment of the cell to the nucleus and also transduces mechanical signals (mechanotransduction) of the substrates to the cell and consequently form the cellular response of the cell to the substrate texture. The *in vivo* environment that cells are exposed to is an extracellular matrix (ECM). We had a closer look in the structure and physical properties of the elements that make up this matrix. We fabricated our patterns with fibronectin which is one of the ECM molecules. In order to have a better understanding of the role of cell adhesion, we provided a detailed review of the fibronectin molecule and fibronectin matrices. Chapter one gives essential knowledge about the biology and mechanobiology of the cell, substrate and cell-substrate that is needed to understand the rest of this thesis and our findings.

In chapter 2, we give a very detailed description of the protocols that we have used in this study such as cell culture and maintenance, preparation of 3D ridge-groove PDMS patterns, micro-contact printing of fibronectin on the substrate, fluorescent staining, transfection, Raman microspectroscopy, nanolayer coating etc. In addition, using schematic graphics we introduced the main concepts of the methods we used in this study such as confocal, Reflection Interference Contrast (RIC), Differential Interference Contrast (DIC) and phase contrast microscopy and e-beam evaporation coating.

Chapter 3 gives a brief history of studies on the effect of topographical patterns of the substrate on cellular behaviour by reviewing some of the earliest important work in the field. Furthermore, we also reviewed important work in the field that gives us insight into the concepts that we subsequently need to analyse our findings in the results sections.

Fibroblasts are differentiated from mesenchymal stem cells and are the most common cells of the connective tissue. They play critical roles in many situations, producing ECM and supporting the growth of stem cells. They consequently have a central role in wound healing and development of reparative extra fibrous connective tissue in response to injuries (fibrosis). In our cultures, we observed some 3T3 fibroblasts with well-spread round and branched shape and some with an elongated spindle-like morphology. The nuclei of 3T3 fibroblasts usually had multiple nucleoli. When they were cultured at a high density, they did not show any local alignment and were oriented randomly. 3T3 fibroblasts are adherent cells and when they fail to adhere to the substrate or when they form a weak adhesion, they undergo a type of apoptotic cell death called anoikis by showing some classic features of apoptosis such as blebbing. The cells usually undergo necrotic cell death and dissociate from the substrate in approximately 10 days to 2 weeks. Our measurements showed that the diameter of 3T3 fibroblasts in suspension is $\sim 17.2\ \mu\text{m}$ and the diameter of the nucleus is $\sim 13.2\ \mu\text{m}$ immediately after detachment. When the nuclei were given 35 minutes to relax, the size of 3T3 nuclei reduced by $\sim 10\%$ without significant changes in aspect ratio and circularity of the nuclei. We

hypothesize that this homogenous decreasing of the nuclear size occurs because of the formation of wrinkles on the nuclear surface during relaxation time.

We microprinted fibronectin stripes with different widths on the PDMS substrate. The stripes simulate some of the textures that cells are exposed to in their microenvironments *in vivo* (Alvarez-Prats et al. 2018) (Figure 5-5(d)). The cytoskeleton of spread cells is confined to the stripes and elongate in the direction of stripes. The aspect ratio of cells increases on the narrower patterns so that cells on 25 μm and 10 μm stripes had aspect ratio ~ 2.5 and ~ 9.5 times more compared to fibroblasts on unpatterned (homogeneous) fibronectin-coated substrates. The nuclei of fibroblasts also elongated more on the narrower stripes but to a lower extent compared to the cytoskeleton. The nuclei of fibroblasts on 25 μm and 10 μm elongated about $\sim 5\%$ and $\sim 85\%$ more compared to the nuclei of cells on unpatterned control substrates. Our RIC microscopy results show that different parts of cells on unpatterned control substrates sit at different distances from the substrate. Filopodia in the periphery of the cell are strongly anchored to the substrate by the focal adhesions while the cell membrane in the region of the lamellipodia of the cell, which is closer to the centre of the cell is at a greater distance from the substrate. The distance between the substrate and cell membrane varies in the periphery of the nucleus where lamellum is located. Under the nucleus, there is a flat region in which the distance between the cell membrane and the substrate is constant. On narrower patterns, the filopodia were only observable at the two ends of the elongated cell and were anchored to the substrate, while in the rest of cell, the membrane was at a constant distance from the substrate (see Figure 5-6(a)). We imaged the 3D shape of the cells using confocal fluorescence microscopy. Our results show that the maximum thickness of the cells increases on narrower stripes. The thickness of fibroblasts increases on 25 μm , 12 μm and 10 μm stripes by $\sim 5\%$, $\sim 20\%$ and $\sim 30\%$ respectively compared to the unpatterned substrate. We believe that the thickness of the cell is negatively correlated with the number of perinuclear actin stress fibers as a greater number of stress fibers results in a bigger compressive force that flattens the nucleus and consequently decreases the height of the cell. Our results show that the number of perinuclear actin stress fibers among cells on 25 μm and 10 μm stripes reduces by $\sim 35\%$ and $\sim 80\%$ compared to cells on the unpatterned control substrate. Our observations gave us a clearer image of the configuration of actin stress fibres and associated focal adhesions in adherent cells (see Figure 5-11). Our results also revealed that both nuclear and cellular volume is decreasing among cells that spread on narrower stripes. The cellular volume of cells on 25 μm and 10 μm stripes reduces by $\sim 15\%$ and $\sim 45\%$ compared to cells on unpatterned control substrate while the nuclear volume of cells on 25 μm and 10 μm stripes reduces by $\sim 25\%$ compared the nuclei of control cells.

We studied the effect of 5 μm stripes (with 11 μm spacing) on 3T3 fibroblasts. We called these patterns ‘subnuclear’ stripes pattern as the width of the stripes were almost $1/3$ of the nuclei of 3T3 fibroblasts. A large number of cells were relatively round and spread on the patterns with only local alignment to the patterns at the periphery of the cells. A smaller group of cells spread over the patterns

in the central part of the cell and showed elongated branches on several adjacent stripes. Another small group of cells were confined and elongated on a single fibronectin stripe. The average aspect ratio of 3T3 fibroblasts was ~50% higher than the cells on an unpatterned control substrate while the average aspect ratio of the nuclei on the subnuclear patterns was ~10% higher than nuclei of cells on control patterns. The fibroblasts spread about 50% less than cells on the unpatterned control substrate. This is expected as the PDMS hinders the cell spreading due to its high hydrophobicity. The nuclei of fibroblasts also spread ~10% less on subnuclear patterns compared to nuclei of the cells on the control substrate. In order to study the alignment of fibroblasts with the direction of stripe patterns, we measured the deviation angle of the major axis of the best fitting ellipse with the direction of the stripes (Θ). More than 50% of cells deviate by less than 10° relative to the pattern direction and ~65% of cells deviate less than 20° from the direction of stripes. This effect shows itself as a deep well in the potential energy landscape around $\Theta = 0^\circ$, which forces the cell body to align itself with the direction of patterns. We observed that nuclei of fibroblasts also align themselves with the direction of patterns to a slightly lesser extent. More than 40% of fibroblasts deviate by less than 10° ($|\Theta| < 10^\circ$) relative to the pattern direction and ~60% of nuclei deviate less than 20° from the direction of stripes. This shows also itself as a deep minimum potential energy landscape for the nucleus alignment around $\Theta = 0^\circ$.

Stem cells are different from somatic adult cells in nature and importance in their clinical application. In chapter 4, we gave a detailed description of stem cells and their characteristics. We gave a timeline about the important events in the history of stem cell research. Furthermore, we provide a detailed review of the differentiation hierarchy of stem cells and the classification of the stem cells. Later in the chapter, we focused on human mesenchymal stem cells (hMSCs), their origin of isolation, their differentiation pathways and their importance in regenerative medicine and tissue engineering. To cover the subject of study, we presented a comprehensive review of the physical properties of hMSCs and the cell lines that differentiated from them. A wide range of physical cues such as substrate stiffness and topographical patterns of the substrate can affect the cellular behaviour of the hMSCs. We reviewed the most important studies that have been carried out to study these effects and the literature that elaborates the role of the mechanical structure of the cells in forming the effects. Particularly, we focused on different substrate patterns that have been used to study the response of hMSCs to substrate texture. Understanding the effects of the patterns that are used in these studies on cellular elements such as the actin cytoskeleton, nucleus and focal adhesions is essential to explain our findings of the effect of our patterns on hMSCs.

hMSCs have a different morphology when they spread in the culture flask. Some of them are branched and well spread and another group are spindle-like elongated cells. The histogram of the aspect ratio of the hMSCs showed that a big majority of the cells are from the first group and the number of cells drops quite rapidly as they elongate further. We also observed that unlike 3T3

fibroblast, hMSCs elongate and make some local alignment with each other when they are seeded in high density. In detached form, the diameter of hMSCs was measured as 21.7 μm and their nuclei diameter as 11.4 μm . This shows that hMSCs are bigger compared to fibroblasts while their nuclei are smaller. When the nuclei of hMSCs were given time to relax for 30 minutes, their average diameter reduced about 10% while their aspect ratio and circularity did not change significantly. This is consistent with what we observed for 3T3 fibroblasts and we think this is also because of wrinkles that are formed on the nuclear envelope. Similar to 3T3 fibroblasts, hMSCs that failed to adhere to the substrate or adhered weakly showed apoptotic cell death signs such as blebbing. However, unlike 3T3 fibroblasts, hMSCs stayed in culture for a long period of time (~ 40 days) without considerable morphological abnormalities or classic signs of apoptotic and necrotic cell death, although we suggest that these hMSCs may lose some of their differentiation and self-renewal capabilities.

We cultured hMSCs on 10 μm , 25 μm fibronectin stripes and unpatterned fibronectin coated controls. The cells were spread less as stripes become narrower so that hMSCs on 10 μm and 25 μm stripes spread about $\sim 25\%$ and $\sim 55\%$ of cells on the control substrate. On the other hand, the cells on 10 μm and 25 μm elongated more with an average aspect ratio of ~ 5.5 and ~ 2.5 times more than cells on the control substrate. The nuclei of hMSCs also spread less and elongate more on narrower stripes but in a lesser extent compared to the cytoskeleton. The nuclei of hMSCs on 10 μm and 25 μm spread $\sim 70\%$ and $\sim 80\%$ of the size of nuclei of cells on the control substrate and elongate $\sim 15\%$ and $\sim 60\%$ more than the control nuclei. By measuring the angle between the major axis of best fitting ellipses to the cytoskeleton and nucleus (α), we observed that the nuclei of hMSCs on narrower stripes are more aligned with the cytoskeleton. Although in a relatively large portion of cells ($\sim 40\%$), the nucleus is aligned with the cytoskeleton ($|\alpha| < 10^\circ$), there is a considerable number of nuclei that are not aligned with the cytoskeleton. On the 25 μm patterns, the alignment increases to 78% and we saw almost no nuclei that are not significantly orientated with respect to the cytoskeleton. Almost all (96%) cells on 10 μm stripes are closely aligned with the cell body. We concluded that thick actin edge bundles that are observed in narrower stripes and perinuclear actin fibres which are more aligned with the cytoskeleton force the nucleus to greater alignment with the cell.

Single cell correlation between the size of nucleus and cell shows that the correlation is stronger among fibronectin coated control substrate ($r = 0.64$) and it gets weaker with decreasing width of the stripes on 25 μm fibronectin stripes ($r = 0.49$) and 10 μm stripes ($r = 0.19$). We observed a lower number of conventional basal fibers on narrower stripes and therefore we hypothesize that the smaller number of these fibers prevent the cell to stretch the nucleus effectively as the cytoskeleton spread on the substrate.

3D confocal fluorescent microscopy of hMSCs shows that the cells are thinner on control unpatterned substrate and the height of the cell increases on 25 μm and 10 μm stripes by $\sim 15\%$ and $\sim 50\%$

respectively. We think that the thinner cells arise because of the higher number of perinuclear actin fibers which flatten the nucleus and consequently exert a compressive force towards the substrate. Our results show that the number of perinuclear actin fibers among cells on 25 μm and 10 μm stripes is $\sim 40\%$ and $\sim 80\%$ smaller compared to the cells on the unpatterned control pattern. We observed a negative correlation between cell thickness and the number of perinuclear actin fibers in a single cell on all patterns. However, the negative correlation is weaker among cells on the control substrate ($r = -0.3840$) and significantly increases with decreasing width of stripes among cells on 25 μm ($r = -0.6041$) and 10 μm stripes ($r = -0.7758$). We hypothesize that the flattened nuclei of cells on the unpatterned substrate are stiffer and therefore are less sensitive to the number of perinuclear stress fibers, while the nuclei of hMSCs on narrower stripes are less compressed and less stiff and consequently more sensitive to the number of perinuclear actin stress fibers.

We observed three major morphological types of shape among hMSCs on subnuclear patterns (5 μm fibronectin stripes with 11 μm spacing). A large number of cells were relatively round and spread on the patterns with only local alignment to the patterns at the periphery of the cells. A smaller group of cells spread over the patterns in the central part of the cell and extended elongated branches onto several adjacent stripes. A very small group of cells were confined and elongated on a single fibronectin stripe. The average aspect ratio of hMSCs did not change significantly on subnuclear patterns while the aspect ratio of their nuclei increased by $\sim 5\%$ compared to cells on unpatterned control substrates. We hypothesize that the hMSCs that are round on the unpatterned substrate would make up the first group on the subnuclear patterns. However, hMSCs that have a tendency to elongate and make a spindle-like morphology would make the branched or highly elongated cells on subnuclear patterns. Both cytoskeleton and nuclei of hMSCs spread $\sim 20\%$ less on the subnuclear stripe pattern compared to the fibronectin-coated control. This is expected as subnuclear patterns have more exposed PDMS and the PDMS hinders the cell spreading because of its high surface hydrophobicity.

Almost 50% of cells deviate by less than 10° relative to the pattern direction and more than 70% of cells deviate less than 20° from the direction of stripes. This shows itself as a deep well in the potential energy landscape around $\Theta = 0^\circ$ which forces the cell to align itself with the direction of patterns. The nuclei of hMSCs are aligned to the direction of patterns to a lesser extent. About $\sim 25\%$ of nuclei showed a deviation less than 10° relative to the stripe direction and the percentage of nuclei that exhibited a deviation angle less than 20° was $\sim 40\%$. This means that in the potential energy landscape there is a smaller minimum around $\Theta = 0^\circ$ for the nuclei of hMSCs. In addition, we observed a relatively large number of nuclei (17% of total nuclei) that are almost perpendicular to the direction of patterns ($80^\circ < |\Theta| < 90^\circ$). This shows itself as a second but smaller minimum in the potential energy curve. We believe that the perpendicular nuclei occur at the beginning of adhesion process, if the cell lands on two adjacent stripes on the pattern and the nucleus is locked by the actin fibers underneath and in the periphery of the nucleus to the substrate through focal adhesion. Our

geometrical model shows that the probability of landing on two adjacent stripes is $\sim 66\%$ for hMSCs while this probability will be $\sim 38\%$ for 3T3 fibroblasts. In addition, a bigger detached cell size of hMSCs gives much more available area for the formation of focal adhesions to support the nucleus in the perpendicular orientation. A higher number of focal adhesions will reduce the probability of alignment of the nucleus by perinuclear actin stress fibers in the process of cell spreading.

Raman microspectroscopy is a powerful tool to study cellular behaviour. The method gives comprehensive morpho-chemical information about the cell at a micrometre scale which means that it potentially can be used to study the cytoskeleton, different cell organelles and the nucleus at a sub-nuclear level. Furthermore, It can be performed both on live and fixed cells. In chapter 7, we gave an introduction about the principles of Raman microspectroscopy and its application in cell science. When we applied Raman microspectroscopy on 3T3 fibroblasts that are spreading on fibronectin-coated PDMS substrate, we observed some cellular structures such as nucleus by spatial visualization of a DNA/RNA associated peak (730 cm^{-1}). However, the strong background signal from the PDMS substrate did not allow us to visualize other cell structures. The strong background signal from polymers such as PDMS has limited the use of this microscopy technique in studying cellular response to topographical patterns. In order to address the background signal problem from the PDMS, we proposed two solutions for both 2D and 3D topographical patterns. For 2D patterns, we used a gold-coated mirror which was protected by a layer of silica. When we analysed the Raman spectra of a 3T3 cell on this setup, we observed important peaks that are associated with major biological molecules such as DNA, RNA, proteins, lipids and carbohydrates without major background peak from the substrate. Using the spatial distribution of these sharp peaks such as a peak centred at 780 cm^{-1} , we could visualize cellular structure such as nuclear in a relatively high resolution. Furthermore, we analysed the morphological effects of this setup on 3T3 fibroblasts. The fibroblasts spread $\sim 60\%$ less on the mirrors compared fibronectin-coated control substrate. However, diverse shapes of spreading were observed among the cells on the mirror similar to what was observed among the cells spreading on the fibronectin-coated substrates which as an indicator of biocompatibility of the setup for cells. Furthermore, the fibroblasts elongated $\sim 55\%$ more compared to fibroblasts on the control substrate which was explained by higher stiffness of the silica compared to the PDMS. We believe that using microprinting techniques, we can print our desired patterns made of ECM molecules such as fibronectin or collagen on the mirrors and consequently this method will allow more extensive application of Raman microspectroscopy to study the effect of 2D patterns on cellular behaviour in the future.

For 3D patterns, we shielded the groove-ridge PDMS patterns with a layer of conductor (30nm gold and 5nm Titanium) and a layer of silica (40nm) using e-beam evaporation. Our calculations showed

that this thickness of the metal layer can attenuate the effective background noise from the underlying PDMS by 10^{-7} . Beside some macroscopic wrinkles, the coating did not distort the shape of 3D patterns. However, the main peaks from PDMS (485 cm^{-1} , 610 cm^{-1} and 705 cm^{-1}) were present in the Raman spectrum of coated patterns. We concluded that the coating locally melted and the Raman signal came from the underlying PDMS as we observed a complete burn down of the coating with powers more than 120mw for 785nm and 15mw for 488nm laser. We expect that the heating problem will be solved partly if we use some medium on the top of cells (necessary for live cell imaging) and if we collect the Raman signal from a focal plane above the coating. In addition, a thicker silica protective layer can be considered to increase the laser power that causes melting.

Conventional fluorescent staining has serious limitations for live cell microscopies such as toxic effects on the cell and photo-bleaching. Live cell imaging is required for the study of dynamic of the response of the cell to topographical patterns. The actin cytoskeleton plays a major role in the biomechanical machinery of the cell and therefore it contains key information about the effect of physical cues on the cell. We genetically modified the 3T3 fibroblasts by introducing a designed DNA vector (plasmid) called pCMVLifeAct-TagGFP2. The vector has a DNA sequence that encodes a protein that binds to filamentous actin and a DNA sequence that encodes a fluorescent tag. The genetically modified cell expresses the DNA content of the vector by its own gene expressing machinery and therefore allows the performance of live cell microscopy over a long period of time. Previous studies have shown that cells that undergo the transfection process express some morphological abnormalities. We quantified some of the morphological changes that the transfection has induced on cells. Transfected cells spread $\sim 20\%$ less on the polystyrene culture flask compared to unmodified control 3T3 fibroblasts and the Feret's diameter of them was $\sim 15\%$ smaller than control cells which we think is an indication of effects of transfection on actin polymerization dynamics. The transfected cells also elongated less and were slightly more round compared to the control cells as their aspect ratio is $\sim 5\%$ smaller and their circularity is $\sim 10\%$ bigger than the control cell. We conclude that this is another indication of partially inhibited actin polymerization among the transfected cells.

The nucleus is the biggest organelle of the cell and is the organelle that reacts to the transduced mechanical signals by expressing different genes. Therefore, in order to understand the effect of substrate texture on cellular behaviour, it is crucial to study the response of the nucleus on the patterns. We genetically modified 3T3 fibroblasts by transfection them with pBABE-puro-GFP-wt-lamin plasmid vector. The vector has a DNA sequence that encodes a protein in the presence of Lamin A structure of the nucleus. The nuclear lamina is a structure in the inner periphery of the nucleus and plays the main role in maintaining the mechanical structure of the cell. In addition, the vector encodes a fluorescent tag which when expressed by the cell allows visualization of the nucleus using fluorescent microscopy.

Using the transfected 3T3 cell lines that we created, we can study the dynamic response of the cell to substrate topography which will help us to shed lights on some the questions that we need to answer in order to have a better understanding of cellular behaviour on our patterns. Some of these ideas are presented in the future work section (see section 8.2)

8.2 Suggested further work

When we seeded 3T3 fibroblasts at a higher density (~ 15000 cells/cm²) on 15 μ m fibronectin stripes, we observed some very big cells whose cytoskeleton looked like a cytoskeleton of a single cell which was confined to the patterns and elongated on the stripe (Figure 8-1(a), lower panel). However, when we looked at the nucleus, we observed multiple nuclei in the cell (Figure 8-1(a), lower panel). Some cells in the body such as muscle cells have multiple nuclei (Manhart et al. 2018). However, as we observed before in chapter 5, fibroblasts normally only have one nucleus (see Figure 5-6(c),(d)&(e)). We believe that the single cell is a result of the fusion of multiple cells that have landed close to each other on the stripes and connected together to form a single cell with multiple nuclei. We observed some cells that build connection in the early stages of adherence to the substrate (Figure 8-2(b)). We think it would be very interesting to study these fibroblasts with several nuclei and the effect of patterns on them. For example, when we visualized the perinuclear actin cap of these cells in the apical focal plane, the actin stress fibers looked similar to cells on fibronectin stripes with a single nucleus (Figure 8-1 (a), upper panel). As was mentioned in previous chapters, actin stress fibers are mechanically coupled with the nucleus through nuclear lamina and play a key role in regulating the nuclear shape and consequently may have an important role in cellular behaviour. The interesting question here is how the actin cap is regulating multiple nuclei and how in return each of these nuclei is contributing to the formation of perinuclear actin fibrers.

In addition, one interesting idea is to study the dynamics of the cells with multiple nuclei on the patterns to see if the cells will remain connected over time or they will separate at some point from each other. To study the dynamics of these process, we can use 3T3 cell lines that we have genetically modified to visualize the actin cytoskeleton and nucleus (see chapter 7.2). Ideally, a microfluidic device can be designed to put cells at known distances from each other on the patterns to study what is the minimum distance between cells on time of landing on patterns that can make them connected to each other and behave like a single cell.

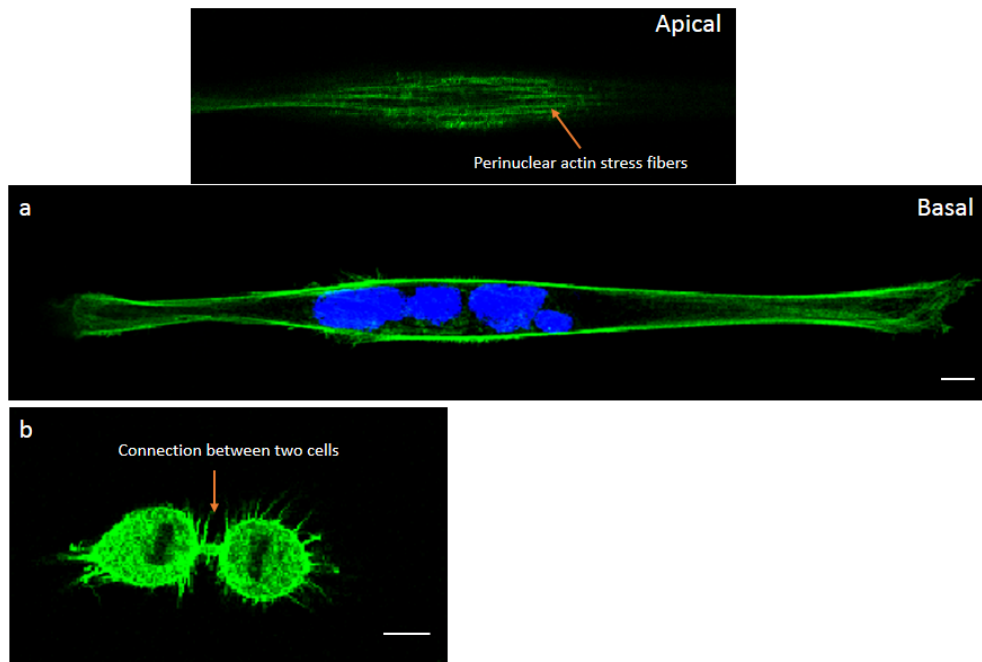


Figure 8-1: Connected 3T3 fibroblasts. (a) lower panel: Basal focal plane view of a 3T3 fibroblast with a big cytoskeleton that morphologically looks similar to a cytoskeleton of a single cell on the fibronectin stripes; however, it has multiple nuclei (blue), because of the big size of the cell, two images were stitched together to make the micrograph of the cytoskeleton. Upper panel: Apical plane view of the same cell showing the perinuclear actin fibers that look similar to cells with a single nucleus of fibronectin stripes. (b) Two 3T3 fibroblasts in the early stage of spreading on the substrate, the cells are connected with an actin bridge. The cells are fixed with formaldehyde and stained with Phalloidin for F-actin (green) and TO-PRO-3 for the nucleus (blue). Green and blue channels are overlaid by Image J. Scale bars are 10 μm .

As we stated in chapter 5 and chapter 6, the effect of subnuclear stripes can be described by an effective potential energy landscape. Some local or global minima in the potential energy curve for the cytoskeleton or nucleus of the cells were formed by the patterns, in which the majority of the cells were orientated in the directions dictated by those minima. Previous studies that have tracked the migratory path of adherent cells have shown that cells move in a relatively straight direction for a substantial period of time before they reorient themselves in a stochastic manner (Petrie et al. 2009). Spatial cues or chemical gradients (chemotaxis) will affect the migration direction (Welf et al. 2012). It would be interesting to study how the depth and location of those minima change over time and how population migration between those minima will occur. For example, whether all the cells migrate in a way that they align themselves with the patterns or not. By monitoring the dynamics of cells on the patterns, we can also answer interesting questions such as how the landing spot of the cell relative to the fibronectin stripes will change the adhesion process and the final fate of the cell

between taking each of the three morphologies that we observed for cells on subnuclear patterns. In addition, patterns with different stripe and spacing widths can be fabricated to verify our geometrical model that explained the existence of perpendicular nuclei of hMSCs on the subnuclear stripe patterns (see chapter 6.4).

In chapter 5 and chapter 6, we showed that the nuclei of both detached 3T3 fibroblasts and hMSCs get homogenously smaller when they were given approximately half an hour to relax after detachment from the substrate. It would be interesting to see if relaxation changes the behaviour cells on topographical patterns such as fibronectin stripes. It is likely that this relaxation will change the dynamics of cellular behaviour on the stripes while on a longer time period, the cells maybe will behave similarly. Therefore, it is important to use genetically modified cells with fluorescent tags to monitor the early stages after seeding on the patterns.

As was reviewed in detail in chapter 4, topographical cues and mechanical properties of the substrate can alter the differentiation behaviour of hMSCs. In addition, change in the shape of the nucleus, which is packed with negatively charged DNA, results in changes in the gene expression behaviour of the cell (Guilluy & Burrridge 2015). These changes can be effectively tracked by Raman microspectroscopy, which is a non-invasive method to track the morphological and chemical changes in the cell on a micrometre scale. We think using the setups that we established would enable us to take Raman spectra from both 2D and 3D patterns. We could study the chemical changes among the cells on various topographical patterns, both for live cell imaging and imaging of fixed cells. For example, it is interesting to see how the DNA density distribution is affected inside the nuclei of cells on fibronectin stripes with different widths. This can be done by visualization of DNA related peaks such as 780 cm^{-1} . In addition, the distribution of RNA or protein can be monitored as a measure of the effect of stripes on gene expression inside the cell.

As it was mentioned in chapter 5, we observed multiple dividing nuclei among cell on the unpatterned control substrate; however, dividing nuclei were rare on the narrower fibronectin stripes. It would be interesting to investigate the effect of fibronectin stripes on cell division over a longer period of time. In addition to our genetically modified cells with fluorescent tags, conventional dyes for visualizing the cell cycle can give us important information about the effect of the patterns on mitotic cell division, which carries substantial importance for biological and clinical applications particularly in the case of hMSCs.

Bibliography

- Abagnale, G. et al., 2015. Surface topography enhances differentiation of mesenchymal stem cells towards osteogenic and adipogenic lineages. *Biomaterials*, 61, pp.316–326.
- Aebi, U. et al., 1986. The nuclear lamina is a meshwork of intermediate-type filaments. *Nature*, 323(6088), pp.560–564.
- Aghazadeh, Y. & Nostro, M.C., 2017. Cell Therapy for Type 1 Diabetes: Current and Future Strategies. *Current Diabetes Reports*, 17(6), p.37.
- Van Agthoven, J.F. et al., 2014. Structural basis for pure antagonism of integrin $\alpha V\beta 3$ by a high-affinity form of fibronectin. *Nature structural & molecular biology*, 21(4), pp.383–8.
- Ahmed, W.W., Fodor, É. & Betz, T., 2015. Active cell mechanics: Measurement and theory. *Biochimica et Biophysica Acta (BBA) - Molecular Cell Research*, 1853(11), pp.3083–3094.
- Alberts B, Johnson A, Lewis J, et al., 2002. *Molecular Biology of the Cell* 4th ed., Newyork: Garland Science.
- Alberts, B. et al., 2002a. Eggs.
- Alberts, B. et al., 2002b. Fibroblasts and Their Transformations: The Connective-Tissue Cell Family.
- Alberts, B.J.A.L.J.R.M. coaut. coaut. coaut. B.A.A.J.J.L.M.R.K.R.P.W., 2008. *Molecular biology of the cell*,
- Albrecht-Buehler, G., 1987. Role of cortical tension in fibroblast shape and movement. *Cell Motility and the Cytoskeleton*, 7(1), pp.54–67.
- Alvarez-Prats, A. et al., 2018. Schwann-Cell-Specific Deletion of Phosphatidylinositol 4-Kinase Alpha Causes Aberrant Myelination. *Cell Reports*, 23(10), pp.2881–2890.
- Alvarez-Viejo, M. et al., 2013. Quantifying Mesenchymal Stem Cells in the Mononuclear Cell Fraction of Bone Marrow Samples Obtained for Cell Therapy. *Transplantation Proceedings*, 45(1), pp.434–439.
- Anderson, H.J. et al., 2016. Mesenchymal Stem Cell Fate: Applying Biomaterials for Control of Stem Cell Behavior. *Frontiers in Bioengineering and Biotechnology*, 4, p.38.
- Anon, 4. The Adult Stem Cell | stemcells.nih.gov. Available at: <https://stemcells.nih.gov/info/2001report/chapter4.htm> [Accessed July 23, 2018a].
- Anon, Addgene: Protocol - How to Create a Bacterial Glycerol Stock. Available at: <https://www.addgene.org/protocols/create-glycerol-stock/> [Accessed October 10, 2018b].
- Anon, Alexa Fluor 488 Phalloidin - Thermo Fisher Scientific. Available at: <https://www.thermofisher.com/order/catalog/product/A12379> [Accessed November 1, 2018c].
- Anon, Confocal microscopy. Available at: https://www.jic.ac.uk/microscopy/more/T5_8.htm [Accessed October 19, 2018d].
- Anon, Embryonic Stem Cells | stemcells.nih.gov. Available at:

- https://stemcells.nih.gov/info/Regenerative_Medicine/2006Chapter1.htm [Accessed July 29, 2018e].
- Anon, Endoplasmic Reticulum (Rough and Smooth) | British Society for Cell Biology. Available at: <https://bscb.org/learning-resources/softcell-e-learning/endoplasmic-reticulum-rough-and-smooth/> [Accessed October 14, 2018f].
- Anon, 2011. EUKARYOTIC CELL. *Eukaryotic Cell*, 10(1), pp.1–19.
- Anon, File:Dark field and phase contrast microscopies.ogv - Wikipedia. Available at: https://en.wikipedia.org/wiki/File:Dark_field_and_phase_contrast_microscopies.ogv [Accessed November 9, 2018g].
- Anon, Hoechst 33342 Solution (20 mM) - Thermo Fisher Scientific. Available at: <https://www.thermofisher.com/order/catalog/product/62249> [Accessed November 1, 2018h].
- Anon, Introduction to Phase Contrast Microscopy | MicroscopyU. Available at: <https://www.microscopyu.com/techniques/phase-contrast/introduction-to-phase-contrast-microscopy> [Accessed November 9, 2018i].
- Anon, Mid-Infrared Enhanced Protected Gold Mirrors. Available at: https://www.thorlabs.com/newgrouppage9.cfm?objectgroup_id=12178 [Accessed March 2, 2019j].
- Anon, Roughness Parameters - Rubert & Co Ltd. Available at: <http://www.rubert.co.uk/faqs/roughness-parameters/> [Accessed October 20, 2018k].
- Anon, TO-PRO-3 Iodide (642/661) - 1 mM Solution in DMSO - Thermo Fisher Scientific. Available at: <https://www.thermofisher.com/order/catalog/product/T3605> [Accessed November 1, 2018l].
- Anselme, K. & Bigerelle, M., 2011. Role of materials surface topography on mammalian cell response. *International Materials Reviews*, 56(4), pp.243–266.
- Aramaki, Y., Takano, S. & Tsuchiya, S., 1999. Induction of apoptosis in macrophages by cationic liposomes. *FEBS Letters*, 460(3), pp.472–476.
- Araña, M. et al., 2013. Adipose Tissue-Derived Mesenchymal Stem Cells: Isolation, Expansion, and Characterization. In *Methods in molecular biology (Clifton, N.J.)*. pp. 47–61.
- Augello, A. & De Bari, C., 2010. The Regulation of Differentiation in Mesenchymal Stem Cells. *Human Gene Therapy*, 21(10), pp.1226–1238.
- Badique, F. et al., 2013. Directing nuclear deformation on micropillared surfaces by substrate geometry and cytoskeleton organization. *Biomaterials*, 34(12), pp.2991–3001.
- Badylak, S.F. et al., 2012. Engineered whole organs and complex tissues. *Lancet (London, England)*, 379(9819), pp.943–952.
- Ballen, K., 2017. Update on umbilical cord blood transplantation. *F1000Research*, 6, p.1556.
- Barilari, M. et al., 2017. ZRF1 is a novel S6 kinase substrate that drives the senescence programme. *The EMBO Journal*, 36(6), pp.736–750.
- Barr, V.A. & Bunnell, S.C., 2009. Interference reflection microscopy. *Current protocols in cell biology*

- / editorial board, Juan S. Bonifacino ... [et al.], Chapter 4, p.Unit 4.23.
- Bartalena, G. et al., 2012. Biomaterial surface modifications can dominate cell–substrate mechanics: the impact of PDMS plasma treatment on a quantitative assay of cell stiffness. *Soft Matter*, 8(3), pp.673–681.
- Bauer, A.L., Jackson, T.L. & Jiang, Y., 2009. Topography of Extracellular Matrix Mediates Vascular Morphogenesis and Migration Speeds in Angiogenesis A. Czirók, ed. *PLoS Computational Biology*, 5(7), p.e1000445.
- Becker, A.J., McCULLOCH, E.A. & TILL, J.E., 1963. Cytological Demonstration of the Clonal Nature of Spleen Colonies Derived from Transplanted Mouse Marrow Cells. *Nature*, 197(4866), pp.452–454.
- Ben-Yehudah, A. et al., 2012. Mutated Human Embryonic Stem Cells for the Study of Human Genetic Disorders. In *Methods in molecular biology (Clifton, N.J.)*. pp. 179–207.
- Berry, C.C. et al., 2004. The influence of microscale topography on fibroblast attachment and motility. *Biomaterials*, 25(26), pp.5781–5788.
- Bianco, P., 2014. “Mesenchymal” Stem Cells. *Annual Review of Cell and Developmental Biology*, 30(1), pp.677–704.
- Bindu A, H. & B, S., 2011. Potency of Various Types of Stem Cells and their Transplantation. *Journal of Stem Cell Research & Therapy*, 01(03).
- Birnboim, H.C. & Doly, J., 1979. A rapid alkaline extraction procedure for screening recombinant plasmid DNA. *Nucleic acids research*, 7(6), pp.1513–23.
- Bischofs, I.B. et al., 2008. Filamentous Network Mechanics and Active Contractility Determine Cell and Tissue Shape. *Biophysical Journal*, 95(7), pp.3488–3496.
- Borowicz, P. et al., 2012. Deep-ultraviolet Raman investigation of silicon oxide: thin film on silicon substrate versus bulk material. *Advances in Natural Sciences: Nanoscience and Nanotechnology*, 3(4), p.045003.
- Brackenbury, R., Rutishauser, U. & Edelman, G.M., 1981. Distinct calcium-independent and calcium-dependent adhesion systems of chicken embryo cells. *Proceedings of the National Academy of Sciences of the United States of America*, 78(1), pp.387–91.
- Bretscher, M.S., Cho, S. & Wirtz, D., 2008. On the shape of migrating cells--a “front-to-back” model. *Journal of cell science*, 121(Pt 16), pp.2625–8.
- Buckley, R.H., 2011. Transplantation of hematopoietic stem cells in human severe combined immunodeficiency: longterm outcomes. *Immunologic research*, 49(1–3), pp.25–43.
- Budday, S. et al., 2015. Mechanical properties of gray and white matter brain tissue by indentation. *Journal of the mechanical behavior of biomedical materials*, 46, pp.318–30.
- Burnap, R.L. & Vermaas, W.F.J., 2012. *Functional genomics and evolution of photosynthetic systems*, Springer.
- Burridge, K. & Chrzanowska-Wodnicka, M., 1996. Focal adhesions, contractility, and signaling.

- Annual review of cell and developmental biology*, 12, pp.463–518.
- Burton, P.R., Hinkley, R.E. & Pierson, G.B., 1975. Tannic acid-stained microtubules with 12, 13, and 15 protofilaments. *The Journal of cell biology*, 65(1), pp.227–33.
- Cai, D. et al., 2010. Raman, mid-infrared, near-infrared and ultraviolet–visible spectroscopy of PDMS silicone rubber for characterization of polymer optical waveguide materials. *Journal of Molecular Structure*, 976(1–3), pp.274–281.
- Câmara, D.A.D. et al., 2016. Advances and Challenges on Cancer Cells Reprogramming Using Induced Pluripotent Stem Cells Technologies. *Journal of Cancer*, 7(15), pp.2296–2303.
- Cassimeris, L. et al., 2011. *Lewin's cells.*, Jones and Bartlett Publishers.
- Chalut, K.J. et al., 2010a. Deformation of stem cell nuclei by nanotopographical cues. *Soft matter*, 6(8), pp.1675–1681.
- Chalut, K.J. et al., 2010b. Deformation of stem cell nuclei by nanotopographical cues. *Soft matter*, 6(8), pp.1675–1681.
- Cheng, X., Tyaboonchai, A. & Gadue, P., 2013. Endodermal Stem Cell Populations Derived from Pluripotent Stem Cells. *Current opinion in cell biology*, 25(2), p.265.
- Chizhik, S.A. et al., 2010. Properties of Cartilage on Micro- and Nanolevel. *Advances in Tribology*, 2010, pp.1–8.
- Chong, P.-P. et al., 2012. Human peripheral blood derived mesenchymal stem cells demonstrate similar characteristics and chondrogenic differentiation potential to bone marrow derived mesenchymal stem cells. *Journal of Orthopaedic Research*, 30(4), pp.634–642.
- Chuah, Y.J. et al., 2016. Simple surface engineering of polydimethylsiloxane with polydopamine for stabilized mesenchymal stem cell adhesion and multipotency. *Scientific Reports*, 5(1), p.18162.
- Clark, P. et al., 1990. Topographical control of cell behaviour: II. Multiple grooved substrata. *Development (Cambridge, England)*, 108(4), pp.635–44.
- Codan, B. et al., 2013. Atomic force microscopy of 3T3 and SW-13 cell lines: an investigation of cell elasticity changes due to fixation. *Materials science & engineering. C, Materials for biological applications*, 33(6), pp.3303–8.
- Conde, C. & Cáceres, A., 2009. Microtubule assembly, organization and dynamics in axons and dendrites. *Nature reviews. Neuroscience*, 10(5), pp.319–32.
- Cooper, G.M., 2000. Microtubules.
- Corall, S. et al., 2014. $\alpha 5 \beta 1$ -integrin and MT1-MMP promote tumor cell migration in 2D but not in 3D fibronectin microenvironments. *Computational Mechanics*, 53(3), pp.499–510.
- Da Costa, R. et al., 2018. Spectral features of nuclear DNA in human sperm assessed by Raman Microspectroscopy: Effects of UV-irradiation and hydration. *PloS one*, 13(11), p.e0207786.
- Coutinho, H.D.M. et al., 2009. Molecular ageing in progeroid syndromes: Hutchinson-Gilford progeria

- syndrome as a model. *Immunity & ageing : I & A*, 6, p.4.
- Cowan, C.A. et al., 2005. Nuclear Reprogramming of Somatic Cells After Fusion with Human Embryonic Stem Cells. *Science*, 309(5739), pp.1369–1373.
- Crisp, M. et al., 2006. Coupling of the nucleus and cytoplasm. *The Journal of Cell Biology*, 172(1), pp.41–53.
- Crow, J.F., 1992. Erwin Schrödinger and the hornless cattle problem. *Genetics*, 130(2), pp.237–9.
- Curtis, A., 2004. Small is beautiful but smaller is the aim: Review of a life of research. *European Cells and Materials*, 8, pp.27–36.
- Curtis, A. & Wilkinson, C., 1997. Topographical control of cells. *Biomaterials*, 18(24), pp.1573–83.
- Curtis, A.S., 1964. The mechanism of adhesion of cells to glass. A study by interference reflection microscopy. *The Journal of cell biology*, 20, pp.199–215.
- Cuvelier, D. et al., 2007. The Universal Dynamics of Cell Spreading. *Current Biology*, 17(8), pp.694–699.
- Dahl, K.N., Ribeiro, A.J.S. & Lammerding, J., 2008a. Nuclear shape, mechanics, and mechanotransduction. *Circulation research*, 102(11), pp.1307–18.
- Dahl, K.N., Ribeiro, A.J.S. & Lammerding, J., 2008b. Nuclear shape, mechanics, and mechanotransduction. *Circulation research*, 102(11), pp.1307–18.
- Dahl, K.N., Ribeiro, A.J.S. & Lammerding, J., 2008. Nuclear Shape, Mechanics, and Mechanotransduction. *Circulation Research*, 102(11), pp.1307–1318.
- Dahmani, F. et al., 1998. Nanoindentation technique for measuring residual stress field around a laser-induced crack in fused silica. *Journal of Materials Science*, 33(19), pp.4677–4685.
- Dalby, M.J. et al., 2007. The control of human mesenchymal cell differentiation using nanoscale symmetry and disorder. *Nature Materials*, 6(12), pp.997–1003.
- Darling, E.M. et al., 2008. Viscoelastic properties of human mesenchymally-derived stem cells and primary osteoblasts, chondrocytes, and adipocytes. *Journal of Biomechanics*, 41(2), pp.454–464.
- Delaine-Smith, R.M. & Reilly, G.C., 2011. The Effects of Mechanical Loading on Mesenchymal Stem Cell Differentiation and Matrix Production. In *Vitamins and hormones*. pp. 417–480.
- Delmas, P., Hao, J. & Rodat-Despoix, L., 2011. Molecular mechanisms of mechanotransduction in mammalian sensory neurons. *Nature Reviews Neuroscience*, 12(3), pp.139–153.
- Deng, H.-W. et al., 2009. EFFECTIVE SKIN DEPTH FOR MULTILAYER COATED CONDUCTOR. *Progress In Electromagnetics Research M*, 9, pp.1–8.
- Díaz-Tocados, J.M. et al., 2017. Magnesium Chloride promotes Osteogenesis through Notch signaling activation and expansion of Mesenchymal Stem Cells. *Scientific reports*, 7(1), p.7839.
- Discher, D.E., Janmey, P. & Wang, Y.-L., 2005. Tissue Cells Feel and Respond to the Stiffness of Their Substrate. *Science*, 310(5751), pp.1139–1143.
- Döbereiner, H.-G. et al., 2004. Dynamic Phase Transitions in Cell Spreading. *Physical Review Letters*,

- 93(10), p.108105.
- Docheva, D. et al., 2008. Researching into the cellular shape, volume and elasticity of mesenchymal stem cells, osteoblasts and osteosarcoma cells by atomic force microscopy. *Journal of Cellular and Molecular Medicine*, 12(2), pp.537–552.
- Duncan, M.R. & Berman, B., 1989. Differential regulation of collagen, glycosaminoglycan, fibronectin, and collagenase activity production in cultured human adult dermal fibroblasts by interleukin 1- α and β and tumor necrosis factor- α and β . *The Journal of investigative dermatology*, 92(5), pp.699–706.
- Efremov, Y.M. et al., 2014. Mechanical properties of fibroblasts depend on level of cancer transformation. *Biochimica et Biophysica Acta (BBA) - Molecular Cell Research*, 1843(5), pp.1013–1019.
- Encyclopædia Britannica, cell | Definition, Types, & Functions | Britannica.com. Available at: <https://www.britannica.com/science/cell-biology/media/101396/112877> [Accessed October 14, 2018].
- Engler, A.J. et al., 2006. Matrix elasticity directs stem cell lineage specification. *Cell*, 126(4), pp.677–89.
- Eriksson, M. et al., 2003. Recurrent de novo point mutations in lamin A cause Hutchinson–Gilford progeria syndrome. *Nature*, 423(6937), pp.293–298.
- Ermis, M., Antmen, E. & Hasirci, V., 2018. Micro and Nanofabrication methods to control cell-substrate interactions and cell behavior: A review from the tissue engineering perspective. *Bioactive materials*, 3(3), pp.355–369.
- Evseenko, D. et al., 2010. Mapping the first stages of mesoderm commitment during differentiation of human embryonic stem cells. *Proceedings of the National Academy of Sciences of the United States of America*, 107(31), pp.13742–7.
- Fardin, M.A. et al., 2010. Cell spreading as a hydrodynamic process. *Soft matter*, 6, pp.4788–4799.
- Ferrera, D. et al., 2014. Lamin B1 overexpression increases nuclear rigidity in autosomal dominant leukodystrophy fibroblasts. *FASEB journal : official publication of the Federation of American Societies for Experimental Biology*, 28(9), pp.3906–18.
- Fitzpatrick, R., Propagation in a conductor. Available at: <http://farside.ph.utexas.edu/teaching/em/lectures/node102.html> [Accessed March 4, 2019].
- Fitzpatrick, V. et al., 2017. Signal mingle: Micropatterns of BMP-2 and fibronectin on soft biopolymeric films regulate myoblast shape and SMAD signaling. *Scientific Reports*, 7(1), p.41479.
- Fletcher, D.A. & Mullins, R.D., 2010a. Cell mechanics and the cytoskeleton. *Nature*, 463(7280), pp.485–492.
- Fletcher, D.A. & Mullins, R.D., 2010b. Cell mechanics and the cytoskeleton. *Nature*, 463(7280),

pp.485–492.

- Frantz, C., Stewart, K.M. & Weaver, V.M., 2010. The extracellular matrix at a glance. *Journal of cell science*, 123(Pt 24), pp.4195–200.
- Friedenstein, A.J. et al., 1974. Stromal cells responsible for transferring the microenvironment of the hemopoietic tissues. Cloning in vitro and retransplantation in vivo. *Transplantation*, 17(4), pp.331–40.
- Friedenstein, A.J., Chailakhjan, R.K. & Lalykina, K.S., 1970. The development of fibroblast colonies in monolayer cultures of guinea-pig bone marrow and spleen cells. *Cell and tissue kinetics*, 3(4), pp.393–403.
- Frisch, S.M. & Francis, H., 1994. Disruption of epithelial cell-matrix interactions induces apoptosis. *The Journal of cell biology*, 124(4), pp.619–26.
- Fuchs, E. & Weber, K., 1994. Intermediate filaments: structure, dynamics, function, and disease. *Annual review of biochemistry*, 63, pp.345–82.
- Fujita, S., Ohshima, M. & Iwata, H., 2009. Time-lapse observation of cell alignment on nanogrooved patterns. *Journal of The Royal Society Interface*, 6(suppl_3).
- Fujiwara, I. et al., 2002. Microscopic analysis of polymerization dynamics with individual actin filaments. *Nature Cell Biology*, 4(9), pp.666–673.
- Garikipati, V.N.S. et al., 2018. Isolation and characterization of mesenchymal stem cells from human fetus heart J. Rajasingh, ed. *PLOS ONE*, 13(2), p.e0192244.
- Ge, J. et al., 2013. Standard fluorescent imaging of live cells is highly genotoxic. *Cytometry. Part A : the journal of the International Society for Analytical Cytology*, 83(6), pp.552–60.
- Geiger, B., Spatz, J.P. & Bershadsky, A.D., 2009. Environmental sensing through focal adhesions. *Nature Reviews Molecular Cell Biology*, 10(1), pp.21–33.
- Gepstein, L., 2002. Derivation and potential applications of human embryonic stem cells. *Circulation research*, 91(10), pp.866–76.
- Gerlitz, G. & Bustin, M., 2011. The role of chromatin structure in cell migration. *Trends in Cell Biology*, 21(1), pp.6–11.
- Ghibardo, M. et al., 2009. Substrate Topography Induces a Crossover from 2D to 3D Behavior in Fibroblast Migration. *Biophysical Journal*, 97(1), pp.357–368.
- Giancotti, F.G., 2003. A structural view of integrin activation and signaling. *Developmental cell*, 4(2), pp.149–51.
- Gilbert, P.M. et al., 2010. Substrate Elasticity Regulates Skeletal Muscle Stem Cell Self-Renewal in Culture. *Science*, 329(5995), pp.1078–1081.
- Gilkes, D.M., Semenza, G.L. & Wirtz, D., 2014. Hypoxia and the extracellular matrix: drivers of tumour metastasis. *Nature Reviews Cancer*, 14(6), pp.430–439.
- Giorgini, M.G., Musso, M. & Torii, H., 2005. Concentration-dependent frequency shifts and Raman spectroscopic noncoincidence effect of the C=O stretching mode in dipolar mixtures of

- acetone/dimethyl sulfoxide. Experimental, theoretical, and simulation results. *The journal of physical chemistry. A*, 109(26), pp.5846–54.
- Gluckman, E. & Rocha, V., 2005. History of the clinical use of umbilical cord blood hematopoietic cells. *Cytotherapy*, 7(3), pp.219–227.
- Greggio, C. et al., 2013. Artificial three-dimensional niches deconstruct pancreas development in vitro. *Development*, 140(21), pp.4452–4462.
- GREGOIRE, F.M., SMAS, C.M. & SUL, H.S., 1998. Understanding Adipocyte Differentiation. *Physiological Reviews*, 78(3), pp.783–809.
- Grinnell, F., Billingham, R.E. & Burgess, L., 1981. Distribution of fibronectin during wound healing in vivo. *The Journal of investigative dermatology*, 76(3), pp.181–9.
- Gruenbaum, Y. et al., 2003. The nuclear lamina and its functions in the nucleus. *International review of cytology*, 226, pp.1–62.
- Gruenbaum, Y. & Foisner, R., 2015. Lamins: nuclear intermediate filament proteins with fundamental functions in nuclear mechanics and genome regulation. *Annual review of biochemistry*, 84, pp.131–64.
- Grzanka, D., Gagat, M. & Izdebska, M., 2013. Actin is required for cellular death. *Acta histochemica*, 115(8), pp.775–82.
- Guilak, F., Tedrow, J.R. & Burgkart, R., 2000. Viscoelastic Properties of the Cell Nucleus. *Biochemical and Biophysical Research Communications*, 269(3), pp.781–786.
- Guillotin, B. & Guillemot, F., 2011. Cell patterning technologies for organotypic tissue fabrication. *Trends in Biotechnology*, 29(4), pp.183–190.
- Guilluy, C. & Burrridge, K., 2015. Nuclear mechanotransduction: Forcing the nucleus to respond. *Nucleus*, 6(1), pp.19–22.
- Gumbiner, B.M., 1996. Cell adhesion: the molecular basis of tissue architecture and morphogenesis. *Cell*, 84(3), pp.345–57.
- Guz, N. et al., 2014. If cell mechanics can be described by elastic modulus: study of different models and probes used in indentation experiments. *Biophysical journal*, 107(3), pp.564–575.
- Hanson, L. et al., 2015a. Vertical nanopillars for in situ probing of nuclear mechanics in adherent cells. *Nature nanotechnology*, 10(6), pp.554–62.
- Hanson, L. et al., 2015b. Vertical nanopillars for in situ probing of nuclear mechanics in adherent cells. *Nature nanotechnology*, 10(6), pp.554–62.
- Hanson, L. et al., 2015c. Vertical nanopillars for in situ probing of nuclear mechanics in adherent cells. *Nature Nanotechnology*, 10(6), pp.554–562.
- Hardy, K., Handyside, A.H. & Winston, R.M., 1989. The human blastocyst: cell number, death and allocation during late preimplantation development in vitro. *Development (Cambridge, England)*, 107(3), pp.597–604.
- Harrison, R.G., 1912. The cultivation of tissues in extraneous media as a method of morpho-genetic

- study. *The Anatomical Record*, 6(4), pp.181–193.
- Harrison, R.G., 1914. The reaction of embryonic cells to solid structures. *Journal of Experimental Zoology*, 17(4), pp.521–544.
- Hass, R. et al., 2011. Different populations and sources of human mesenchymal stem cells (MSC): A comparison of adult and neonatal tissue-derived MSC. *Cell communication and signaling : CCS*, 9, p.12.
- Heino, J., 2007. The collagen family members as cell adhesion proteins. *BioEssays*, 29(10), pp.1001–1010.
- Heo, S.-J. et al., 2016. Differentiation alters stem cell nuclear architecture, mechanics, and mechanosensitivity. *eLife*, 5.
- Hernandez-Verdun, D., 2006. Nucleolus: from structure to dynamics. *Histochemistry and Cell Biology*, 125(1–2), pp.127–137.
- Herrmann, H. et al., 2007. Intermediate filaments: from cell architecture to nanomechanics. *Nature reviews. Molecular cell biology*, 8(7), pp.562–73.
- Hirokawa, N. et al., 2009. Kinesin superfamily motor proteins and intracellular transport. *Nature reviews. Molecular cell biology*, 10(10), pp.682–96.
- Hodgson, B. et al., 2018. The Regulation of Differentiation of Mesenchymal Stem-cells into Skeletal Muscle: A Look at Signalling Molecules Involved in Myogenesis. *Current Stem Cell Research & Therapy*, 13(5), pp.384–407.
- Hoffman-Kim, D., Mitchel, J.A. & Bellamkonda, R. V, 2010. Topography, cell response, and nerve regeneration. *Annual review of biomedical engineering*, 12, pp.203–31.
- Hoffmann, E.K., Lambert, I.H. & Pedersen, S.F., 2009. Physiology of cell volume regulation in vertebrates. *Physiological reviews*, 89(1), pp.193–277.
- Höger, T.H. et al., 1991. Immunolocalization of lamins in the thick nuclear lamina of human synovial cells. *European journal of cell biology*, 54(1), pp.150–6.
- Holy, T.E. & Leibler, S., 1994. Dynamic instability of microtubules as an efficient way to search in space. *Proceedings of the National Academy of Sciences of the United States of America*, 91(12), pp.5682–5.
- Honoki, K., 2017. Preventing aging with stem cell rejuvenation: Feasible or infeasible? *World journal of stem cells*, 9(1), pp.1–8.
- Hu, Y. et al., 2003. Isolation and identification of mesenchymal stem cells from human fetal pancreas. *Journal of Laboratory and Clinical Medicine*, 141(5), pp.342–349.
- Huang, C.-K. & Donald, A., 2014a. Revealing the dependence of cell spreading kinetics on its spreading morphology using microcontact printed fibronectin patterns. *Journal of The Royal Society Interface*, 12(102), pp.20141064–20141064.
- Huang, C.-K. & Donald, A., 2014b. Revealing the dependence of cell spreading kinetics on its spreading morphology using microcontact printed fibronectin patterns. *Journal of The Royal Society*

- Interface*, 12(102), pp.20141064–20141064.
- Huang, C., 2015. Contact Guidance. , (March).
- Huang, H.-L. et al., 2010. Trypsin-induced proteome alteration during cell subculture in mammalian cells. *Journal of biomedical science*, 17(1), p.36.
- Huh, S. et al., 2012. Apoptosis detection for adherent cell populations in time-lapse phase-contrast microscopy images. *Medical image computing and computer-assisted intervention : MICCAI ... International Conference on Medical Image Computing and Computer-Assisted Intervention*, 15(Pt 1), pp.331–9.
- Hütter, G., 2016. Stem cell transplantation in strategies for curing HIV/AIDS. *AIDS Research and Therapy*, 13(1), p.31.
- ibidi-cells in focus, LifeAct Plasmid | Actin Visualization in Living Cells | ibidi. Available at: <https://ibidi.com/lifeact-actin-visualization/83-pcmv-lifeact.html> [Accessed March 6, 2019].
- Ichimura, T. et al., 2014. Visualizing Cell State Transition Using Raman Spectroscopy L. Kreplak, ed. *PLoS ONE*, 9(1), p.e84478.
- Imagej.nih.gov, Analyze Menu. Available at: <https://imagej.nih.gov/ij/docs/menus/analyze.html> [Accessed February 6, 2019].
- Imagej.nih.gov, 2012. ImageJ User Guide - IJ 1.46r | Edit Menu. Available at: <https://imagej.nih.gov/ij/docs/guide/146-27.html> [Accessed March 24, 2019].
- in 't Anker, P.S. et al., 2003. Amniotic fluid as a novel source of mesenchymal stem cells for therapeutic transplantation. *Blood*, 102(4), pp.1548–1549.
- Ingber, D.E., 2006. Cellular mechanotransduction: putting all the pieces together again. *The FASEB Journal*, 20(7), pp.811–827.
- Jaasma, M.J., Jackson, W.M. & Keaveny, T.M., 2006. The Effects of Morphology, Confluency, and Phenotype on Whole-Cell Mechanical Behavior. *Annals of Biomedical Engineering*, 34(5), pp.759–768.
- Jacobson, M., 1978. *Developmental neurobiology*, Plenum Press.
- Janmey, P.A. & McCulloch, C.A., 2007. Cell mechanics: integrating cell responses to mechanical stimuli. *Annual review of biomedical engineering*, 9, pp.1–34.
- Jarvinen, L. et al., 2008. Lung resident mesenchymal stem cells isolated from human lung allografts inhibit T cell proliferation via a soluble mediator. *Journal of immunology (Baltimore, Md. : 1950)*, 181(6), pp.4389–96.
- Jensen, E.C., 2013. Overview of Live-Cell Imaging: Requirements and Methods Used. *The Anatomical Record: Advances in Integrative Anatomy and Evolutionary Biology*, 296(1), pp.1–8.
- Jiang, H. & Sun, S.X., 2013. Cellular pressure and volume regulation and implications for cell mechanics. *Biophysical journal*, 105(3), pp.609–19.
- Joon Kwon, H. & Yasuda, K., 2013. Chondrogenesis on sulfonate-coated hydrogels is regulated by their mechanical properties. *Journal of the Mechanical Behavior of Biomedical Materials*, 17,

pp.337–346.

- Jordan, M.A. & Wilson, L., 2004. Microtubules as a target for anticancer drugs. *Nature Reviews Cancer*, 4(4), pp.253–265.
- Jungebluth, P. et al., 2011. Tracheobronchial transplantation with a stem-cell-seeded bioartificial nanocomposite: a proof-of-concept study. *Lancet (London, England)*, 378(9808), pp.1997–2004.
- Kaivosoja, E. et al., 2012. Chemical and physical properties of regenerative medicine materials controlling stem cell fate. *Annals of Medicine*, 44(7), pp.635–650.
- Karp, G., 2010. *Cell and molecular biology : concepts and experiments*, John Wiley.
- Kasten, A. et al., 2014. Guidance of Mesenchymal Stem Cells on Fibronectin Structured Hydrogel Films A. J. Engler, ed. *PLoS ONE*, 9(10), p.e109411.
- Katayama, Y. et al., 2006. Signals from the Sympathetic Nervous System Regulate Hematopoietic Stem Cell Egress from Bone Marrow. *Cell*, 124(2), pp.407–421.
- Kelleher, C.M. & Vacanti, J.P., 2010. Engineering extracellular matrix through nanotechnology. *Journal of the Royal Society, Interface*, 7 Suppl 6(Suppl 6), pp.S717-29.
- Khatau, S.B. et al., 2009. A perinuclear actin cap regulates nuclear shape. *Proceedings of the National Academy of Sciences of the United States of America*, 106(45), pp.19017–22.
- Khatau, S.B. et al., 2009a. A perinuclear actin cap regulates nuclear shape. *Proceedings of the National Academy of Sciences*, 106(45), pp.19017–19022.
- Khatau, S.B. et al., 2009b. A perinuclear actin cap regulates nuclear shape. *Proceedings of the National Academy of Sciences*, 106(45), pp.19017–19022.
- Kihara, T. et al., 2011. Physical properties of mesenchymal stem cells are coordinated by the perinuclear actin cap. *Biochemical and Biophysical Research Communications*, 409(1), pp.1–6.
- Kilian, K.A. et al., 2010. Geometric cues for directing the differentiation of mesenchymal stem cells. *Proceedings of the National Academy of Sciences of the United States of America*, 107(11), pp.4872–7.
- Kim, D.-H. et al., 2012. Actin cap associated focal adhesions and their distinct role in cellular mechanosensing. *Scientific Reports*, 2(1), p.555.
- Kim, D.-H. et al., 2015. Volume regulation and shape bifurcation in the cell nucleus. *Journal of cell science*, 128(18), pp.3375–85.
- Kim, D.-H., Chambliss, A.B. & Wirtz, D., 2013. The multi-faceted role of the actin cap in cellular mechanosensation and mechanotransduction. *Soft matter*, 9(23), pp.5516–5523.
- Kim, D.-H., Chambliss, A.B. & Wirtz, D., 2013. The multi-faceted role of the actin cap in cellular mechanosensation and mechanotransduction. *Soft Matter*, 9(23), p.5516.
- Kim, D.-H., Cho, S. & Wirtz, D., 2014. Tight coupling between nucleus and cell migration through the perinuclear actin cap. *Journal of cell science*, 127(Pt 11), pp.2528–41.
- Kim, D.-H., Cho, S. & Wirtz, D., 2014a. Tight coupling between nucleus and cell migration through

- the perinuclear actin cap. *Journal of Cell Science*, 127(11), pp.2528–2541.
- Kim, D.-H., Cho, S. & Wirtz, D., 2014b. Tight coupling between nucleus and cell migration through the perinuclear actin cap. *Journal of Cell Science*, 127(11), pp.2528–2541.
- Kim, M.-C. et al., 2013. Dynamic modeling of cell migration and spreading behaviors on fibronectin coated planar substrates and micropatterned geometries. *PLoS computational biology*, 9(2), p.e1002926.
- King, N.M. & Perrin, J., 2014. Ethical issues in stem cell research and therapy. *Stem Cell Research & Therapy*, 5(4), p.85.
- Kingma, K.J. & Hemley, R.J., 1994. Raman spectroscopic study of microcrystalline silica. *American Mineralogist*, 79(3–4), pp.269–273.
- Klein, K. et al., 2012. Label-free live-cell imaging with confocal Raman microscopy. *Biophysical journal*, 102(2), pp.360–8.
- Kreplak, L. & Fudge, D., 2007. Biomechanical properties of intermediate filaments: from tissues to single filaments and back. *BioEssays : news and reviews in molecular, cellular and developmental biology*, 29(1), pp.26–35.
- Kühnel, W. & Kühnel, W., 2003. *Color atlas of cytology, histology, and microscopic anatomy*, Thieme.
- Kulangara, K. et al., 2014. The effect of substrate topography on direct reprogramming of fibroblasts to induced neurons. *Biomaterials*, 35(20), pp.5327–5336.
- Kung, K.S. et al., 2011. The development of anisotropic behaviours of 3T3 fibroblasts on microgrooved patterns. *The European physical journal. E, Soft matter*, 34(3), p.23.
- L.M. Khoo, M., Tao, H. & D.F. Ma, D., 2011. Mesenchymal Stem Cell-Based Therapies for Parkinson's Disease: Progress, Controversies and Lessons for the Future. *Journal of Stem Cell Research & Therapy*, 01(S2), p.
- Lammerding, J. et al., 2006. Lamins A and C but Not Lamin B1 Regulate Nuclear Mechanics. *Journal of Biological Chemistry*, 281(35), pp.25768–25780.
- Law, J.X. et al., 2016. Tissue-engineered trachea: A review. *International Journal of Pediatric Otorhinolaryngology*, 91, pp.55–63.
- Lee, C.H., Moiola, E.K. & Mao, J.J., 2006. Fibroblastic differentiation of human mesenchymal stem cells using connective tissue growth factor. *Conference proceedings : ... Annual International Conference of the IEEE Engineering in Medicine and Biology Society. IEEE Engineering in Medicine and Biology Society. Annual Conference*, 1, pp.775–8.
- Lee, O.K. et al., 2004. Isolation of multipotent mesenchymal stem cells from umbilical cord blood. *Blood*, 103(5), pp.1669–1675.
- Lee, S. et al., 2015. Cell Adhesion and Long-Term Survival of Transplanted Mesenchymal Stem Cells: A Prerequisite for Cell Therapy. *Oxidative Medicine and Cellular Longevity*, 2015, pp.1–9.
- Lee, Y. et al., 2013. Three-dimensional fibroblast morphology on compliant substrates of controlled

- negative curvature. *Integrative Biology*, 5(12), p.1447.
- Li, S. et al., 2017. Combined effects of multi-scale topographical cues on stable cell sheet formation and differentiation of mesenchymal stem cells. *Biomaterials Science*, 5(10), pp.2056–2067.
- Lim, Y.-B. et al., 2000. Disruption of Actin Cytoskeleton Induces Chondrogenesis of Mesenchymal Cells by Activating Protein Kinase C- α Signaling. *Biochemical and Biophysical Research Communications*, 273(2), pp.609–613.
- Limozin, L. & Sengupta, K., 2009. Quantitative reflection interference contrast microscopy (RICM) in soft matter and cell adhesion. *Chemphyschem: a European journal of chemical physics and physical chemistry*, 10(16), pp.2752–68.
- Liu, Y., Zhu, Y. & Li, Z., 2014. Application of Raman spectroscopy in Andrology: non-invasive analysis of tissue and single cell. *Translational andrology and urology*, 3(1), pp.125–33.
- Liu, Z. et al., 2008. Multiplexed multicolor Raman imaging of live cells with isotopically modified single walled carbon nanotubes. *Journal of the American Chemical Society*, 130(41), pp.13540–1.
- Llames, S. et al., 2015. Feeder Layer Cell Actions and Applications. *Tissue engineering. Part B, Reviews*, 21(4), pp.345–53.
- Lo, B. & Parham, L., 2009. Ethical issues in stem cell research. *Endocrine reviews*, 30(3), pp.204–13.
- Lodish, H. et al., 2000a. Cell-Cell Adhesion and Communication.
- Lodish, H. et al., 2000b. Microtubule Structures.
- Lodish, H.F., 2000. *Molecular cell biology*, W.H. Freeman.
- Loye, A.M. et al., 2018. Regulation of Mesenchymal Stem Cell Differentiation by Nanopatterning of Bulk Metallic Glass. *Scientific Reports*, 8(1), p.8758.
- Lv, H. et al., 2015. Mechanism of regulation of stem cell differentiation by matrix stiffness. *Stem cell research & therapy*, 6(1), p.103.
- Ma, K. et al., 2012. Variations in chondrogenesis of human bone marrow-derived mesenchymal stem cells in fibrin/alginate blended hydrogels. *Acta biomaterialia*, 8(10), pp.3754–64.
- Macchiarini, P. et al., 2008. Clinical transplantation of a tissue-engineered airway. *The Lancet*, 372(9655), pp.2023–2030.
- MacKintosh, F., Käs, J. & Janmey, P., 1995. Elasticity of semiflexible biopolymer networks. *Physical review letters*, 75(24), pp.4425–4428.
- Maeshima, K. et al., 2011. Nuclear size, nuclear pore number and cell cycle. *Nucleus*, 2(2), pp.113–118.
- Mahan, J.E., 2000. *Physical vapor deposition of thin films*, Wiley.
- Mahla, R.S., 2016a. Stem Cells Applications in Regenerative Medicine and Disease Therapeutics. *International Journal of Cell Biology*, 2016, pp.1–24.
- Mahla, R.S., 2016b. Stem Cells Applications in Regenerative Medicine and Disease Therapeutics.

- International Journal of Cell Biology*, 2016, pp.1–24.
- Mamaghani, P. (University of B.C., 2015. *CELL DEATH DYNAMICS MONITORING USING RAMAN MICRO-SPECTROSCOPY*. University Of British Columbia.
- Mandai, M. et al., 2017. Autologous Induced Stem-Cell-Derived Retinal Cells for Macular Degeneration. *New England Journal of Medicine*, 376(11), pp.1038–1046.
- Manhart, A. et al., 2018. Mechanical positioning of multiple nuclei in muscle cells O. A. Igoshin, ed. *PLOS Computational Biology*, 14(6), p.e1006208.
- Maninová, M. & Vomastek, T., 2016. Dorsal stress fibers, transverse actin arcs, and perinuclear actin fibers form an interconnected network that induces nuclear movement in polarizing fibroblasts. *The FEBS Journal*, 283(20), pp.3676–3693.
- VON DER MARK, K. et al., 1977. Relationship between cell shape and type of collagen synthesised as chondrocytes lose their cartilage phenotype in culture. *Nature*, 267(5611), pp.531–532.
- Marmaras, A. et al., 2012. Topography-mediated apical guidance in epidermal wound healing. *Soft Matter*, 8(26), p.6922.
- Martinac, B., 2004. Mechanosensitive ion channels: molecules of mechanotransduction. *Journal of cell science*, 117(Pt 12), pp.2449–60.
- Mathieu, P.S. & Lobo, E.G., 2012. Cytoskeletal and focal adhesion influences on mesenchymal stem cell shape, mechanical properties, and differentiation down osteogenic, adipogenic, and chondrogenic pathways. *Tissue engineering. Part B, Reviews*, 18(6), pp.436–44.
- Matt Carter, J.S., 2015. Lipofection - an overview | ScienceDirect Topics. Available at: <https://www.sciencedirect.com/topics/biochemistry-genetics-and-molecular-biology/lipofection> [Accessed March 6, 2019].
- Maximow, A.A., 1924. RELATION OF BLOOD CELLS TO CONNECTIVE TISSUES AND ENDOTHELIUM. *Physiological Reviews*, 4(4), pp.533–563.
- McBeath, R. et al., 2004. Cell shape, cytoskeletal tension, and RhoA regulate stem cell lineage commitment. *Developmental cell*, 6(4), pp.483–95.
- McKeown-Longo, P.J. & Mosher, D.F., 1984. Mechanism of formation of disulfide-bonded multimers of plasma fibronectin in cell layers of cultured human fibroblasts. *The Journal of biological chemistry*, 259(19), pp.12210–5.
- Melling, M. et al., 2001. Atomic Force Microscopy Imaging of the Human Trigeminal Ganglion. *NeuroImage*, 14(6), pp.1348–1352.
- Metavarayuth, K. et al., 2016. Influence of Surface Topographical Cues on the Differentiation of Mesenchymal Stem Cells in Vitro. *ACS Biomaterials Science & Engineering*, 2(2), pp.142–151.
- Mills, J.C. et al., 1998. Apoptotic membrane blebbing is regulated by myosin light chain phosphorylation. *The Journal of cell biology*, 140(3), pp.627–36.
- Miroslav Holeček, P.K. and Z.T., 2011. *Theoretical Biomechanics* V. Klika, ed., InTech.
- MIT Material Property Database, Gold. Available at: <http://www.mit.edu/~6.777/matprops/gold.htm>

- [Accessed March 4, 2019].
- MIT Material Property Database, 1999. *Materials science & engineering. C, Biomimetic and supramolecular systems.*, Elsevier Science.
- Mitalipov, S. & Wolf, D., 2009. Totipotency, pluripotency and nuclear reprogramming. *Advances in biochemical engineering/biotechnology*, 114, pp.185–99.
- Mitra, S.K., Hanson, D.A. & Schlaepfer, D.D., 2005. Focal adhesion kinase: in command and control of cell motility. *Nature Reviews Molecular Cell Biology*, 6(1), pp.56–68.
- Miyake, K., Satomi, N. & Sasaki, S., 2006. Elastic modulus of polystyrene film from near surface to bulk measured by nanoindentation using atomic force microscopy. *Applied Physics Letters*, 89(3), p.031925.
- Mooney, D.J., Langer, R. & Ingber, D.E., 1995. Cytoskeletal filament assembly and the control of cell spreading and function by extracellular matrix. *Journal of cell science*, 108 (Pt 6), pp.2311–20.
- Movasaghi, Z., Rehman, S. & Rehman, I.U., 2007. Raman Spectroscopy of Biological Tissues. *Applied Spectroscopy Reviews*, 42(5), pp.493–541.
- Mukaka, M.M., 2012. Statistics corner: A guide to appropriate use of correlation coefficient in medical research. *Malawi medical journal : the journal of Medical Association of Malawi*, 24(3), pp.69–71.
- Munevar, S., Wang, Y. & Dembo, M., 2001. Traction force microscopy of migrating normal and H-ras transformed 3T3 fibroblasts. *Biophysical journal*, 80(4), pp.1744–57.
- Murrell, M. et al., 2015. Forcing cells into shape: the mechanics of actomyosin contractility. *Nature Reviews Molecular Cell Biology*, 16(8), pp.486–498.
- Nakamoto, T. et al., 2014. Influence of micropattern width on differentiation of human mesenchymal stem cells to vascular smooth muscle cells. *Colloids and Surfaces B: Biointerfaces*, 122, pp.316–323.
- Nandoe Tewarie, R.S. et al., 2009. Stem cell-based therapies for spinal cord injury. *The journal of spinal cord medicine*, 32(2), pp.105–14.
- Nature reviews, molecular cell biology, 2000. *Nature reviews. Molecular cell biology.*, Nature Pub. Group.
- Nava, M.M., Raimondi, M.T. & Pietrabissa, R., 2012. Controlling Self-Renewal and Differentiation of Stem Cells via Mechanical Cues. *Journal of Biomedicine and Biotechnology*, 2012, pp.1–12.
- Ng, A.P. & Alexander, W.S., 2017. Haematopoietic stem cells: past, present and future. *Cell Death Discovery*, 3, p.17002.
- Nikkhah, M. et al., 2012. Engineering microscale topographies to control the cell–substrate interface. *Biomaterials*, 33(21), pp.5230–5246.
- Nobes, C.D. & Hall, A., 1995. Rho, Rac, and Cdc42 GTPases regulate the assembly of multimolecular focal complexes associated with actin stress fibers, lamellipodia, and filopodia. *Cell*, 81(1), pp.53–

- Noguchi, H., 2010. Pancreatic stem/progenitor cells for the treatment of diabetes. *The review of diabetic studies : RDS*, 7(2), pp.105–11.
- O'Donoghue, K. & Fisk, N.M., 2004. Fetal stem cells. *Best Practice & Research Clinical Obstetrics & Gynaecology*, 18(6), pp.853–875.
- Oakley, C. & Brunette, D.M., 1993. The sequence of alignment of microtubules, focal contacts and actin filaments in fibroblasts spreading on smooth and grooved titanium substrata. *Journal of cell science*, 106 (Pt 1, pp.343–54.
- Ohara, P.T. & Buck, R.C., 1979. Contact guidance in vitro. *Experimental Cell Research*, 121(2), pp.235–249.
- Ohtsuki, R., Sakamaki, T. & Tominaga, S., 2013. Analysis of skin surface roughness by visual assessment and surface measurement. *Optical Review*, 20(2), pp.94–101.
- Ojima, M. et al., 2016. Different methods of detaching adherent cells significantly affect the detection of stem cell antigens in synovial mesenchymal stem cells. *Osteoarthritis and Cartilage*, 24, pp.S509–S510.
- Okotrub, K.A. et al., 2015. Raman spectroscopy for DNA quantification in cell nucleus. *Cytometry Part A*, 87(1), pp.68–73.
- Paguirigan, A.L. & Beebe, D.J., 2009. From the cellular perspective: exploring differences in the cellular baseline in macroscale and microfluidic cultures. *Integrative biology : quantitative biosciences from nano to macro*, 1(2), pp.182–95.
- Paguirigan, A.L. & Beebe, D.J., 2008. Microfluidics meet cell biology: bridging the gap by validation and application of microscale techniques for cell biological assays. *BioEssays : news and reviews in molecular, cellular and developmental biology*, 30(9), pp.811–21.
- Paine, P.L., Moore, L.C. & Horowitz, S.B., 1975. Nuclear envelope permeability. *Nature*, 254(5496), pp.109–114.
- Pajerowski, J.D. et al., 2007. Physical plasticity of the nucleus in stem cell differentiation. *Proceedings of the National Academy of Sciences*, 104(40), pp.15619–15624.
- Pan, Z. et al., 2012. Control of cell nucleus shapes via micropillar patterns. *Biomaterials*, 33(6), pp.1730–5.
- Pankov, R. et al., 2000. Integrin dynamics and matrix assembly: tensin-dependent translocation of alpha(5)beta(1) integrins promotes early fibronectin fibrillogenesis. *The Journal of cell biology*, 148(5), pp.1075–90.
- Pankov, R. & Yamada, K.M., 2002. Fibronectin at a glance. *Journal of cell science*, 115(Pt 20), pp.3861–3.
- Parent, C.A., 2004. Making all the right moves: chemotaxis in neutrophils and Dictyostelium. *Current opinion in cell biology*, 16(1), pp.4–13.
- Parfitt, A.M., 1984. Age-related structural changes in trabecular and cortical bone: cellular mechanisms

- and biomechanical consequences. *Calcified tissue international*, 36 Suppl 1, pp.S123-8.
- Park, J. et al., 2007. Nanosize and Vitality: TiO₂ Nanotube Diameter Directs Cell Fate. *Nano Letters*, 7(6), pp.1686–1691.
- Park, J. et al., 2009. TiO₂ Nanotube Surfaces: 15 nm-An Optimal Length Scale of Surface Topography for Cell Adhesion and Differentiation. *Small*, 5(6), pp.666–671.
- Park, J.S. et al., 2011. The effect of matrix stiffness on the differentiation of mesenchymal stem cells in response to TGF- β . *Biomaterials*, 32(16), pp.3921–3930.
- Park, J.Y. et al., 2010. Increased poly(dimethylsiloxane) stiffness improves viability and morphology of mouse fibroblast cells. *BioChip Journal*, 4(3), pp.230–236.
- Parsons, J.T., Horwitz, A.R. & Schwartz, M.A., 2010a. Cell adhesion: integrating cytoskeletal dynamics and cellular tension. *Nature reviews. Molecular cell biology*, 11(9), pp.633–43.
- Parsons, J.T., Horwitz, A.R. & Schwartz, M.A., 2010b. Cell adhesion: integrating cytoskeletal dynamics and cellular tension. *Nature reviews. Molecular cell biology*, 11(9), pp.633–43.
- Parsons, J.T., Horwitz, A.R. & Schwartz, M.A., 2010. Cell adhesion: integrating cytoskeletal dynamics and cellular tension. *Nature Reviews Molecular Cell Biology*, 11(9), pp.633–643.
- Paul, G. et al., 2012. The Adult Human Brain Harbors Multipotent Perivascular Mesenchymal Stem Cells B. Nelson, ed. *PLoS ONE*, 7(4), p.e35577.
- Păunescu, V. et al., 2007. In vitro differentiation of human mesenchymal stem cells to epithelial lineage. *Journal of Cellular and Molecular Medicine*, 11(3), pp.502–508.
- Petrie, R.J., Doyle, A.D. & Yamada, K.M., 2009. Random versus directionally persistent cell migration. *Nature Reviews Molecular Cell Biology*, 10(8), pp.538–549.
- Phillip, J.M. et al., 2015. The Mechanobiology of Aging. *Annual review of biomedical engineering*, 17, pp.113–141.
- Piroli, M.E. & Jabbarzadeh, E., 2018. Matrix Stiffness Modulates Mesenchymal Stem Cell Sensitivity to Geometric Asymmetry Signals. *Annals of Biomedical Engineering*, 46(6), pp.888–898.
- Pizzute, T., Lynch, K. & Pei, M., 2015. Impact of tissue-specific stem cells on lineage-specific differentiation: a focus on the musculoskeletal system. *Stem cell reviews*, 11(1), pp.119–32.
- Potten, C.S. & Loeffler, M., 1990. Stem cells: attributes, cycles, spirals, pitfalls and uncertainties. Lessons for and from the crypt. *Development (Cambridge, England)*, 110(4), pp.1001–20.
- Qin, D., Xia, Y. & Whitesides, G.M., 2010. Soft lithography for micro- and nanoscale patterning. *Nature protocols*, 5(3), pp.491–502.
- Regehr, K.J. et al., 2009. Biological implications of polydimethylsiloxane-based microfluidic cell culture. *Lab on a chip*, 9(15), pp.2132–9.
- Ricard-Blum, S., 2011. The collagen family. *Cold Spring Harbor perspectives in biology*, 3(1), p.a004978.
- Rieder, C.L., Faruki, S. & Khodjakov, A., 2001. The centrosome in vertebrates: more than a

- microtubule-organizing center. *Trends in Cell Biology*, 11(10), pp.413–419.
- Riedl, J. et al., 2008. Lifeact: a versatile marker to visualize F-actin. *Nature methods*, 5(7), pp.605–7.
- Riveline, D. et al., 2001. Focal contacts as mechanosensors: externally applied local mechanical force induces growth of focal contacts by an mDia1-dependent and ROCK-independent mechanism. *The Journal of cell biology*, 153(6), pp.1175–86.
- Rizzotto, A. & Schirmer, E.C., 2017. Breaking the scale: how disrupting the karyoplasmic ratio gives cancer cells an advantage for metastatic invasion. *Biochemical Society Transactions*, 45(6), pp.1333–1344.
- Rogers, I. & Casper, R.F., 2004. Umbilical cord blood stem cells. *Best Practice & Research Clinical Obstetrics & Gynaecology*, 18(6), pp.893–908.
- Ross, A.M. et al., 2012. Physical Aspects of Cell Culture Substrates: Topography, Roughness, and Elasticity. *Small*, 8(3), pp.336–355.
- Rothbaler, A., Schwartz, T.U. & Kutay, U., 2013. LINCing complex functions at the nuclear envelope. *Nucleus*, 4(1), pp.29–36.
- Rubinstein, P., 2006. Why Cord Blood? *Human Immunology*, 67(6), pp.398–404.
- Ruoslahti, E., 1984. Fibronectin in cell adhesion and invasion. *Cancer metastasis reviews*, 3(1), pp.43–51.
- Sabass, B. et al., 2008. High resolution traction force microscopy based on experimental and computational advances. *Biophysical journal*, 94(1), pp.207–20.
- De Santis, G. et al., 2011. How can cells sense the elasticity of a substrate? An analysis using a cell tensegrity model. *European Cells and Materials*, 22, pp.202–213.
- Scaffidi, P. & Misteli, T., 2008a. Lamin A-dependent misregulation of adult stem cells associated with accelerated ageing. *Nature Cell Biology*, 10(4), pp.452–459.
- Scaffidi, P. & Misteli, T., 2008b. Lamin A-dependent misregulation of adult stem cells associated with accelerated ageing. *Nature Cell Biology*, 10(4), pp.452–459.
- Schäfer, R. & Schmidt, P.C. eds., 2012. *Methods in Physical Chemistry*, Weinheim, Germany: Wiley-VCH Verlag GmbH & Co. KGaA.
- Schöler, H.R., 2016. The Potential of Stem Cells: An Inventory. , pp.45–72.
- Scuteri, A. et al., 2011. Mesenchymal stem cells neuronal differentiation ability: a real perspective for nervous system repair? *Current stem cell research & therapy*, 6(2), pp.82–92.
- Seethapathy, S. & Górecki, T., 2012. Applications of polydimethylsiloxane in analytical chemistry: a review. *Analytica chimica acta*, 750, pp.48–62.
- Selvaraj, V. et al., 2010. Switching cell fate: the remarkable rise of induced pluripotent stem cells and lineage reprogramming technologies. *Trends in biotechnology*, 28(4), pp.214–23.
- Shell, M.S., 2015. The canonical partition function. In *Thermodynamics and Statistical Mechanics*. Cambridge: Cambridge University Press, pp. 319–342.
- Shemesh, T. et al., 2005. Focal adhesions as mechanosensors: a physical mechanism. *Proceedings of*

- the National Academy of Sciences of the United States of America*, 102(35), pp.12383–8.
- Shen, X. et al., 2017. Differentiation of mesenchymal stem cells into cardiomyocytes is regulated by miRNA-1-2 via WNT signaling pathway. *Journal of biomedical science*, 24(1), p.29.
- Shi, S. & Gronthos, S., 2003. Perivascular Niche of Postnatal Mesenchymal Stem Cells in Human Bone Marrow and Dental Pulp. *Journal of Bone and Mineral Research*, 18(4), pp.696–704.
- Short, B. & Barr, F.A., 2000. The Golgi apparatus. *Current Biology*, 10(16), pp.R583–R585.
- Smith, D.J. et al., 2009. Human sperm accumulation near surfaces: a simulation study. *Journal of Fluid Mechanics*, 621, p.289.
- Song, S. et al., 2015. The synergistic effect of micro-topography and biochemical culture environment to promote angiogenesis and osteogenic differentiation of human mesenchymal stem cells. *Acta Biomaterialia*, 18, pp.100–111.
- Sorokin, D. V et al., 2014. Visualizing stable features in live cell nucleus for evaluation of the cell global motion compensation. *Folia biologica*, 60 Suppl 1, pp.45–9.
- Stephens, D.J. & Allan, V.J., 2003. Light microscopy techniques for live cell imaging. *Science (New York, N.Y.)*, 300(5616), pp.82–6.
- Stevenson, P.M. & Donald, A.M., 2009. Identification of three regimes of behavior for cell attachment on topographically patterned substrates. *Langmuir: the ACS journal of surfaces and colloids*, 25(1), pp.367–76.
- Stuart, E.S. & Moscona, A.A., 1967. Embryonic morphogenesis: role of fibrous lattice in the development of feathers and feather patterns. *Science (New York, N.Y.)*, 157(3791), pp.947–8.
- Stupack, D.G. et al., 2001. Apoptosis of adherent cells by recruitment of caspase-8 to unligated integrins. *The Journal of cell biology*, 155(3), pp.459–70.
- Stuurman, N., Heins, S. & Aebersold, U., 1998. Nuclear Lamins: Their Structure, Assembly, and Interactions. *Journal of Structural Biology*, 122(1–2), pp.42–66.
- Subramony, S.D. et al., 2013. The guidance of stem cell differentiation by substrate alignment and mechanical stimulation. *Biomaterials*, 34(8), pp.1942–1953.
- Sun, M., Chi, G., Li, P., et al., 2018. Effects of Matrix Stiffness on the Morphology, Adhesion, Proliferation and Osteogenic Differentiation of Mesenchymal Stem Cells. *International journal of medical sciences*, 15(3), pp.257–268.
- Sun, M., Chi, G., Xu, J., et al., 2018. Extracellular matrix stiffness controls osteogenic differentiation of mesenchymal stem cells mediated by integrin $\alpha 5$. *Stem cell research & therapy*, 9(1), p.52.
- Swift, J. et al., 2013. Nuclear Lamin-A Scales with Tissue Stiffness and Enhances Matrix-Directed Differentiation. *Science*, 341(6149), pp.1240104–1240104.
- Symeonidou, A. et al., 2013. Human Mesenchymal Stem Cell Response to 444 Ferritic Stainless Steel Networks. *MRS Proceedings*, 1569, pp.mrss13-1569-nn01-01.
- Szymanski, H.A., 1967. *Raman Spectroscopy: Theory and Practice*, Springer US.
- Takahashi, K. & Yamanaka, S., 2006. Induction of Pluripotent Stem Cells from Mouse Embryonic and

- Adult Fibroblast Cultures by Defined Factors. *Cell*, 126(4), pp.663–676.
- Tamiello, C., Bouten, C.V.C. & Baaijens, F.P.T., 2015. Competition between cap and basal actin fiber orientation in cells subjected to contact guidance and cyclic strain. *Scientific reports*, 5, p.8752.
- Tang, Q.Y. et al., 2015. Control of cell migration direction by inducing cell shape asymmetry with patterned topography. *Journal of Biomedical Materials Research Part A*, 103(7), pp.2383–2393.
- Tchieu, J. et al., 2017. A Modular Platform for Differentiation of Human PSCs into All Major Ectodermal Lineages.
- The Lancet, T., 2018. The final verdict on Paolo Macchiarini: guilty of misconduct. *Lancet (London, England)*, 392(10141), p.2.
- Theocharis, A.D. et al., 2016. Extracellular matrix structure. *Advanced Drug Delivery Reviews*, 97, pp.4–27.
- ThermoFisher scientific, Culturing Mesenchymal Stem Cells (MSCs) in 2% Reduced Serum Medium - UK.
- Thery, M., 2010. Micropatterning as a tool to decipher cell morphogenesis and functions. *Journal of Cell Science*, 123(24), pp.4201–4213.
- Théry, M. et al., 2007. Experimental and theoretical study of mitotic spindle orientation. *Nature*, 447(7143), pp.493–496.
- Thistlescientific.co.uk, pCMV/pCAG-LifeAct Plasmids | Thistle Scientific. Available at: <https://www.thistlescientific.co.uk/product/pcmvpcag-lifeact-plasmids/> [Accessed March 19, 2019].
- Tilghman, R.W. & Parsons, J.T., 2008. Focal adhesion kinase as a regulator of cell tension in the progression of cancer. *Seminars in Cancer Biology*, 18(1), pp.45–52.
- Timpl, R. et al., 1979. Laminin--a glycoprotein from basement membranes. *The Journal of biological chemistry*, 254(19), pp.9933–7.
- Titushkin, I.A. & Cho, M.R., 2009. Controlling cellular biomechanics of human mesenchymal stem cells. In *2009 Annual International Conference of the IEEE Engineering in Medicine and Biology Society*. IEEE, pp. 2090–2093.
- Toh, K.C., Ramdas, N.M. & Shivashankar, G. V, 2015. Actin cytoskeleton differentially alters the dynamics of lamin A, HP1 α and H2B core histone proteins to remodel chromatin condensation state in living cells. *Integrative biology : quantitative biosciences from nano to macro*, 7(10), pp.1309–17.
- Toh, Y.-C. et al., 2007. A novel 3D mammalian cell perfusion-culture system in microfluidic channels. *Lab on a Chip*, 7(3), p.302.
- Toma, J.G. et al., 2001. Isolation of multipotent adult stem cells from the dermis of mammalian skin. *Nature Cell Biology*, 3(9), pp.778–784.
- Tracy, L.E., Minasian, R.A. & Caterson, E.J., 2016. Extracellular Matrix and Dermal Fibroblast

- Function in the Healing Wound. *Advances in wound care*, 5(3), pp.119–136.
- Trickey, W.R., Vail, T.P. & Guilak, F., 2004. The role of the cytoskeleton in the viscoelastic properties of human articular chondrocytes. *Journal of orthopaedic research : official publication of the Orthopaedic Research Society*, 22(1), pp.131–9.
- Trounson, A. & McDonald, C., 2015. Stem Cell Therapies in Clinical Trials: Progress and Challenges. *Cell stem cell*, 17(1), pp.11–22.
- Tschumperlin, D.J., 2013. Fibroblasts and the ground they walk on. *Physiology (Bethesda, Md.)*, 28(6), pp.380–90.
- Tsuji, K. et al., 2017. Effects of Different Cell-Detaching Methods on the Viability and Cell Surface Antigen Expression of Synovial Mesenchymal Stem Cells. *Cell transplantation*, 26(6), pp.1089–1102.
- Turgeon, M.L., 2004. *Clinical hematology : theory and procedures*, Lippincott Williams & Wilkins.
- Turinetto, V., Vitale, E. & Giachino, C., 2016. Senescence in Human Mesenchymal Stem Cells: Functional Changes and Implications in Stem Cell-Based Therapy. *International journal of molecular sciences*, 17(7).
- Tzur, Y.B., Wilson, K.L. & Gruenbaum, Y., 2006. SUN-domain proteins: “Velcro” that links the nucleoskeleton to the cytoskeleton. *Nature Reviews Molecular Cell Biology*, 7(10), pp.782–788.
- U.S. National library of Medicine, 2016. MeSH Browser. Available at: <https://meshb.nlm.nih.gov/record/ui?name=Transfection> [Accessed March 6, 2019].
- Uccelli, A., Moretta, L. & Pistoia, V., 2008. Mesenchymal stem cells in health and disease. *Nature Reviews Immunology*, 8(9), pp.726–736.
- Valarmathi, M.T. & W. Fuseler, J., 2011. Mammalian Cardiac Muscle Regeneration: Structural and Functional Modulation of Adult Marrow Stromal Stem Cells. *Anatomy & Physiology*, 01(01), pp.1–3.
- Vellasamy, S. et al., 2012. Isolation and characterisation of mesenchymal stem cells derived from human placenta tissue. *World journal of stem cells*, 4(6), pp.53–61.
- Vitale, M. et al., 1999. Apoptosis induced by denied adhesion to extracellular matrix (anoikis) in thyroid epithelial cells is p53 dependent but fails to correlate with modulation of p53 expression. *FEBS Letters*, 462(1–2), pp.57–60.
- Vogel, V. & Sheetz, M., 2006. Local force and geometry sensing regulate cell functions. *Nature Reviews Molecular Cell Biology*, 7(4), pp.265–275.
- Voglis, G. & Tavernarakis, N., 2005. Mechanotransduction in the Nematode *Caenorhabditis elegans*.
- Wachsstock, D.H., Schwartz, W.H. & Pollard, T.D., 1993. Affinity of alpha-actinin for actin determines the structure and mechanical properties of actin filament gels. *Biophysical journal*, 65(1), pp.205–14.
- Wagers, A.J. & Weissman, I.L., 2004. Plasticity of Adult Stem Cells. *Cell*, 116(5), pp.639–648.
- WALTON, W.H., 1948. Feret’s Statistical Diameter as a Measure of Particle Size. *Nature*, 162(4113),

- pp.329–330.
- Wanders, R.J.A. & Waterham, H.R., 2006. Biochemistry of Mammalian Peroxisomes Revisited. *Annual Review of Biochemistry*, 75(1), pp.295–332.
- Wayne Rasband, 2000. Circularity. Available at: <https://imagej.nih.gov/ij/plugins/circularity.html> [Accessed March 24, 2019].
- Webster, M., Witkin, K.L. & Cohen-Fix, O., 2009. Journal of Cell Science. *J. Cell Sci.*, 112(13), pp.2253–2264.
- Webster, M., Witkin, K.L. & Cohen-Fix, O., 2009. Sizing up the nucleus: nuclear shape, size and nuclear-envelope assembly. *Journal of cell science*, 122(Pt 10), pp.1477–86.
- Weiss, P., 1945. Experiments on cell and axon orientation in vitro: The role of colloidal exudates in tissue organization. *Journal of Experimental Zoology*, 100(3), pp.353–386.
- Weiss, P., 1934. In vitro experiments on the factors determining the course of the outgrowing nerve fiber. *Journal of Experimental Zoology*, 68(3), pp.393–448.
- Weiss, P., 1941. *Self-differentiation of the basic patterns of coordination*, Williams & Wilkins Baltimore.
- Welf, E.S. et al., 2012. Migrating fibroblasts reorient directionality by a metastable, PI3K-dependent mechanism. *J Cell Biol*, 197(1), pp.105–114.
- Wennerberg, A. & Albrektsson, T., 2009. Effects of titanium surface topography on bone integration: a systematic review. *Clinical Oral Implants Research*, 20, pp.172–184.
- Wiche, G., 1998. Role of plectin in cytoskeleton organization and dynamics. *Journal of cell science*, 111 (Pt 1, pp.2477–86.
- Wiemerslage, L. & Lee, D., 2016. Quantification of mitochondrial morphology in neurites of dopaminergic neurons using multiple parameters. *Journal of Neuroscience Methods*, 262, pp.56–65.
- WIKTOR, B.R. et al., 2015. *Nanostructured gold surfaces coated by silica-based layers as SPR and MS imaging platform*, AVESTIA Publishing.
- Wilmut, I. et al., 1997. Viable offspring derived from fetal and adult mammalian cells. *Nature*, 385(6619), pp.810–813.
- Wilson, D.N. & Doudna Cate, J.H., 2012. The structure and function of the eukaryotic ribosome. *Cold Spring Harbor perspectives in biology*, 4(5), p.a011536.
- Wipff, P.-J. et al., 2009. The covalent attachment of adhesion molecules to silicone membranes for cell stretching applications. *Biomaterials*, 30(9), pp.1781–9.
- Wislet-Gendebien, S. et al., 2005. Astrocytic and neuronal fate of mesenchymal stem cells expressing nestin. *Brain Research Bulletin*, 68(1–2), pp.95–102.
- Woods, A., Wang, G. & Beier, F., 2005. RhoA/ROCK Signaling Regulates Sox9 Expression and Actin Organization during Chondrogenesis. *Journal of Biological Chemistry*, 280(12), pp.11626–

11634.

- Xiong, Y. et al., 2010a. Mechanisms Controlling Cell Size and Shape during Isotropic Cell Spreading. *Biophysical Journal*, 98(10), p.2136.
- Xiong, Y. et al., 2010b. Mechanisms Controlling Cell Size and Shape during Isotropic Cell Spreading. *Biophysical Journal*, 98(10), pp.2136–2146.
- Xu, J. et al., 2017. Effect of matrix stiffness on the proliferation and differentiation of umbilical cord mesenchymal stem cells. *Differentiation*, 96, pp.30–39.
- Yang, W. et al., 2016. Surface topography of hydroxyapatite promotes osteogenic differentiation of human bone marrow mesenchymal stem cells. *Materials Science and Engineering: C*, 60, pp.45–53.
- Yeager, K., LibGuides: SPSS Tutorials: Pearson Correlation.
- Yim, E.K.F. et al., 2010. Nanotopography-induced changes in focal adhesions, cytoskeletal organization, and mechanical properties of human mesenchymal stem cells. *Biomaterials*, 31(6), pp.1299–306.
- Yin, Z., Kanade, T. & Chen, M., 2012. Understanding the phase contrast optics to restore artifact-free microscopy images for segmentation. *Medical image analysis*, 16(5), pp.1047–62.
- Yoon, S.-H. & Mofrad, M.R.K., 2011. Cell adhesion and detachment on gold surfaces modified with a thiol-functionalized RGD peptide. *Biomaterials*, 32(30), pp.7286–96.
- Young, S.G. et al., 2014. Nuclear lamins and neurobiology. *Molecular and cellular biology*, 34(15), pp.2776–85.
- Yousef, G. et al., 2010. Shear stress induces osteogenic differentiation of human mesenchymal stem cells. *Regenerative Medicine*, 5(5), pp.713–724.
- Yu, H. et al., 2010. Mechanical behavior of human mesenchymal stem cells during adipogenic and osteogenic differentiation. *Biochemical and Biophysical Research Communications*, 393(1), pp.150–155.
- Yuan, Y., Gao, J. & Ogawa, R., 2015. Mechanobiology and Mechanotherapy of Adipose Tissue-Effect of Mechanical Force on Fat Tissue Engineering. *Plastic and reconstructive surgery. Global open*, 3(12), p.e578.
- Zand, M.S. & Albrecht-Buehler, G., 1989. What structures, besides adhesions, prevent spread cells from rounding up? *Cell Motility and the Cytoskeleton*, 13(3), pp.195–211.
- Van Zant, G. & Liang, Y., 2003. The role of stem cells in aging. *Experimental hematology*, 31(8), pp.659–72.
- Zernike, F., 1955. How I discovered phase contrast. *Science (New York, N.Y.)*, 121(3141), pp.345–9.
- Zhong, X. & Rescorla, F.J., 2012. Cell surface adhesion molecules and adhesion-initiated signaling: understanding of anoikis resistance mechanisms and therapeutic opportunities. *Cellular*

signalling, 24(2), pp.393–401.